Pushing the boundaries of microscopy in time and space: a microscope built for high-speed single-molecule imaging and a microscope built for microgravity

A thesis submitted in fulfilment of the requirements for the degree of Doctor of Philosophy by:

Katrina Easter Crompton

Newcastle University

Biosciences Institute – Faculty of Medical Sciences

July 2024

Abstract

Cell signalling is a fundamental biological activity by which cells respond and adapt to chemical signals in their environment. All cells have these processes; from single-celled organisms such as yeast to cells to multi-cellular organisms. Optical microscopy is the most common method for observing the activity of living cells, including cell signalling. This thesis describes work pushing microscopy to new heights, both figuratively and literally.

Firstly the limits of size and timescale were pushed to observe individual molecules of signal transduction proteins in live cells. Transcription factors are proteins that control gene expression, it is not yet fully known how these correctly find their DNA binding sites in a maze of many throughout the genome. It is thought that clustering may be a mechanism by which this is done, single-molecule fluorescence microscopy and *in vivo* stoichiometry analysis can elucidate this. Here a single-molecule fluorescence microscope was developed and optimised for highly inclined laminated optical-sheet (HILO) imaging capabilities and was used to image the transcription factors Mig1 in yeast, RelA in U2OS cancer cell lines and the androgen receptor (AR) in prostate cancer cell lines. Mig1-GFP results were compared to those previously obtained to assess the microscope function. HILO microscopy was used on cells before and after stimulation and the images analysed to measure changes in molecular complex size of these transcription factors before and after activation.

Secondly the limits of where microscopes can be used were explored. Gravityscope is a new microscope built to operate on board a parabolic flight, which offers microgravity (10^{-2}g) and hypergravity (2g) conditions. Cell signalling has been shown to be severely affected by low gravity across diverse areas from the human immune system, metabolism and in microorganisms such as yeast. Gravityscope was used to image yeast, a model cell signalling experiment: uptake of fluorescent glucose in yeast.

Declaration of work carried out

Chapter 1

The entire literature review was carried out by myself.

Chapter 2

Before I began work on the HILO/TIRF microscope, Adam Wollman had already added basic 488nm excitation optics to the Nikon microscope. I added further excitation optics for the 561nm laser including ND filters, a dichroic mirror, a beam shutter and a third flip lens. I also added a DV2 image splitter and temperature and CO_2 incubation modules. I carried out analysis on the microscope functionality including measuring the beam angle in relation to displacement of the HILO/TIRF lens, measuring the image pixel length and Airy Disk radius of GFP. All MATLAB functions were written by Wollman *et al.* I used these functions to analyse *in vitro* GFP simulations. I conducted fluorescent beads assays and analysed intensity results using the Wollman MATLAB functions. Lastly, I performed *in vitro* GFP assays and used the Wollman MATLAB functions to characterise image intensity.

Chapter 3

Vials of Mig1-EGFP::His3 NRD1-mCherry::hgrB yeast cells were created by Adam Wollman in 2019. I used these to culture yeast cells and imaged them using various conditions with the HILO/TIRF microscope. I used the Wollman MATLAB functions to characterise image intensity and cell stoichiometry. I compared some of my results to those published in Wollman *et al.* (2017). I also took some images of PAR6-GFP in *C. elegans* embryos which had been grown by Rodriguez *et al*. I analysed these images using the Wollman MATLAB functions and characterised the image intensity and cell stoichiometry. Lastly, I took images of 488-Aβ1-42 and 568-apoE2 which had been created by Haapasalo *et al.* I analysed these images using the Wollman MATLAB functions and characterised the image intensity and stoichiometry.

Chapter 4

U2OS cells at passage 20 had been acquired from the Newcastle University tissue culture facility cryogenic storage. I cultured these cells and transfected them with an eGFP-RelA plasmid. I took images of these cells using the HILO/TIRF microscope and used the Wollman MATLAB functions to characterise image intensity and cell stoichiometry. I also imaged AR-GFP

in LNCaP cells which had been cultured and transfected by Coffey *et al*. I used the Wollman MATLAB functions to characterise the image intensity and cell stoichiometry.

Chapter 5

The Gravityscope microfluidic syringe pump was designed by Connor Richardson and built by Jack Dawson, Yusuf Ugurluoglu and Alex Stokes. The Gravityscope microscope was based on the SQUID microscope design by Hongquan Li *et al.* (2020). Hongquan assisted with Gravityscope design for flight. The microfluidic sample systems and storage were designed by Alex Stokes and myself. Gravityscope and the microfluidic sample systems were built by myself, Alex Stokes, Koren Murphy and Tom Wareing. I conducted the pre-flight yeast strain tests and microscope vibration-resistance tests in the Wollman lab (and external van). Gravityscope flight sample images were taken by myself, Alex Stokes, Koren Murphy and Tom Wareing. I conducted the analyses on all images.

Katrina Easter Crompton

July 2024

Acknowledgements

Undoubtedly, the majority of my praise and gratitude is directed toward my supervisor Dr Adam Wollman. Thank you Adam.

Thank you to the Newcastle University Academic Track Fellowship scheme for funding my supervisor's progression onto a fellowship at Newcastle University and, in turn, my pursuit of a Doctor of Philosophy.

Thank you to the European Space Agency for running the 2022 Fly Your Thesis! Program and funding Team SUGAR's participation in The 79th ESA Parabolic Flight Campaign.

Thank you to the UK Space Agency, the Newcastle University Doctoral Enhancement Fund and the Newcastle University School of Mechanical Engineering for contributing funds which enabled Team SUGAR to build Gravityscope and travel to France to conduct the experiment.

Additionally, thank you to all of the people involved in making the work outlined in this thesis possible: Team SUGAR (Koren Murphy, Thomas Wareing, Annachiara Scalzone, Alex Stokes), Jack Dawson, Yusuf Ugurluoglu, Hongquan Li, Manu Prakesh, Nigel Savage, Yannick Bailhé, Felix Scharnhölz, Jeffrey Gorrissen, Neil Perkins, Iglika Ivanova, Sergey Melnikov, Majlinda Lako, Connor Richardson, Josana Rodriguez, John Packer, Mislav Oreb, Dereck McCusker, Kelley Coffey, Thiri San, Dimitra Chanzi, Helen Glenwright. Louise Hollingsworth. Michael Crompton.

Aus den Augen, aus dem Sinn.

If we do not observe, how are we to know?

Contents

Chapter 1 – Introduction

1.1 Introduction to optical microscopy

Optical microscopy is the most common method for observing and imaging living cells and microorganisms. Various inventions and breakthroughs make up the fabric of the field of microscopy from the very first, very basic two-lens compound microscope system created by Hans & Zacharias Janssen at the end of the sixteenth century (A. J. M. Wollman et al., 2015) to Hirschfield observing the first single molecule in 1976 using fluorescence microscopy (Hirschfeld, 1976).

Fluorescence microscopy has seen its own advances including manipulating the angle of the lightbeam before it hits the sample. At high angles this becomes total internal reflection fluorescence (TIRF) microscopy, first explained by Axelrod in 1981, whereby high signal is achieved by only illuminating a few hundred nanometres into the sample. A highly inclined laminated optical sheet (HILO) can also be used to achieve better signal by illuminating only a part of the cell, as first described by Tokunaga *et al.* in 2008. Part of this thesis focuses on developing and testing a single-molecule fluorescence microscope and optimising it for HILO microscopy. Various biological processes were imaged to test the microscope capabilities. This included tracking transcription factors such as the glucose repressor Mig1 in *Saccharomyces cerevisiae,* the NFkB immune-response regulator RelA in U2OS breast cancer cells and androgen receptor (AR) in LNCaP prostate cancer cells.

Throughout microscopy history several hurdles had to be overcome to improve sample image quality, the highest of these hurdles being image resolution. Image resolution remained an issue for hundreds of years and was thought to be a hard limit until the advent of super-resolution microscopy in 1993 with scanning near-field optical microscopy (SNOM) outlined by Betzig *et al.* (Betzig and Chichester, 1993) followed by stimulated emission depletion (STED) microscopy created by Hell in 2000 (Klar et al., 2000).

The field of microscopy is one of constant change with new approaches and image analysis techniques developing all the time. Microscopes have been developed to image biological processes and organisms in various environments, including in varying gravity conditions. Part of this thesis focuses on developing a new microscope for use on a parabolic flight offering microgravity (10^{-2}g) and hypergravity (2g) conditions. The capabilities of this microscope were

tested by imaging fluorescent glucose uptake by *Saccharomyces cerevisiae* on the ground and in flight.

1.1.1 Basic single convex lens magnification

An incident beam of light passing through a convex lens (figure 1.1) is focussed to a point, the focal point, F. The focal length, f, of a lens is defined by the thickness and curvature of the lens (Abramowitz et al., 2002). The size of an image of an object seen through a lens is determined by the real size of the object, I_R and the distance, d_j between the object and the lens system. The closer an object is to the lens, the greater the magnification. This is because the angle, θ_j subtended by I_R and d_j at the lens is increased (Abramowitz et al., 2002). This is depicted in figure 1.2; for the same size sample, the greater d_j is, the smaller θ_j becomes, for $j = 1,2,3$. This is defined as the angular distance. The greater this angular distance, the more information, or light, from the sample is magnified by the lens.

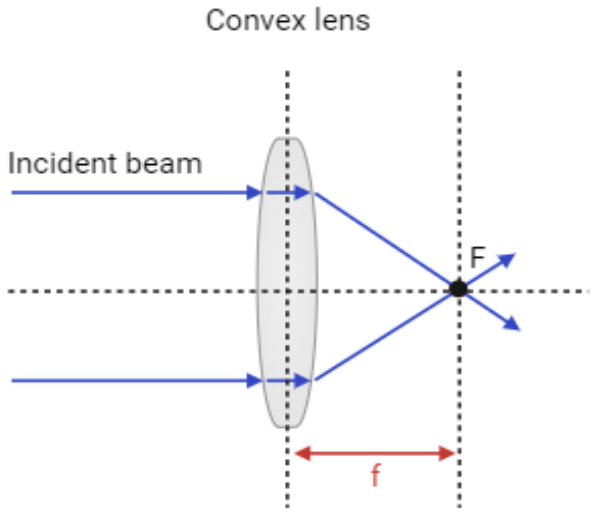

Figure 1.1 *Depiction of the focal length, f and focal point, F of a convex lens with an incident beam passing through. Image created in BioRender.com*

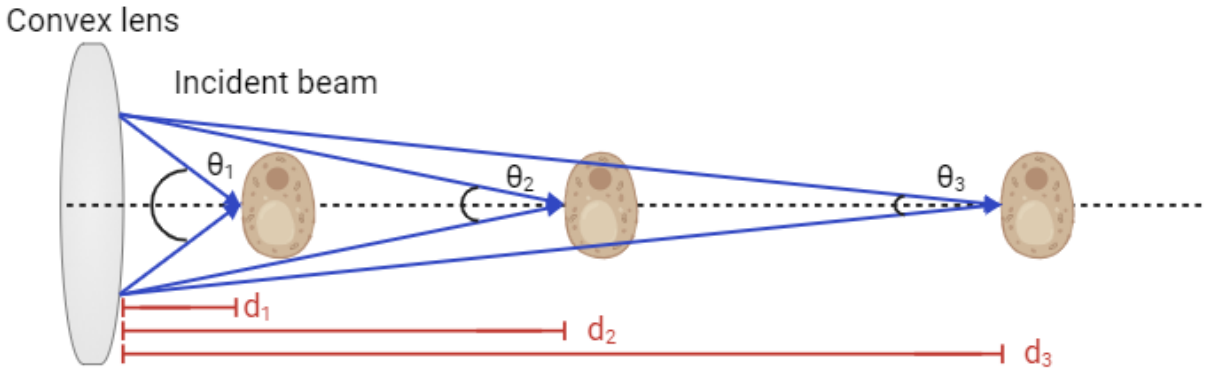

Figure 1.2 *Depiction of the angular distance of a convex lens. The angle, $\theta_j, j = 1,2,3$ is subtended by the size of the object and the distance, $d_j, j = 1,2,3$ between the object and the convex lens. For larger values of d_j we obtain larger angles, therefore a greater angular distance. Image created in BioRender.com*

A simplification of image magnification, m is given by;

$$m = \frac{I_A}{I_R} \quad (1)$$

where I_A is apparent size of the object (the size of the object we see when it is magnified by the lens) and I_R is the real size of the object.

In 1665, *Micrographia* by Hooke was published, it detailed several magnified observations he made with a single lens system including the eye of a fly, parts of plants and cork (Hooke et al., 1665). He described sections of cork as 'cells', resulting in the use of the word 'cell' in biology today (Mazzarello, 1999). Following this, van Leeuwenhoek used a single lens to observe samples magnified by up to 280 times. He was the first to describe blood cells and to describe the striations in muscle tissue (Carpenter, 1856).

1.1.2 The compound microscope

The compound microscope (figure 1.3) usually consists of at least two lenses; an objective lens which is placed near the sample for magnification and an ocular lens, an eyepiece used for viewing. The objective lens is responsible for image formation and magnification (Abramowitz et al., 2002).

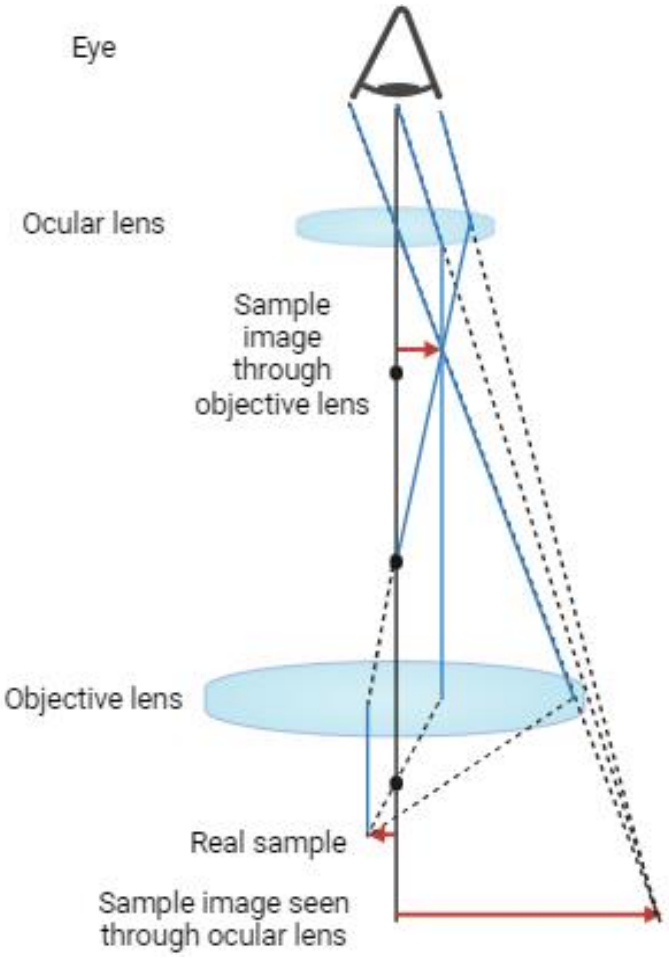

Figure 1.3 *Depiction of a simple compound microscope with an objective lens and ocular lens. The sample sits below the objective and an enlarged image is created just in front of the imaginary focal point of the ocular lens. A magnified image of the sample can be seen with the human eye. Image created in BioRender.com*

The distance between the objective lens and the ocular lens is known as the tube length, this is usually fixed as it depends on the focal lengths of objective and ocular lens. Adding any other optical instruments within this distance results in the objective or ocular lens having to be moved to correct magnification and resolution. However, more modern microscopes have another lens within the lens tube, the tube lens, and if the light rays passing from the objective to the ocular lens are parallel to one another then the light is focussed at infinity. The tube lens creates a real image of the object at the focus of the ocular lens. Therefore, the space between

the objective and tube lens can be of any length and any number of optical instruments can be added to it (Vangindertael et al., 2018).

The objective is placed close to the sample with either air or a medium of complementary refractive index, n between the angular aperture of the objective lens and the sample (Abramowitz et al., 2002). This medium can be water, oil, silicone oil or glycerol.

1.1.2.1 The refractive index and Snell's Law

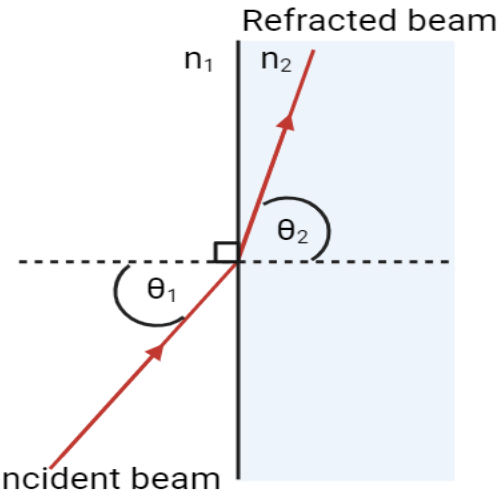

Figure 1.4 *Depiction of Snell's Law showing an incident beam of light in a medium of refractive index, n_1 travelling at angle θ_1 through a medium of refractive index, n_2, the refracted beam has a new angle of θ_2. Image created in BioRender.com*

The refractive index, describes how much a light beam, initially travelling at an angle θ_1, is bent, or refracted, when it passes from one medium with refractive index, n_1 through another medium with refractive index, n_2. The resulting angle, θ_2 of the refracted light beam through a medium with refractive index, n_2 is given by Snell's Law (figure 1.4);

$$n_1 \sin\theta_1 = n_2 \sin\theta_2 \quad (2)$$

The product of the angular aperture of the objective and the refractive index is known as the numerical aperture, NA given by;

$$NA = n \sin\theta \quad (3)$$

where $\theta = {}^{\theta_j}/_{2}$ is the half angle of light that the objective can collect. Objectives with higher NA can capture more light, or signal, from the sample. Typically, objective lenses which use air as a medium have NA values ranging from 0.1-0.95 and have lower magnification than water-based, silicone-oil-based and oil-based objectives which have NA values 1-1.51.

1.1.2.2 The magnification of a microscope

The magnification ability of an optical microscope is affected by the focal lengths of the lenses. The focal length, f of a convex lens is a measure of how much the lens converges to a focal point, F. Magnification in microscopy occurs when the sample is closer to the objective lens; a shorter focal length results in higher magnification. For a beam of light of radius, r_1 incident

upon a lens of focal length, f_1 and emerging at a radius, r_2 from a second lens of focal length, f_2, we have;

$$\frac{r_j}{f_j} = \tan(\theta_j), j = 1,2 \quad (4)$$

where θ_1, θ_2 are the half angles of the normal through the focal points of each lens. Due to the law of vertically opposite equal angles, we have $\theta_1 = \theta_2$, thus after rearranging we obtain;

$$\frac{f_2}{f_1} = \frac{r_2}{r_1} \quad (5)$$

If we define the ratio between the emergent beam radius, r_2 and the incident beam radius, r_1 as the magnification, M_1, we have;

$$M_1 = \frac{f_2}{f_1} \quad (6)$$

Equation (6) describes magnification as the ratio between the focal lengths of lenses that a beam of light travels through. Typically, optical microscopes are composed of a series of lenses used to magnify a sample illuminated by a light source, therefore, the overall magnification, M of a lightbeam travelling through k lenses of focal lengths $f_1, f_2, f_3, \dots f_k$ is given by;

$$M = \left(\frac{f_2}{f_1}\right)\left(\frac{f_4}{f_3}\right) \dots \left(\frac{f_k}{f_{k-1}}\right)\left(\frac{f_i}{f_{obj}}\right) \quad (7)$$

where f_i is the ocular lens and f_{obj} is the objective lens (Leake, 2013).

As brilliant as optical microscopy was for capturing some of the first microscopic organisms, there were several limitations to the spatial resolution, chromatic and spherical aberration, sample illumination, image contrast and imaging depth.

1.2 Limitations of optical microscopy

1.2.1 Resolution and Airy Disks

The resolution of a microscope is the smallest distance between two points such that the two points can be distinguished as separate from one another (Vangindertael et al., 2018). The spatial resolution of a light microscope is affected by the diffraction limit. Light microscopes utilise the far-field regime whereby there is a distance of several wavelengths of light between the light source and the detector (e.g. a camera). Fluorophores visualised with the far-field regime exhibit diffraction (Shashkova and Leake, 2017). The apertures of a light microscope are usually round and when light propagates through these they produce an Airy disk. The

shape of the Airy disk is determined by the point-spread function (PSF) of the microscope (Shashkova and Leake, 2017).

The PSF can be better explained using the single-slit experiment; the waves of a coherent light source passing through a pinhole or a small linear slit will change their behaviour. Before travelling through the slit, the waves move in the direction of propagation, however when passing through the slit, they convert to a cylindrical wavefront (Hecht, 2002). When the slit size increases, the wavefronts start to interfere with one another, causing diffraction patterns (Vangindertael et al., 2018). The PSF of a microscope refers to the concentric geometrical pattern resulting from the diffraction of light from a lightsource passing through a lens, which acts as a circular aperture, being spread out when it reaches the detector (e.g. camera) (Vangindertael et al., 2018) (figure 1.5). The bright circle surrounded by alternating dim and bright concentric rings pattern produced on the image plane is referred to as the Airy pattern, the centre of which being the Airy Disk (Hecht, 2002).

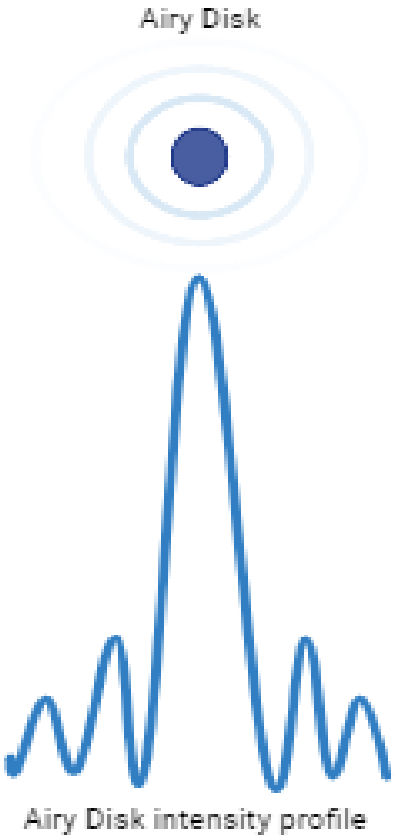

Figure 1.5 *An Airy Disk profile showing a point object surrounded by concentric light and dim rings, following an intensity profile shown below. Image created in BioRender.com*

A 2D Bessel function can be used to describe the intensity profile of an Airy Disk ring pattern. The first of the dimmer circles has diffraction angle, α and satisfies;

$$\sin\alpha \approx 1.22\frac{\lambda_m}{2r} = 0.61\frac{\lambda_m}{r} \tag{8}$$

where r is the is the radius of the circular aperture through which the light passes and λ_m is the wavelength of light when it is in the imaging medium with refractive index, n, given by;

$$\lambda_m = \frac{\lambda}{n} \tag{9}$$

where λ is the wavelength of light in a vacuum.

Usually for a microscope, the circular aperture through which the light passes is an objective lens of focal length, f and therefore we have a lateral distance, d from the optic axis to the first dim ring given by;

$$d = f \sin \alpha_{max} \tag{10}$$

where $\alpha_{max}$is the maximum diffraction angle of the first dim ring. If we substitute equation (9) into equation (8) and substitute in a rearranged equation (10) where $\frac{d}{f}$ is the subject then rearrange and substitute these into equation (3) then we obtain;

$$d = 0.61 \frac{\lambda}{NA} \tag{11}$$

where d is the minimum distance that can differentiated between two points, λ is the wavelength of the incident light and NA is the numerical aperture of the objective. This is the equation as set out by Abbe in the nineteenth century (Hecht, 2002). If two Airy Disks overlap, the distance between them will be equal to d. The Rayleigh Criterion for the optical resolution limit states that two point sources can be resolved as distinct from one another if the distance between their images is at or above the value of the Airy Disk radius (equation (11)).

For many years after the description of the diffraction limitation to light microscopy by Abbe, improvements to spatial resolution were only made by using lower wavelengths of light such as UV or using electrons (electron microscopy (Hayat, 1974)) rather than photons to illuminate samples (A. J. Wollman et al., 2015). However, electron microscopy cannot be used in live- cell microscopy as samples are always fixed due to the nature of illumination. Electrons do not interact well with organic material so samples are stained with heavy metals which the electrons interact better with (Day, 2014).

1.2.2 Chromatic and spherical aberration

A further limitation of light microscopy is chromatic aberration caused by dispersion; when a lens does not focus all wavelengths of light onto the same point. Chromatic aberration causes blur of the sample image.

The achromatic lens was invented by Chester Moore Hall and consisted of two lenses made of two different materials fused together; these focussed light of different wavelengths onto the same focal point (Willach and Cook, 1997). This reduced the impact of chromatic aberration during microscopy.

A further microscopy issue caused by lens quality is spherical aberration; light wavelets incident upon a spherical lens that don't hit the centre of the lens are refracted or reflected more than those that do hit the centre; this means that not all of the light wavelets converge to the focal point. Abbe invented an apochromatic lens which fuses more lenses together and reduces both chromatic and spherical aberrations (A. J. Wollman et al., 2015).

1.2.3 Sample illumination

Early-day optical microscopes had limited sample illumination abilities. One example being image glare; an image of the lightsource being visible in the image of the sample.

In the nineteenth century, Abbe invented a system to focus light with multiple lenses, the *Abbe Condenser* (A. J. Wollman et al., 2015). This collects light from the microscope lightsource and concentrates it into a light cone. At higher magnifications, a condenser lens can make images appear sharper, however at lower magnifications the condenser lens can limit the field of view (FOV).

In 1893, *Köhler Illumination* was first demonstrated (figure 1.6). Light from the lightsource collected by a collector lens is focussed through an aperture iris diaphragm. This focussed light is projected onto the sample by a condenser lens. The objective lens collects transmitted light from the sample, this is then focussed through a field iris diaphragm before it is collected by the ocular lens. Due to its advantages such as reducing image glare and providing uniform illumination of the sample, Köhler Illumination is still used in modern brightfield microscopy.

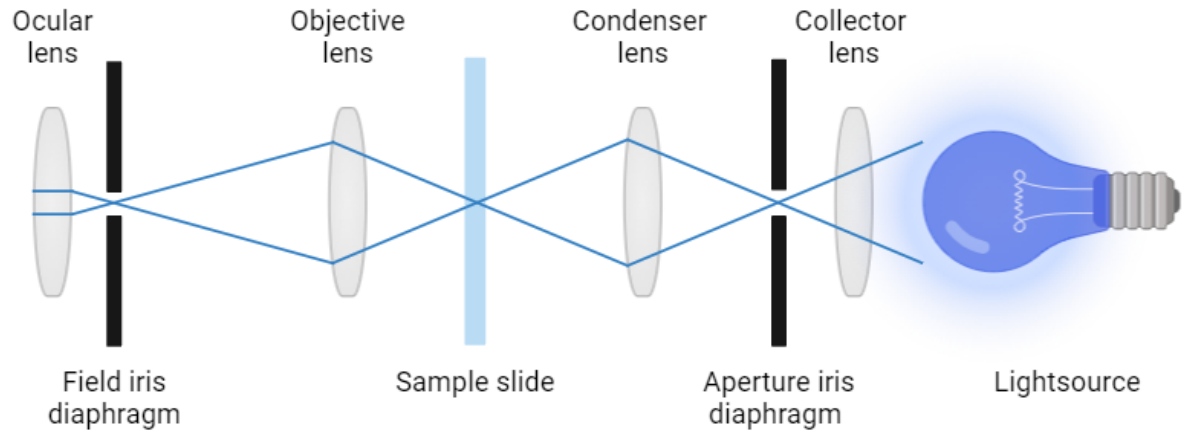

Figure 1.6 *Depiction of Köhler illumination (from right to left); an excitation beam from a lightsource travels through the collector lens and is focussed through an aperture iris diaphragm. The light then passes through a condenser lens before focussing at the sample. The emission light from the sample travels through the objective lens and a field iris diaphragm and the image of the sample is projected on an ocular lens (e.g. a camera). Image created in BioRender.com*

1.2.4 Image contrast

Optical microscopes also suffer from reduced image contrast; biological samples are usually composed of water and are surrounded by a water-based solution, causing meagre transmitted image intensity and limitations in the ability to distinguish a sample from the background media surrounding it. Various methods have been developed to improve image contrast in light microscopy including phase contrast, differential interference contrast (DIC) and darkfield.

1.2.4.1 Phase contrast microscopy

Phase contrast microscopy, developed by Zernike (Zernike, 1942), illuminates a transparent sample by converting the light phase shifts that pass through it into brightness changes in the image (Zernike, 1955). A ring of illumination is created by placing a circular annulus in front of the lightsource. Light passing through the sample is out of phase, shifted by 90° relative to the background light. A circular phase plate below the objective shifts the incoming light by 90° so it is in phase, therefore improving image contrast (A. J. Wollman et al., 2015). A disadvantage of phase contrast microscopy is that the circular plates used reduce the working NA of the objective which reduces image resolution. The circular plates can also create artifacts in the image, therefore reducing image quality. However, apodised phase contrast microscopy reduces these artifacts and increases image contrast by utilising selective amplitude filters (Dokland, 2006).

1.2.4.2 Differential interference contrast (DIC) microscopy

Differential phase interference contrast (DIC) microscopy was created and further developed by Smith (Smith, 1955) and Nomarski (Nomarski and Weill, 1955) in 1955. For DIC, unpolarised light entering the microscope is polarised at 45°. A Nomarski-modified Wollaston prism is used to separate this light into two rays polarised orthogonally to each other; one ray is the sample ray and the other is the reference ray. These rays pass through the condenser lens and adjacently hit the sample where they experience different optical path lengths due to differences in the refractive index of the sample. A phase change occurs in one ray but not the other. The rays then pass back through the objective and though a second Nomarski-modified Wollaston prism which combines the rays to create an image. A disadvantage of DIC is that, as in phase contrast microscopy, artifacts can be created in the image from the phase changes.

1.2.4.3 Darkfield microscopy

In darkfield microscopy light is sent through the condenser lens to the sample at an angle that cannot pass through the angular aperture of objective. The light can only pass through if it is diffracted, refracted or reflected by the sample. This creates an image of a light sample atop a dark background (Dokland, 2006).

Advantages of darkfield microscopy are that it is relatively straightforward to set up and can be used on living samples. Additionally, unlike phase contrast microscopy and DIC, artifacts are not created in the image as it does not utilise interference or circular plates.

1.2.5 Depth of field and working distance

The depth of field is the distance (usually in microns) between the closest, in-focus object plane and the farthest, in-focus object plane. The depth of field is usually referred to as the axial (z-direction) resolving power of the microscope objective and it is dependent on the NA. With higher NA, the depth of field reduces. This means there is a trade-off between magnification and resolution. The optical microscope has a limited depth of field and can only focus on narrow sections of the sample at a time which can cause parts of the sample to be blurred.

The working distance is the distance between the objective and the sample and determines how far into the sample we can focus. Usually the working distance decreases as the NA increases. Increasing the working distance allows us to see further into the sample. This results in another trade-off between magnification and resolution.

The Schmidt objective (Voigt et al., 2023) uses a spherical mirror and a refractive correction plate instead of lenses; this yields a higher NA (0.69-1.08), larger FOV (1.1-1.7mm) and a longer working distance (11mm) for optical microscopy (Balasubramanian et al., 2023).

1.3 Utilising fluorescence in optical microscopy

The observation of fluorescence has its origins rooted in 1845 when Herschel scrutinised the emission of blue light from quinine as it was hit with sunlight (Herschel, 1997). After this, Helmholtz noted that objects within an image can be better differentiated if, rather than just being illuminated by an external lightsource, they were intrinsically fluorescent (von

Helmholtz, 1874). The turn of the twentieth century saw Zeiss and Reichert develop the first fluorescence microscopes (Heimstädt, 1911; Lehmann, 1913; Reichert, 1911). Sixty years later, in 1976, Hirschfield observed the first single molecule using fluorescence microscopy (Hirschfeld, 1976). Since then, fluorescence microscopy has been used extensively to study and image many biological processes such as transcription (Janissen et al., 2022; Munsky et al., 2015), diffusion (Xiang et al., 2020) and signalling (Marchetti et al., 2013; Tian et al., 2017).

1.3.1 Fluorescence

Fluorescence occurs when a single light photon is absorbed by a fluorophore at a particular wavelength, an electron within the fluorophore which is at ground state is excited and transitions to a higher energy state. A photon is emitted with a longer wavelength than the excitation wavelength when the electron relaxes to a lower energy state. A Jablonski diagram (figure 1.7) can be used to depict the transitions between these energy states (Jablonski, 1933).

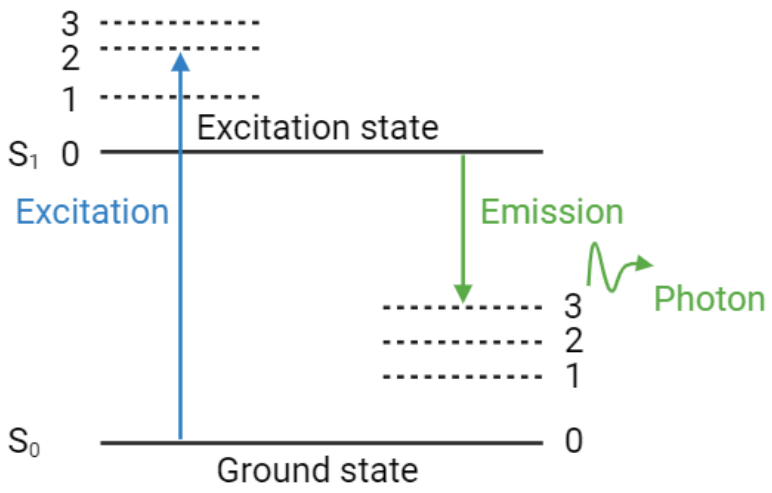

Figure 1.7 *Jablonski diagram. Excitation of photons from ground state, S_0, to a higher energy level state, S_1 then during emission, the photon loses energy and returns to S_0. Image created in BioRender.com*

1.3.2 Fluorescent tags and dyes

To observe a molecule of interest in a sample using fluorescence microscopy, the molecule must first have a fluorescent tag or dye attached to it. These emit light when excited, thus allow the user to see the molecules within a sample. There are a range of methods including fluorescent proteins, organic fluorophores, immunofluorescence labelling and PAINT.

1.3.2.1 Fluorescent proteins

Fluorescent proteins (FPs) are molecules typically of mass 25-30kDa that exhibit fluorescence (Kremers et al., 2011). The green fluorescent protein (GFP) was discovered in 1962 in the *Aequorea victoria* Jellyfish (Shimomura et al., 1962) and was cloned in 1992 (Prasher et al., 1992). Usually, an FP is introduced to the cell through genetic encoding; the FP is expressed as a fusion tag to the protein of interest.

Multicolour labelling can be achieved by expressing multiple FP 'colours' in cell samples, allowing simultaneous imaging of multiple cellular processes, compartments or proteins (Hickey et al., 2022). However, FPs have wide fluorescence profiles so there is spectral overlap between the different 'colour' markers (Specht et al., 2017; Wei et al., 2017).

Advantages of using FPs are that the sample cell does not need to be permeabilised unlike when using other probing methods (Miyawaki and Yusuke, 2015) and that cells do not need to be fixed (Hickey et al., 2022). A disadvantage of FPs is that they tend to have a lot of background fluorescence. However, recently Wu *et al.* used FPs bound to RNA aptamers to trigger a 'turn-on' fluorescence response, allowing visualisation of mRNA in human embryonic kidney 293 (HEK293) cells using an inverted microscope with epifluorescence (Wu et al., 2019), thus improving background fluorescence. A further disadvantage of standard FPs is that they irreversibly photobleach following a certain time period, they cannot be tracked after this, meaning they aren't well-suited to imaging on longer timescales (Shashkova and Leake, 2017). Although, SNAP-tags and HALO-tags are linkers that allow a fluorescent probe to be added to a protein; the encoding DNA of a primary protein probe is genomically fused to the protein of interest. The name SNAP-tag is a registered trademark of New England Biolabs. A SNAP-tag is labelled to the protein of interest and then a fluorescently labelled guanine is added which links to a cysteine on the protein of interest through a chemical reaction. HALO involves using a haloalkane dehalogenase enzyme (Los et al., 2008). Following these processes, the cell is incubated with a secondary fluorescently labelled probe, this binds to the primary protein probe. A brighter and more photostable fluorophore, compared to standard FPs, is yielded using this method, thus yielding greater localisation precision of the protein of interest (Shashkova and Leake, 2017).

GFP was used as the label of choice for all of the work outlined in this thesis, including *in vitro* GFP assays, Mig1-GFP in yeast cells and RelA-GFP in U2OS cancer cells and AR-GFP in LNCaP cells. This was because GFP is widely used and well-characterised. Additionally, the Wollman strain of budding yeast was stably transfected with GFP (Wollman et al., 2017). This work was used as a basis for comparison when imaging Mig1-GFP with the HILO/TIRF microscope to observe if the same results could be obtained, it was also used as a basis of comparison for the clustering characteristics of transcription factors. Furthermore, GFP was an easy label to use in *in vitro* assays which were important to initially test differences between imaging

conditions before imaging GFP labels in other organisms. It was also relatively easy and inexpensive to transfect U2OS cells with a RelA-GFP plasmid.

1.3.2.2 Organic fluorophores

Organic fluorophores are composed of fluorescent chemicals such as rhodamine, cyanine, oxazine, bodipy and perylene which emit light when excited. They can be used as a fluorescent dye by covalently bonding to molecules within the sample (Ha and Tinnefeld, 2012).

An advantage of organic fluorophores is their size; they are one hundred to one thousand times smaller than FPs [161] and are thus less invasive to a cell (Zheng et al., 2014). A further advantage is that they can act as drug-masks, thus allowing the visualisation of drug delivery in real time (Hickey et al., 2022). Gunnlaugsson *et al.* studied chemosensors based on the 1,8-naphthalimide scaffold and visualised glycosidase activity in cancer cell lines (Calatrava-Pérez et al., 2016).

1.3.2.3 Immunofluorescence labelling

A further labelling method is immunofluorescence; a method by which single molecules can be dyed with antibodies (Coons et al., 1942). There are direct and indirect immunofluorescence approaches. The direct approach employs the use of a primary antibody only, this antibody is chemically linked to a fluorophore and binds to the molecule of interest. The indirect approach first uses a primary (non-fluorescent) antibody to bind to the molecule, a secondary antibody (fluorescent) is then attached. Direct immunofluorescence labelling is often quicker to implement than indirect as there are less steps involved in the process (Vangindertael et al., 2018). The advantage of indirect immunofluorescence labelling over direct lies in variety – for a primary antibody, many secondary antibodies and detection methods can be used. However, disadvantages, in general, of antibody labelling are owed to their relatively large size, approximately 10nm, because of this, cells need to be fixed to let the antibody enter and once inside it can be difficult to localise accurately (Vangindertael et al., 2018).

1.3.2.4 Point accumulation in nanoscale topography (PAINT)

Original PAINT involves targeting molecules with freely diffusing dyes (Sharonov and Hochstrasser, 2006). An advantage of PAINT is that photoswitching can be implemented without the need of particular experimental conditions. However, when using PAINT it is difficult to specifically label more molecules of different kinds (Schnitzbauer et al., 2017).

DNA-PAINT is similar to original PAINT, but also allows the user to use DNA molecules as imaging and labelling probes which can be programmed. DNA-PAINT has been used to observe cellular proteins on the nanometre scale (Schnitzbauer et al., 2017).

An advantage of DNA-PAINT is that more photons can be collected during imaging than with other labelling methods because DNA-PAINT is not affected by photobleaching as the labels can be replenished from solution (Jungmann et al., 2016). However, using DNA-PAINT results in a lot of background fluorescence, therefore it can only really be used with oblique illumination microscopy methods such as TIRF or light-sheet microscopy. Additionally, DNA-PAINT is not best used on living cells due to unforeseen stress effects that would be imposed on the cell by introducing nucleic acids (Schnitzbauer et al., 2017).

1.3.3 Fluorescence microscopy

To get a better picture of cellular processes, it is important to observe single molecules within cells. Mammalian cells are typically on the lengthscale of microns while the molecules within them such as protein complexes and membrane domains are on the lengthscale of nanometres (Möckl and Moerner, 2020). Fluorescence microscopy improves image contrast by utilising a narrow emission fluorescent beam incident upon the sample. The beam wavelength is absorbed by the labelled molecules in the sample and light is emitted from the labels at a longer wavelength (Lichtman and Conchello, 2005). A dichroic mirror is used, usually positioned at an angle of 45°, to separate excitation from emission light by reflecting excitation light but allowing emission light, of a longer wavelength, to pass through to the detector (Vangindertael et al., 2018).

1.3.3.1 Epifluorescence microscopy

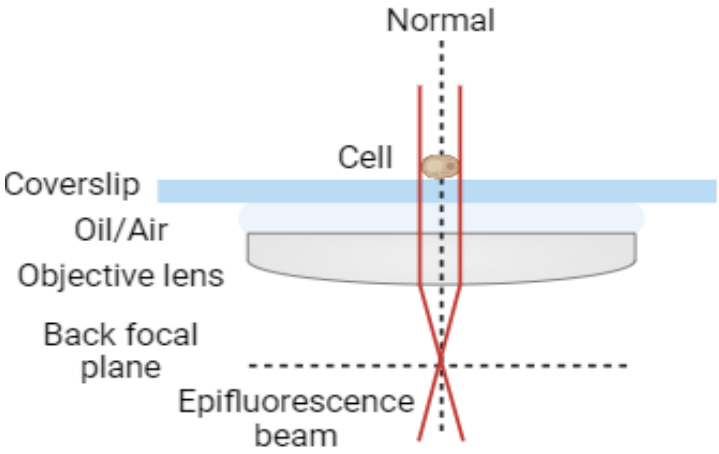

Figure 1.8 *Depiction of an epifluorescence beam profile which passes through the objective lens parallel to the Normal position. Image created in BioRender.com*

Epifluorescence microscopy (figure 1.8) usually involves using the objective as both the magnifier and condenser lens (Vangindertael et al., 2018). The angle of the excitation beam incident upon the sample is 0°, therefore is parallel to the emission beam; this generally illuminates an entire cell.

Slimfield epifluorescence involves sending a collimated beam through the objective lens. This increases the beam focus, therefore exciting smaller areas of the sample with higher intensity (Reyes-Lamothe et al., 2010). The SNR can be increased by employing this method. This method was utilised by Wollman *et al.* to capture Mig1-GFP translocating in budding yeast cells (Wollman et al., 2017). Narrowfield epifluorescence involves collimating the beam after it has passed through the objective and can be used to increase SNR and to image only sub-cellular features (Leake, 2013). When the angle of incidence reaches a critical angle, θ_c=61°, we have Total Internal Reflection Fluorescence (TIRF) microscopy.

1.3.3.2 TIRF Microscopy

When the angle of incidence of an excitation lightbeam reaches a critical angle, θ_c=61° then total internal reflection occurs whereby the incident beam is reflected off the bottom of the sample slide rather than passing through the sample (Jialei Tang and Young Han, 2018). This is called Total Internal Reflection

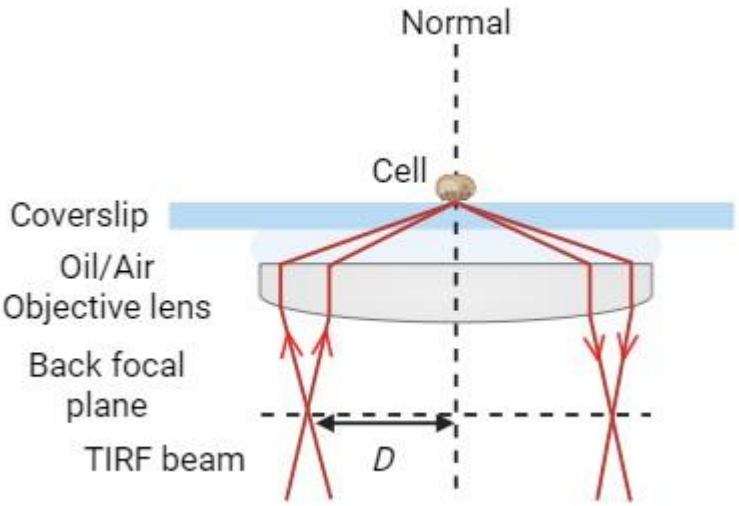

Figure 1.9 *Depiction of a TIRF beam profile though an objective lens where D is the distance of the incident beam from the Normal position. Image created in BioRender.com*

Fluorescence (TIRF) microscopy (figure 1.9).

The critical angle, θ_c can be determined by rearranging Snell's Law of refraction (equation (2)), providing a trigonometric relationship between the critical angle and the refractive indexes of the glass sample slide, n_g and the water surrounding the sample, n_w;

$$\theta_c = \arcsin\left(\frac{n_w}{n_g}\right) \tag{12}$$

Typically these values are measured to be n_w=1.33 and n_g=1.52 yielding a typical critical beam angle of 61°. This results in the beam being reflected when it reaches the sample slide.

The TIRF method was first described by Axelrod in 1981 and was used to visualise the membrane and underlying cytoplasmic structures at cell substrate contacts while dramatically reducing autofluorescence from debris and thick cells. This method involved placing a quartz cube in optical contact with the upper surface of a coverslip, in contact with the sample, with a thin layer of glycerol (Axelrod, 1981).

In 1989 Axelrod & Stout described conditions to achieve TIRF microscopy without the need of a quartz cube, instead they modified the epifluorescence beam angle by placing an opaque disk in the illumination path, allowing the epifluorescence beam to travel at supercritical angles (Stout and Axelrod, 1989). The usual setup for TIRF microscopy now is not to use a prism, but to use *through-the-objective* TIRF with an inverted microscope with a beam profile resembling that in figure 1.9 (Axelrod, 2003).

Single molecules were first detected using TIRF in 1995; ATP turnover was monitored in *in vitro* single myosin molecules (Funatsu et al., 1995) and live cells were first imaged using TIRF in 2000 on fluorescently labelled epidermal growth factor (EGF) receptors (Sako et al., 2000).

During TIRF microscopy, none of the excitation beam itself is transmitted into the sample, rather parts of the sample which are close to the surface of the sample slide are illuminated by the energy, $E(z)$ released from the beam in the form of an evanescent wave. This energy is an exponential decay function of the vertical distance, z of the beam of wavelength, λ from the sample;

$$E(z) = E(0)e^{-\frac{z}{d_e}} \tag{13}$$

where the depth of penetration, d_e of the beam energy into the sample is given by;

$$d_e = \lambda\left[4\pi\sqrt{n_g^2 \sin^2\theta - n_w^2}\right]^{-1} \quad (14)$$

The intensity of the evanescent wave depletes exponentially with distance from the interface between the sample and the slide (Shashkova and Leake, 2017).

There have been several variable-angle (VA-TIRF) and multi-angle (MA-TIRF) approaches to improve the penetration depths of the evanescent waves by altering the beam angle during TIRF microscopy. Burmeister *et al.* used VA-TIRF microscopy to image well-spread bovine aortic endothelial cells stained with a membrane-bound carbocyanine dye. At angles above the critical angle of 64°, the dorsal and ventral membranes were illuminated. At angles above 66°, only focal contacts were illuminated and at angles above 74°, images were dominated by background noise (Burmeister et al., 1994).

An advantage of TIRF microscopy is that it reduces background signal because only single molecules close to the slide surface are illuminated. However, only objects very close to the surface are observable with TIRF (Axelrod, 1981). Hence, TIRF is mainly used to observe phenomena occurring at the cell membrane while other methods such as HILO microscopy can be used to observe activity within the cell.

1.3.3.3 HILO microscopy

An excitation beam positioned at angles above epifluorescence and below the critical angle generates what is known as HILO (Highly Inclined Laminated Optical-sheet) microscopy (figure 1.10A). This involves inclining the excitation beam and reducing the illumination area (Tokunaga et al., 2008a).

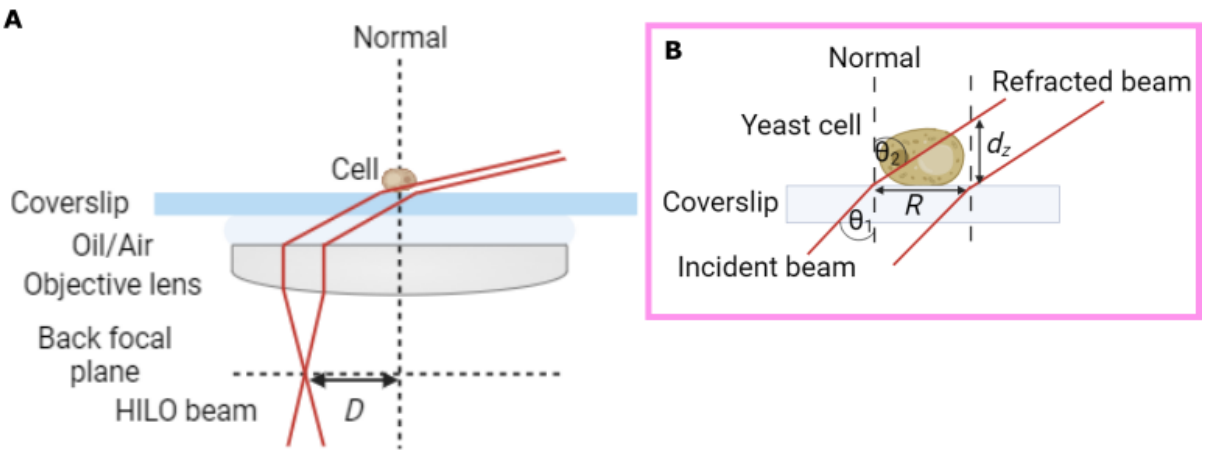

Figure 1.10 A. *Depiction of a HILO fluorescence beam profile travelling through an objective lens where D is the distance of the incident beam from the Normal position whereby* ***B.*** *the incident beam is at*

angle θ_1 and is refracted to an angle θ_2 as it passes through the coverslip. The refracted beam has thickness d_z which illuminates the sample area with radius R. Image created in BioRender.com

The beam is inclined by increasing the angle of incidence, θ by displacing the beam on the objective. Only the parts of the cell which the excitation beam passes through are illuminated. An advantage of this is that it makes for increased SNR due to a decrease in background signal. HILO has been used to achieve up to 7.6 times improved SNR relative to epifluorescence (Gardini et al., 2023) and has been used in various widefield and single-molecule localisation applications (Chong et al., 2018; Ganji et al., 2018; Hansen et al., 2017; Izeddin et al., 2014; Jungmann et al., 2014; Landgraf et al., 2012; Nozaki et al., 2017; van de Linde et al., 2011).

The thickness, d_z of the refracted lightsheet is given by;

$$d_z = \frac{R}{\tan\theta} \tag{15}$$

where R is the diameter of the illuminated area at the sample plane and θ is the angle of the beam as it hits the plane (figure 1.10B). Therefore, the beam can be made thinner by decreasing R or increasing θ (Gardini et al., 2023).

The usage of HILO microscopy as a method for increasing image intensity while reducing background intensity yielding an SNR 8 times greater than that of epifluorescence was first described by Tokunaga *et al.* in 2008 (Tokunaga et al., 2008a). Ten years later, Tang & Han described a HILO method involving a confocal slit detection, producing 2 times thinner illumination and over 40 times larger imaging area than conventional HILO microscopy, again increasing the SNR (Jialei Tang and Young Han, 2018). More recently, Gardini *et al.* presented the impact of reducing the HILO beam thickness to dimensions smaller than cell radii (less than 3µm); this reduced the background fluorescence from out-of-focus planes and improved image quality (Gardini et al., 2023). Additionally, HILO microscopy has been combined with software techniques to produce background-free images by subtracting the estimated background, one such being the V-HiLo-ED edge detection method proposed by Hu *et al.* (Hu et al., 2022). HILO has been described to improve SNR by up to 32% compared to epifluorescence and has been used to achieve a 118% increase in the number of single molecules detected within stationary phase particles (Neria and Kisley, 2023). HILO has also been used to image, several micrometres deep, the interaction of GFP-importin-β and nuclear pore complexes in *C.elegans* embryos (Tokunaga et al., 2008b).

Epifluorescence microscopy was used in some of the imaging of Mig1-GFP in yeast outlined in this thesis. This was to produce comparisons to (Wollman et al., 2017) to verify the microscope capabilities. HILO microscopy was used to image Mig1-GFP in yeast, *in vitro* GFP and fluorescent beads in various ways, such as changing the angle of the HILO profile, from 45° to 56°, and changing the placement of the beam centre while using a HILO profile. After this, HILO microscopy was used to image RelA-GFP in U2OS cancer cells before and after stimulation with tumour necrosis factor α (TNF-α) and to image AR-GFP in LNCaP cells before and after stimulation by R1881 to test if the microscope could capture clusters of transcription factors.

1.3.3.4 Confocal microscopy

Confocal microscopy (figure 1.11), first patented by Minsky in 1961 (Minsky, 1961), involves using a pinhole in front of the lightsource which results in only a small point of the sample being illuminated. Another pinhole resides behind the detector which results in only focussed signal being collected (Minsky, 1988).

Later, confocal laser scanning microscopy (CLSM) was invented whereby the small pinhole of light is scanned across the sample (Pawley, 2006). An advantage of confocal microscopy and CLSM is greatly increased SNR because a lot of unfocussed background fluorescence is removed. However, a disadvantage of CLSM is the long time it takes to scan an entire sample (Shashkova and Leake, 2017).

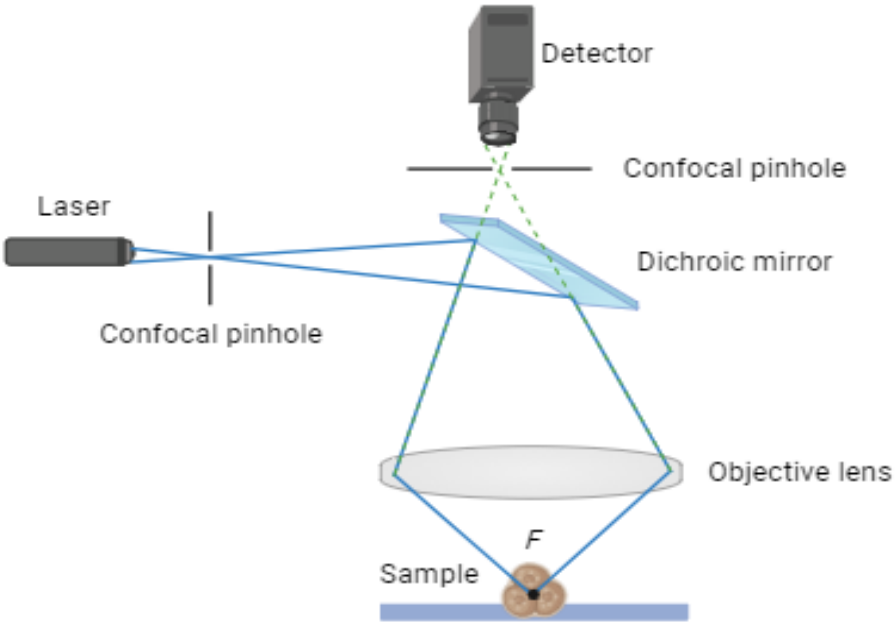

Figure 1.1 1 *Depiction of confocal microscopy where F is the focal point of the objective lens. Excitation light from a lightsource passes through a confocal pinhole before reaching the sample and emission light from the sample also passes through a confocal pinhole before reaching the detector. Image created in BioRender.com*

1.4 Super resolution microscopy

Super-resolution microscopy occurs when optical imaging can be used to produce spatial information above the limit set by the Rayleigh Criterion (Shashkova and Leake, 2017).

1.4.1 Scanning near field optical microscopy (SNOM)

The advent of super resolution microscopy came in the form of scanning near field optical microscopy (SNOM) developed by Betzig in 1993 (Betzig and Chichester, 1993). This involves focussing an excitation beam through an aperture with a diameter smaller than the excitation wavelength which creates an evanescent wave. This thin beam only penetrates a small section of the sample at a time with small sample penetration. An image is created by scanning the beam across the entirety of the sample (A. J. Wollman et al., 2015).

1.4.2 Stimulated emission depletion (STED) microscopy

In 2000, Hell described stimulated emission depletion (STED) microscopy (Hell and Wichman, 1994; Klar et al., 2000; Klar and Hell, 1999) which involves utilising two laser beams; one excitation beam and one stimulated emission beam. The emission beam is approximately 200-300nm offset from the excitation beam and has a longer wavelength (Leake, 2013). All fluorophores except those in the centre of the illumination volume are switched off (Klar et al., 2000). The image is formed by scanning the focal point across the sample. The lateral resolution, R_x that can be yielded when using STED microscopy is given by;

$$R_x = \frac{\lambda}{2NAI_{sq}} \tag{16}$$

where λ is the wavelength of the incident light and;

$$I_{sq} = \sqrt{1 + \frac{I_{STED}}{I_{sat}}} \tag{17}$$

where I_{STED} is the STED intensity and I_{sat} is the saturation intensity of the fluorophore (Vangindertael et al., 2018). Usually, I_{sat} takes on values in the order of 0.1-1GWcm^{-2} (Blom and Widengren, 2017; Vicidomini et al., 2011) which is much higher than saturation intensities applied in other microscopy methods such as confocal. This can cause photobleaching and phototoxic effects in live cells (Blom and Widengren, 2017). However, photoswitchable fluorophores can be used to improve this (Vangindertael et al., 2018).

STED can be used to minimise the width, w of the Airy disk which is given by;

$$w = \frac{\Lambda}{2NA\sqrt{1+\frac{I_f}{I_s}}} \quad (18)$$

where Λ is the STED depletion beam wavelength, NA is the numerical aperture, I_f is the excitation intensity centred on the fluorophore and I_s is the saturating intensity of the STED depletion beam (Ando et al., 2002; Hell and Wichman, 1994; Klar and Hell, 1999).

Alvelid *et al.* combined STED microscopy with widefield imaging for event detection to automatically select events such as protein recruitment and biosensor activity and image them with high resolution. Using GPU accelerated peak detection, they processed data in milliseconds (Alvelid et al., 2022). Groβe *et al.* used STED to show that the apoptotic Bax protein forms rings on the surface of mitochondria (Große et al., 2016).

Advantages of STED are that it can be used to image thicker samples, it has *in vivo* applications due to its fast acquisition and no image-processing is required after imaging, the super-resolution image is immediately available (Tam and Merino, 2015). However, it can be slower to create images with larger FOVs.

1.4.3 Structured illumination microscopy (SIM)

Also in 2000, Gustafsson developed structured illumination microscopy (SIM) (figure 1.12) whereby lateral resolution is improved through use of uniform illumination and controlled modulation of excitation light. SIM can be used to improve image resolution by twice as much (Gustafsson, 2000).

A moving grid is projected onto the sample and multiple images are recorded while the grid moves and creates a Moiré effect interference pattern (Gustafsson, 2000). Recently, the image-processing algorithm for SIM has been enhanced and can provide a spatial resolution of about 60nm (Hickey et al., 2022). Figure 1.12 depicts SIM and is similar to the depiction in the paper (Gustafsson, 2000). The lenses L_1 and L_2 are in telecentric arrangement with the objective; achieving constant magnification despite the distance or location of an item in the FOV.

SIM can be used to image dynamic events as it employs the use of digital cameras rather than single point detectors for detection, allowing frame rates exceeding 100 frames per second (Hinsdale et al., 2021). However, the interference pattern can produce artefacts on the final image (Shashkova and Leake, 2017).

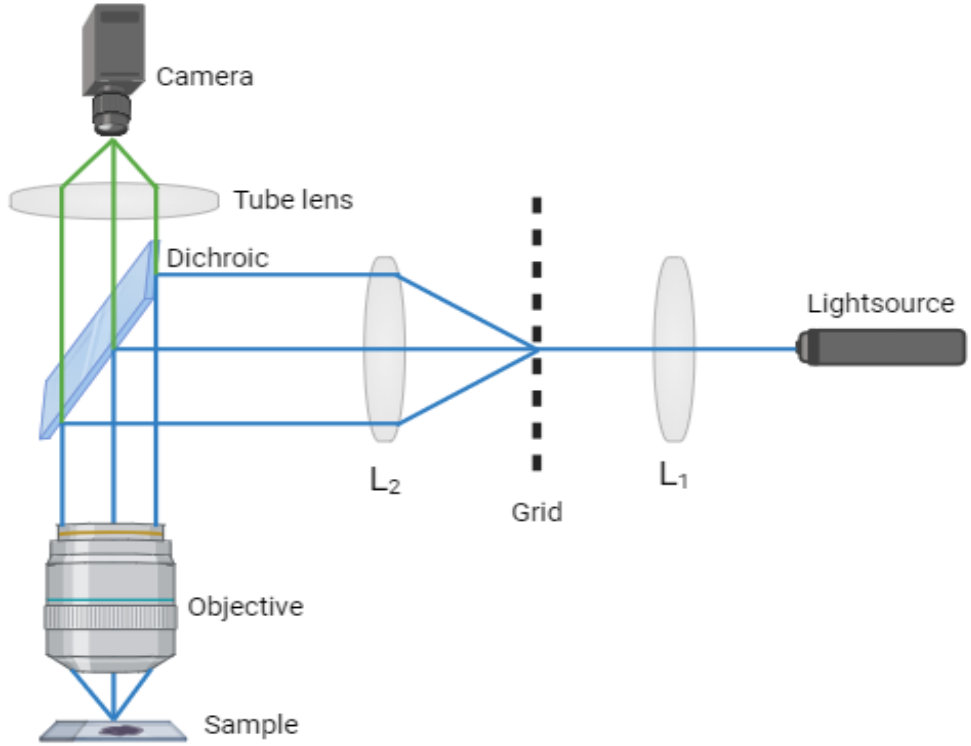

Figure 1.12 *Depiction of structured illumination microscopy (SIM) whereby the excitation beam passes through a grid before reaching the sample. Image created in BioRender.com.*

SIM has been used to image the actin skeleton of a HeLa cell (Gustafsson, 2000). Advantages of SIM include the fact that sample preparation is relatively simple when compared to other super-resolution techniques, it is the same as that for confocal microscopy, and SIM building materials can be easily acquired from numerous microscope manufacturers (Vangindertael et al., 2018). However, during SIM, the sample is exposed to high illumination intensities for prolonged periods, leaving it open to phototoxic effects and as imaging takes time, it is prone to sample drift issues (Vangindertael et al., 2018). Additionally, multiple images per focal plane are required to be taken as well as having to shift through the sample in small steps in the axial direction, both of these hinder the imaging speed (Heintzmann and Huser, 2017).

1.4.4 STORM and PALM

Stochastic Optical Reconstruction Microscopy (STORM) (Rust et al., 2006a) and Photo-Activation Localisation Microscopy (PALM) (Betzig et al., 2006) methods involve the use of photoswitchable fluorescent probes which can change their light absorption or emission wavelength properties (Yamanaka et al., 2014).

During PALM most of the fluorophores in a sample are converted to a dark state, by photoswitching or photobleaching, the rest, less than about 1%, are switched on. The probability that any two fluorophores will be in close proximity is quite small, this means that their PSFs wont overlap and they will be distinguishable and therefore each one can be isolated and their movement tracked. Once these fluorophores have photobleached and information has been gathered from them, a new collection of fluorophores is switched on elsewhere in the sample. The spatial distribution of the lit up fluorophores is used to reconstruct the structure in the image (Vangindertael et al., 2018).

The localisation precision of the fluorophore locations is the spread of the position estimates, x_{p_e} around the mean, $\overline{x_p}$ and the localisation accuracy is the deviation of $\overline{x_p}$ from the true positions, x_p of the fluorophores. The localisation precision is given as;

$$\sigma_{xy}^2 = \left(\frac{s^2}{N_{coll}}\right) + \left(\frac{a^2/_{12}}{N_{coll}}\right) + \left(\frac{8\pi s^4 b^2}{a^2 N_{coll}^2}\right) \quad (19)$$

where N_{coll} is the total number of detected photons, s is the standard deviation of the PSF of each fluorophore, a is the size of each pixel and b is the background noise of each pixel (Thompson et al., 2002).

For STORM, synthetic dyes like Cy3-Cy5 are used with alternating laser wavelengths to image a small number of fluorescent probes at a time. Like PALM, the individual images are combined into a super-resolution image (Rust et al., 2006b). Often dSTORM (direct STORM) is used instead of STORM; fluorophores are in a blinking state so more random localisations can be collected over time (Vangindertael et al., 2018).

DNA vectors with a transgene that encodes a fusion between the protein being observed and a fluorescent protein compatible with PALM is the method often used for labelling in PALM while primary and/or secondary antibodies, tetracysteine tags (Griffin et al., 1998), eDHFR tags (Miller et al., 2005), CLIP tags, SNAP tags or HaloTags (Gautier et al., 2008; Griffin et al., 1998; Keppler et al., 2004) are usually used for STORM.

An advantage of PALM over STORM is that the diffraction-limited areas of fluorophores tend not to overlap as only a small number of them are excited at any one time (Shashkova and Leake, 2017). Drawbacks of STORM and PALM are that they usually produce many thousands of frames, therefore taking substantial time to image (Hess et al., 2006; Legant et al., 2016).

1.4.5 Light sheet microscopy

Light-sheet microscopy (figure 1.13) utilises one or two illumination objectives to create a sheet of light (Huisken et al., 2004; Huisken and Stainier, 2007) taking on a Gaussian top-hat profile. The sheet is scanned across the sample while imaging (Daetwyler and Fiolka, 2023). Widefield detection is used to detect the fluorescent signal from the illuminated plane (Daetwyler and Huisken, 2016).

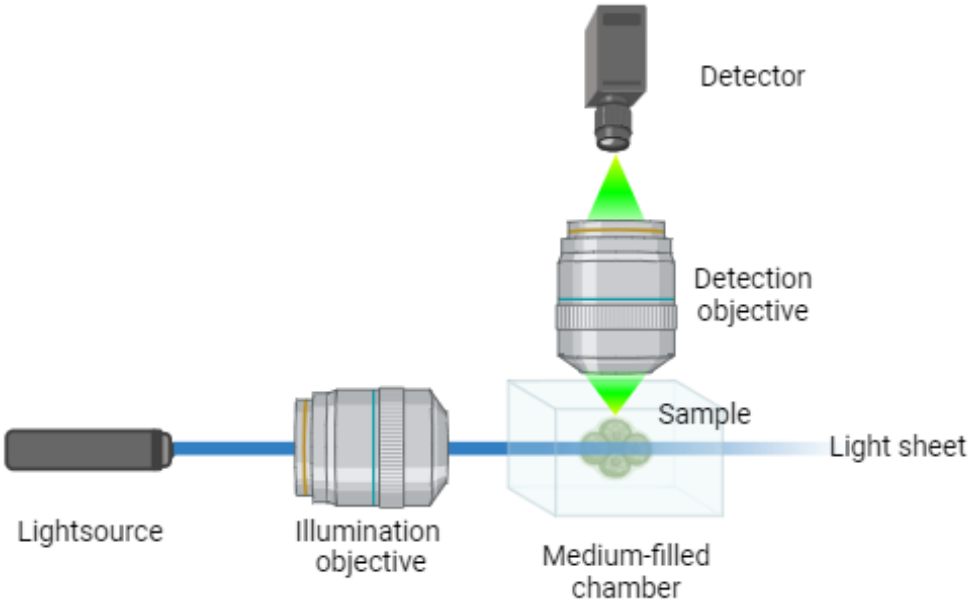

Figure 1.13 *Depiction of light-sheet microscopy. A light sheet created by the illumination objective hits the sample which is usually within a medium-filled chamber. Sample emission passes through the detection objective and is collected by the detector. Image created in BioRender.com.*

A disadvantage of light-sheet microscopy is that it is not the best for imaging deeper into samples as the widefield detection reduces the optical penetration depth (Daetwyler and Fiolka, 2023). On the other hand, there are a few methods that have been developed to improve optical penetration depth such as multi-photon excitation (Horton et al., 2013; Lecoq et al., 2019; Zipfel et al., 2003) or using an immersion medium with a refractive index better matched to that of the sample (Boothe et al., 2017; Iijima et al., 2021) which reduces scattering. Advantages of light-sheet microscopy include reduced out-of-plane excitation, producing better sectioning (Daetwyler and Fiolka, 2023). It also confines illumination, in the shape of a sheet, to the focal plane, therefore samples are less likely to experience phototoxic effects (Balasubramanian et al., 2023). Additionally, when the sample is rotated, multiple views can be acquired; recently, light-sheet microscopes utilising four objectives have been made to alternate between sheet illumination and detection (Krzic et al., 2012; Schmid et al., 2013; Tomer et al., 2012). Light-sheet microscopy has been criticised in the past for its cumbersome

sample mounting issues. Although, open top (Glaser et al., 2019; Mcgorty et al., 2017) and oblique plane microscopes (OPM) (Bouchard et al., 2015; Dunsby, 2008; Sapoznik et al., 2020) have been developed, these leave space available to place samples of various sizes (Daetwyler and Fiolka, 2023).

1.4.6 MINFLUX microscopy

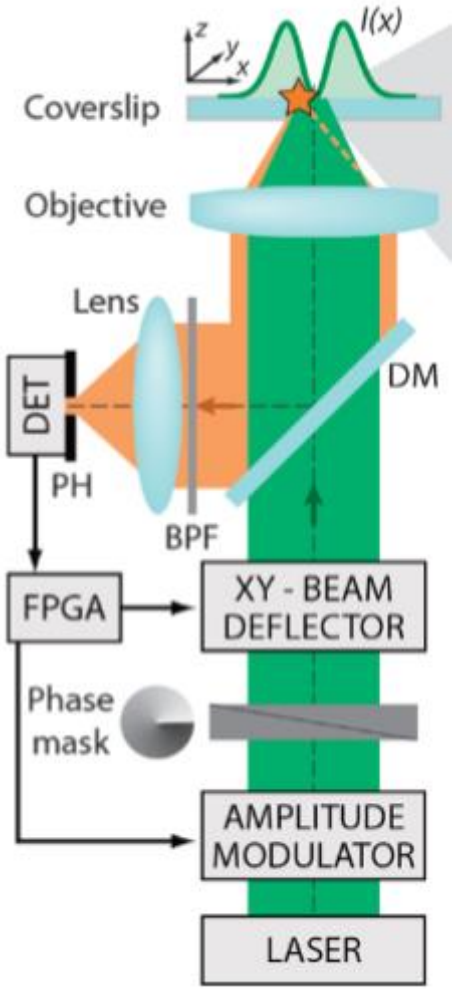

Figure 1.14 *Depiction of MINFLUX microscopy from Balzarotti et al. (2017). A doughnut-shaped excitation beam is directed through an amplitude modulator, XY deflector and dichroic mirror (DM) and scanned around a fluorescent molecule position (star). Photons emitted from the fluorescent molecule pass through the objective before being directed by the DM through a bandpass filter (BPF) and confocal pinhole (PH). The detector (DET) picks up the photons and a field-programmable gate array (FPGA) makes recordings.*

Minimal photon flux (MINFLUX) (Balzarotti et al., 2017) microscopy (figure 1.14) involves scanning a doughnut-shaped beam around a single fluorophore. A vortex phase mask is used to create a doughnut-shaped excitation beam. This beam is then modulated by an amplitude modulator and deflected in XY so that it shifts around a fluorescent molecule position (star in figure 1.14). Photons emitted from the fluorescent molecules are collected through the objective into a fluorescence bandpass filter (BPF) and confocal pinhole (PH). Fluorescent photons are picked up by a detector (DET) in each location where the doughnut beam is positioned. A field-programmable gate array (FPGA) is used to record intensity modulation and detection and photon counting (Balzarotti et al., 2017).

The scanning of the doughnut beam follows a specified pattern with multiple positions. Photons are detected in these positions and are used to estimate the position of the fluorophore. The precision, P of this estimate is proportional to the pattern size, S and depends on the photon count, N yielding the relationship;

$$P = \frac{S}{2\sqrt{2N}} \tag{20}$$

Better localisation precision is achieved by iteratively decreasing S and centring it on the fluorophore (S. Liu et al., 2022). Gwosch *et al.* used MINFLUX microscopy to image Nup96 proteins tagged with mMaple in U20S

cells and achieved a 1-3nm fluorophore localisation precision (Gwosch et al., 2020). More recently, Remmel *et al.* demonstrated a MINFLUX technique which increases fluorophore localisation up to 30 times by using spontaneously blinking fluorophores with blinking times that are close to the iterative MINFLUX localisation times (Remmel et al., 2023).

An advantage of MINFLUX is that it is highly efficient, UV can be used at high intensities until a fluorophore is detected whereby the UV laser is switched off, this makes it a great method to use during live-cell imaging with photoconvertible fluorescent proteins (S. Liu et al., 2022). However, currently MINFLUX imaging speeds are too slow to capture dynamic live cell activity (S. Liu et al., 2022).

1.4.7 Super resolution optical fluctuation imaging (SOFI) microscopy

When imaging fluorophores, the fluorescence intensity does not remain the same over time but fluctuates. Each pixel in the image represents an intensity distribution of this fluorescence. SOFI microscopy (Dertinger et al., 2009) involves using cumulants to calculate the fluorescence distribution in each image pixel. The number of cumulants used on each pixel, n is referred to as the n^{th} order cumulant. When n=1, the pixel fluorescence is averaged over, when n=2 the pixel fluorescence standard deviation is calculated. Therefore a SOFI image is one of the sample whereby the value of each pixel is the value of the cumulant, the n^{th} order image is given by;

$$SOFI_n(\underline{r}) = \sum_{k=1}^{N} U^n(\underline{r} - \underline{r}_k)\epsilon g \tag{21}$$

where r_k is the position of a fluorophore, U is the PSF of the microscope, ϵ is the brightness of the fluorophores and g depends on the dynamics of the fluorophores which is a constant if all fluorophores have the same emission properties (Vangindertael et al., 2018). We also have N, the total number of cumulants, this value can theoretically rise to infinity.

An advantage of SOFI is that spatial resolution and contrast of images are more enhanced than for images taken using PALM or STORM (Dertinger et al., 2009). Additionally, for $n = 2$, only a few hundred frames are needed to yield a super-resolution image, making it a fast imaging method. However, a drawback of SOFI is that for $n > 4$ the cumulants are more susceptible to noise (Vangindertael et al., 2018).

1.5 3D microscopy

Various techniques have been developed to produce 3D images of samples, some methods are built upon existing fluorescence and super resolution microscopy and others are completely novel ideas.

1.5.1 3D-COL0RME

A 3D super-resolution approach to TIRF was developed, the 3D-COL0RME, which uses a 3D reconstruction procedure using MA-TIRF in the axial plane in combination with sparsity-based modelling for molecule localisation and intensity estimation in the lateral plane. This significantly improves image resolution (Stergiopoulou et al., 2022).

1.5.2 3D confocal microscopy

The multiple z-stacks that make up a 2D image in confocal microscopy can also be used to produce a 3D image. A disadvantage of this method is that repeated laser excitation has to be used to acquire the multiple z-stacks, this increases the time taken to image and increases cell phototoxicity (Hickey et al., 2022).

1.5.3 3D STED microscopy

One method for achieving 3D STED microscopy involved fluorescently labelling fixed samples which were sliced into thin sections and embedded in polymer resin. The sections were imaged using nanoscale resolution STED microscopy with up to 80nm resolution (Punge et al., 2008).

A further method involved placing phase plates into the STED beams; this boosted the lateral and axial resolution. When compared to the above method, this is non-invasive to the sample and produces a 3D stack which doesn't require alignment afterwards (Wildanger et al., 2009).

1.5.4 3D SIM

3D-SIM was achieved by using a grated illumination pattern which was both laterally and axially structured to diffract laser light (Gustafsson et al., 2008). 3D-SIM was used to view eukaryotic cell division and the function of the centrosome in this process (Lawo et al., 2012).

1.5.5 3D PALM

PALM was combined with Single Particle Tracking (SPT) analysis to make sptPALM and was used to observe the influence of membrane lipids on TNF-α by spatially mapping diffusion coefficients to observe where molecules are and are not mobile (Heidbreder et al., 2012).

Bi-plane PALM utilises the fact that the PSF is inherently a 3D entity; emission light is split from the sample and the two halves of the EM-CCD camera capture the image in two different focal planes, the 3D PSF is used to fit the emitter positions in each dataset, pinpointing xyz positions simultaneously (Juette et al., 2008; Ram et al., 2008, 2007).

1.6 Opensource microscopy

Opensource microscopy refers to microscopy analysis software and hardware designs freely available on open platforms and editable by whomever uses them for their bespoke requirements.

1.6.1 Opensource microscopy data management

The Open Microscopy Environment (OME), developed by Swedlow in 2002, is a platform which offers microscopy data management. OME formats and software are freely available and designed to work with commercial platforms (Brooks, 2023). Almost twenty years later, Zarr was created; this was aimed to improve storage and download solutions of large data on the cloud (Brooks, 2023). In 2021, Moore *et al.* described a way for OME and Zarr to be used together as a next-generation file format (NGFF) for bioimaging (Moore et al., 2021) and in 2023, OME-Zarr was launched with the aim of providing biologists with specialist tool designs and programming libraries (Brooks, 2023).

1.6.2 Opensource microscope designs

1.6.2.1 The miCube

The miCube fluorescence microscope designed by Hohlbein *et al. is* constructed from a combination of 3D-printed parts and computer-numerically-controlled (CNC) machined aluminium parts (Strack, 2019). miCube can be used for single-molecule FRET (fluorescence resonance energy transfer) and was recently used to track CRISPR-Cas9 with 40nm precision in gram-positive bacteria (Martens et al., 2019). However, this microscope can be quite expensive to build (Almada et al., 2019).

1.6.2.2 The K2TIRF and liteTIRF

K2 total internal reflection (TIR) fluorescence microscope designed by Ganzinger *et al.* built with focus stabilisation and multi-colour imaging capabilities (Niederauer et al., 2023). K2TIRF and miCube are both modular so are easy to upgrade when better technology is released (Almada et al., 2019). The liteTIRF microscope developed by Jungmann *et al.* was used for high resolution PAINT imaging and made entirely from off-the-shelf components (Danial et al.,

2022). Although, the liteTIRF is not modular so it is difficult to change or upgrade built-in components.

1.6.2.3 The WOSM

The WOSM (Warwick opensource microscope) (Danial et al., 2022) designed by Cross *et al.* for high quality super-resolution imaging includes a smaller distance between the sample mounting position and the top side of the microscope chassis, this is claimed to allow for long-duration, high-resolution imaging without needing drift correction. However, the WOSM is not ideal for high-throughput, multi-sample imaging due to a short travel range in xyz and it can be complicated to construct as some parts require milling through large sheets of aluminium. Furthermore, there is no complete list of components for this microscope available (Danial et al., 2022).

1.6.2.4 The cellSTORM2

The cellSTORM2 (Diederich et al., 2020) is a 3D-printed mobile-phone-based super resolution microscope and can achieve up to 100nm spatial resolution. The cellSTORM2 is relatively affordable due to the use of low-cost opto-mechanical components and the use of deep learning for image processing. However, maintaining a low cost for this microscope results in reduced spatial resolution abilities (Danial et al., 2022).

1.6.2.5 The Flexiscope

The Flexiscope (Courtney et al., 2020) is a microscopy and electrophysiology system capable of infrared illumination, multi-channel fluorescent imaging and automatic 3D scanning of larger samples with easy conversion between upright, inverted and electrophysiology configurations.

1.6.2.6 The NanoPro 1.0

The NanoPro 1.0 (Danial et al., 2022) is a super resolution microscope constructed with multiple low-cost lasers capable of imaging at 20nm resolution and has step-by-step instructions for construction. It can be used to achieve epifluorescence, HILO or TIRF, STORM or PAINT imaging.

1.6.2.7 The miEye

The miEye (Alsamsam et al., 2022), built using a milled aluminium microscope body and other commercially available parts with a Python interface, can be used for high-resolution widefield fluorescence microscopy.

1.6.2.8 The openFrame

The openFrame, developed by Cairn Research in collaboration with researchers at Imperial College London, is an inverted light microscope frame with a stack of functional layers (Lightley et al., 2023). Starting with three layers for widefield microscopy to five or more layers for multichannel microscopy. Layers include, but are not limited to, a focus layer, epi-illumination layer, tube-lens layer, detection layer and base layer.

1.6.2.9 The SQUID

The Simplifying Quantitative Imaging Platform Development and Deployment (SQUID) developed by Li *et al.* (2020) (Li et al., n.d.) is an opensource setup of microscopy software and hardware designed for fluorescence microscopy and is considerably cheaper than commercial microscope systems.

Chapter 5 of this thesis outlines the development and use of Gravityscope which was based on the SQUID design. Work to modify the SQUID design for use on a parabolic flight was carried out with Li *et al.*

1.7 Aims and objectives of this PhD work

Three objectives were outlined for the work outlined in this thesis, namely;

1. *Build and optimise a two-colour HILO microscope*

This work involved building upon the Wollman lab single-molecule fluorescence HILO/TIRF microscope. This included designing and building excitation optics for two different wavelength laser beams to illuminate samples simultaneously or individually. This work also involved measuring the beam angle and testing image quality depending on different imaging conditions used, including using different angles between HILO and TIRF. This work is covered in Chapter 2.

2. *Test HILO imaging of Mig1-GFP in yeast, comparing results to published work*

After building and optimising the HILO/TIRF microscope, it was used to take fluorescence images of Mig1-GFP in yeast using similar methods as those used by Wollman *et al.* (2017). Images were analysed to characterise the stoichiometry of clusters of Mig1 transcription factor molecules. Images were first taken using epifluorescence, to observe if they were comparable

to published results (Wollman et al., 2017) and then HILO imaging was tested based on these and *in vitro* GFP results. This work is covered in Chapter 3.

3. *Image NFkB transcription factors in human cancer cell lines and measure their stoichiometry*

After cluster detection methods had been fully developed during the work done to achieve objectives 1 and 2, these methods were used to image the NFkB transcription factor RelA tagged with GFP in U2OS cell lines. The aim being to characterise the clustering behaviour of RelA-GFP molecules in response to stimulation by TNF-α. This work is covered in Chapter 4.

This PhD work also took a space-related research direction in the form of the development of a microscope and microfluidic syringe pump designed, built and tested by Team SUGAR (Saccharomyces cerevisiae Uptake of Glucose Applying Real-time imaging) for The 79th European Space Agency (ESA) Parabolic Flight Campaign as part of the Fly Your Thesis 2022 Program. The work carried out by myself and Team SUGAR is covered in Chapter 5. This work was carried out with Team SUGAR and various other parties. The two aims of this research were;

1. *To build and optimise a fluorescence microscope that will work in varying gravity conditions and use it to take images of fluorescent signal uptake in budding yeast*

A relatively simple and inexpensive fluorescence microscope, *Gravityscope,* was co-developed based on the opensource Simplifying Quantitative Imaging platform Development and Deployment (SQUID) microscope designed by Li *et al.* (Li et al., n.d.). This microscope design was optimised to be able to withstand vibrations experienced during a parabolic flight and ensure it would be sensitive to capturing metabolic activity in yeast cells.

2. *To observe glucose uptake in budding yeast cells in microgravity and hypergravity*

Gravityscope was used alongside a microfluidic syringe pump to take images of fluorescent glucose uptake by budding yeast while the yeast samples were injected with the glucose through a microfluidic sample system during flight.

Chapter 2: Developing a single-molecule HILO/TIRF fluorescence microscope for the lab

Single-molecule fluorescence microscopy involves using fluorescence microscopy to take images of samples and determine the spatial location of single fluorophores within these samples by fitting PSFs to bright spots in the image. The intensity of fluorophores in images can be characterised. For fluorescence microscopy, a narrow fluorescent beam is incident upon a sample, the beam wavelength is absorbed by the labelled molecules within the sample and light is emitted from the labels at a longer wavelength (Lichtman and Conchello, 2005). Excitation and emission beams are usually separated by a dichroic mirror before reaching the detector. In epifluorescence microscopy, the objective lens is used as both a magnifier and a condenser lens (Vangindertael et al., 2018). The angle of the excitation beam incident upon the sample is 0° and is parallel to the sample emission beam, this generally illuminates the entire cell. At angles above the critical angle, θ_c=61°, total internal reflection occurs whereby the incident beam is reflected off the bottom of the sample slide rather than passing through the sample (Jialei Tang and Young Han, 2018). This is called Total Internal Reflection Fluorescence (TIRF) microscopy. The sample is illuminated by the energy released from the beam in the form of an evanescent wave. This energy is an exponential decay function of the vertical distance of the beam from the sample. A highly inclined laminated optical sheet (HILO) is created at excitation incidence beam angles between 0° and the critical angle. Only the parts of the cell which the excitation beam passes through are illuminated. An advantage of this is that it makes for increased SNR due to a decrease in background signal. HILO has been used to achieve over 7 times improved SNR relative to epifluorescence (Gardini et al., 2023).

This chapter covers the building and optimisation of a two-colour HILO/TIRF single-molecule fluorescence microscope for the lab. The work done adhered to the first of the five main objectives of this PhD, namely;

1. *To build and optimise a two-colour HILO microscope*

A suite of MATLAB tracking functions was built by Wollman *et al.* (Miller et al., 2015; Wollman and Leake, 2022) and these were used to analyse images taken with the HILO/TIRF microscope. The efficiency of the MATLAB *tracker* function at identifying bright spots in an image video frame and tracking them across the video was tested by analysing simulated *in vitro* GFP data. From this, an optimal parameter script was created that could be used with the tracker function to analyse further images of GFP-tagged proteins. The performance of the HILO/TIRF

microscope was tested by taking images of fluorescent beads and *in vitro* GFP. The results of analysing images of fluorescent bead images demonstrated the impact of changing the beam angle on image intensity while the results from analysing *in vitro* GFP images demonstrated the impact of different imaging conditions, such as camera exposure time and beam intensity, on bright spot intensity in the images.

2.1 Microscope development

The HILO/TIRF microscope started as a *Nikon* TiE with a 488nm laser. More was added to improve the excitation optics, including a second 561nm laser, two neutral density filter lens wheels, a beam shutter, beam expansion lenses and an image splitter.

2.1.1 The microscope and user interface

The main body of the microscope (figure 2.1) was a *Nikon* TiE. Adam Wollman fitted a 67.5 frames per second (FPS) *Teledyne Photometrics* CCD Evolve delta (512x512)ROI camera which produced 90nm width image pixels. I fitted a *Teledyne* DV2 image-splitter to allow for imaging with two emission wavelengths. The objective used was an *Apo TIRF 100X/1.49 oil ∞/0.13-0.20 WD 0.12 DIC N2 MRD01991* with $NA = 1.49$. Nikon LDF immersion oil with a refractive index of n=1.52 was used with glass coverslips for refractive index correction. The total magnification factor from sample to detector was calculated by the ratio between the lens tube length (150mm) and the objective focal length (2mm) yielding a total magnification factor of 75X.

I attached removable temperature and CO_2 control units to the microscope stage to allow the user to image samples in various controlled environments. Also included were a control unit for the brightfield lamp which had a binary power switch and a dial to control bulb intensity and a unit which allowed the user to manually shift the sample stage in the x and y directions with an analogue joystick and shift the objective height (z direction) with a dial, the sensitivity of both could be adjusted with this unit. The user could see and take images of the sample using Nikon Elements software on the PC. The software also allowed the user to change various

imaging conditions such as the size (in pixels squared) of the region of interest (ROI) and the exposure time (in ms).

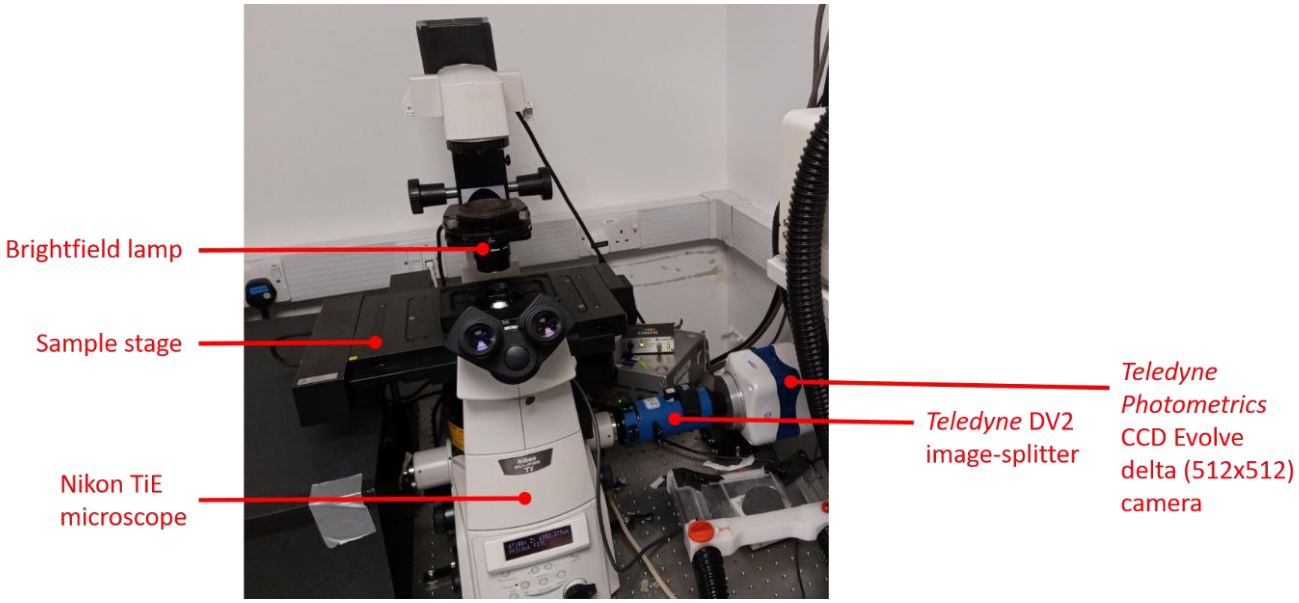

Figure 2.1 *The main body of the HILO/TIRF microscope showing a Nikon TiE microscope fitted with a Teledyne DV2 image splitter and Teledyne Photometrics CCD Evolve delta (512x512)ROI camera.*

2.1.2 The microscope excitation optics

For fluorescence illumination, a bespoke excitation optics setup was created (figure 2.2). This included a *Coherent* OBIS™ blue laser with wavelength 488nm (fitted by Adam Wollman) and a *Coherent* Sapphire™ green laser with wavelength 561nm (which I fitted). The 488nm laser could be controlled by the user with a USB connection on the PC using *Coherent* connection software; with this, the user could switch the laser on and off and control the beam intensity, ranging 1-50mW. The 561nm laser was switched on/off manually and had a peak beam intensity of 20mW which could be altered using neutral density (ND) filters. Planning was required to determine where the 488nm and 561nm lasers could sit and where lenses and mirrors would be placed to ensure both beam paths would reach the sample together or individually. Figure 2.3A-B demonstrates the excitation and emission optics with detailed views of the excitation optics using two different flip lenses.

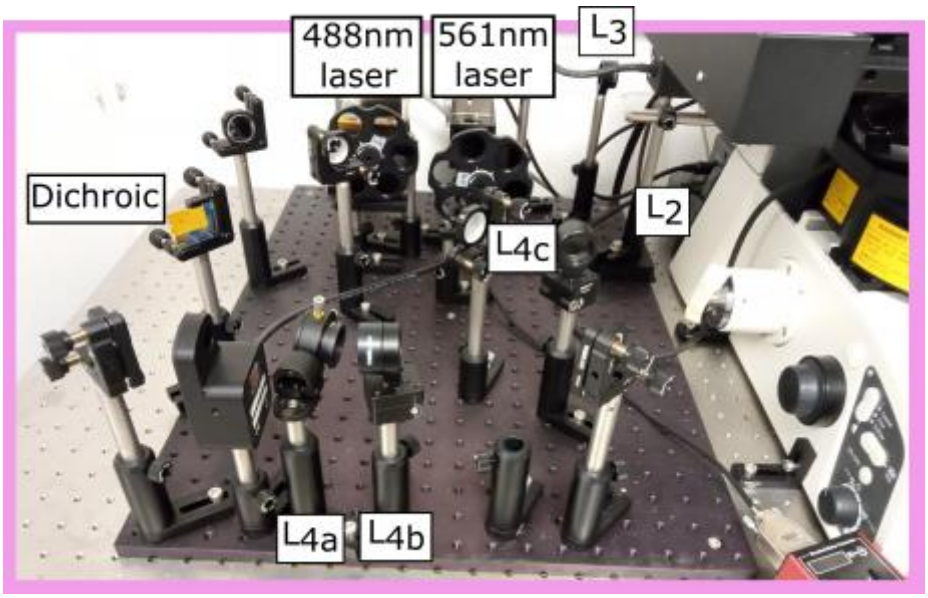

Figure 2.2 *Photo of the HILO/TIRF microscope excitation optics with annotated positions of the 561nm and 488nm lasers, dichroic and lenses $L_{4a}, L_{4b}, L_{4c}, L_3$ and L_2.*

Each of the 488nm and 562nm beams first passed through a *Thorlabs* ND filter wheel. The wheels were fitted with ND lenses of $ND = 0, 0.5, 1, 2, 3, 4$. The filter wheels could be rotated manually by the user to reduce beam power, P_{ND} according to;

$$P_{ND} = \frac{P}{10^{ND}} \tag{21}$$

where P is the power of the beam without the ND filter. After this, the 488nm beam was reflected by a standard mirror and the 561nm beam was reflected by two standard mirrors.

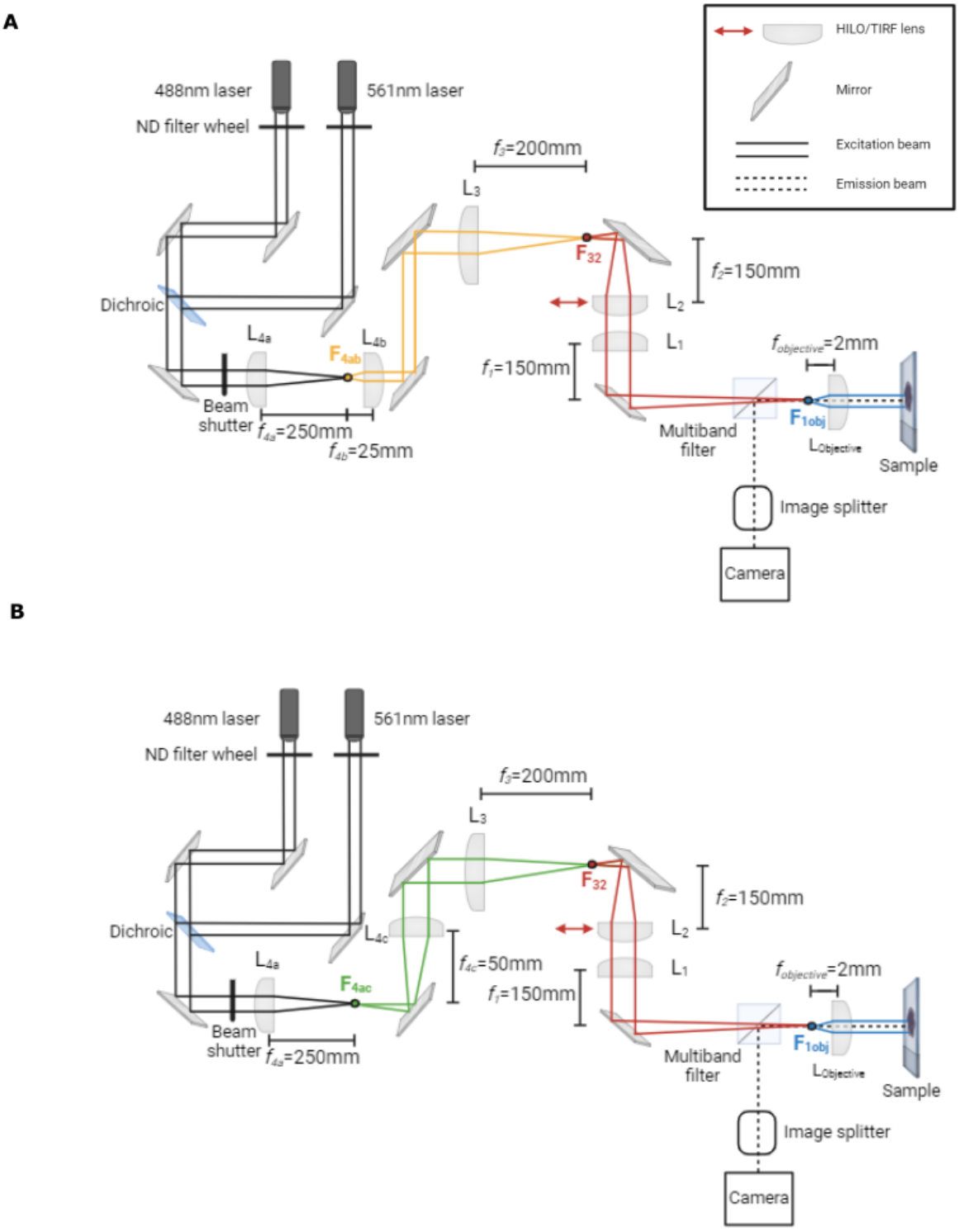

Figure 2.3 *Depiction of the HILO/TIRF microscope excitation and emission optics paths including the mirrors, the dichroic and the lenses, $L_{4a}, L_{4b}, L_{4c}, L_3, L_2, L_1$ and L_{obj} that the 488nm and 561nm excitation beams passed through resulting in beam expansion by* ***A.*** *10X when flip lenses L_{4a} and L_{4b} were up and by* ***B.*** *5X when the flip lenses L_{4a} and L_{4c} were up. Lens L_2 was the HILO/TIRF lens that could be shifted to alter the beam angle before it hit the sample. L_{obj} was the objective lens. The sample was excited by the beam(s) and emission passed through a multiband filter and the image splitter before reaching the camera. Not to scale. Image created in BioRender.com*

Both beams then hit a Chroma T565lpxr dichroic mirror which transmitted 570-700nm and reflected 450-560nm. The orientation of the dichroic (figure 2.3A-B) allowed both the 488nm and 561nm beams to travel to another standard mirror before passing through a *Thorlabs* SHO5 ½'' beam shutter which allowed the user to control whether the beams hit the sample. This was done using the *Thorlabs* SC10 Shutter Controller.

With the telescopic flip lenses L_{4c}, L_{4b} L_{4a} all down (narrowfield excitation), the excitation beams passed through lens L_3 before passing through L_2. Shifting lens L_2 left and right changed the angle of the excitation beam before it hit the sample. After passing through lens L_2 , the beams passed through mirrors and lenses within the Nikon microscope before passing through a Semrock LED-DA/FI/TR/Cy5-B-000 multi-band filter set cube and then through the objective lens, L_{obj} before hitting the sample.

The lens $L_{4c}$was at a distance of 300mm from lens L_{4a} and when these were simultaneously up (intermediate-narrowfield excitation) the beam was expanded by 5 times. The lens $L_{4b}$was at a distance of 275mm from lens L_{4a} and when these were simultaneously up (widefield excitation) the beam was expanded the beam by 10 times (figure 2.3A-B).

2.1.3 Keplerian beam expansion in the excitation optics

Keplerian beam expansion (figure 2.4) involves using two converging lenses to expand a collimated beam. The collimated beam passes through lens 1 where is it focussed on the focal point, ϕ, the beam then passes through lens 2 and is expanded. For the beam expansion to work, the lenses must be at a distance of F from each other where F is the sum of the focal lengths of lens 1, f_1, and lens 2, f_2.

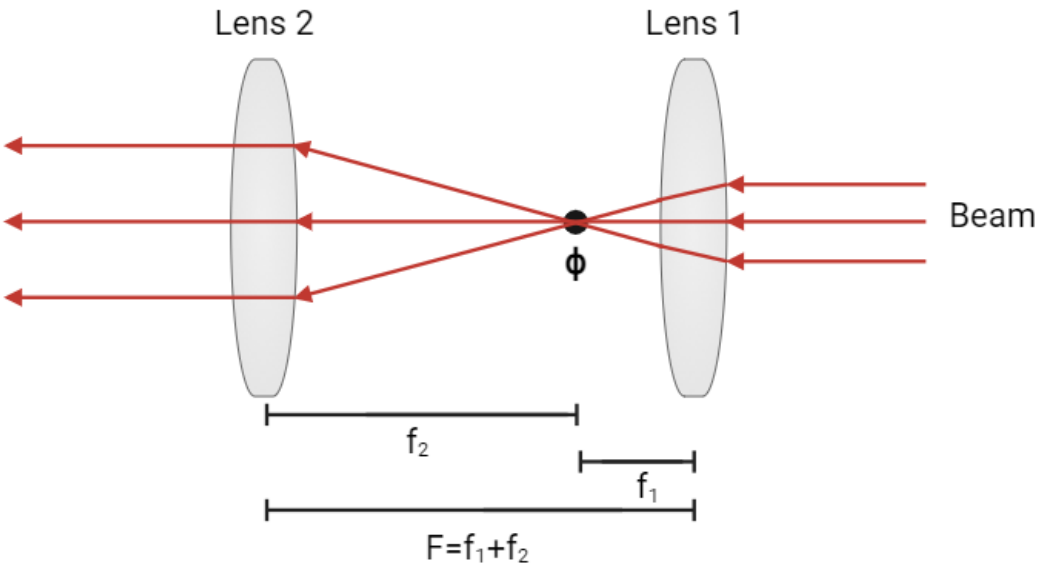

Figure 2.4 *Depiction of Keplerian beam expansion. A collimated beam of light travels through lens 1 where it is focussed to the focal point, ϕ, of lens 2. The beam then emerges from lens 2 with an expanded width. For the expansion to work, the lenses must be at a distance of F (mm) from one another where F is the sum of the focal length of lens 1, f_1, and lens 2, f_2. Image created in BioRender.com.*

It is beneficial to have the option to expand or attenuate an excitation beam in microscopy because there are multiple sample types and ROI sizes that require wider or narrower excitation beams. This is because the power of the beam is inversely proportional to the width of the beam aperture. Therefore, a narrow beam focusses more intense light onto an area of a sample; this increases the beam intensity and can increase the rate of the fluorophores photobleaching. However, despite the increase in onset of photobleaching, it may be beneficial to use higher beam intensities to increase SNR, faster acquisition times can be used to gather enough information before the sample completely photobleaches. An example of this in use is imaging the transcription factor Mig1, tagged with GFP, in budding yeast; this protein moves quickly, so fast acquisition times can be used to capture the protein dynamics in live yeast cells. In other cases, it may be more beneficial to use a wider beam aperture, and hence lower intensity, if longer acquisition times are to be used. An example of this in use is imaging the protein PAR6, labelled with GFP, in *C.elegans* embryos. PAR6 is a protein which drives the cell division in the embryo (Rodriguez et al., 2017), this is a slow-moving protein and longer imaging times can be used to observe the dynamics of this protein, and embryo division, in live developing eggs.

Three beam size options were added to the excitation optics of the HILO/TIRF microscope using three flip lenses, L_{4a}, L_{4b}, L_{4c} (figure 2.3A-B). When all three of the flip lenses were down, the beam remained collimated, this was termed narrowfield excitation. When lenses L_{4a} and L_{4c}

were up, the beam was expanded 5 times (calculated as $\frac{250mm}{50mm}$), this was termed intermediate-narrowfield excitation. When lenses L_{4a} and L_{4b} were up, the beam was expanded 10 times (calculated as $\frac{250mm}{25mm}$), this was termed widefield excitation.

2.1.4 Measuring image pixel size

The pixel size of the images taken using the HILO/TIRF microscope was measured using an image of a graticule with a resolution of 80lp/mm (40 dark lines alternating with 40 light lines) and linewidth 6.3μm. An image was taken of this line and ImageJ(Fiji) was used to measure the length of the line; a vertical marker line was placed over the image line and the angle of the marker line against the image line was displayed in the ImageJ(Fiji) toolbar. The average marker line angle was 1.75°. A new vertical marker line at 90° was made over the image line and the original marker line angle was added, making the new marker line angle 91.75°. The length of the new marker line was measured at 67.53pixels, displayed in the ImageJ (Fiji) toolbar. This graticule linewidth (6.3μm) was divided by this measurement to obtain an overall image pixel length of 0.0933μm ≈ 93nm.

2.1.5 Measuring the excitation beam diameter

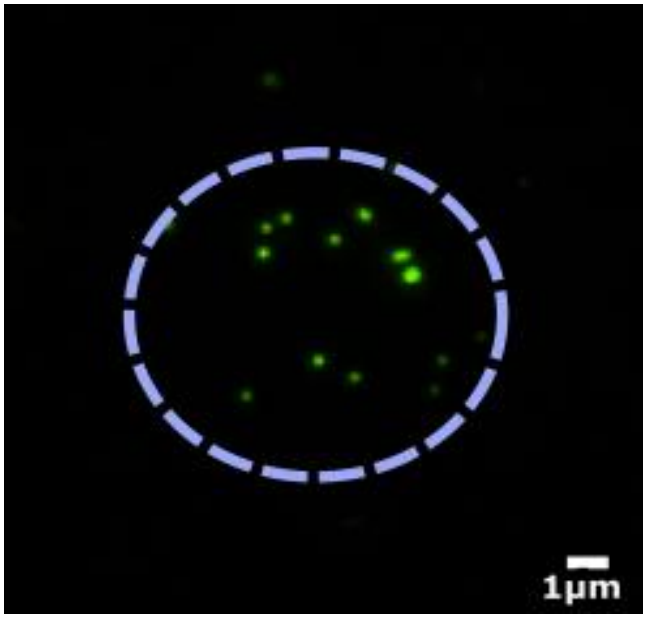

Figure 2.5 *Image of green fluorescent beads taken with the HILO/TIRF microscope using a 40mW 488nm narrowfield epifluorescence beam at 50ms exposure with a (512x512)ROI. The blue dashed circle indicates the width of beam coverage.*

The excitation beam diameter was measured by taking images of green fluorescent beads using a 40mW 488nm narrowfield epifluorescence beam at 50ms exposure with a (512x512)ROI (figure 2.5). After establishing the image pixel length as 93nm, this was set in the pixel scale in ImageJ(Fiji). The fluorescent bead images were opened in ImageJ(Fiji) and the multipoint measure tool was used to measure the distance between two beads at the very edges of the beam coverage (blue dashed circle in figure 2.5).

Several measurements were taken and the average distance between the beads, and hence the beam diameter, was $7.6 \pm 1.1 \mu$m.

2.1.6 Calculating the microscope spatial resolution

Image spatial resolution is dependant on the sampling interval and the sample spatial frequency. The sampling interval is the number of pixels contained in the sample image and the distance between these pixels. Details in the sample image are created by brightness transitions, cycling between light and dark. The cycle rate between light and dark is referred to as the sample spatial frequency. According to the Nyquist criterion, spatial resolution is preserved in a sample image by ensuring that the sampling interval is twice the highest sample spatial frequency.

The spatial resolution of the HILO/TIRF microscope when imaging GFP was calculated using the Rayleigh Criterion (equation (11)). In this case, the emission wavelength, λ was that of GFP, 508nm and the HILO/TIRF microscope objective numerical aperture was, NA=1.49. Therefore, the spatial resolution was 208nm. This is just over two pixels, therefore fulfilling the Nyquist criterion.

2.1.7 The microscope emission optics

The sample emission passed back through the objective and through the Semrock LED-DA/FI/TR/Cy5-B-000 multi-band filter set cube before reaching the *Teledyne Photometrics* CCD Evolve delta (512x512)ROI camera. The *Teledyne* DV2 image-splitter was fitted between the Nikon microscope and the camera and was fitted with two filters, a Chroma ET520/20M which transmits 511-526nm and absorbs 450-500nm and 530-600nm and a Chroma ET630/75m which transmits 588-662nm and absorbs 550-580nm and 670-750nm.

2.1.8 Changing and measuring excitation beam angle

In epifluorescence microscopy, the angle of the excitation beam incident upon the sample is 0° and is parallel to the sample emission beam, this generally illuminates an entire cell. When the excitation beam is at an angle above the critical angle, θ_c=61°, we have total internal reflection (TIRF) microscopy which illuminates the cell membrane with an evanescent wave. When the excitation beam is at angles between zero and the critical angle, we achieve highly

inclined laminated optical sheet (HILO) microscopy; only the parts of the cell which the excitation beam passes through are illuminated.

Attached to lens L_2 was a *ThorLabs* Kinesis Brushed Motor Controller, the motor shifted this lens and altered the angle of the excitation beam before it hit the sample. ATP software was installed to control the motor displacement via a control unit or via the PC through USB connection. A displacement value (in mm) corresponding to the beam angle was displayed on the PC.

If a relationship could be determined between the displacement of the motor moving lens L_2 and the excitation beam angle then the beam angle could be changed by typing a displacement value into the software. An approach to measuring the excitation beam angle is by using an oily prism (figure 2.6A(i)), a prism, of depth P, manufactured by adhering multiple glass sample slides together with immersion oil. The top of the objective (figure 2.6A(ii)) is lubricated with immersion oil and the prism is placed on top of it. A piece of paper is placed on the top of the prism and the location of the epifluorescence excitation beam (angle at 0°) is marked in pen. When the excitation beam angle is altered by shifting lens L_2 left or right, the position of the refracted excitation beam through the prism shifts left or right of the marked epifluorescence point. The deviation, D from this point can also be marked down and measured using a ruler. Figure 2.6B is a depiction of the deviation of the refracted excitation beam from the epifluorescence excitation beam.

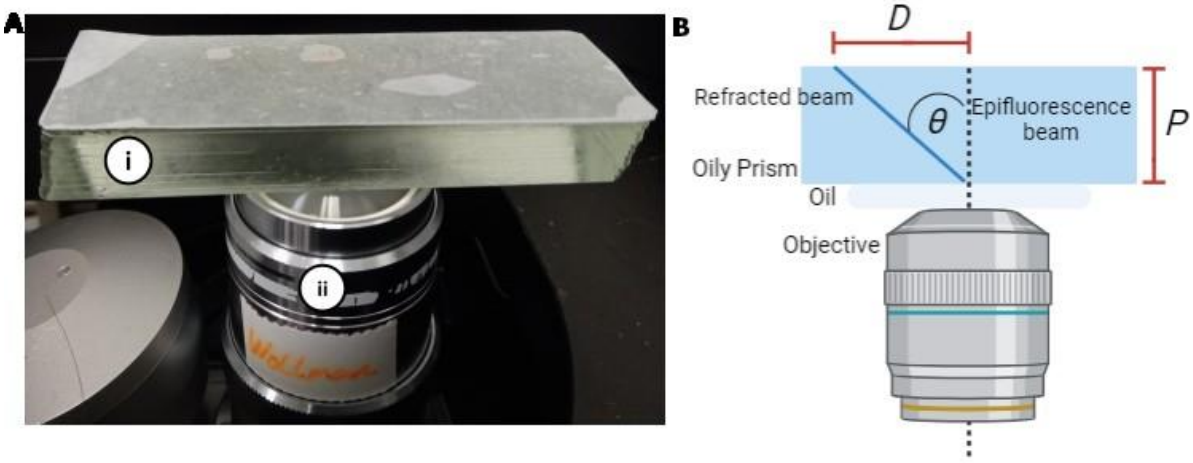

Figure 2.6 A. *(i) An oily prism manufactured by adhering multiple glass sample slides together with immersion oil on top of (ii) the microscope objective.* ***B.*** *Depiction of the oily prism method showing the deviation, D, of the refracted beam from the epifluorescence beam through an oily prism of depth, P on top of an objective lubricated with immersion oil. Image created in BioRender.com.*

An oily prism was manufactured using ten glass sample slides, each of refractive index n=1.52 and width 0.1cm. These were adhered together using *Nikon* immersion oil (refractive index n=1.52). After the epifluorescence excitation beam centre was marked on the paper on the top of the prism, the motor was used to shift lens L_2 left or right.

The deviation, D of the refracted excitation beam from the epifluorescence excitation beam mark was measured with a ruler and the excitation beam angle was calculated using;

$$\tan\theta = \frac{D}{P} \Rightarrow \theta = \arctan\left(\frac{D}{P}\right) \tag{22}$$

where P is the prism depth (in this case 1cm). The D measurements were taken in increments of 0.1cm, starting from 0cm and ending at 2cm.

The beginning of the TIRF illumination profile occurred at the critical angle, 61°, calculated using equation (13). By rearranging and substituting the critical angle into equation (22), the critical length was determined to be 1.8cm. The TIRF illumination profile occurred when the excitation beam was at and above 61° and D was at and above 1.8cm.

The HILO illumination profile occurred at the angles and lengths between epifluorescence and TIRF. The plot in figure 2.7 shows the average motor displacement vs excitation beam angle following normalisation (to measure displacement change as opposed to displacement value).

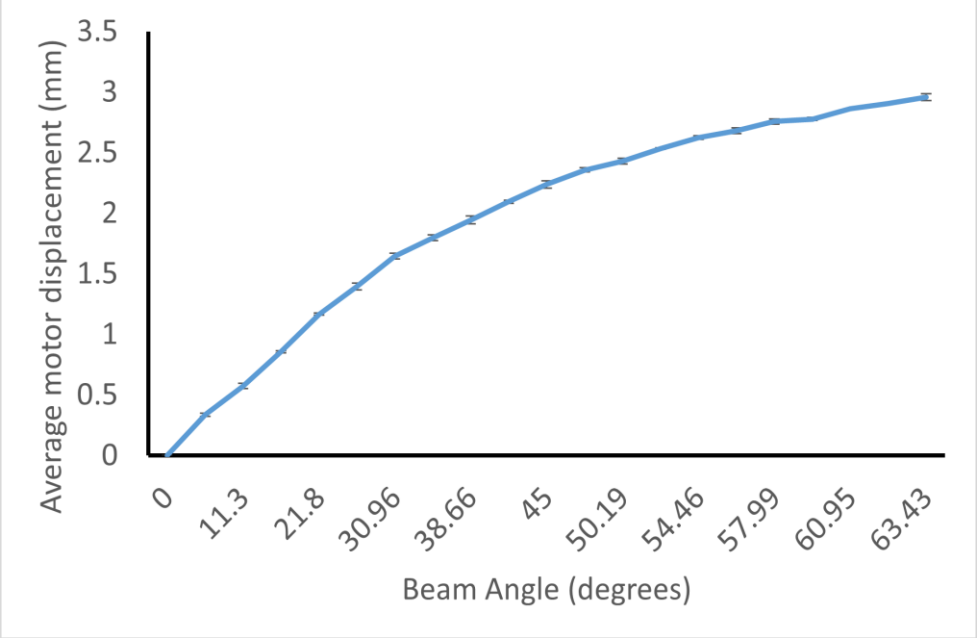

Figure 2.7 *Plot of motor displacement (mm) against beam angle (degrees) where beam angle was determined by using an oily prism.*

The plot shows a positive relationship between excitation beam angle and average motor displacement. As the excitation beam angle increases, from epifluorescence at 0° to TIRF, ~61°,

the average motor displacement increases; the shift (in mm) of the lens is greater. This is the trend that was expected. However, each time the excitation beam alignment was adjusted, the displacement had to be recalibrated as it began with different values after every adjustment, meaning that it was only the displacement change that retained a pattern not the displacement value itself.

2.2 Single particle tracking of images

Fluorescent proteins such as GFP or mCherry in sample images appear as point-sources of light (bright spots) (Wollman and Leake, 2022). A suite of MATLAB functions were designed by Wollman *et al.* (Miller et al., 2015) to identify and track these bright spots across image video frames and assign trajectories to them. The camera pixel intensity of bright spots in the image is measured (in counts) and a value for the intensity of a single fluorophore is determined by analysing intensity step data. Following this, stoichiometry is determined by estimating the initial photon intensity; this is done using one of many methods.

2.2.1 Introduction to single particle tracking

Single particle tracking (SPT) works by first localising particles in sample images, these appear as bright spots in the image that correspond to the location of a fluorescent probe in the sample (Manzo and Garcia-Parajo, 2015). The intensity of each bright spot, in an (x, y) coordinate in the image follows a diffraction pattern; an Airy Disk at the centre, where over 80% of the intensity is concentrated, surrounded by dimmer concentric rings. The intensity of the dim rings is a function of the distance of the ring from the Airy Disk. The intensity profile of the centre of the Airy Disk, $I(x, y)$ can be approximated by a 2D Gaussian;

$$I(x,y) = I_0 e^{-\frac{1}{2}\left(\frac{(x-x_0)}{\sigma}\right)^2} e^{-\frac{1}{2}\left(\frac{(y-y_0)}{\sigma}\right)^2} \quad (23)$$

where I_0 is the intensity at the centre of the Airy Disk and σ is the standard deviation of the intensity profile (the PSF of the microscope). The full-width-half-maximum (FWHM) of this Gaussian is given by $\frac{\lambda}{2NA}$ (Manzo and Garcia-Parajo, 2015). Fluorophores that are further apart from one another than this distance are categorised as distinct from one another. Particle localisation involves separating the bright spot intensity from the background and determining the centroid coordinates of the bright spots (Manzo and Garcia-Parajo, 2015). After this, the localisations are tracked across frames to produce a trajectory. In its most simple form, this involves joining spots that are near to one another throughout frames. One method for doing

this is by using the nearest-neighbour algorithm (Crocker and Grier, 1996). The algorithm is based on the Brownian motion of particles. The probability that N noninteracting particles each undergoing Brownian motion will diffuse at a distance, δ_j in the image plane at time, τ is given by

$$P(\{\delta_j\}:\tau) = \left(\frac{1}{4\pi D\tau}\right)^N \exp\left(-\sum_{j=1}^{N}\frac{\delta_j^2}{4D\tau}\right) \quad (24)$$

where D is the self-diffusion coefficient of a particle. Particles between consecutive frames that maximise this probability are linked. A similar method, and the method used in the Wollman *et al.* MATALB tracking functions, involves linking bright spots in the image between frames using distance thresholding (Sheperd et al., 2021). Particles that fit within this distance threshold over consecutive frames are categorised to be the same particle.

A further method for joining spots between frames is multiple hypothesis tracking (MHT) (Chenouard et al., 2009) which involves linking bright spots between frames after information is gathered from future frames. Information on several possible associations between bright spots are considered, stored and then these associations are compared. A disadvantage of the MHT method, however, is its high demand for computational processing due to increased number of measurements. On the other hand, modern processors are more able to meet this hefty demand. SPT programmes that exist include TrackMate (Ershov et al., 2022), Cell-ACDC (Padovani et al., 2022), DeepTree (Ulicna et al., 2021) and ELEPHANT (Sugawara et al., 2022).

2.2.2 The tracking code

A suite of MATLAB functions was built Wollman *et al.* (Miller et al., 2015; Wollman and Leake, 2022) and later also built in Python (Sheperd et al., 2021). These are designed to identify fluorophores in cell image videos and track them across frames. Two master functions were designed to elucidate fluorophore intensity and trajectory characteristics, these are tracker and overTracker.

2.2.2.1 Tracking particles in images

Inputs for the tracking software include the cell image video, usually a .nd2 or a .tif file, and a parameter script, the parameters of which are user-specified. Most noteworthy changeable parameters are the inner_circle_radius and subarray_halfwidth. The function works by identifying bright spots in the image frame which are above a certain intensity threshold specified by the user. A circle, the inner_circle, of specified radius (in pixels) is placed around

a candidate spot and around the circle, a square, the subarray, of certain length (in pixels) is placed (figure 2.8B). If the inner_circle_radius and subarray_halfwidth parameters are optimal, the circle should capture a bright spot. The intensity of the bright spot is given as the sum of the intensities of the individual pixels within the inner_circle; it is background-corrected by subtracting the mean intensity of the pixels inside the subarray from the inner_circle. The mean local background of the bright spot is given by the mean value of the intensity in the subarray. The intensity and local background are recorded in an output matrix.

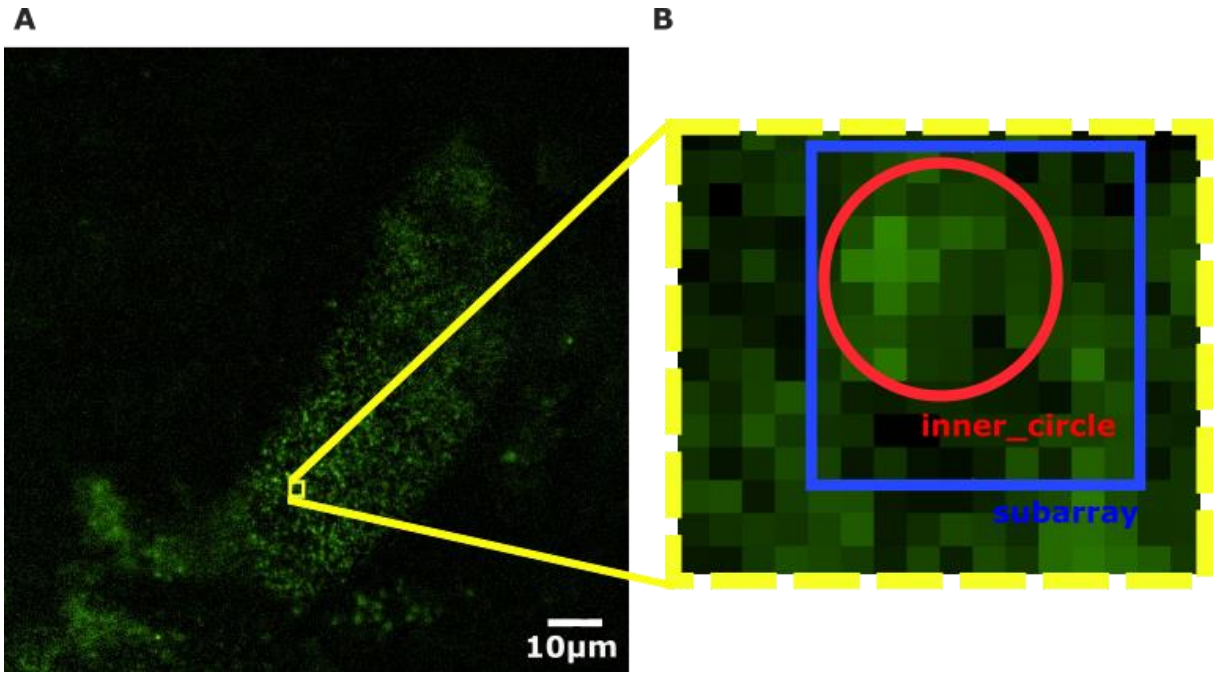

Figure 2.8 A. *Fluorescence image of PAR6-GFP in a C.elegans embryo taken with the HILO/TIRF microscope with a 20mW 488nm widefield HILO beam at 50ms exposure with a (512x512)ROI.* ***B.*** *Zoomed-in square of the fluorescence image depicting how the MATLAB tracker function chooses bright spots in the image. An inner_cirlce of radius (in pixels) specified by the user in a parameter script within a subarray of length (in pixels) specified by the user in a parameter script. The inner_circle fits around a bright spot with pixel intensity above a certain threshold and the subarray fits over the inner_circle and defines the local background of the bright spot.*

Figure 2.8 depicts the process of the tracker function identifying a bright spot in an image frame. The radius of the inner_circle and half-length of the subarray are specified in the parameter script by the user. Figure 2.8A shows a fluorescence image of the membrane protein, PAR6, labelled with GFP in an early stage *C. elegans* embryo taken with the HILO/TIRF microscope with a 20mW 488nm widefield HILO beam at 50ms exposure with a (512x512)ROI. A square is chosen (figure 2.8B) of local background (the subarray) with the bright spot within it (the inner_circle). The inner_circle is of radius 3 pixels and the subarray_halfwidth is 5 pixels. These were determined by visual inspection to be optimal sizes for the square and circle. If the inner_circle is too small, the function may consider some of a candidate spot to be part of

the background, thus the candidate spot will not be recorded. If the inner_circle is too big, the function may not capture as many candidate spots as there are that exist in the image.

The tracker function identifies these candidate spots from the first bright frame of the video and a smaller function built within the tracker function assigns a trajectory number to each spot. A spot trajectory exists if a spot remains between a specified number of frames in the video (i.e. before the spot photobleaches). Spots in multiple frames are considered as the same one spot if they are closer in space than d_01_max pixels to one another, where d_01_max is a distance defined by the user in the parameter script. If the spots are the same between frames then they are assigned trajectory numbers. Tracking continues until the onset of photobleaching, when the bright spot intensity decays to zero.

The main output of the tracker function is a (12xK) matrix, called SpotsCh1, where K is the number of spots found and recorded. The columns include the x and y coordinates of the spot when it was first found in the video, the mean local background, the total spot intensity, the frame number the spot was first found in, the trajectory number assigned to the spot and the frame in which laser exposure first began.

Additionally, the signal to noise ratio (SNR) of each spot is calculated as follows;

$$SNR = \frac{\bar{I}}{I_{SD}} \tag{25}$$

where $\bar{I}$ is the average spot intensity and I_{SD} is the standard deviation of the local background (in the subarray) intensity. Bright spots are only accepted and added to the output matrix if they have an SNR above an SNR threshold, called SNR_min. The SNR threshold, SNR_min, is specified by the user in the parameter script. An optimal value for this was determined by the user after several tests using *in vitro* GFP simulations.

2.2.2.2 Analysing tracks data

An image video can also be tracked for a specified number of frames after bright spots have photobleached. The SpotsCh1 matrix is used as an input into an *overTracker* function. The point of using this function is for the user to verify that the bright spots are indicative of single molecules. A plot of intensity vs time (frame) for a single molecule should look stepwise with the step height at the initial intensity of the molecule followed by a sharp, discontinuous drop in filtered intensity to a value at, or very close to, zero, indicating single-molecule photobleaching (figure 2.9B, Chung-Kennedy filter).

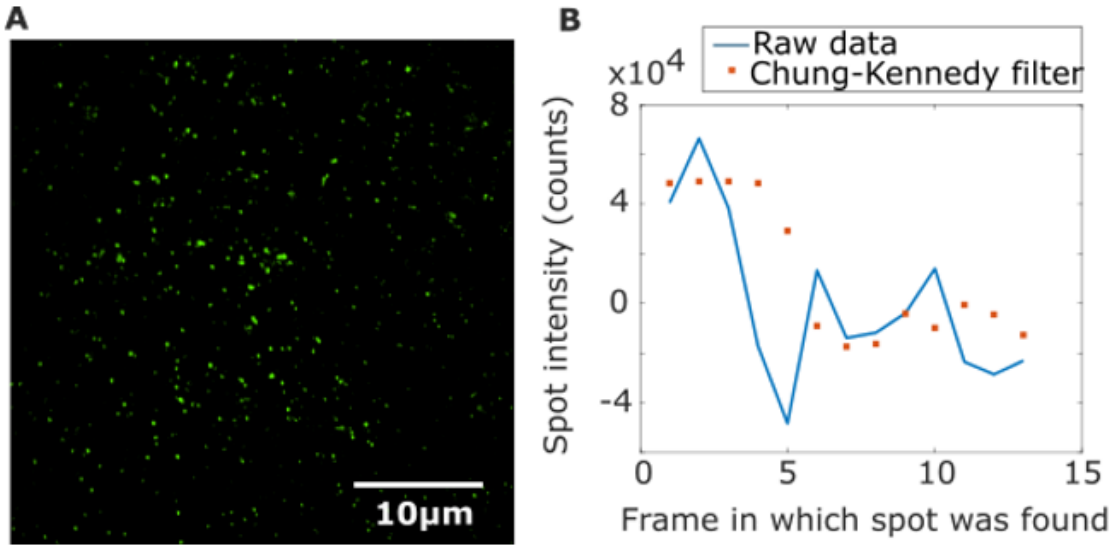

Figure 2.9 A. *Fluorescence image of in vitro GFP taken with the HILO/TIRF microscope with a 20mW 488nm widefield epifluorescence beam at 50ms exposure with a (512x512)ROI and* ***B.*** *Plot of spot intensity against the frame in which bright spot was found, the blue curve indicates the raw intensity data while the red dotted curve indicates the raw data after a Chung-Kennedy filter had been run on it. The Chung-Kennedy filter data shows a stepwise pattern with a step height at 41000 and a discontinuous drop to intensity values around zero.*

The overTracker function can be used on the tracks data produced by the tracker function to test if the tracker function really is only tracking spots before they have photobleached and not tracking them after they have photobleached. If the tracker function continued to track a spot after it had photobleached, this would lead to erroneous results and conclusions about various protein properties such as diffusion and stoichiometry. The overTracker function is used to track the image video for a user-specified number of frames after most/all of the bright spots in the image have photobleached (the image video looks dark with no green bright spots at this point). The overTracker function creates a (12xM) matrix, called spotsBaseline, of values in the same categories as those in the SpotsCh1 matrix, such as bright spot intensity, local background etc. Figure 2.9A is a fluorescence image of *in vitro* GFP taken with the HILO/TIRF microscope with a 20mW 488nm widefield epifluorescence beam at 50ms with a (512x512)ROI. For one bright green spot in this image, a plot of its intensity against video frame can be made (figure 2.9B, raw data). It is worth noting that negative intensity values can result when using the overTracker function. This is because bright spots are being tracked after they have photobleached. After photobleaching signal is very low, very close to zero, and the surrounding background is at or above these values. Therefore, when the background is subtracted from the intensity of the bright spot, this can produce negative values. A Chung-Kennedy filter removes noise while maintaining steps in the data (Chung and Kennedy, 1991). The filter algorithm works by running a shifting average filter over the data. The size of the

filter is defined by the user. The filter shifts forwards and backwards from a point in time. The forwards or backwards average is chosen based on it having the lowest variance. This process preserves steps in the data. We apply a Chung-Kennedy filter to the raw bright spot intensity, we end up with a stepwise curve (figure 2.9B, Chung-Kennedy filter); the top step is at the peak intensity of the bright spot (in this case around 41000). This is followed by a sharp, discontinuous drop to a bottom step at values at or close to zero. These steps indicate the initial single fluorophore intensity (the top step) and the single fluorophore when it has photobleached whereby it emits no fluorescence (the bottom step). The data in the plot in figure 2.9B is indicative of one track; a bright spot that has been tracked in the image video until it has photobleached.

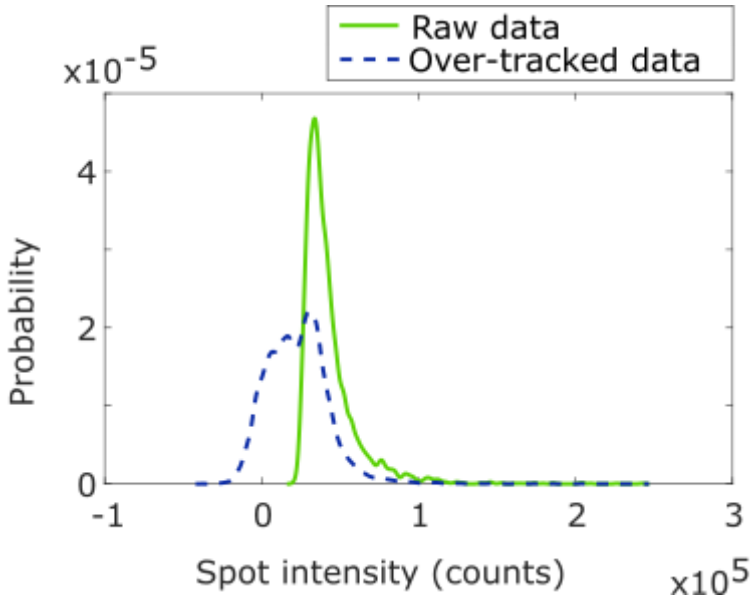

Figure 2.10 *KDF distribution plots of spot intensity after the tracker function had been run on image A (raw data) and after the overTracker function had been run on this data (over-tracked data).*

Usually in image videos, we have many tracks and we can plot a distribution of bright spot intensity using a kernel density function (KDF) plot (figure 2.10, raw data). The peak of the KDF plot is the single bright spot intensity for all tracks in the dataset. For the *in vitro* GFP image, we have a peak of 34000±8500 which is pretty close to the value of the top step in the Chung-Kennedy plot figure 2.9B. This peak value is referred to as I_{single}, the intensity of a single fluorophore prior to it photobleaching. Upon plotting a KDF distribution of spot intensity from the data produced by the overTracker function (figure 2.10, over-tracked data), the plot should have two peaks for bright spot intensity; one at, or very close to, zero, and a second peak that sits within the half-width-half-maximum of the KDF plot of spot intensity for all tracks produced by the tracker function (figure 2.10, raw data). If this is the case, this would indicate that the tracker function had indeed stopped tracking bright spots after they had photobleached, otherwise the over-tracked data KDF spot intensity peak would extend beyond the half-width-half-maximum of the tracker spot intensity.

2.2.3 *in vitro* GFP simulations

Wollman *et al.* had previously built a single-molecule fluorescence microscope using bespoke dual-colour beam excitation. Specifications of this microscope included 50mW 488nm and 561nm dual or single excitation, 1.49NA oil objective and an *Andor* IS EMCCD camera with 80nm/image pixel and capable of 5ms exposure times (Wollman et al., 2017). This microscope was used to capture activity of the transcription factor Mig1 in live budding yeast. The images were analysed using the MATLAB functions and they were able to elucidate important clustering behaviour of the transcription factors (Wollman et al., 2017). The HILO/TIRF microscope was built not only to emulate these results but to capture the activity of other transcription factors and proteins in various living cell types such as the NFkB transcription factor RelA in U2OS cancer cells and the androgen receptor transcription factor in LNCaP cancer cells. Not very much detail separates the previous Wollman *et al.* microscope from the HILO/TIRF microscope, except the image pixel length, 80nm/image pixel for the Wollman *et al.* microscope and 93nm/image pixel for the HILO/TIRF microscope, and the camera bit depth, 14bit depth for the Wollman *et al.* microscope camera and 16bit depth for the HILO/TIRF microscope camera. Therefore it was necessary to optimise parameters used in the parameter script when using the MATLAB functions to analyse image videos created using the HILO/TIRF microscope. This optimisation was carried out in the form of simulations of *in vitro* GFP molecules. The utility of three different parameter scripts were compared to each another. The inner_circle_radius, subarray_halfwidth and SNR_min values were changed and the impact of these changes was tested by the ability of the MATLAB tracker function to identify real bright spots in a simulated dataset containing real bright spots and false bright spots.

2.2.3.1 Methods

A computer-generated *in vitro* GFP image (figure 2.11) was created using an array of randomly assigned bright spots in xy coordinates (n x m), in a user-specified number of frames, t, with Gaussian intensity. This took several steps; the first was to create a (n x m x t) normrand (Marsaglia and Tsang, 1984; “Queuing Formulas,” 2010) matrix of randomly assigned normally distributed image background intensity values with user-specified mean μ_{BG} and standard deviation σ_{BG} which were the typical average and standard deviation background intensity for an *in vitro* GFP image respectively.

The next step involved creating a (N_nx2) matrix of randomly assigned uniformly distributed values in xy that fit within user-specified dimensions (in nanometres), these were simulated spots, for a total user-specified number, N_n of spots allowed to be in each frame of the

simulation, for t frames. A Gaussian intensity profile was applied to the spots over frames, t using;

$$G(x,y,t) = \frac{I}{2\pi w^2} e^{\left[\frac{(x-x_S)^2}{2w^2} + \frac{(y-y_S)^2}{2w^2}\right]} \quad (26)$$

where I was a normrand with user-specified mean intensity and standard deviation, w was the width of the point-spread-function (PSF), this was also user-specified. The term $(x - x_s)$ was the simulated spot coordinates in x subtract the simulated spot coordinates in x multiplied by a user-specified scale factor, similarly for y. The MATLAB tracker function was run on this simulated image video using one of three parameter scripts, p_old, p1 and p2 (see Appendices A,B,C respectively). The outputs per frame of the simulation included, N_e, the number of false positive bright spots. False positive spots were defined to be spots in the SpotsCh1 matrix, produced by using the tracker function on the simulated *in vitro* GFP image, that were a distance of more than 2 pixels, in xy, away from the location of the spots, N_n defined by the user to be in the simulated image, for the same xy coordinates (figure 2.11, false positive). The number of spots in the simulated image that were not identified by the tracker function was referred to as the number of spots missed, N_m (figure 2.11, missed spot). This occurred if the SpotsCh1 matrix had less spots in xy coordinates than were in the simulated spots matrix. The number of real positive bright spots, N_r was defined as the difference between the total of spots in the simulated image and the number of spots missed, $N_r = N_n - N_m$ (figure 2.11, real positive).

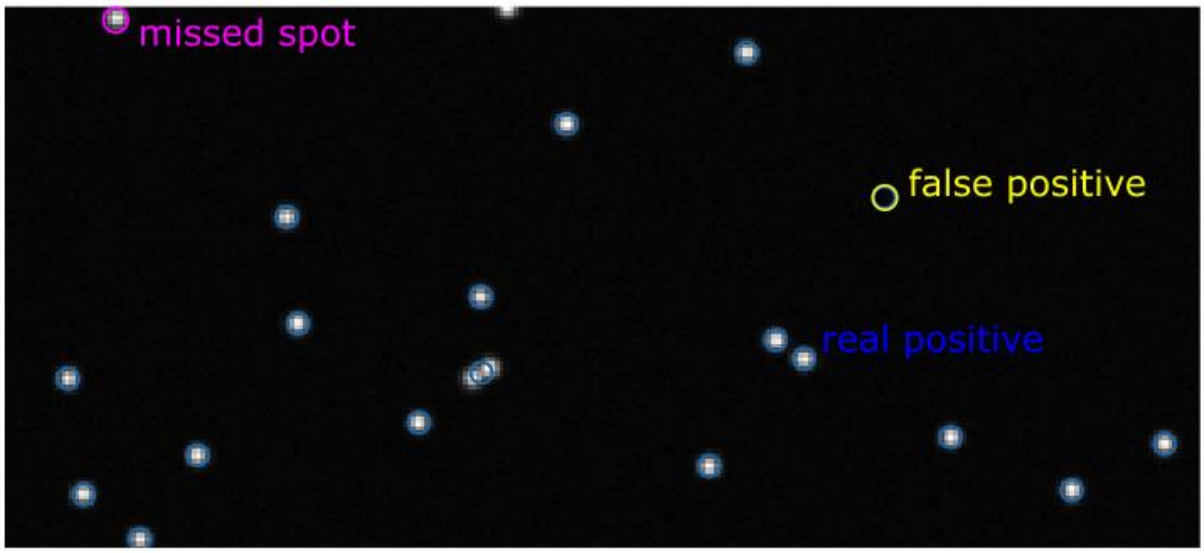

Figure 2.11 *Image of simulated in vitro GFP created in MATLAB indicating where the MATLAB tracker function has identified a false positive bright spot (a circle around an area where there is no bright*

spot), a real positive bright spot (a circle around a bright white spot) and where the tracker function has missed a spot (a bright white spot without a circle around it).

Table 1 outlines the differences between the parameter scripts. The subarray_halfwidth and inner_circle_radius were measured in pixels. The subarray_halfwidth and inner_circle_radius were changed in the parameter scripts to observe the differences in results these would produce when the parameter script was used with the tracker function. Parameter script p_old was used with the MATLAB functions in the analysis of fluorescence images of Mig1-GFP in yeast cells (Wollman et al., 2017). Fluorescence images of *in vitro* GFP were taken using the HILO/TIRF microscope and the size of a bright spot was inspected by eye to be either 2 or 3 pixels in radius, this was done using the method depicted in figure 2.8B. The gauss_mask_sigma parameter of the parameter script was set as 2 in p_old and as 1 in p1 and p2. The gauss_mask_sigma was the standard deviation of the Gaussian profile fitted over bright spots over time. This was chosen to be lower for parameter scripts p1 and p2 as these scripts were used on images produced by the HILO/TIRF microscope which had a camera with a larger image pixel size (93nm/pixel) than the camera used take images for the Wollman *et al.* (2017) data (80nm/pixel) which the p_old parameter script was used with the tracker function to analyse.

	p_old	**p1**	**p2**
subarray_halfwidth	8	5	5
inner_circle_radius	5	2	3
gauss_mask_sigma	2	1	1

Table 1 *Table of differences in parameters between parameter scripts p_old, p1 and p2*

The parameter scripts p_old, p1 and p2 were used with the tracker function on a (256x256)ROI simulation of bright spots of *in vitro* GFP which was 10 frames long with a single bright spot intensity of 31600±12400. This was a representative single intensity of a GFP molecule determined from images of *in vitro* GFP taken with the HILO/TIRF microscope with a 20mW 488nm intermediate-narrowfield epifluorescence beam at 20ms exposure with a (256x256)ROI.

The total number of bright spots in each frame, defined by the user, was N_n=50. Different values of the threshold parameter SNR_min were used in the simulation, starting at 0.4 then ranging from 0.6 to 1 in increments of 0.1. The effect of changing the threshold parameter

SNR_min on the number of real positive, N_r and false positive, N_e bright spots found was analysed.

2.2.3.2 Results

The mean number of real positive and false positive bright spots recorded off the simulation by the tracker function were plotted in jitterplots (figure 2.12A-B). The jitterplot in figure 2.12A demonstrates that the number of real positives decreases with increasing values of the SNR threshold (SNR_min), this is due to the nature of the MATLAB tracker function. Candidate bright spots with an SNR value below the SNR_min threshold are not accepted as bright spots. Therefore, as this threshold increases, less candidate spots will be accepted; the number of both false positives and real positives will decrease. For different values of SNR_min, the mean number of real positives identified was very similar when using p1 and p2. This indicates that the size of the inner_circle_radius did not have much of an impact on finding real bright spots in the image, as this was the only difference between p1 and p2, all other parameters were the same. There is a 9.5% difference between the mean number of real positives captured by p_old with SNR_min=0.4 and by p1 with SNR_min=0.4 and an 8.9% difference between the mean number of real positives captured by p_old and p2 both with SNR_min=04. This indicates that p_old captures up to 10% less real positive right spots in the image than p1 or p2. Therefore, this indicates that the subarray_halfwidth and inner_circle_radius in p_old are too large and not capturing enough real bright spots. Parameter scripts p1 and p2 are more efficient at capturing real bright spots in an image than the parameter script p_old. A diameter of 2,3 pixels is the correct size to capture a real bright spot.

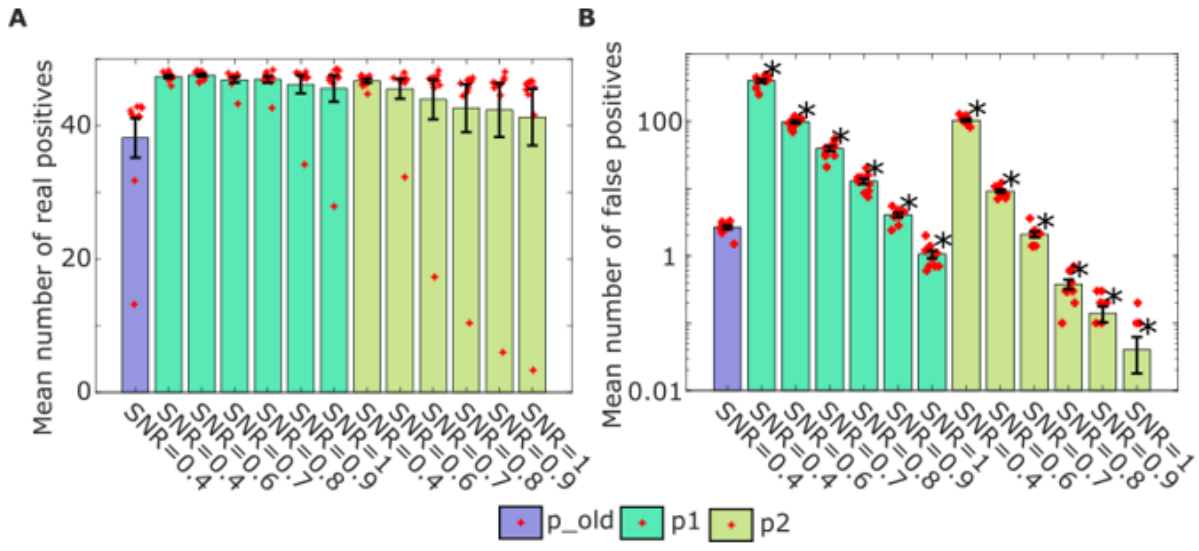

Figure 2.12 *Jitterplots of* ***A.*** *Mean number of real positive bright spots and* ***B.*** *Mean number of false positive bright spots recorded by the MATLAB tracker code when run on the in vitro GFP simulation for*

p_old (purple), p1 (green) and p2 (yellow) given different values of the signal to noise ratio (SNR) threshold (SNR_min) in the parameter script, values of the SNR_min threshold ranged from 0.6-1 and a threshold of 0.4 was also included as this was the original threshold specified in the p_old parameter script.

The jitterplot in figure 2.12B indicates that the tracker function captures less false positive bright spots when parameter scripts p1 and p2 are used with higher values of SNR_min, with p2 resulting in even less false positives being captured than when using p1. From this plot, it is shown that the parameter script p2 with SNR_min=1 performed the best and captured the least mean number of false positive bright spots in the image, capturing only an average of 0.04±0.02 false positives to an average of 40±5 real positives (figure 2.12A) out of a total of 50 real spots per frame. Neither the mean number of false positives nor the mean number of real positives data are normally distributed, so statistical tests were run on log distributions of the data which makes it approximately normally distributed. Since tests were conducted using two different parameter scripts, samples are independent from another. Therefore, an independent sample t-test was conducted on the log data for each parameter script. Upon running an independent sample t-test at the 5% significance level on the log data of the number of real positives between using parameter scripts p1 and p2 with different SNR_min threshold sizes (figure 2.13A) a p value less than 0.05 was obtained, indicating a significant decrease at the 5% significance level in the mean number of real positive bright spots found by the tracker function when using the p2 script compared to using the p1 script. Similarly, upon running an independent sample t-test at the 5% significance level on the log data of the number of real positives between using parameter scripts p1 and p2 with different SNR_min threshold sizes (figure 2.13B) a p value less than 0.05 was obtained. This indicates that the mean number of false positives identified by the tracker function also decreases at the 5% significance level when using parameter script p2 compared to using parameter script p1.

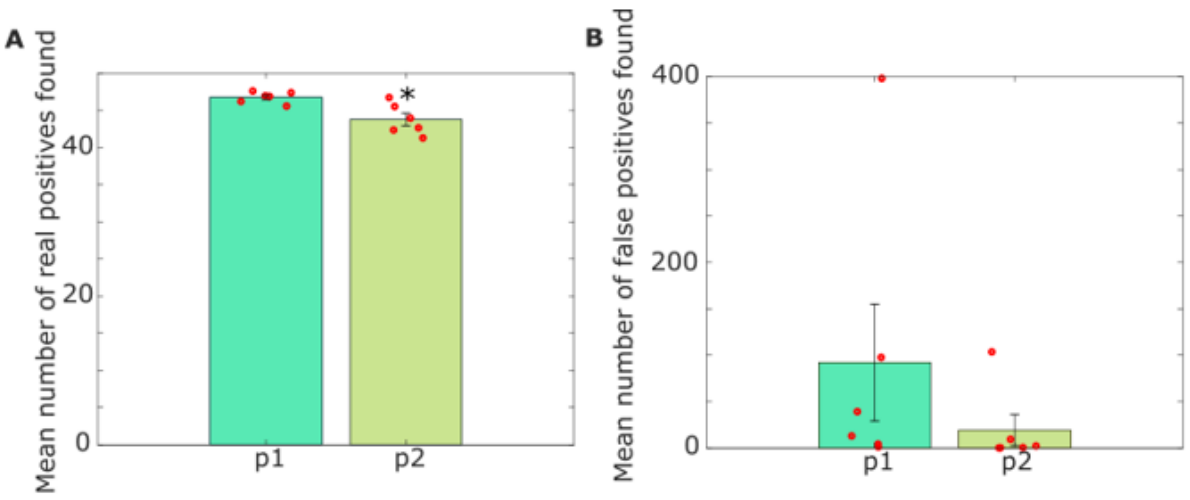

Figure 2.13 *Jitterplots of* ***A.*** *mean number of real positives found, for all sizes of SNR_min, by the tracker function when using parameter scripts p1 and p2.* ***B.*** *mean number of false positives found, for all sizes of the SNR_min threshold, by the tracker function when using the parameter scripts p1 and p2.*

The plots in figure 2.13A-B indicate decreases in the number of real positives and false positives recorded by the tracker function with increases in the size of SNR_min. These differences were found to be significant at the 5% significance level for both parameter scripts for different SNR_min threshold sizes (figure 2.13A-B). However, this was not enough data to determine the optimal parameter script. More analysis was conducted to determine which parameter script was best used to capture more real positives.

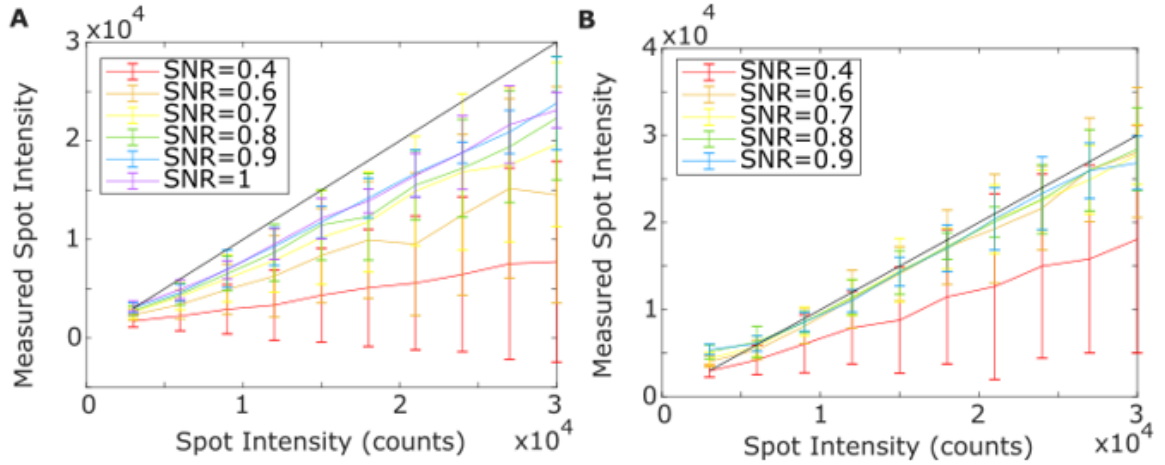

Figure 2.14 *Errorbar plots of measured spot intensity vs spot intensity for different values of signal to noise ratio (SNR) threshold (SNR_min) in the parameter script, values of the SNR_min threshold ranged from 0.6-1 and a threshold of 0.4 was also included as this was the original threshold specified in the p_old parameter script. For parameter scripts with* ***A.*** *inner_circle_radius=2 and* ***B.*** *inner_circle_radius=3. The black line is a line of measured spot intensity equal to spot intensity.*

The bright spot intensity measured by the tracker function when using the parameter scripts p1 and p2 was plotted against the real bright spot intensity in the simulation. Figure 2.14A

shows this for parameter script p1 given different sizes of SNR_min and figure 2.14B shows this for parameter script p2 given different sizes of SNR_min. The black plot on each graph is the line of the measured spot intensity being equal to the spot intensity. Both graphs indicate that the spot intensity measured by the tracker function is closer to the real spot intensity with higher values of SNR_min for both parameter scripts p1 and p2. Although, the values are even closer when p2 is used than when p1 is used. This indicates that using an inner_circle_radius value of 3 pixels was better than an inner_circle_radius of 2 for capturing bright spots in an image when trying to capture GFP molecules. Furthermore, using a SNR_min size of 0.8 was optimal as it contributed to producing the lowest number of false positive bright spots found (figure 2.12B) and highest number of real positives found (figure 2.12A) while retaining a low error in the data and contributing to recording bright spot intensity values closest to the real bright spot intensity values.

2.2.3.3 Conclusion

Both parameter scripts p1 and p2 were better than parameter script p_old at capturing more real positive bright spots while capturing less false positive bright spots on average when using the HILO/TIRF microscope. In turn, parameter script p2 was better than parameter script p1 at capturing the real intensity values of the bright spots. Therefore, parameter script p2 with a SNR_min=0.8 was chosen as the script to use with the MATLAB functions when analysing GFP molecules in fluorescence images of the transcription factors Mig1 in budding yeast, RelA in U2OS cells and AR in LNCaP cells.

2.3 Fluorescent beads assays

Fluorescence images of fluorescent beads were taken using four imaging conditions, epifluorescence (excitation beam incidence angle at 0°), HILO45 (excitation beam incidence angle at 45°), HILO56 (excitation beam incidence angle at 56.31°) and TIRF (excitation beam incidence angle at 62.24°), to assess the impact of these beam angle changes on the amount of detail captured in the images. Green fluorescent beads were imaged using the 488nm beam and red fluorescent beads were imaged using the 561nm beam, these images were analysed and their intensity was characterised to assess the dual-colour imaging performance of the microscope.

2.3.1 Assessing microscope performance when using different beam angles

2.3.1.1 Methods

A channel slide was manufactured by taping two pieces of double-sided tape parallel to one another onto a glass sample slide with a narrow gap between them, excess tape was cut away. On top of the tape, a glass coverslip was placed and 10μL of green beads in phosphate-buffered saline (PBS) at a dilution of 1:1000 (beads to PBS) was wicked through the channel. Slides were then labelled and ready for imaging.

Images were taken using the 488nm narrowfield beam with four different beam angles including epifluorescence (excitation incidence beam angle 0°), HILO45 (excitation incident beam angle at 45°), HILO56 (excitation incidence beam angle at 56.31°) and first TIRF (excitation incidence beam angle at 62.24°). The images were taken in the same field of view (FOV) with low laser power, at 5mW, and high ND, at 2-3. The region of interest (ROI) was (512x512) and a 50ms exposure time was used.

2.3.1.2 Results

Bright spots in the images were picked out by the user with the cursor (figure 2.15A) and then tracked with the MATLAB functions to characterise the spot intensity (figure 2.15B).

The jitterplot in figure 2.15B demonstrates that average spot intensity increases as the beam angle grows steeper yielding a brighter profile for TIRF than for epifluorescence with HILO showing incremental changes between these. The intensity distribution for each imaging condition was not normally distributed, so a nonparametric test was used. The data were paired since the same sample was imaged and the same analysis methods were used on the data. A Wilcoxon test was run at the 5% significance level on the paired data to compare the results of using different imaging conditions. Upon running the paired Wilcoxon tests at the 5% significance level on the average spot intensity between the epifluorescence condition and the HIOL45, HILO56 and TIRF conditions, we obtain p values of 1.1e-09, 1.4e-18 and 8.2e-25 respectively. This indicates that each imaging condition produces images with bright spot intensity that is significantly increased compared to the bright spot intensity of images taken using epifluorescence. This is what was expected as published results suggest that increasing the beam angle increases the signal to noise ratio (SNR) of the image (Axelrod, 1981; Axelrod and Axelrod, 2021; Gardini et al., 2023; Jialei Tang and Young Han, 2018; Tokunaga et al., 2008a).

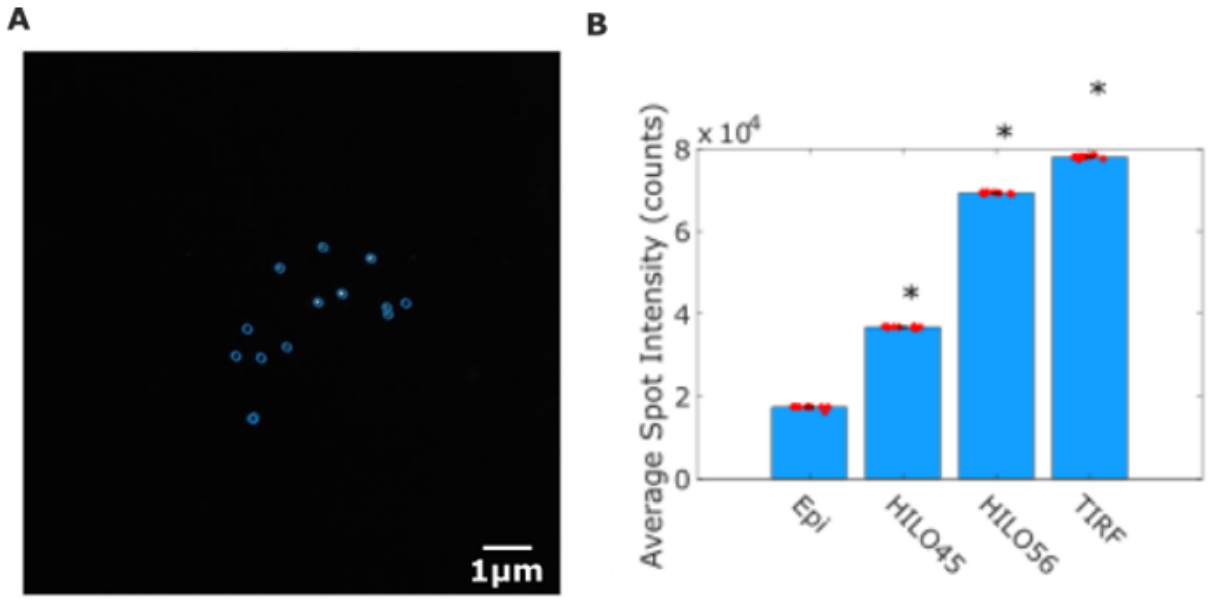

Figure 2.15 A. *Bright spots picked out by the user with the cursor (blue circles) in an epifluorescence image of green beads taken with a (5x10^{-2})mW 488nm narrowfield beam with (512x512)ROI at 50ms exposure.* ***B.*** *Jitterplot of bright spot intensity compared to illumination profiles, epifluorescence, HILO 45°, HILO 56° and TIRF 62° for fluorescence images of green fluorescent beads taken using (5x10^{-2})mW 488nm widefield beam with (512x512)ROI at 50ms exposure.*

2.3.1.3 Conclusion

The trends in bright spot intensity compared to excitation beam angle captured were useful as they demonstrated that increasing the angle increased the intensity, in line with published results. Using HILO angles of 45-57° were sufficient to observe increases in image signal. This means high image signal can be achieved without the need to only image at the surface of a cell (TIRF angles).

2.3.2 Assessing microscope dual-colour-imaging performance

2.3.2.1 Methods

A channel slide was manufactured by taping two pieces of double-sided tape parallel to one another onto a glass sample slide with a narrow gap between them, excess tape was cut away. A glass coverslip was placed on top of the tape. In a 1.5mL Eppendorf tube, 1μL of green beads solution and 1μL of red beads solution was mixed with 1mL of PBS. 10μL of the mixed beads solution was wicked through the channel.

Images were taken using the 488nm and 561nm intermediate-narrowfield beams with four different beam angles including epifluorescence (excitation incident beam angle 0°), HILO45 (excitation incident beam angle at 45°), HILO56 (excitation incident beam angle at 56.31°) and first TIRF (excitation incident beam angle at 62.24°). The images were taken in different FOVs

with low laser power, at 5mW, and high ND, at 2-3. The ROI (512x512) and a 50ms exposure time was used.

2.3.2.2 Results

Bright spots in beads images were identified by the tracker function and intensity was characterised. Figure 2.16 shows fluorescence images of the 488nm channel, 561nm channel and merged channels.

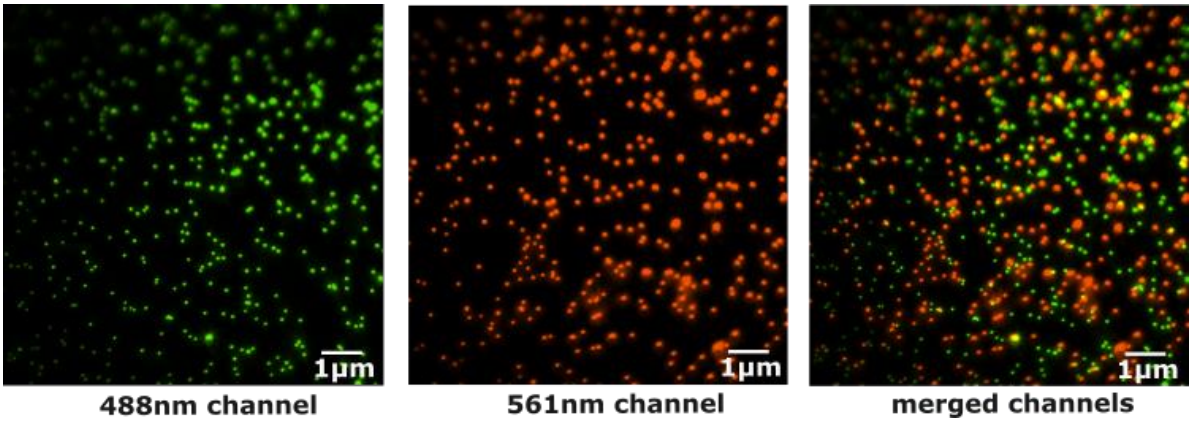

Figure 2.16 *Fluorescence image of green fluorescent beads (left) taken with 488nm intermediate-narrowfield beam at 5x10²mW at HILO 45° angle with a (512x512)ROI and 50ms exposure and fluorescence image of red fluorescent beads (middle) taken with 561nm intermediate-narrowfield beam at 5x10²mW at HILO 45° angle with a (512x512)ROI and 50ms exposure and both channels merged (right).*

Images became more intense with steeper beam angles and, for all beam angles, 488nm channel images (figure 2.17A) were dimmer than 561nm channel images (figure 2.17B).

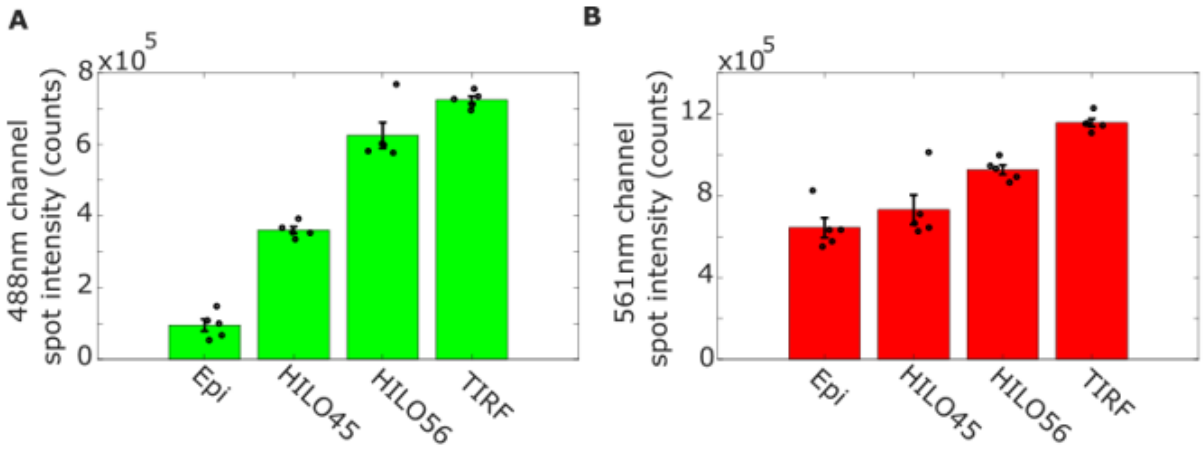

Figure 2.17 A. *Jitterplot of spot intensity for images of green fluorescent beads (left) taken with 488nm intermediate-narrowfield beam at 5x10²mW at epifluorescence, HILO 45°, HILO 56.31° and TIRF 62.24° angles with a (512x512)ROI and 50ms exposure.* ***B.*** *Jitterplot of spot intensity for images of red fluorescent beads (middle) taken with 561nm intermediate-narrowfield beam at 5x10²mW at epifluorescence, HILO 45°, HILO 56.31° and TIRF 62.24° angles with a (512x512)ROI and 50ms exposure.*

The intensity data doesn't follow a normal distribution, therefore a statistical test was run on the log distribution of the data. An independent sample test was used as the data was produced using different samples and different imaging conditions were compared against the epifluorescence condition. Upon running an independent sample t-test at the 5% significance level on the log distribution of the intensity data between epifluorescence and the HILO45, HILO56 and TIRF conditions for the 488nm channel, we obtain p values of 0.0012, 1.9e-04 and 1e-06 respectively. This indicates that the means are significantly different at the 5% significance level and mean spot intensity did indeed increase with increasing beam angle. Similarly, when we run independent sample t-test at the 5% significance level on the log distribution data between epifluorescence and the HILO45, HILO56 and TIRF conditions for the 561nm channel, we obtain p values of 6.8e-05, 0.0016 and 5.9e-04 respectively. As in the 488nm channel, when increasing beam angle, mean spot intensity in the 561nm channel images increases.

2.3.2.3 Conclusion

The results from the 488nm and 561nm channel images demonstrate a proof of concept that the HILO/TIRF microscope is capable of multi-colour imaging and that increasing beam angle increases image intensity in both channels.

2.4 *in vitro* GFP assays

To investigate if the HILO/TIRF microscope was sensitive enough to capture single fluorescent protein molecules, *in vitro* GFP was imaged using various imaging conditions and image intensity was characterised. Different imaging conditions were used to observe if expected trends, such as increasing beam power during imaging to increase image intensity, could be captured after using the MATLAB functions on the images for intensity analysis.

2.4.1 Methods

A channel slide was manufactured by placing two pieces of double-sided tape onto a glass sample slide parallel to one another with a narrow gap between them. A plasma-cleaned glass coverslip was then stuck onto the tape over the top of the channel and excess tape was cut away. The coverslips were plasma-cleaned to remove fluorescent residue which is left on them following manufacture.

After this, 10μL of anti-GFP at a dilution of 1:2000 in PBS was wicked through the channel and the slide was placed in a bespoke humidity chamber (fashioned from a weigh-boat filled with

damp blueroll with another weigh-boat used as a lid) for five minutes. After this, the slide was washed through with 10μL of PBS twice. After this, 10μL of GFP at a dilution of 1:100,000 in PBS was wicked through. The slide was then placed in the humidity chamber for a further five minutes. After the five minutes had elapsed the slide was washed again with 10μL of PBS twice and 10μL of white beads solution at a dilution of 1:1000 in PBS was wicked through and the slide was placed in the humidity chamber for a final five minutes before imaging.

Various imaging conditions were used; the ROI size, exposure time, beam size and beam power were all changed to observe the impact of changing these on whether or not single molecules could still be observed in the image. Continuous recording was required rather than switching the camera on and off to limit exposure time. The intent was to maximise exposure time to fill the entire video length to gather the most information about the protein activity. Table 2 outlines the imaging conditions used with the 488nm excitation beam.

	ROI	**Exposure**	**488nm beam power**	**488nm beam size**	**Beam angle**
Conditions 1,2,3	(64x64)	5ms	5,10,20mW	Narrowfield	Epi
Conditions 4,5,6	(128x128)	10ms	2,5,10mW	Intermediate narrowfield	Epi
Conditions 7,8	(512x512)	50ms	20mW	Widefield	Epi, HILO56

Table 2 *Imaging conditions used on in vitro GFP samples*

2.4.2 Results

The HILO/TIRF microscope performance at capturing single GFP molecules was tested. After this, optimal imaging conditions for capturing single GFP molecules at correct intensity values were compared against one another.

2.4.2.1 Microscope performance at capturing single GFP molecules

The tracker and overTracker functions were used on the *in vitro* GFP images and the intensity of images was characterised. Figure 2.18 demonstrates the differences between *in vitro* GFP images taken using the HILO/TIRF when using a 20mW 488nm epifluorescence narrowfield beam with a (64x64)ROI at 5ms exposure (figure 2.18A), and when using a 10mW 488nm epifluorescence intermediate-narrowfield beam with a (128x128)ROI at 10ms exposure (figure 2.18B) and when using a 20mW 488nm HILO56 widefield beam with a (512x512)ROI at 50ms exposure (figure 2.18C).

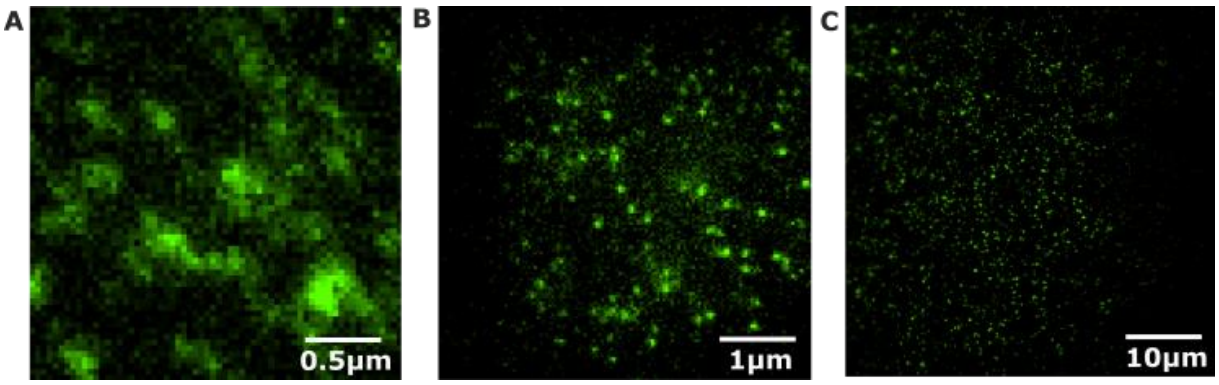

Figure 2.18 A. *in vitro GFP imaged using a (64x64)ROI with a 20mW 488nm epifluorescence narrowfield beam at 5ms exposure.* ***B.*** *in vitro GFP imaged using a (128x128)ROI with a 10mW 488nm epifluorescence intermediate-narrowfield beam at 10ms exposure.* ***C.*** *in vitro GFP imaged using a (512x512)ROI with a 20mW 488nm HILO56 widefield beam at 50ms exposure.*

KDF distribution plots of bright spot intensity and Chung-Kennedy filter plots of bright spot intensity were constructed. Figure 2.19B is a KDF distribution plot of spot intensity for the tracked and overtracked data for an *in vitro* GFP image taken using a (128x128)ROI with a 5mW 488nm intermediate-narrowfield epifluorescence beam at 10ms exposure. Figure 2.19A is a plot of spot intensity vs frame in which the spot was found for one bright spot in the image. Again, negative raw intensity values are due to the presence of background which is brighter than the photobleached bright spot. A Chung-Kennedy filter has been fitted to the data. The blue curve is the raw overtracked data, the red points are the raw overtracked data after a Chung-Kennedy filter was run on it. The peak intensity of the KDF distribution plot for the raw data (before the overTracker function was used on the data) is 3700±1600. The Chung-Kennedy filter plot has a step-height at approximately 3700. After analysing several Chung-Kennedy plots for several bright spots recorded by the tracker function it was evident that most of the Chung-Kennedy filter plots had similar step-heights to the peak of the kernel density plot. This indicates that the peak intensity of the KDF plot is indeed that of a single GFP molecule. This means that the tracker function and the microscope were indeed capturing single molecules in the image data.

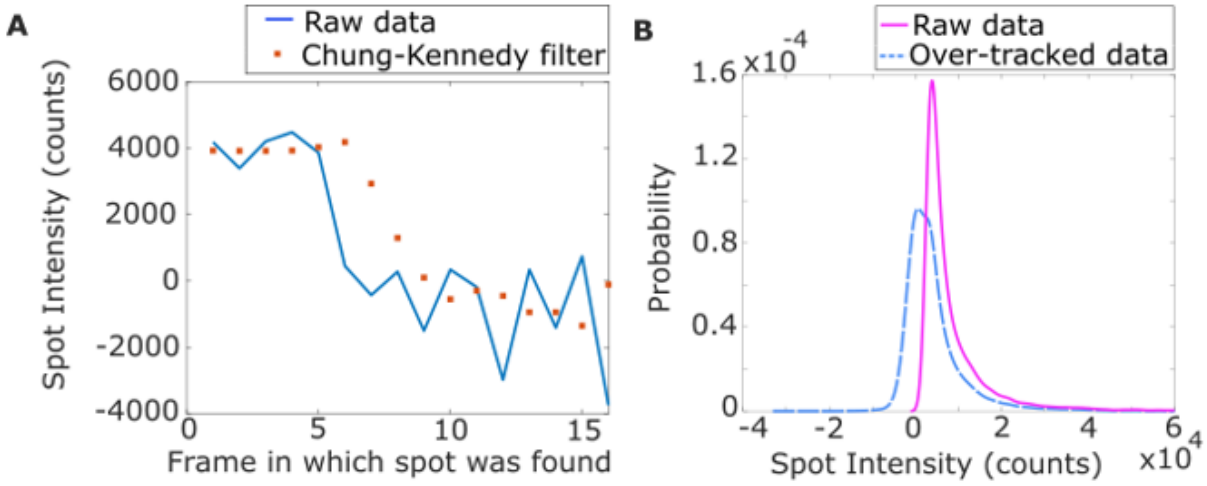

Figure 2.19 A. *Plot of spot intensity vs the frame in which the spot was found for one bright spot with a Chung-Kennedy filter fitted for in vitro GFP assay image data taken with (128x128)ROI, 5mW 488nm intermediate-narrowfield beam at 10ms exposure.* ***B.*** *Kernel density plot of spot intensity for in vitro GFP assay image data taken with (128x128)ROI, 5mW 488nm intermediate-narrowfield beam at 10ms exposure.*

2.4.2.2 Determining optimal imaging conditions for GFP molecules

After demonstrating that the HILO/TIRF microscope and tracker function could be used to capture single GFP molecules in images, the next step was to find out which imaging conditions were optimal to capture the most intense bright spots in sample images.

Bright spot intensity produced by the imaging conditions outlined in Table 2 was analysed and compared by running the tracker function on all images and producing a jitterplot of bright spot intensity against imaging condition (figure 2.20).

The jitterplot indicates that when using a (64x64)ROI at 5ms exposure and a (128x128)ROI at 10ms exposure, bright spot intensity increases with an increase in beam power, this is as expected. Bright spot intensity is similar for (64x64)ROI and (128x128)ROI for 5ms and 10ms exposure respectively when the beam is set at 5,10mW. The bright spot intensity is approximately 15,000 at 5mW beam power for 5,10ms exposure with an ROI of (64x64) and (128x128) respectively. For 10mW, this intensity increases to 20,000.

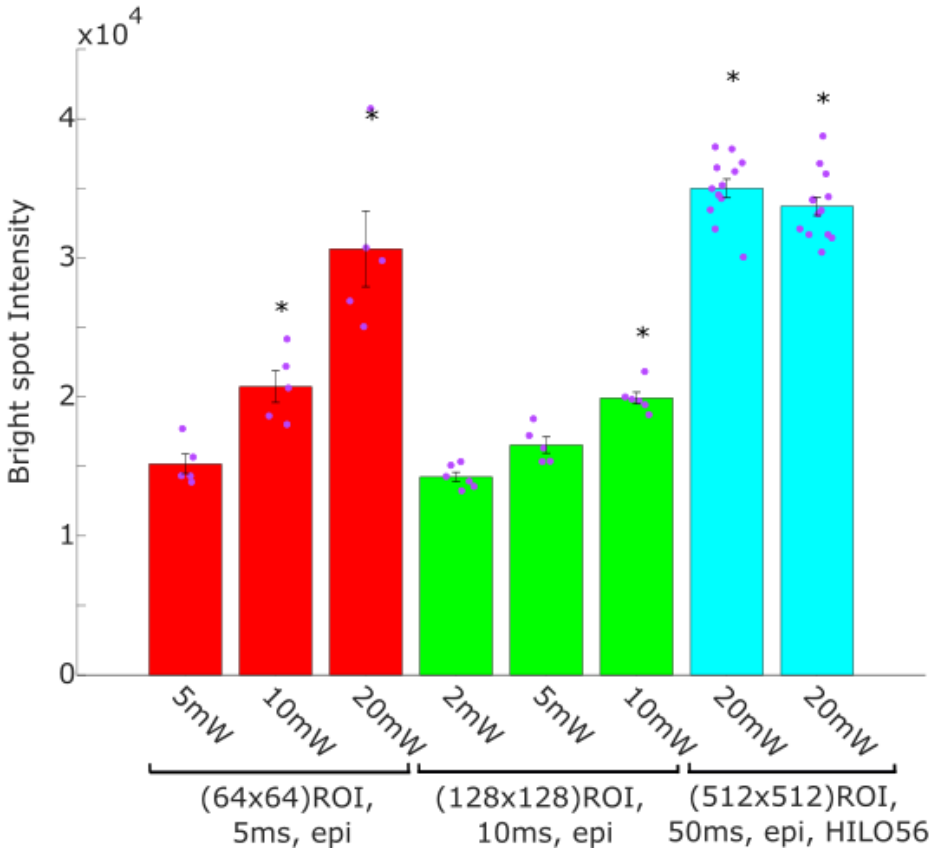

Figure 2.20 *Jitterplot of bright spot intensity for in vitro GFP images taken using various imaging conditions*

Intensity of a single GFP molecule is highest, about 35,000, when beam power is at 20mW and the ROI is (512x512) with a 50ms exposure. However, a larger ROI means slower imaging as a 50ms exposure must be used with the CCD Evolve Delta camera capabilities. This is too slow to capture and track single molecules.

Fastest imaging, at 5ms, can be achieved when using a (64x64)ROI. The jitterplot in figure 2.20 indicates that a beam power of 20mW produces images with the most intense single molecules. The *in vitro* GFP intensity data is not normally distributed and different imaging conditions were tested against each other, therefore an independent sample t-test was used on the log distribution of the data. Upon running an independent sample t-test at the 5% significance level between the (64x64)ROI with 5ms exposure condition when using 5mW beam power and using 20mW beam power, we obtain a p value less than 0.05. This indicates that average bright spot intensity significantly increases when beam power is increased, as expected.

2.4.3 Conclusion

The HILO/TIRF microscope was able to capture single *in vitro* GFP molecules from *in vitro* GFP samples when using different imaging conditions. This indicates that the microscope is able to capture single molecules regardless of imaging condition. Although image intensity is greater when longer exposure times (20-50ms) are used, imaging speed is too slow to capture the dynamics of the single molecules. Faster imaging speeds can be achieved by using a smaller ROI, (64x64). Higher beam powers can be used to increase image intensity, although this does come with the cost of a faster onset of photobleaching. However, when considering stoichiometry analysis in chapters 3 and 4, data from the first few frames of image videos, about 20 frames, is the most valuable as further frames introduce more noise into the analysis (Wollman and Leake, 2022).

2.5 Chapter conclusion

A HILO/TIRF microscope with 488nm and 561nm beam excitation and epifluorescence, HILO and TIRF imaging abilities was built. MATLAB functions were used to analyse images taken with this microscope. The ability of the functions to capture single GFP molecules was tested using simulations of *in vitro* GFP. From this, optimal function parameters were identified and used in analysis of real *in vitro* GFP images taken with the microscope.

The impact of changing the beam angle on image intensity was tested using fluorescent beads assays. Steeper beam angles produced more intense images, this is in line with published results (Axelrod, 1981; Axelrod and Axelrod, 2021; Burmeister et al., 1994; Gardini et al., 2023; Jialei Tang and Young Han, 2018; Neria and Kisley, 2023; Tokunaga et al., 2008a) and a proof of concept that the microscope is functional. The fluorescent beads assays further demonstrated the HILO/TIRF microscope dual-colour imaging capability.

The *in vitro* GFP analysis elucidated the optimal imaging conditions using the HILO/TIRF microscope to capture single GFP molecules. A (64x64)ROI with 5ms exposure and 488nm beam power of 20mW will be used to image Mig1-GFP in budding yeast cells to compare to published results (Wollman et al., 2017) to test that the results the HILO/TIRF microscope is obtaining are biologically correct.

Chapter 3- Using the single-molecule fluorescence HILO/TIRF microscope to image cell-signalling processes

After using fluorescence microscopy to obtain images of *in vitro* proteins or proteins in cells and the intensity of bright spots in the image has been characterised, molecules in singular or cluster form can be tracked over image video frames and the stoichiometry characterised. Stoichiometry in this case refers to the number of fluorescently labelled biomolecules that are in a tracked object (Sheperd et al., 2021).

This chapter covers the work carried out to fulfil the second of the five main objectives of this PhD, namely;

2. *Test HILO imaging of Mig1-GFP in yeast and compare it to published results*

The HILO/TIRF microscope was used to image Mig1-GFP in budding yeast and compare the stoichiometry results to those outlined in literature (Wollman et al., 2017). These results showed that the transcription factor, Mig1, in yeast forms clusters. This was a novel piece of research which elucidated the clustering behaviour of transcription factors through observation, beforehand this behaviour was only determined through models (Wollman et al., 2017). If the same stoichiometry values could be observed when analysing images taken with the HILO/TIRF microscope, this would serve as a proof of concept that the HILO/TIRF microscope was sensitive to single molecules and their clustering behaviour. Stoichiometry values for cells imaged were the same as those for glucose (+) conditions in the Wollman *et al.* paper. The results of using two different analysis methods on the Mig1-GFP yeast cell images were compared against each other. One method involved categorising the trajectories of molecules in images to estimate the stoichiometry and could only be used on faster videos, such as those taken using a 5ms exposure. The other method involved categorising the bright spots in the image to calculate the stoichiometry and, because it did not use trajectory information, could be used to analyse the stoichiometry of cells in videos using longer exposure times and on images with slow-moving particles or static proteins. The aim was to find out if both methods yielded biologically correct results that were significantly similar to each other. If they did, this would indicate that stoichiometry results were not a product of the analysis method used, but rather were reflective of the single molecule stoichiometry of the sample that the microscope was able to capture. Indeed, both methods produced the same biologically significant results.

Further images of Mig1-GFP in yeast were taken with a HILO beam at approximately 45° which was shifted slightly left or right of the cell ROI. The theory was that a shifted ROI would result in more molecules being captured in the image due to capturing the cell nucleus more often during imaging. However, when compared to epifluorescence and standard HILO images, this was not the case.

The imaging capabilities of the HILO/TIRF microscope were further tested when it was used to image the polarity protein PAR6 labelled with GFP in *C.elegans* embryos, grown by Rodriguez *et al*. Embryos containing temperature-sensitive (TS) and non-temperature-sensitive (non-TS) variants of a key kinase which interacts with PAR6, atypical protein kinase C (apkC) were imaged and the stoichiometry was compared between them. After running statistical tests on the data, significant differences in stoichiometry were observed between the TS and non-TS cells. This was in line with real biological findings (Rodriguez et al., 2017).

Furthermore, the proteins apoE and amyloid beta (Aβ) which are thought to play a key role in the development of Alzheimer's disease were imaged using the HILO/TIRF microscope. The interaction of apoE with Aβ in response to stimulation by complement regulator factor H (FH) was tested using *in vivo* stoichiometry analysis of *in vitro* assay images. After running statistical tests, it was observed that FH did indeed have an impact on Aβ. However, more analysis was required to observe the real impact of FH on apoE. This work was carried out in association with Haapasalo *et al.* and these contributed to published results (Chernyaeva et al., 2023).

The HILO/TIRF microscope performs well when imaging *in vitro* and *in vivo* single molecules and produces images from which biologically significant results can be derived after using one of two methods to characterize stoichiometry.

3.1 Introduction

3.1.1 Basic cell signalling processes

Cell signalling is the process by which cells sense and respond to their environment. All cells have these processes, from single-celled organisms such as yeast to cells from multi-cellular organisms such as U2OS cells from human cancers. The process can begin with a signalling molecule which is received by a receptor protein located at the cell surface, this is step 1 in figure 3.1. The receptor binds the signalling molecule which activates the receptor, step 2 in figure 3.1, this then activates one or multiple intracellular signalling pathways, step 3 in figure

3.1, which depend on intracellular signalling proteins. The signal is processed within the cell and ultimately sent to the related intracellular targets. Effector proteins are activated by the signal. These proteins alter gene expression and the related change in cell behaviour occurs, this is step 4 in figure 3.1 (Alberts et al., 2015).

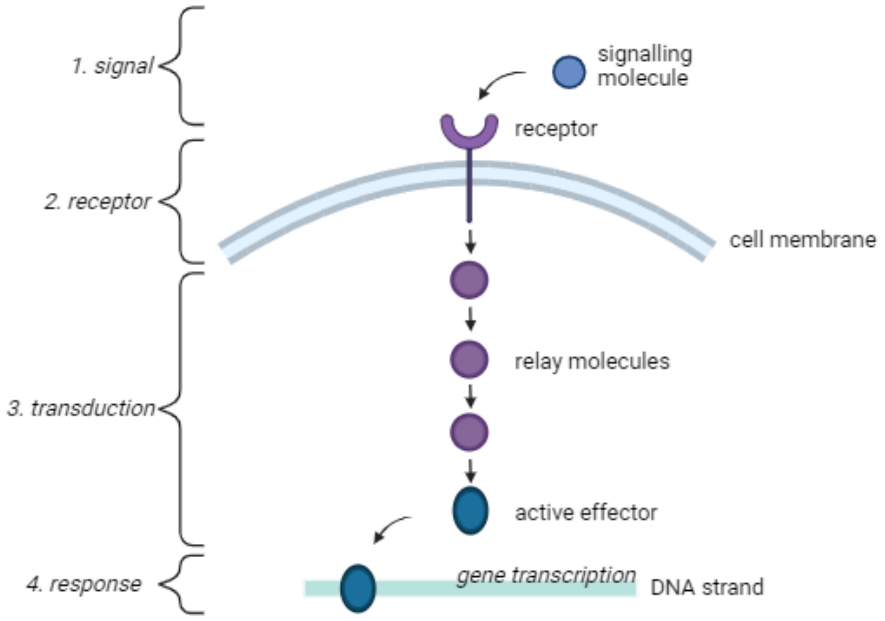

Figure 3.1 *Basic depiction of cell signalling processes. Image created in BioRender.com.*

Intracellular processes can be captured using single-molecule fluorescence imaging by labelling molecules of interest with fluorescent labels. The bright spots in image videos can be identified and tracked across video frames. This information can be used to yield stoichiometry results.

3.1.2 Cell segmentation and stoichiometry analysis methods

3.1.2.1 Cell segmentation methods

There are several methods that can be used to segment cells in images, the most common of these are thresholding, edge detection, region-growing and active contour models. However, recently cell segmentation methods utilise deep learning and neural network databases containing model segmentation datasets from various cell types. Deep learning is a variation of machine learning based on neural networks and has been shown to be very useful in microscopy imaging and image analysis applications such as segmentation of *C.elegans* cell images (Ning et al., 2005), yeast cell images (Kraus et al., 2016), identification of strains (Kraus et al., 2017) and proteins (Pärnamaa and Parts, 2017) in yeast cell images and protein localisation prediction in human and yeast cells (Lu et al., 2019).

For deep learning, a neural network can be a supervised learning network or an unsupervised learning network. In a supervised learning network, a neural network learns to produce desirable data outputs from a paired input and output training dataset. It is told what features are desired in the output based on the features of the input. After training, the neural network can be used on previously unseen data inputs to autonomously produce desirable outputs (Von Chamier et al., 2019). LIVECell, developed by Edlund *et al.* (2021), is a vast dataset of manually annotated phase-contrast images containing over 1.6million cells which is used as a training dataset for deep learning-based segmentation (Edlund et al., 2021). When used in benchmark tests for segmentation, LIVECell achieved average precision scores above 80% (Edlund et al., 2021) compared to 61% achieved by EVICAN, another deep learning database consisting of grayscale images of 30 different cell lines (Schwendy et al., 2020). Scherr *et al.* (2020) demonstrated a novel technique for segmenting touching cells in images which involves using a U-Net convolutional neural network (CNN) to predict the proposed neighbour distances (Scherr et al., 2020).

More traditional segmentation methods such as thresholding, edge detection, region-growing and active contour models can be used to produce segmented cell images for neural network training datasets.

3.1.2.1.1 Thresholding

Thresholding works by turning image pixels into binary, 0s and 1s, data based on an intensity threshold. A value of 0 is assigned to a pixel with intensity below the threshold while a 1 is assigned to a pixel with intensity at or above the threshold. The threshold value can be specified by the user or determined automatically using various thresholding method categories (Sezgin and Sankur, 2004). These categories include, but are not limited to, histogram shape, clustering-based methods and entropy-based methods. The most common method to use in thresholding is Otsu's Method (Otsu, 1979). The Wollman *et al.* segmentation code (Wollman and Leake, 2022) uses thresholding methods.

Otsu's Thresholding Method

This method works to classify pixels as background or foreground. Defining background as class 1 and foreground as class 2, Otsu's method works by computing a histogram of the probabilities of intensity levels then it sets up the probabilities of each class and their means. After this it loops through the possible thresholds from 1 to the maximum intensity, updating

the class probabilities and means within this loop and computing the class variances. The threshold output corresponds to the maximum class variance.

A disadvantage of the thresholding method of segmentation is that it is sensitive to high noise levels. Areas of the background with intensities close to those of cells will be assigned binary values of 1 which could lead to false positives being collected during analysis (Emami et al., 2021). However, morphological transformations can be used to remove artefacts that don't fit into a structural element. A flat binary-valued structural element is a binary matrix with a defined shape that fits over an image. Pixels in the image are assigned a 1 if they fit within the shape and a 0 if they do not. Flat binary-valued structural elements come in many 2D shapes including lines, diamonds, octagons, disks and many more. The Wollman *et al.* segmentation code uses a disk-shaped structural element (Wollman and Leake, 2022).

3.1.2.1.2 Edge detection

Edge detection segmentation involves identifying areas of discontinuous intensity changes (Gonzalez, 2009). These areas are defined as edges and can be used to define areas in an image where depth, material properties or surface orientation change. A disadvantage of the edge detection method is that it is sometimes unable to distinguish between two objects with the same intensity that are very close to each other or overlap (Emami et al., 2021). However, watershed segmentation can be used to overcome this issue. Watershed segmentation involves treating an image as topographic; the intensity of a pixel represents its height (Emami et al., 2021). The algorithm produces segmentation by running lines along the top of height-defined ridges. A further disadvantage of the edge detection method is that it does not work well on low contrast images (Masuzzo et al., 2016) where edges are harder to detect. Although, this can be improved by improving image SNR with the microscopy technique used.

3.1.2.1.3 Region-growing

Region growing segmentation works in two steps. The first step is to identify seed points, these are sub-regions of the image that fit into user-specified criteria. The second step involves categorising the regions that neighbour the seed points. Binary logicals are used to determine if these regions should be added to the same region as seed point or not (Irshad et al., 2014). A 0 is assigned to a region that should not be added to the seed region while a 1 is assigned to a region that should be added to the seed region. If the neighbouring regions are added, this is region-growing, if they aren't, this is region-splitting (Luo et al., 1998). A number of models have been built for coloured image segmentation based on the seeded region-growing

technique (Fan et al., 2001; Garcia Ugarriza et al., 2009; Ikonomatakis et al., 1997; Shih and Cheng, 2005).

3.1.2.1.4 Active contour models (Snakes)

An active contour model, referred to as a *Snake* by its authors (Kass et al., 1988), involves fitting a spline to boundaries in an image. The spline can be deformed iteratively to fit the boundary more closely. Energy optimisation is used in this process; the energy function is the sum of the internal energy and external energy of the spline. The internal energy controls the shape of the active contour and the external energy controls how close the fit of the active contour is to the image boundary. Since the spline is deformable, an advantage of this method is that it can be used to track moving cells. However, a disadvantage of the method is that when the overall contour energy is decreased, smaller features can be omitted which may mean over- or under-segmenting (Emami et al., 2021).

3.1.2.2 Cell stoichiometry analysis methods

Approaches to stoichiometry analysis in microscopy images usually involve counting the number of photobleaching steps in fluorescently labelled samples in single-molecule images. Photobleaching is a discontinuous stepwise decay from maximum intensity of a fluorophore to intensity values at or close to zero (Aurousseau et al., 2016). Methods like the number and brightness (N&B) method, subunit counting and, more recently, deep learning, can be used to determine cell stoichiometry quantitatively.

3.1.2.2.1 Number and Brightness method

Number and Brightness (N&B) method (Qian and Elson, 1990), first demonstrated on a living cell image with confocal laser-scanning microscopy and two-photon excitation in 2008 (Digman et al., 2008), involves creating an apparent brightness map by estimating the apparent brightness and apparent number from photon count fluctuations (Fukushima et al., 2021). For n images and $x_j, (j = 1,2, \dots n)$ the number of photon counts in the j^{th} image, the apparent brightness, B and apparent number, N are given by (Müller, 2004);

$$B = \frac{\sigma - \bar{x}}{\bar{x}} \tag{27}$$

$$N = \frac{\bar{x}^2}{\sigma - \bar{x}} \tag{28}$$

where $\bar{x}$ is the sample mean and $\sigma = (\overline{x^2} - \bar{x}^2)$ is the sample variance (Fukushima et al., 2021). This method can be used to derive information about the cell stoichiometry by using the average and individual photon intensity. An advantage of the N&B analysis method is that it can be used to elucidate properties of diffusing particles joining together in a living cell.

However, a disadvantage of the N&B method is that it is easily effected by biases such as lag time, background intensity or a limited number of frames in the video (Fukushima et al., 2021).

3.1.2.2.2 Subunit counting

Subunit counting is a method which uses tracks data from fluorescence images to determine photobleaching steps of fluorophore intensity in the image. The number of steps corresponds to the number of subunits in the sample (Xu et al., 2019). Firstly, two laser intensities are determined; the observation intensity, at which cells can be observed before photobleaching, and the photobleaching intensity, at which the fluorophores photobleach. These intensities have to be optimised for each imaging condition used and not altered during imaging on the same sample type. It is important that the photobleaching intensity acts slow enough to allow the user to capture photobleaching steps. After imaging the sample, the videos are assessed and molecules are tracked. The number of discontinuous steps in fluorescence intensity for the length of time the track lasts are counted (Aurousseau et al., 2016). This is done for each track in a specified region of the sample image. Fluorescence signal and photobleaching steps can be better seen from the data after filters are applied to remove or lower background noise. Data is recorded from each video frame from every video and custom-built software can be used to perform counting of tracks and steps. Filters such as Chung-Kennedy (Chung and Kennedy, 1991) or Haar wavelet (Kingsbury and Magarey, 1998; Moldovanu and Luminita, 2010) can be used to lower image noise. The data collected after using these is compiled to create a step counting distribution from which the stoichiometry can be determined. Usually, proteins with a fixed stoichiometry follow a binomial distribution (Aurousseau et al., 2016). The Wollman *et al.* stoichiometry analysis code (Wollman and Leake, 2022), which is explained in the next section, works very much like subunit counting.

An advantage of subunit counting is that it can be fairly fast and simple for the user, due to many automation methods (McGuire et al., 2012; Xu et al., 2019). A further advantage is that it allows real-time monitoring of fluorophore behaviour in living cells (Xu et al., 2019). However, like the N&B method, subunit counting results can be skewed by high background noise levels (Tsekouras et al., 2016).

3.1.2.2.3 Deep learning stoichiometry analysis

Deep learning analysis can be used to perform photobleach step counting automatically and relatively quickly compared to techniques used in subunit counting. The convolutional and long-short-term memory deep learning neural network (CLDNN) (Xu et al., 2019) uses single-

molecule photobleaching traces as input data and outputs the number of steps. Training datasets usually consist of experimental data which has been manually labelled or data simulations. After training, the CLDNN can be used to capture stoichiometry results from a large amount of image data relatively quickly and with over 90% accuracy (X. Liu et al., 2022). Further examples of deep learning networks built for image stoichiometry analysis include the DGN, which is able to achieve up to 80% accuracy in counting photobleaching steps (Yuan et al., 2020), and the DLCNN, which could achieve more than 98% accuracy in identifying monomers (Wang et al., 2021).

3.2 Analysing image tracks data

MATLAB functions were built by Wollman *et al.* (Miller et al., 2015; Wollman and Leake, 2022) and later also built in Python (Sheperd et al., 2021). These facilitated the identification and tracking of bright spots in images across image video frames. This was achieved using the tracker and overTracker functions. Further suites of functions were designed to facilitate cell segmentation and stoichiometry analysis. The master functions were thresholdSegment and trackAnalyser.

3.2.1 Segmenting cell images

The Wollman *et al.* thresholdSegment function segments cell images using one of five different thresholding methods. These include Otsu's method, creating a binary image with 1s assigned to pixels fitting within the threshold and 0s elsewhere, the histogram thresholding method and Otsu's method with an adaptive threshold. All methods use a disk-shaped structural element.

Parameters of the MATLAB segmentation function were changed to be optimal for fluorescence images of Mig1-GFP in yeast cells. This was for the cell wall (yellow outline in figure 3.2) and cell nucleus (red outline in figure 3.2). The parameters that produced the most accurate segmentation in over 80% of images in a sample set were chosen as optimal. Figure 3.2 demonstrates the segmentation working on 90% of cell images for the cell wall, using a segmentation threshold of 0.1, and cell nucleus, using a segmentation threshold of 0.5.

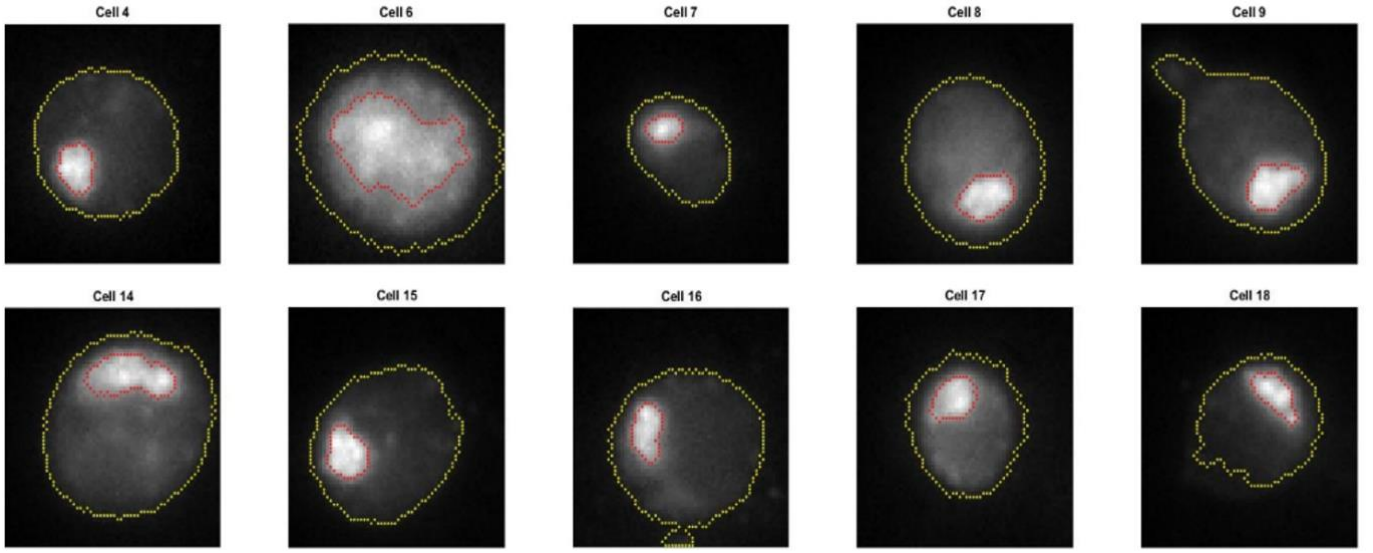

Figure 3.2 *MATLAB segmentation used on a set of fluorescence Mig1-GFP in yeast images taken using a 20mW 488nm epiflourescence narrowfield beam with a (64x64)ROI at 5ms exposure. The red outline indicates nucleus segmentation while the yellow outline is cell wall segmentation.*

These parameters were used on following images of Mig1-GFP in yeast taken using the HILO/TIRF microscope.

3.2.2 Analysing single-molecule tracks

Single-molecule tracks were created by analysing the data created by the tracker and segmentation functions. Bright spots that were assigned trajectories by the tracker function, and were within the boundaries defined by the segmentation function, were used to determine stoichiometry using one of two methods. That is, *in vivo* stoichiometry results could be produced by analysing the bright spots data (spots method) or the tracks data (tracks method).

3.2.2.1 Determining stoichiometry using the spots data (spots method)

A matrix is created by identifying the data in the (12xK) SpotsCh1 matrix produced by the tracker function that is within the segmentation boundaries defined by using the segmentation function within the first n frames of the video. A list of stoichiometry values, $\underline{S}$ is created by dividing the initial bright spot intensity by the I_{single} value. The I_{single} value, as explained in Chapter 2, is the intensity of a single GFP molecule prior to it photobleaching.

The spots method is used on image videos with exposure times longer than 5ms per frame. An exposure time longer than this is not fast enough to track single molecules. Therefore, trajectories cannot be produced from the tracks data. The spots method was used to analyse the fluorescence images of RelA-GFP in U2OS cells taken with a (256x256)ROI at 20ms

exposure, and fluorescence images of AR-GFP in LNCaP cells taken with a (256x256)ROI at 20ms exposure.

3.2.2.2 The trackAnalyser function (tracks method)

After the (12xK) SpotsCh1 matrix is created by the tracker function and cell boundaries are defined by the segmentation function, the trackAnalyser function is used to create a new (15xJ) matrix, called trackArray, with J rows, where J is the number of tracks within the segmentation boundaries.

Columns in the (15xJ) trackArray matrix include data on the trajectory number, the first and last frames of the track, the compartment the track is in (defined by the segmentation data as being in the nucleus or the cytoplasm), the amount of time a track spends in a compartment and the stoichiometry.

Stoichiometry is determined by using the getStoichiometry function. The trackAnalyser function works with a set of parameters set by the user. The parameters include the I_{single} value which is the intensity of a single GFP molecule prior to it photobleaching. The parameters also include the pixel size, in microns, of the image, the exposure time (in ms), between image frames, the bleach time of a GFP bright spot, the stoichiometry method to run and the number of frames over which to use the stoichiometry method.

3.2.2.2.1 The getStoichiometry function

The getStoichiometry function uses one of five methods, defined by the user in the trackAnalyser parameter script, to produce a list of stoichiometry values, $\underline{S}$. The stoichiometry is calculated for each track as;

$$\underline{S} = \frac{I}{I_{single}} \tag{29}$$

where I is the estimated initial intensity of a bright spot and is determined by using one of the five methods, outlined below. In Methods 3,4,5 curve fits are used to estimate the value of I. The curve fits are functions of time, t_n where;

$$t_n = Ex_n \tag{30}$$

where E is the exposure time (in ms) of the image video and x_n is the video frame. Each method can be run over a user-specified total number of frames, N, the time at frame x_N is given by t_N. The plot in figure 3.3 is a plot of bright spot intensity over time for multiple bright

spots. The black curve is the raw data and the red markers is the raw data after a Chung-Kennedy filter had been run on it, maintaining photobleaching steps for the bright spots.

Method 1

When using this method, I is simply the first intensity value in the first frame, I_0;

$$I = I_0 \tag{31}$$

This method has advantages in its simplicity and ease of use, however it does not capture information about trajectories that occur after the first bright frame.

Method 2

When using this method, I is the mean of the spot intensity, I_{mean} which is calculated over the number of frames, defined by the user in the trackAnalyser function parameters, used in the stoichiometry analysis;

$$I = I_{mean} \tag{32}$$

Again, this method is relatively simple to compute, however on the exponential decay plot of bright spot intensity against frame (y in figure 3.3), the average intensity occurs halfway down this plot, but it is the information at the peak of this plot that is important. The further down the intensity decay plot we conduct our analysis, the more noise we introduce into the stoichiometry output; this is because we are analysing tracks that have long since photobleached.

Method 3

For this method, a linear polynomial curve, y_3 (figure 3.3, violet curve) is fitted over the exponential decay curve of spot intensity against frame, y (figure 3.3, black curve). The polynomial fit curve is given by;

$$y_3 = at_n + I_3 \tag{33}$$

where a and I_3 are respectively the gradient and y-intercept of the polynomial curve. Upon using this method, the bright spot initial intensity estimate, I is the y-intercept of the polynomial fit, I_3.

This method is advantageous as it captures initial intensity values at the peak of the intensity decay plot; it captures trajectories before they photobleach, therefore capturing a more realistic stoichiometry value.

Method 4

For this method an exponential decay function, y_4 (figure 3.3, blue dashed curve) with the magnitude of decay defined as the user-specified fixed bleach time, b, is fitted to the intensity decay curve (figure 3.3, black curve). The function is defined as follows;

$$y_4 = I_4 e^{-t_n/b} \tag{34}$$

The estimated initial intensity is given by I_4. This method has its advantages in the fact that it uses information on the bleach time of a GFP molecule and uses data at the beginning of the intensity decay curve. However, because it uses data from the peak of the intensity decay curve, the exponential in equation (32) produces unrealistically high values at higher values of t_n.

Method 5

For this method a nonlinear curve, y_5 (figure 3.3, green dotted curve) is fitted to the exponential decay curve of spot intensity against time, y. The nonlinear fit curve is defined as;

$$y_5 = I_5 e^{-b_n t_n} + I_{single} \tag{35}$$

where b_n is the bleach time which changes with time. As video time goes on, y_5 tends to a value of I_{single} rather than zero because I_{single} is the lowest intensity value. When a molecule has an intensity of zero, it is not sensed by the detector. Higher intensities in images are a result of multiple molecules (clusters).

The estimated initial bright spot intensity, I_5 is the coefficient to be determined by using nonlinear least squares method;

$$\min\left(\sum_{n=1}^{N}\left|\left(I_5 e^{-b_n t_n} + I_{single}\right) - y_{5_n}\right|^2\right) \tag{36}$$

where y_{5_n} are the intensity values for the n^{th} frame for N user-specified number of frames. The coefficient, I_5 is used as the estimate for the initial intensity, I. Method 5 can be used for very intense spot data.

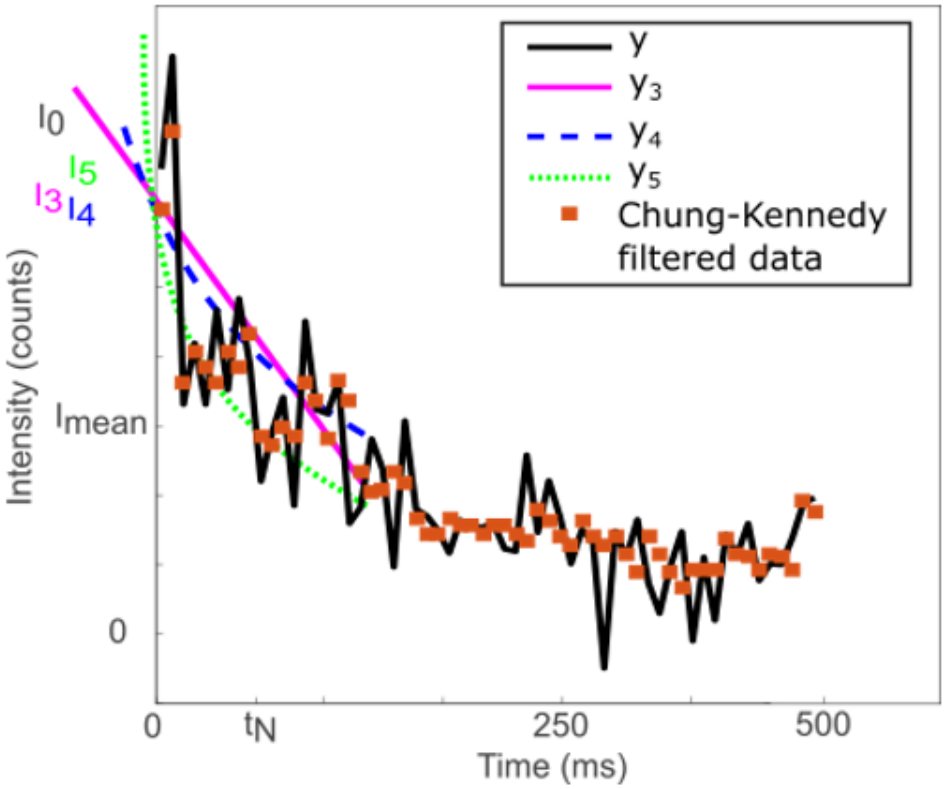

Figure 3.3 *Plot of average bright spot intensity over time, t_n (ms), for multiple bright spots, the black curve, y, for a typical image video that is 500ms long. The red markers indicates steps in the y data after a Chung-Kennedy filter was run on it. Also plotted on the graph are fit curves used to estimate the intensity of a bright spot using Methods 3,4, and 5 of the getStoichiometry function over a user-specified number of frames, N up to time, t_N at frame N. Method 3 is used to create a linear polynomial fit of the form $y_3 = at_n + I_3$ (violet curve) where I_3 is the estimated intensity of a bright spot. Method 4 is used to create an exponential fit of the form $y_4 = I_4 e^{\frac{-t_n}{b}}$ (blue dashed curve) where I_4 is the estimated intensity of a bright spot. Method 5 is used to create a nonlinear least squares fit of the form $y_5 = I_5 e^{-t_n b_n} + I_{single}$ (green dotted curve) where I_5 is the estimated intensity of a bright spot.*

3.3 Imaging Mig1-GFP in budding yeast cells

The HILO/TIRF microscope was used to take images of the transcription factor Mig1 in budding yeast. Image intensity and stoichiometry was characterised and results were compared to those outlined in literature (Wollman et al., 2017). The Wollman *et al.* results showed that the transcription factor, Mig1, in yeast forms clusters. This was a novel piece of research which elucidated the clustering behaviour of transcription factors through observation, beforehand this behaviour was only determined through models (Wollman et al., 2017). If the same stoichiometry values could be observed when analysing images taken with the HILO/TIRF microscope, this would serve as a proof of concept that the HILO/TIRF microscope was sensitive to single molecules and transcription factor clustering behaviour.

3.3.1 Introduction

Mig1 is a repressor transcription factor in budding yeast which travels to the cell nucleus (figure 3.4A) in response to increasing glucose levels outside the cell. Using single-molecule narrowfield microscopy, Wollman *et al.* (2017) established that Mig1 forms clusters. It was observed that these clusters contained approximately seven molecules and were spherical. Further to this, they found that the transcription activator, Msn2 in budding yeast also forms clusters (Wollman et al., 2017). The mobility of the clusters was characterised using the Mean-Squared Displacement (MSD) and this was plotted against a time-interval, τ. The plots in figure 3.4B demonstrate that when Mig1 was activated (Glucose (+)) the clusters in the nucleus were diffusing much slower, so slow as to be immobile. When Mig1 wasn't activated (Glucose (-)), the clusters acted the same whether in the cytoplasm or the nucleus. It was implied that it was in fact the clusters doing the gene regulation. Wollman *et al*. thought that being in a cluster might help transcription factors find their binding sites by binding to multiple segments of DNA simultaneously (Wollman et al., 2017).

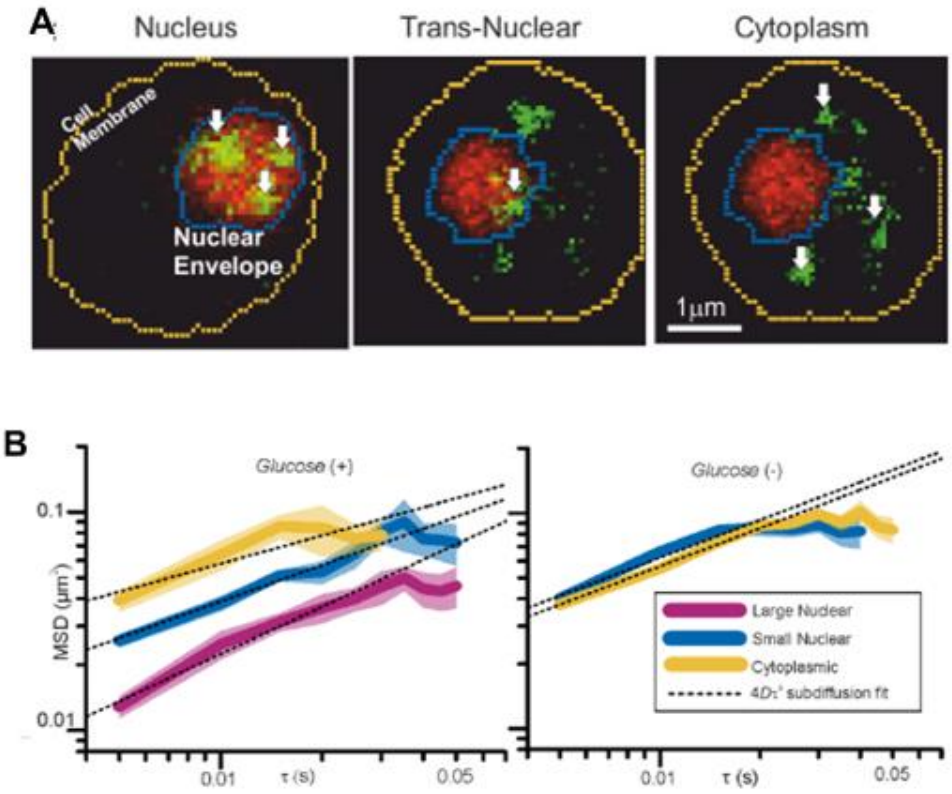

Figure 3.4 A. *Slimfield micrographs of Mig1-GFP foci (green) localisation from the nucleus (left), trans-nuclear (middle) to the cytoplasm (right).* ***B.*** *Mean squared displacement (MSD) vs time interval, τ of foci from cytoplasm (yellow) to small (blue) and large (purple) nuclear. Both images from Wollman et al. (2017).*

3.3.2 Methods

3.3.2.1 Preparing agar dishes

Frozen Mig1-EGFP::His3 NRD1-mCherry::hgrB yeast cells were used. The Mig1 strain was based on the strain YSH1351 using eGFP (Wollman et al., 2017). Yeast-peptone-dextrose (YPD) agar was made using 1g/mL yeast extract, 2g/mL Bacto-peptone and 2g/mL agar supplemented with 4% glucose (w/v). This used to make agar plates. The frozen Mig1-GFP stock was scraped onto the plate and the plate was placed in an incubator at 30°C for two days.

3.3.2.2 Preparing overnight culture tubes

Yeast-Nitrogen-Base (YNB) media was made at 6.9g/L supplemented with 4% glucose. This was put into 2mL pop-tubes with MilliQ water, 40% glucose w/v media and a scraping of the yeast from the agar plate. The pop-tubes were then put into a shaking incubator at 180rpm and 30°C overnight.

3.3.2.3 Preparing sample slides

On a standard glass sample slide, a 65μL (1.5x1.6cm) GeneFrame was stuck down and filled with 30μL of 6.9g/L YNB media supplemented with 4% glucose followed by 30μL of 0.02g/1mL heated agarose using a 1000μL pipette tip. The GeneFrame plastic spreader was immediately placed over the top and gently dragged across the frame, to remove excess agarose, leaving a thin layer within the frame. Finally, 2.5μL of the overnight yeast culture was pipetted, dropwise, in grid-form onto the agarose layer. This was left to rest for five minutes under an open flame before the glass (22x22mm) coverslip was placed on top.

3.3.2.4 Imaging and analysis

Mig1-GFP imaged using a (64x64)ROI at 5ms exposure with an epifluorescence 20mW 488nm intermediate-narrowfield beam. Stoichiometry results from using the trackAnalyser function on the images were compared to stoichiometry results from images taken by Wollman *et al.* (Wollman et al., 2017). The images were also analysed using the spots stoichiometry method and the stoichiometry results for these were compared to those obtained after using the tracks stoichiometry analysis method. Additionally, Mig1-GFP in yeast was imaged using a (256x256)ROI at 20ms exposure and a epifluorescence 40mW 488nm intermediate-narrowfield beam. Stoichiometry results from these images were compared to images taken using a (64x64)ROI at 5ms exposure and epifluorescence 20mW 488nm intermediate-narrowfield beam.

Furthermore, fluorescence images of Mig1-GFP in yeast were taken using a 10mW intermediate-narrowfield 488nm HILO beam profile at approximately 45° at 5ms exposure with a (64x64)ROI and were compared to fluorescence images of Mig1-GFP taken using a 10mW intermediate-narrowfield 488nm HILO beam at 5ms exposure with the (64x64) ROI shifted to the right or left of the cell position to observe if more single molecules could be imaged.

3.3.3 Results

3.3.3.1 Stoichiometry in epifluorescence Mig1-GFP budding yeast images was the same as that in published Wollman results

Fluorescence images of Mig1-GFP in budding yeast were taken with the HILO/TIRF microscope using a 20mW 488nm epifluorescence intermediate-narrowfield beam with a (64x64)ROI at 5ms exposure (figure 3.5). The bright spot intensity and stoichiometry were analysed. The results were compared to those gathered from fluorescence images of Mig1-GFP in yeast taken using a 50mW 488nm slimfield epifluorescence beam with a (128x128)ROI with a 80nm/image pixel Zeiss camera at 5ms exposure by the Wollman lab with results published in (Wollman et al., 2017).

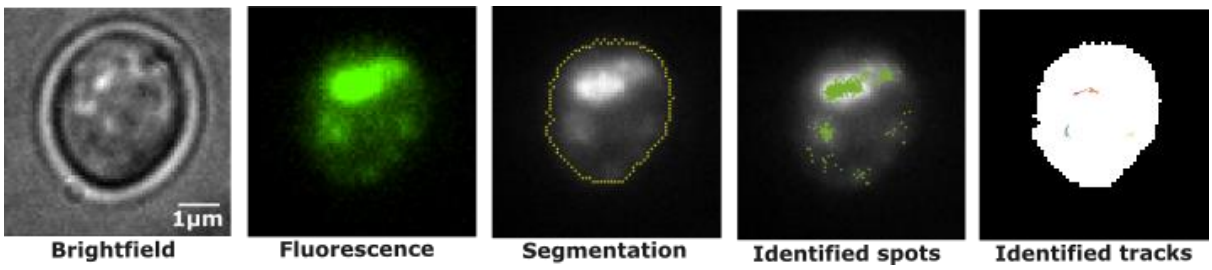

Figure 3.5 *Brightfield and fluorescence images of Mig1-GFP in budding yeast taken with a 20mW 488nm intermediate-narrowfield epifluorescence beam at 5ms exposure with a (64x64)ROI and the segmentation, identified bright spots and identified tracks yielded using the MATLAB segmentation, tracker and trackAnalyser functions.*

The MATLAB tracker function was used to characterise the bright spot intensity of images taken using the two different conditions. Images taken using the HILO/TIRF microscope (new data) had a single molecule intensity of 17200±3000, for N=28 cells, vs 2500±800 for the Wollman data, for N=20 cells (figure 3.6). The difference in intensity between the Wollman data and the New data is due to a combination of bit depth and gain differences. The Wollman data was captured using an Andor EMCCD IS 128ROI camera with 14bit depth, whereas the new data was captured using a Teledyne Photometrics CCD Evolve delta 512ROI camera with 16bit depth. The CCD Evolve delta camera bit depth is four times greater than that for the

Andor EMCCD camera (calculated as $2^{16}/2^{14}=2^2$). The Evolve camera also has a greater gain than the Andor camera. These factors result in the higher intensity values recorded in the New data than in the Wollman data.

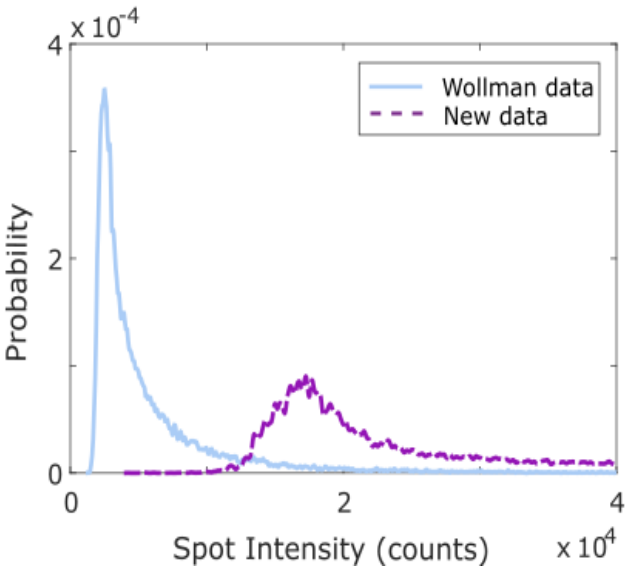

Figure 3.6 *KDF distribution plot of bright spot intensity for fluorescence images of Mig1-GFP in budding yeast cells taken with the Wollman microscope with a 50mW 488nm slimfield beam at 5ms exposure with a (128x128)ROI (Wollman data) and with the HILO/TIRF microscope with a 20mW 488nm intermediate-narrowfield beam at 5ms exposure with a (64x64)ROI (New data).*

The MATLAB trackAnalyser function using getStoichiometry method 3 with 20 frames was used to characterise the stoichiometry for each imaging method (figure 3.7). The mean stoichiometry for images taken with the Zeiss 80nm/image pixel microscope with a 20mW 488nm slimfield epifluorescence beam at 5ms exposure and (128x128)ROI (Wollman data), for n_t=58 tracks, was 28.9±6.7 (figure 3.7B). The peak of the stoichiometry KDF for the Wollman data was 12.1±11.2 (figure 3.7A). The mean stoichiometry for images taken with the HILO/TIRF microscope with a 20mW 488nm intermediate-narrowfield epifluorescence beam at 5ms exposure with a (64x64)ROI (New data), for n_t=88 tracks, was 21.3±3.3 (figure 3.7B). The peak of the stoichiometry KDF for the new data was 12.1±15 (figure 3.7A). Negative stoichiometry values are a result of the large kernel widths used to produce the kernel density function (KDF) plot; kernels plotted over stoichiometry points close to zero have an overlap that extends to negative values.

The stoichiometry data is not normally distributed, therefore statistical tests were run on the log distribution of the data. Different microscopes and imaging conditions were used to create sample image for the new data and the Wollman data, therefore independent sample tests were run when comparing new data stoichiometry and Wollman data stoichiometry. Upon running an independent sample t-test at the 5% significance level between the Wollman data and the New data, we obtain a p value of 0.1836 (figure 3.7B), indicating no significant difference between the means of each dataset at the 5% significance level. This indicates that the HILO/TIRF microscope can be used to obtain images of Mig1-GFP that, when analysed with

the MATLAB tracker and trackAnalyser functions, can yield stoichiometry values that are significantly comparable to those from published results (Wollman et al., 2017). Additionally, the HILO/TIRF microscope is capable of capturing transcription factor clusters.

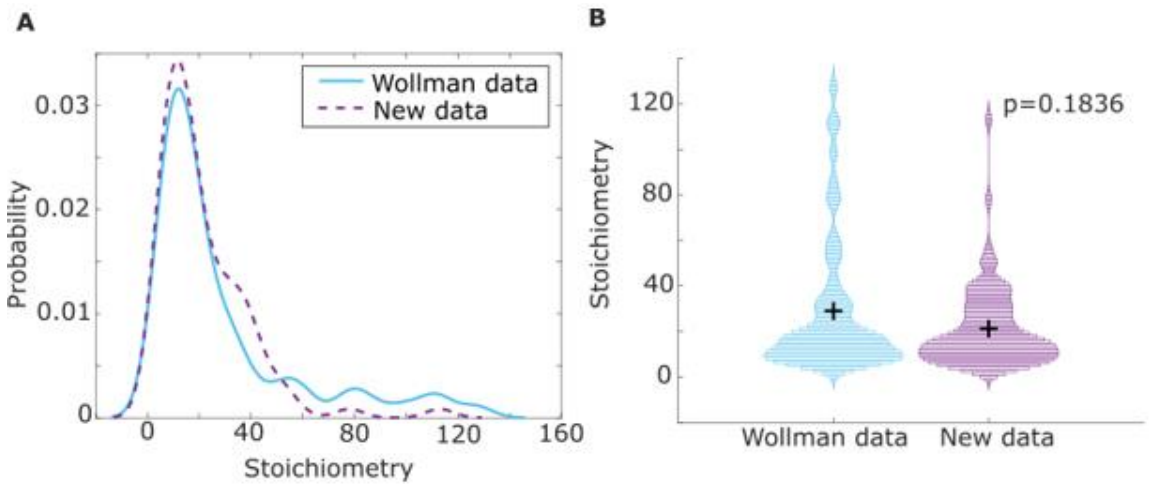

Figure 3.7 A. *KDF distribution plots of stoichiometry and* ***B.*** *Violin plots of stoichiometry for fluorescence images of Mig1-GFP in budding yeast cells taken with a Zeiss 80nm/image pixel microscope with a 50mW 488nm slimfield beam at 5ms exposure with a (128x128)ROI (Wollman data) and with a Nikon 93nm/image pixel microscope with a 20mW 488nm intermediate-narrowfield beam at 5ms exposure with a (64x64)ROI (New data). The violin plots indicate a p value of 0.1836 obtained after running an independent sample t-test at the 5% significance level between the log distribution of the Wollman data and the New data stoichiometry.*

3.3.3.2 Comparing stoichiometry analysis methods on Mig1-GFP yeast images

After establishing that the HILO/TIRF microscope could be used with the tracks analysis method to capture stoichiometry results that were significantly comparable to those in published results (Wollman et al., 2017), the next step was to test if using the spots stoichiometry analysis method could be used to yield stoichiometry values comparable to using the tracks analysis method. While the spots stoichiometry analysis method produces stoichiometry values by dividing the initial bright spot intensity, over a specified number of video image frames, by the single GFP intensity prior to photobleaching, the tracks stoichiometry analysis method uses one of five methods (the getStoichiometry method). The tracks method used to analyse the fluorescence images of Mig1-GFP in yeast involved fitting a linear polynomial to the curve of intensity decay over time for a specified number of frames of the image video (tracks method 3 using 20 frames).

Fluorescence images of Mig1-GFP in budding yeast taken with the HILO/TIRF microscope using a 20mW 488nm intermediate-narrowfield epifluorescence beam at 5ms exposure with a (64x64)ROI were analysed using the MATLAB trackAnalyser function with getStoichiometry

method 3 with 20 frames and using the spots analysis method with 1 frame. The stoichiometry was characterised for each analysis method (figure 3.8). The mean stoichiometry obtained from the image data when using the tracks method 3 with 20 frames, for n_t=88 tracks, was 21.3±3.3 (figure 3.8B). The peak of the stoichiometry KDF was 12.1±15 (figure 3.8A). The mean stoichiometry obtained from the image data when using the spots analysis method with 1 frame, for n_s=147 bright spots, was 20.6±3.1 (figure 3.8B). The peak of the stoichiometry KDF was 9.2±13 (figure 3.8A). Again, negative stoichiometry can be explained by overlaps produced by large kernel widths during KDF plotting.

Even though the same stoichiometry data was analysed, two different methods were used to analyse this data, therefore an independent sample statistical test was used. Again, this stoichiometry data is not normally distributed so the statistical test was performed on the log distribution of the data. Upon running an independent sample t-test at the 5% significance level on the log distribution stoichiometry data obtained using the two different analysis methods, we obtain a p value of 0.5604 (figure 3.8B). This indicates no significant difference between the means of the datasets at the 5% significance level.

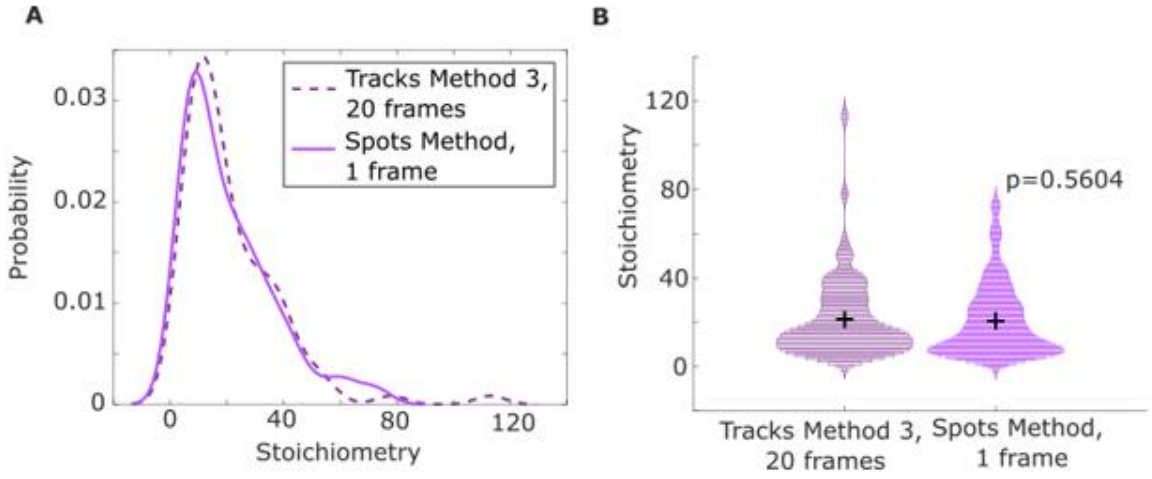

Figure 3.8 A. *KDF distribution plots of stoichiometry and* ***B.*** *Violin plots of stoichiometry for fluorescence images of Mig1-GFP in budding yeast cells taken using a 20mW 488nm intermediate-narrowfield epifluorescence beam at 5ms exposure with a (64x64)ROI and analysed using one of two different analysis methods; tracks method 3 with 20 frames and spots method with 1 frame, the violin plots indicate a p value of 0.5604 obtained when running an independent sample t-test at the 5% significance level between log distribution data acquired from using the two analysis methods.*

These results indicate that using the two different stoichiometry analysis methods yield results that are significantly comparable to one another. Therefore, when imaging single molecules with exposure times greater than 5ms, the spots analysis method can be used to produce biologically correct stoichiometry values for the image data. This was further tested by taking

images of yeast cells at 20ms exposure with a (256x256)ROI and analysing them using the spots analysis method with 3 frames.

3.3.3.3 Comparing stoichiometry results after changing exposure time and ROI size of Mig1-GFP yeast images

Fluorescence images of Mig1-GFP in budding yeast were taken with the HILO/TIRF microscope using a 40mW 488nm epifluorescence intermediate-narrowfield beam at 20ms exposure with a (256x256)ROI (figure 3.9).

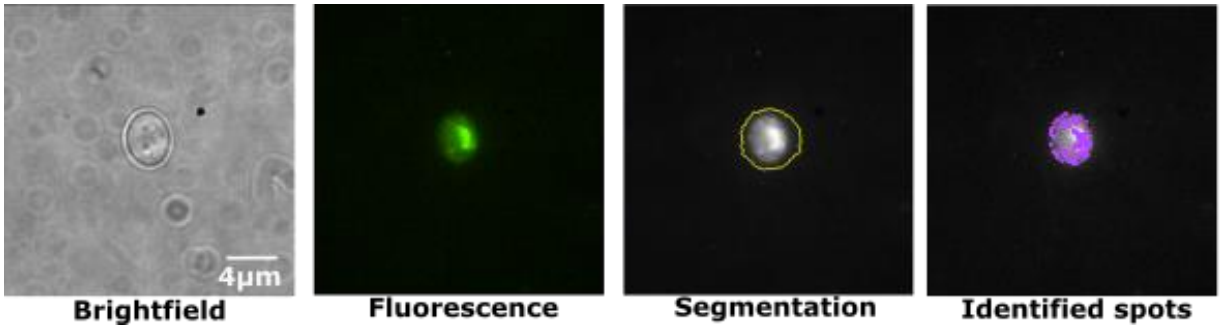

Figure 3.9 *Brightfield and fluorescence images of Mig1-GFP in budding yeast taken with epifluorescence 40mW 488nm intermediate-narrowfield beam at 20ms exposure with a (256x256)ROI and the segmentation identified bright spots and identified tracks yielded using the MATLAB segmentation and tracker functions.*

Images were analysed with the MATLAB tracker function and the bright spot intensity was characterised (figure 3.10). Single molecule intensity, for N=30 cells, was 27000±13800.

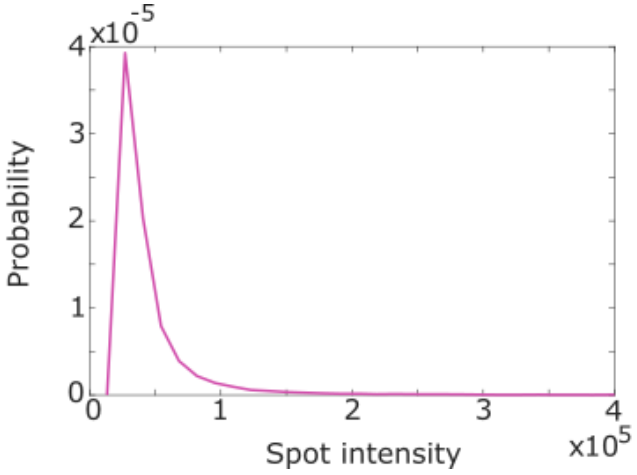

Figure 3.10 *KDF distribution plot of bright spot intensity for fluorescence images of Mig1-GFP in budding yeast cells taken using the HILO/TIRF microscope with a 40mW 488nm intermediate-narrowfield epifluorescence beam at 20ms with a (256x256)ROI.*

The stoichiometry was characterised using the spots analysis method with 3 frames (figure 3.11). The mean stoichiometry, for n_s=1031 bright spots, was 13.7±1.7 (figure 3.11B). The peak of the stoichiometry KDF was 9.3±8.2 (figure 3.11A). This was compared to the stoichiometry of images taken with the HILO/TIRF microscope with a 20mW 488nm intermediate-narrowfield epifluorescence beam at 5ms exposure with a (64x64)ROI analysed using the spots analysis method with 1 frame (which had a mean

stoichiometry of 20.6±3.1 for n_s=147 bright spots) (figure 3.11B). Since different analysis methods for different samples are being compared against one another, an independent sample test is required. Additionally, the stoichiometry data is not normally distributed so a nonparametric test should be used. Upon running an independent sample Mann-Whitney U test at the 5% significance level between the two different imaging conditions and analysis methods stoichiometry results, we obtain a p value of 0.9539 (figure 3.11B), indicating that there is no significant difference between the stoichiometry data population shapes at the 5% significance level. These results demonstrate that the same biological results can be obtained regardless of the conditions used to produce the images and the methods used to subsequently analyse them.

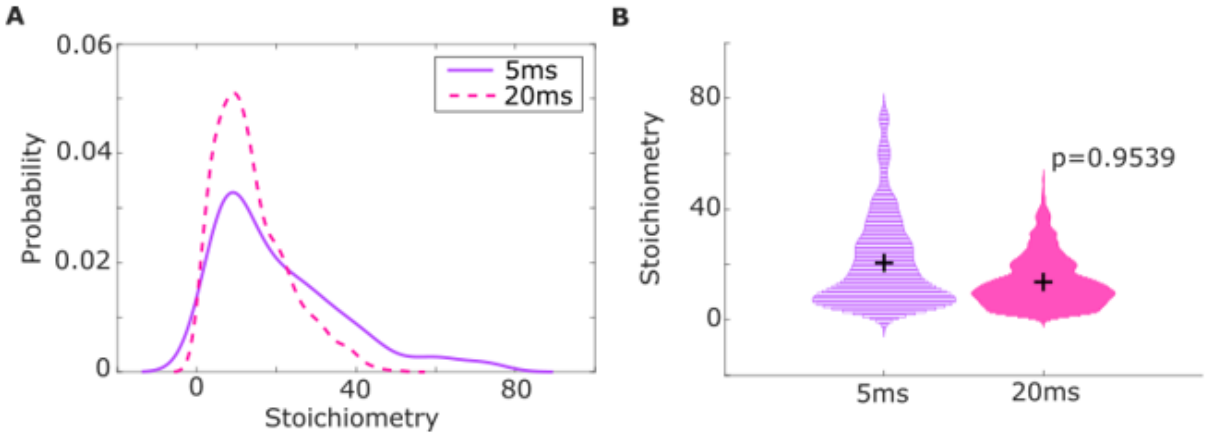

Figure 3.11 A. *KDF distribution plots of stoichiometry and* ***B.*** *Violin plots of stoichiometry for fluorescence images of Mig1-GFP in budding yeast cells taken with the HILO/TIRF microscope with a 20mW 488nm intermediate-narrowfield epifluorescence beam at 5ms exposure with a (64x64)ROI and analysed using the spots analysis method with 1 frame (5ms condition) and taken using the HILO/TIRF microscope with a 40mW 488nm intermediate-narrowfield epifluorescence beam at 20ms exposure with a (256x256)ROI and analysed using the spots analysis method with 3 frames (20ms condition). The violin plots indicate a p value of 0.9639 obtained after running an independent sample t-test at the 5% significance level between log distribution stoichiometry for the 5ms and 20ms conditions.*

3.3.3.4 Comparing imaging conditions on images of Mig1-GFP in budding yeast

When imaging with a HILO beam, the beam-to-cell profile looks like that in figure 3.12A; the beam travels through the cell. It was assumed that shifting this beam slightly to the right (or

left) of the cell position (figure 3.12B) then there would be a 50% chance of imaging the nucleus (depending on the cell orientation).

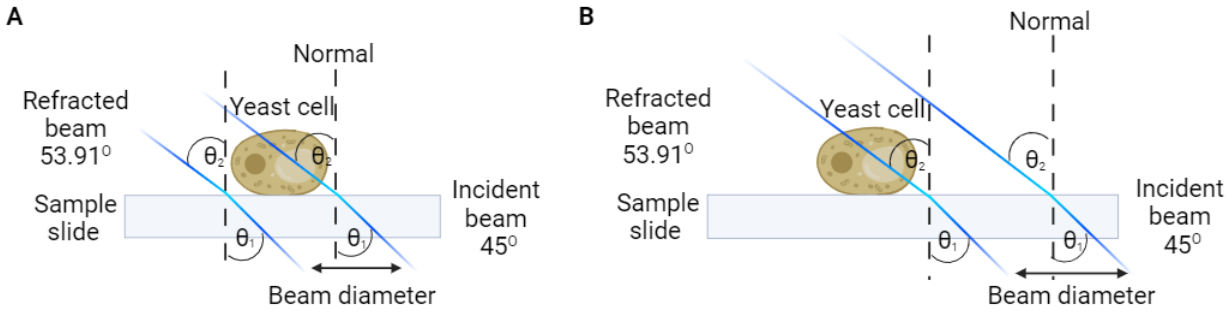

Figure 3.12 A *Depiction of a HILO beam with angle of incidence 45°in relation to a yeast cell position and* ***B*** *a depiction of the same incident beam shifted slightly to the right of the yeast cell position. Images created in BioRender.com.*

This theory was tested by imaging Mig1-GFP in yeast cells using a 10mW 488nm intermediate-narrowfield beam with a (64x64)ROI and 5ms exposure. Three different beam angles were used, namely epifluorescence (excitation beam incidence angle at 0°), HILO45 (excitation beam incidence angle at 45°) (figure 3.12A) and HILO45shift (excitation beam incidence angle at 45° with the beam shifted to the right or left of cell position) (figure 3.12B). The HILO45shift profile was achieved by identifying the cell position on the Nikon Elements software with a centred beam square, then shifting the ROI to the right or left of this before imaging. The centre beam square was a (64x64) pixel square that was traced over the beam centre using an annotation tool in Nikon Elements. The beam centre was identified prior to this using fluorescent beads; the narrowfield beam was raster-scanned in xy across a (512x512) ROI and the beam centre was identified as the position where the beads were brightest. The bright spot intensity (figure 3.14A) and stoichiometry (figure 3.14B-C) of cell images were characterised and compared against each other.

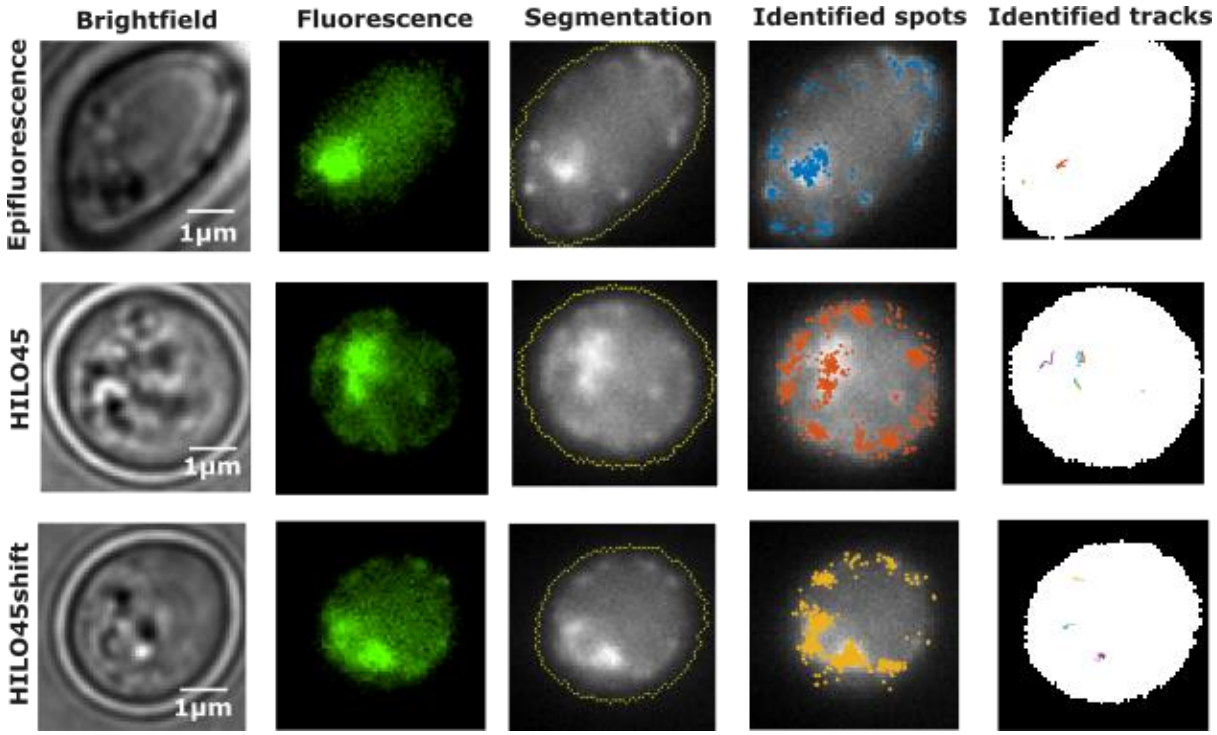

Figure 3.13 *Row 1: brightfield images of budding yeast, Row 2: fluorescence images of Mig1-GFP in budding yeast, Row 3: fluorescence images of Mig1-GFP in budding yeast segmented using the MATLAB segmentation function, Row 4: fluorescence images of Mig1-GFP in budding yeast with identified bright spots from using the MATLAB tracker function, Row5: fluorescence images of Mig1-GFP in budding yeast with identified tracks from using the trackAnalyser MATLAB function when using the epifluorescence, HILO45 and HILO45shift 10mW 488nm intermediate-narrowfield beam at 5ms exposure with a (64x64)ROI.*

Figure 3.13 shows the fluorescence images of Mig1-GFP in yeast cells taken using the three imaging conditions. Cells were segmented and bright spots were identified using the MATLAB tracker function, then tracks were characterised using the getStoichiometry Method 3 with 20 frames with the MATLAB trackAnalyser function.

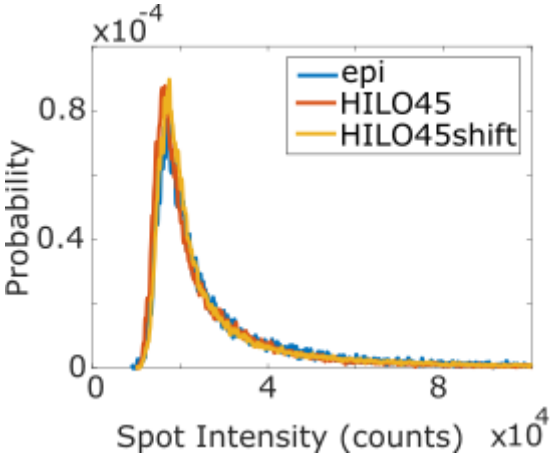

Figure 3.14 *KDF distribution plots of bright spot intensity (counts) for fluorescence images of Mig1-GFP in yeast cells taken using a 10mW 488nm intermediate-narrowfield beam at epifluorescence, HILO45 and HILO45shift profiles with a (64x64)ROI at 5ms exposure.*

Single molecule intensity for cell images in the epifluorescence condition, for N=12 cells, was 17500±3800 and was, for N=18 cells, 15900±3500 for the HILO45 condition and was, for N=30 cells, 17200±3500 for the HILO45shift condition (figure 3.14).

Stoichiometry for the epifluorescence condition, for n_t=67 tracks, was 10.4±7.

Stoichiometry for the HILO45 condition, for n_t=77 tracks, was 12.9±10.4 and for the HILO45shift condition and stoichiometry, for n_t=140 tracks, was 9.2±7.5 (figure 3.15A). The stoichiometry data is not normally distributed, therefore a statistical test was run on the log distribution of the stoichiometry data for the HILO45 and HILO45shift imaging conditions. Additionally, since two different imaging conditions were compared to each other, an independent sample test was used. Upon running an independent sample t-test at the 5% significance level on stoichiometry between the HILO45 and HILO45shift conditions, we obtain a p value much less than 0.05 (figure 3.15B). This indicates a significant difference between the means of the datasets at the 5% significance level. This demonstrates that when we shift the beam slightly to the left or right of the cell position, it does not yield the same results as when it is centred on the cell position. These results suggest that using a shifted HILO45 beam is not needed to improve the spot intensity and stoichiometry of cell images when imaging GFP molecules. Using a standard HILO beam at approximately 45-56° suffices.

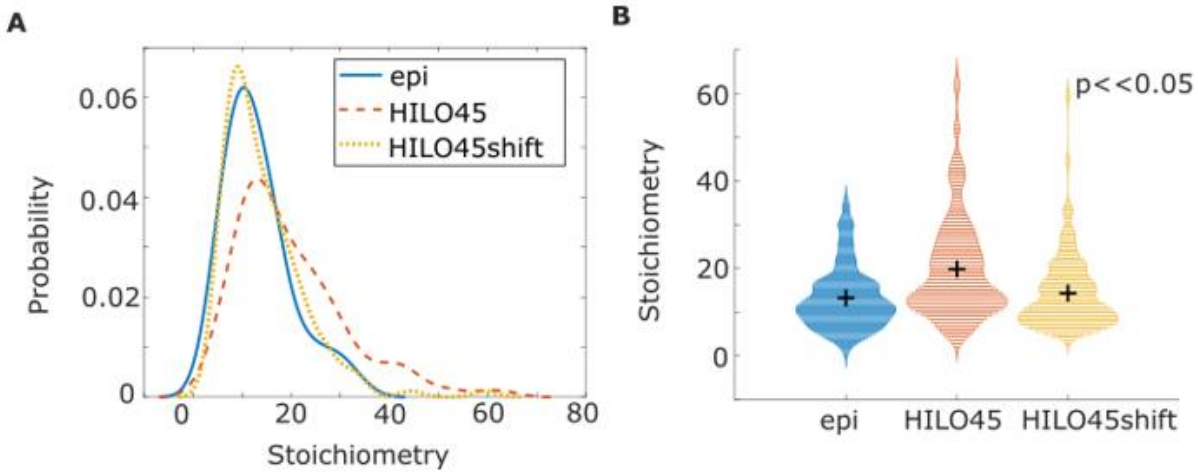

Figure 3.15 A. *KDF distribution plots and* ***B.*** *Violin plots of stoichiometry for fluorescence images of Mig1-GFP in yeast cells taken using a 10mW 488nm intermediate-narrowfield beam at epifluorescence, HILO45 and HILO45shift profiles with a (64x64)ROI at 5ms exposure indicating a p<<0.05 between n the HILO45 and HILO45shift conditions after running an independent sample t-test at the 5% significance level on the log distributed stoichiometry.*

3.3.4 Conclusion

The HILO/TIRF microscope was able to capture images of the transcription factor Mig1 tagged with GFP. When these images were analysed with two different functions to characterise stoichiometry, results were significantly similar to those previously published. The results demonstrated that the HILO/TIRF microscope was not only sensitive to single molecules in samples, but could also capture clusters of transcription factors. Additionally, it can be

concluded that using standard HILO excitation beam angles of 45-56° are enough to capture single molecules in sample images with improved SNR.

3.4 Imaging PAR6-GFP in C.elegans embryos

The polarity effector protein PAR6 in the nematode worm *Caenorhabditis elegans* (*C. elegans*) was tagged with GFP and imaged with the HILO/TIRF microscope. This work was carried out with Rodriguez *et al.*

3.4.1 Introduction

Localisation of partitioning-defective (PAR) polarity effector proteins to membrane-associated cortical domains is a vital step during the polarisation of metazoan cells (Rodriguez et al., 2017). Many aspects of embryonic development such as epithelial organisation and asymmetric cell division are coordinated by localised activation of signalling pathways and the regulation of PAR proteins is essential in this process (Goldstein and Macara, 2007; St Johnston and Ahringer, 2010). Cell polarity on one side of a cell is driven by proteins PAR6, PAR3, CDC-42 and aPKC working together to drive asymmetry (Goehring, 2014; McCaffrey and Macara, 2012; Suzuki et al., 2004; Ziomek et al., 1982).

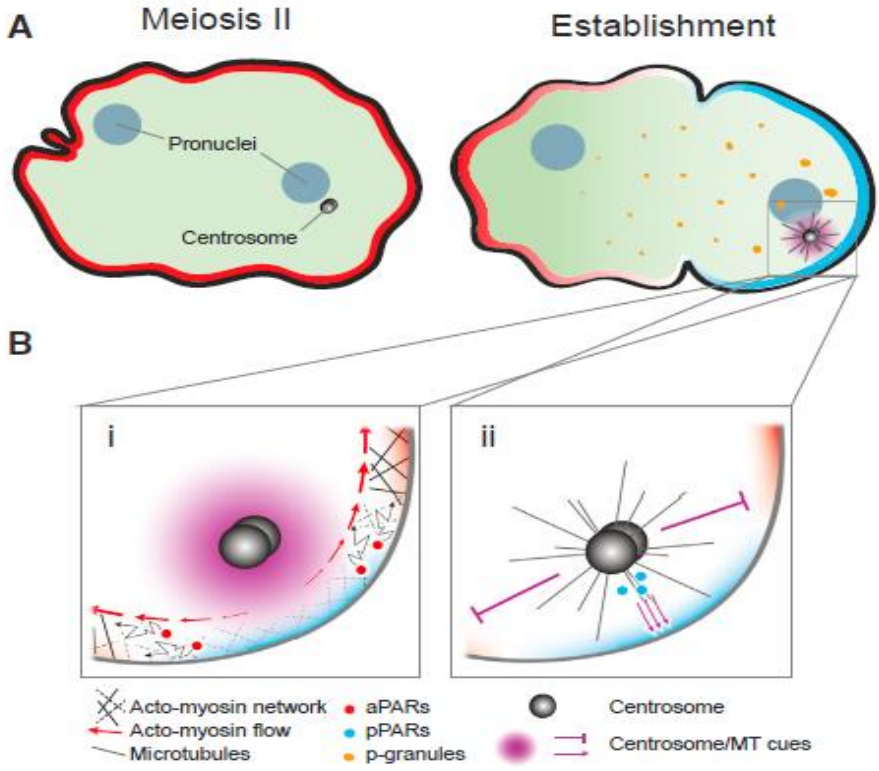

Figure 3.16 A. *Depiction of the establishment stage of cell division in C. elegans driven by PAR proteins* ***B.*** *The PAR proteins driving cell division in C. elegans embryos. Both images from Rodriguez et al. 2017.*

C. elegans are considered a model for understanding activities such as cell death and ageing (Ellis and Horvitz, 1986; Kenyon, 2010; Riddle et al., 1997) in humans (Markaki and Tavernarakis, 2020). The anterior domain in an embryo or zygote of a *C. elegans* is massively defined by the PAR proteins (figure 3.16A-B) (Rodriguez et al., 2017). The size of a PAR protein cluster determines the anterior-directed movement of this protein through the embryo (Cheeks et al., 2004; Labbé et al., 2003). Therefore, studying the dynamics and characteristics of these PAR proteins, such as the size of the PAR clusters (stoichiometry) is important because cell fate defects and embryo death can result when they work incorrectly (Etemad-Moghadam et al., 1995; Kay and Hunter, 2001; Tabuse et al., 1998; Watts et al., 1996).

3.4.2 Methods

JJ1579 (PAR6-GFP) and JA1596 (PAR6-GFP, ne4246) strains of the nematode *Caenorhabditis elegans* (*C. elegans*) were plated by Rodriguez *et al.* six days before imaging. On the day of imaging, plates were kept in a heatblock at 28°C to ensure agar remained at approximately 25°C during the imaging session. 200μL of 25°C egg buffer and agarose (0.5:0.5) was pipetted into a cooling chamber and the worms were picked into 40μL of 25°C egg buffer and put onto a coverslip with 4μL of egg buffer using an eyelash, then approximately 10-13 worms were sliced on glass coverslips before imaging. The sample stage was maintained at approximately 25°C.

Non-temperature-sensitive (wildtype) embryo strains and temperature-sensitive (aPKC kinase defective mutants) embryo strains were imaged using the HILO/TIRF microscope with a 20mW 488nm widefield TIRF beam at 50ms exposure with a (512x512)ROI.

3.4.3 Results

Fluorescence images were taken of PAR6-GFP in *C. elegans* embryos using a 20mW 488nm widefield TIRF beam at 50ms exposure with a (512x512)ROI (figure 3.17B) for temperature-sensitive (TS) and non-temperature sensitive (non-TS) cells.

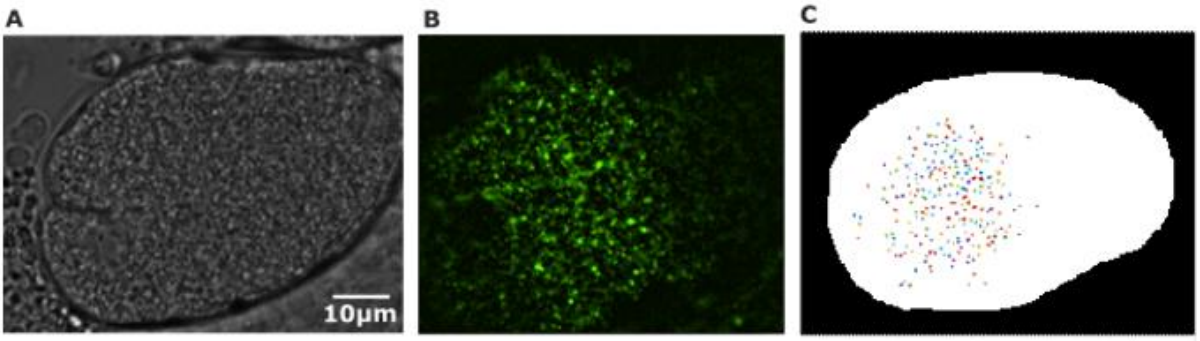

Figure 3.17 A. *Brightfield image of C.elegans embryo.* ***B.*** *Fluorescence image of PAR6-GFP in a C.elegans embryo imaged using a 20mW 488nm widefield TIRF beam at 50ms exposure with a (512x512)ROI.* ***C.*** *C.elegans embryo mask, coloured spots indicate the position of tacks identified by the trackAnalyser MATLAB function.*

The MATLAB tracker function was used on fluorescence images of PAR6-GFP in TS and non-TS *C.elegans* embryos. Single molecule intensity for non-TS cells, for N=8 cells, was 56100±23300, while single molecule intensity for TS cells, for N=5 cells, was 53300±19900 (figure 3.18). The MATLAB trackAnalyser function using getStoichiometry method 3 with 20 frames was used to characterise the stoichiometry. The tracks stoichiometry analysis could be used in this case, despite videos being slower with a 50ms exposure time, because the PAR6 proteins within the *C.elegans* embryos move at a slower rate than the transcription factor Mig1 in yeast cells. The mean stoichiometry for non-TS cells was, for a total of n_t=1398 identified tracks, 3.7±0.9 (figure 3.19B). The peak of the stoichiometry KDF was 2.3±1.1 (figure 3.19A). The mean stoichiometry for TS cells was, for a total of n_t=404 tracks, 2.7±0.8 (figure 2.19B). The peak of the stoichiometry KDF was 1.7±1.1 (figure 3.19A).

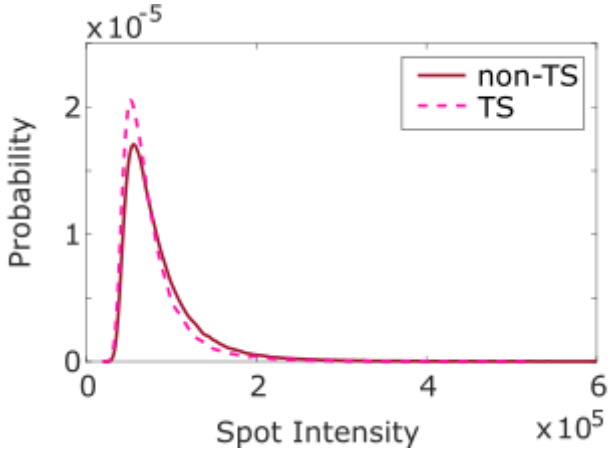

Figure 3.18 *KDF distribution plot of bright spot intensity for fluorescence images of PAR6-GFP in a C.elegans embryo imaged using a 20mW 488nm widefield TIRF beam at 50ms exposure with a (512x512)ROI.*

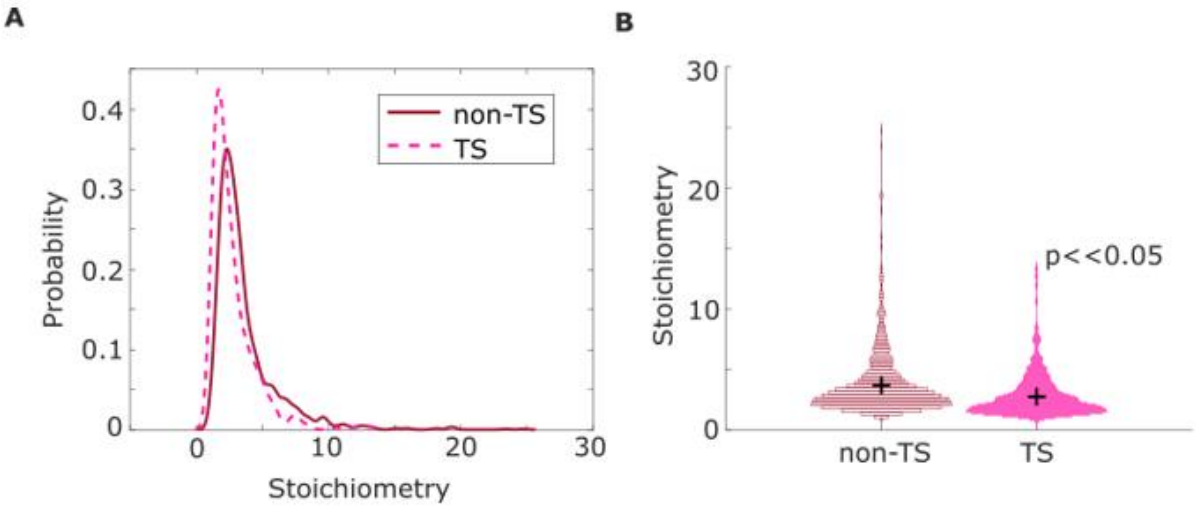

Figure 3.19 A. *KDF distribution plots and* ***B.*** *violin plots of stoichiometry for fluorescence images of PAR6-GFP in non-temperature sensitive (non-TS) and temperature sensitive (TS) C.elegans embryos taken using the HILO/TIRF microscope with a 20mW 488nm widefield TIRF beam at 50ms exposure with a (512x512)ROI. The violin plots indicate a p<<0.05 after running an independent sample t-test between log distributed non-TS and TS cell stoichiometry at the 5% significance level.*

The stoichiometry data was not normally distributed, therefore a statistical test was run on the log distribution of the data. This was an independent sample test because two different samples were compared against each other, namely temperature-sensitive and non-temperature-sensitive. Upon running an independent sample t-test at the 5% significance level between TS and non-TS datasets we obtain a p value much less than 0.05 (figure 3.19B) indicating that mean stoichiometry was significantly higher in non-TS cells than in TS cells. Higher stoichiometry values were indeed expected in non-TS cells as PAR6 forms more clusters with PAR3 than with CDC-42 in these cells, whereas the opposite occurs in TS cells. When PAR6 forms clusters with CDC-42, it diffuses, hence stoichiometry is expected to be lower (Rodriguez et al., 2017).

3.4.4 Conclusion

The HILO/TIRF microscope can be used to image proteins in wild-type and modified sample stains and when the intensity and stoichiometry of these images are analysed with the MATLAB functions, the significant biological differences between these strains can be identified. These results point to a proof of concept that the HILO/TIRF microscope is sensitive to biological differences between modified cells and strains and controls.

3.5 Imaging apoE2 and Amyloid Beta

The apoE2 variant of the apolipoprotein E (apoE) labelled with Alexa Fluor™ 568 C5 Maleimide and the amyloid beta (Aβ) 1-42 variant, Aβ1-42 labelled with HiLyte™ Fluor 488 were imaged *in vitro* with the HILO/TIRF microscope using TIRF microscopy with and without complement regulator factor H (FH) stimulation. This work was carried out with Haapasalo *et al.* (Chernyaeva et al., 2023).

3.5.1 Introduction

Increased aggregation and decreased clearance of amyloid beta (Aβ) can cause it to accumulate in the brain and Aβ plaques in the brain have been associated with the risk of Alzheimer's disease (Lambert et al., 2009). Microglia cells have been found to be activated by Aβ aggregates in the brain and contribute to neuroinflammation and neurotoxicity (Shen and Meri, 2003; Zhang et al., 2011). The binding of apoE to protein complexes involved in the innate immune system has implicated apoE as a major protein related to Alzheimer's disease (Vogt et al., 2020; Yin et al., 2019) along with the fact that Aβ plaques contain large amounts of apoE. It is suggested that apoE contributes to the clearance of Aβ, however this process is not fully understood. apoE interacts with FH and Haapasalo *et al.* aimed to observe the interactions between FH and various apoE isoforms and how these interactions contribute to reducing Aβ toxicity, plaque formation and neuroinflammation in Alzheimer's disease (Chernyaeva et al., 2023). The stoichiometry of Aβ1-42 and apoE2 was characterized to determine their oligomeric state; determining the interactions between these proteins to elucidate their function. The size of Aβ1-42 oligomers is important to know as apoE2 may contribute to clearing these Aβ1-42 oligomers (plaques) (Chernyaeva et al., 2023).

3.5.2 Methods

apoE2 labelled with Alexa Fluor™ 568 C5 Maleimide, 568-apoE2, and Aβ1-42 labelled with HiLyte™ Fluor 488, 488-Aβ1-42 were sent to the Wollman lab and stored at -80°C. Two sample tubes were created; in the first tube 1μM 568-apoE2 was incubated with 1.7μM 1mg/mL FH and 18.5μM 1mg/1mL 488-Aβ1-42 at room temperature for 72 hours (with FH). In the second tube 1μM 568-apoE2 was incubated with 18.5μM 1mg/1mL 488-Aβ1-42 at room temperature for 72 hours (without FH) (Chernyaeva et al., 2023). Prior to imaging, plasma cleaned glass coverslips were attached to glass sample slides with double-sided tape, creating a flow channel through which 10μL (1:100) 5μg/mL anti-Aβ or 10μL (1:100) 6.7mg/mL anti-apoE was pipetted, then the channel was washed with 20μL PBS and 10μL (1:1000) white beads to PBS were pipetted through the channel before the channel was washed again and the samples were imaged using a 20mW 488nm widefield TIRF beam and 20mW 561nm TIRF beam both at 50ms exposure with a (512x512)ROI (figure 3.20). The channels were also merged (figure 3.21).

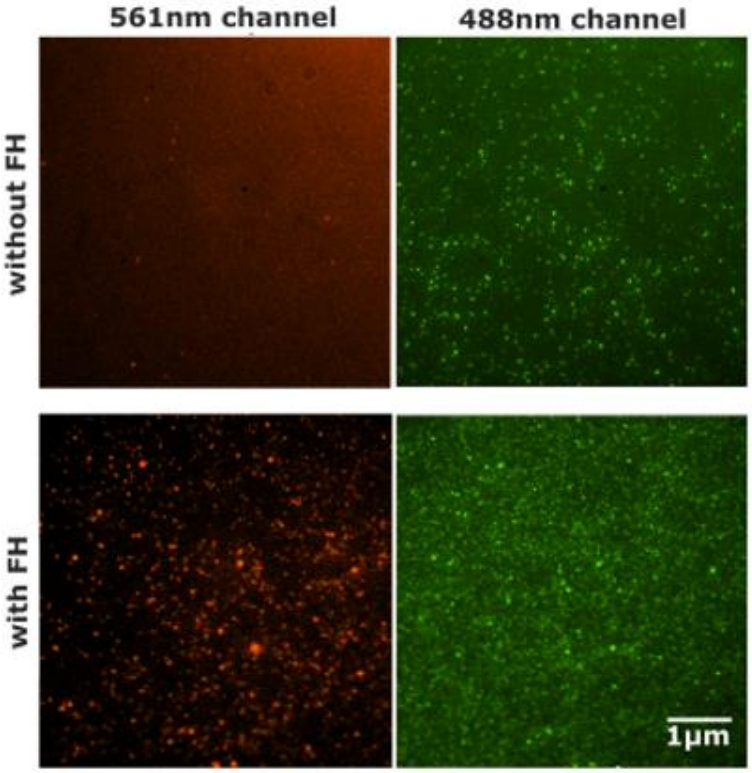

Figure 3.20 *Fluorescence images of 568-apoE2 taken with a 20mW 561nm TIRF widefield beam at 50ms exposure with a (512x512)ROI and without and with FH stimulation (left column) and of 488-Aβ1-42 taken with a 20mW 4881nm TIRF widefield beam at 50ms exposure with a (512x512)ROI without and with FH stimulation (right column).*

3.5.3 Results

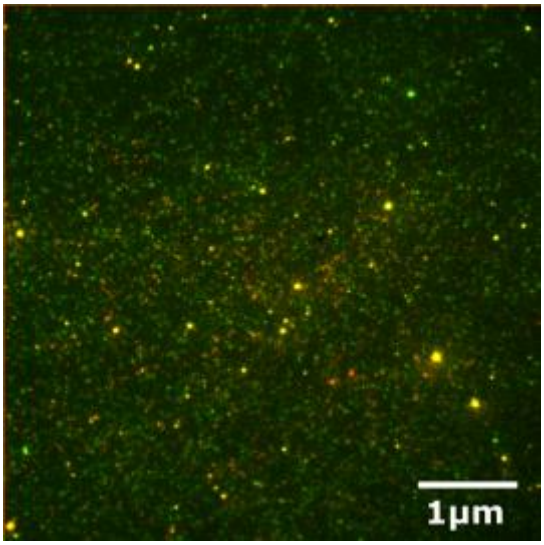

Figure 3.21 *Merged red (568-apoE2) and green (488-Aβ1-42) channel fluorescence image taken with the HILO/TIRF microscope with 20mW widefield TIRF 488nm and 561nm beams at 50ms exposure with a (512x512)ROI.*

Fluorescence images of 568-apoE2 were taken with the HILO/TIRF microscope using a 20mW 561nm widefield TIRF beam at 50ms exposure with a (512x512)ROI and fluorescence images of 488-Aβ1-42 were taken with the HILO/TIRF microscope using a 20mW 488nm widefield TIRF beam at 50ms exposure with a (512x512)ROI. The MATLAB tracker function was used on the images to characterise bright spot intensity. Single molecule intensity for 488-Aβ1-42 without FH stimulation, for N=12 FOVs, was 31200±16000 and was, for N=13 FOVs, 32800±8800 with FH stimulation (figure 3.22A). Single molecule intensity for 568-apoE2 without FH stimulation, for N=12 FOVs, was 16800±14800 and was, for N=13 FOVs, 29600±12700 with FH stimulation (figure 3.22B).

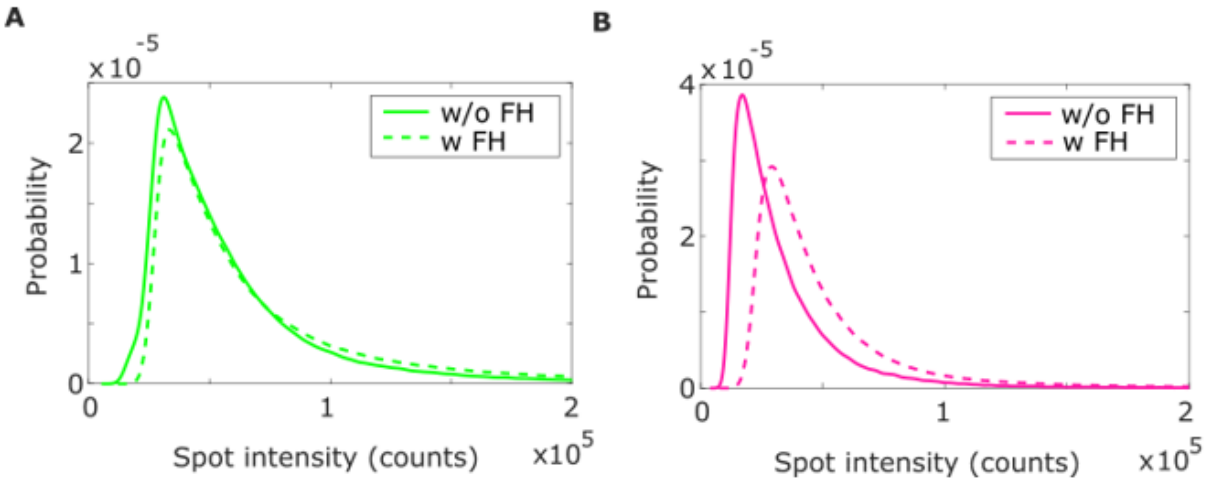

Figure 3.22 A. *KDF distribution plots of spot intensity of 488-Aβ1-42 with (w FH) and without (w/o FH) FH stimulation.* ***B.*** *KDF distribution plots of spot intensity of 568-apoE2 with (w FH) and without (w/o FH) FH stimulation.*

The MATLAB trackAnalyser function using getStoichiometry Method 1 with 20 frames was used to characterise the stoichiometry of both channels. Despite the increased exposure time of 50ms of the image videos, the tracks stoichiometry analysis method could be used with these images because molecules were static, like those in the *in vitro* GFP images. The stoichiometry was characterised for 488-Aβ1-42 and 568-apoE2 with and without FH

stimulation. Considering that the stoichiometry data was not normally distributed, a nonparametric test was used. This test was run for independent samples as the stoichiometry data was created from different samples and two conditions were compared against each other, namely with FH and without FH. The mean stoichiometry for 488-Aβ1-42 without FH stimulation, for n_t=12313 tracks, was 3.4±0.9 (figure 3.23B). The peak of the stoichiometry KDF without FH stimulation was 1.6±1 (figure 3.23A). The mean stoichiometry for 488-Aβ1-42 with FH stimulation, for n_t=15826 tracks, 4.8±1.2 (figure 3.23B). The peak of the stoichiometry KDF was 2.3±1.2 with FH stimulation (figure 3.23A). For 568-apoE2 without FH stimulation, the mean stoichiometry, for n_t=972 tracks, was 2.3±1.4 (figure 3.23D). The peak of the stoichiometry KDF without FH stimulation was 1.6±0.8 (figure 3.23C). The mean stoichiometry for 568-apoE2 with FH stimulation was, for n_t=9985 tracks, 3.1±1.2 (figure 3.23D). The peak of the stoichiometry KDF with FH stimulation was 1.5±0.8 (figure 3.23C). Upon running an independent sample Mann-Whitney U test at the 5% significance level on the 488-Aβ1-42 stoichiometry data without and with FH stimulation, we obtain a p<<0.05 (figure 3.23B), indicating a significant increase at the 5% significance level in mean Aβ1-42 stoichiometry following FH stimulation. These results suggest that the introduction of FH had an effect on the number of foci for Aβ. After running an independent sample Mann-Whitney U test at the 5% significance level on the 568-apoE2 stoichiometry with and without FH stimulation, a p value of 0.4221 was obtained (figure 3.23D). This indicates no significant difference, at the 5% significance level, in average 568-apoE2 stoichiometry between the FH and no FH conditions. However, unlike the results in the Chernyaeva *et al.* (2023) paper, this data does not include colocalization analysis characterising the stoichiometry of colocalised and non-colocalised Aβ and apoE.

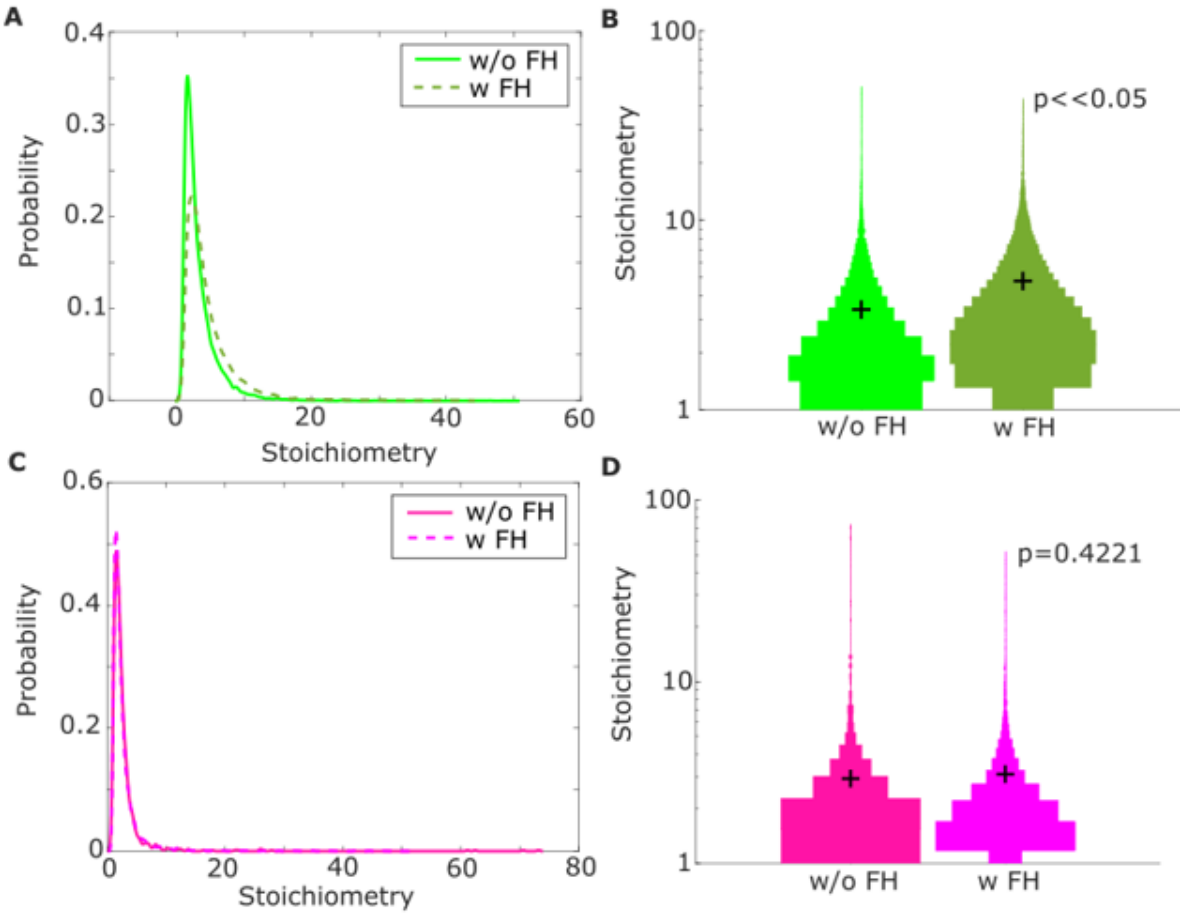

Figure 3.23 A. *KDF distribution plots of 488-Aβ1-42 stoichiometry with (w FH) and without (w/o FH) FH stimulation and* ***B.*** *Violin plots of 488-Aβ1-42 stoichiometry with and without FH stimulation indicating a p<<0.05 after running an independent sample Mann-Whitney U test at the 5% significance level between the without FH and with FH conditions for fluorescence images of 488-Aβ1-42 taken with the HILO/TIRF microscope with a 20mW 488nm widefield TIRF beam at 50ms exposure with a (512x512)ROI (y axis is on log scale).* ***C.*** *KDF distribution plots of 568-apoE2 stoichiometry with (w FH) and without (w/o FH) FH stimulation and* ***D.*** *Violin plots of 568-apoE2 stoichiometry with and without FH stimulation indicating a p value of 0.4221 after running an independent sample Mann-Whitney U test at the 5% significance level between the w/o FH and w FH conditions for fluorescence images of 568-apoE2 taken with the HILO/TIRF microscope with a 20mW 561nm widefield TIRF beam at 50ms exposure with a (512x512)ROI (y axis is on log scale).*

3.5.4 Conclusion

The HILO/TIRF microscope was used to detect stoichiometry changes in *in vitro* apoE2 and A*β* with and without complement factor H. The results from using the MATLAB functions to conduct stoichiometry analysis on the images demonstrated that the HILO/TIRF microscope was indeed sensitive to single molecules in samples and could detect changes in stoichiometry in response to stimulation. However, more in-depth biological conclusions are obtained through further analysis, including conducting colocalisation analysis.

3.6 Chapter conclusion

The HILO/TIRF microscope can be used to take images of proteins *in vitro* or within cells and when the images obtained are analysed using the MATLAB functions, biologically significant results can be obtained. The molecules within images taken using 5ms exposure move fast enough that they can be analysed using the tracks analysis method whereby bright spots are identified in image frames and their intensity and stoichiometry can be subsequently tracked across frames. This was tested by imaging the transcription factor Mig1, tagged with GFP, in budding yeast using one of two methods, the tracks method and the spots method. Using the MATLAB trackAnalyser function (the tracks method) on these images yielded stoichiometry results that were significantly comparable to those published (Wollman et al., 2017). A function was built to characterise bright spot stoichiometry simply by using the bright spot intensity (the spots method), the utility of this function was tested on the same images of Mig1-GFP in yeast and yielded stoichiometry results significantly comparable to using the tracks stoichiometry analysis method. Therefore, for image videos taken using a longer exposure time or when imaging slow-moving *in vivo* protein or static *in vitro* molecules, the spots stoichiometry analysis method suffices and yields biologically significant results. These results point to the utility of the imaging and analysis methods to capture transcription factors within live mammalian cells and characterise their stoichiometry with the potential to reveal clustering behaviour of the transcription factors following extracellular stimulation.

Chapter 4 – Using the microscope to image transcription factor activity in mammalian cells

Transcription factors are proteins which regulate gene expression. The Nuclear Factor kappa B (NFkB) transcription factor activator family consists of five proteins, including RelA. Before stimulation, these proteins remain in inactive form in the cell cytoplasm. Several steps following stimulation allow the NFkB proteins to enter the cell nucleus to regulate gene expression. This chapter covers work carried out to fulfil the third of the five main objectives of this PhD;

3. *Image NFkB in human cancer cell lines and measure its stoichiometry*

The NFkB transcription factor RelA in U2OS cancer cell lines before and after stimulation by TNF-α was imaged and the intensity and stoichiometry were characterised. Nucleus stoichiometry post stimulation was significantly higher following TNF-α stimulation with RelA appearing to form two homodimers and a heterodimer, possibly with p50, its usual dimer partner. Results demonstrated the sensitivity of the HILO/TIRF microscope to single-molecules and acted as further evidence supporting the paradigm that transcription factors use clustering as a mechanism to facilitate intracellular processes following extracellular stimulation (Black et al., 2020; Boehning et al., 2018; Chen et al., 2016; Cho et al., 2018; Chong et al., 2018, 2018; Cisse et al., 2013; Z. Liu et al., 2014; Meeussen, et al., 2023; Sabari et al., 2018; Shahein et al., 2022; Wollman et al., 2017). This paradigm was further tested by imaging the activity of the transcription factor androgen receptor (AR) in LNCaP cells before and after stimulation by R1881 using HILO and TIRF microscopy. This work was carried out in association with Koffey *et al.* In the HILO condition, stoichiometry was significantly increased in the cytoplasm and nucleus following stimulation and molecules appeared to dimerize, therefore indicating that the microscope was able to capture the R1881 stimulation affecting the molecules. The TIRF imaging condition showed significant increases in AR stoichiometry at the cell membrane immediately for the first twenty minutes following stimulation. Following this, stoichiometry returned to levels the same as those before stimulation. These results support propositions in recent literature that suggest that AR is active at the cell membrane, not only the nucleus, following extracellular stimulation (Cinar et al., 2007; Ding et al., 1998; Nakhla et al., 1990). For a period of approximately 20 minutes following stimulation, AR clusters travel to the membrane before returning to the cytoplasm or translocating to the nucleus.

4.1 Introduction

Transcription factors make up approximately 8% of human genes (Lambert et al., 2018); they are proteins which can turn genes on and off. Traditional models suggest that regulatory transcription factors bind to *cis*-regulatory sequences of DNA (Mitsis et al., 2020) to turn genes on and off. The double-helix of a DNA strand contains major and minor grooves, transcription factors work to recognise *cis*-regulatory sequences in these grooves. The transcription factors can do this because their surface is complementary to that of the *cis*-regulatory sequence (Alberts et al., 2015). The affinity and specificity of transcription factor binding is increased by transcription factors forming dimers from monomers. Thus, the length of the *cis*-regulatory sequence is doubled, this increases the chances of matching sequences (Alberts et al., 2015). In eukaryotes, once the transcription factors have bound to the DNA they can either assist transcription (hence are termed activators) or can block transcription (hence are termed repressors) (Rebeiz and Tsiantis, 2017).

However, there are many unknowns concerning eukaryotic transcription factors, for example it is not fully know how the transcription factors find the correct binding sites amongst many non-specific binding sites (Wollman et al., 2017). Also, transcription factors must find a specific DNA strand within a complex DNA maze – it is unclear how they do this. The same transcription factor can be responsible for regulating multiple different genes in different cell types (Gertz et al., 2012). Transcription factor clustering (Wollman et al., 2017) is perhaps a mechanism by which transcription factors might increase their affinity and specificity (Schmidt et al., 2014).

4.1.1 Transcription factors clustering

Much evidence for the clustering properties of transcription factors has arisen in the past ten years. One of the earliest reports of transcription factor clusters came from Yan *et al.* (2013). They analysed the binding pattern of multiple expressed transcription factors in human colorectal cancer cells and found that transcription factor binding was highly clustered and almost all clusters were formed around the protein complex cohesin. They suggested that cohesin-binding serves as cellular memory that promotes re-establishment of transcription factor clusters after the DNA replication and chromatin condensation stages of transcription (Yan et al., 2013). Following this, observations of clustering of Sox2 were made in stem cells by Liu *et al.* (2014) using lattice light sheet microscopy. Sox2 is a transcription factor which keeps stem cells unspecialized by binding to DNA sequences in the cell nucleus and

maintaining the correct gene expression levels. By tracking single-molecules and mapping out immobile ones, they found that the Sox2 enhancer sites form clusters (Z. Liu et al., 2014).

The first observation of transcription factors translocating across cells as whole clusters was made in budding yeast by Wollman *et al.* (Wollman et al., 2017) outlined in chapter 3. Further evidence of clustering transcription factors in yeast was given by Black *et al.* (2020); the beginning of the budding yeast cell division cycle, the G1 phase, was termed 'Start' by Hartwell *et al.* (1974). G1/S transcription is required for Start to commence, two transcription factor complexes control this. These are the SCB-binding factor and the MCB-binding factor (Black et al., 2020). Black *et al.* (2020), using PALM, found that G1/S transcription factors in budding yeast not only form clusters, of about eight molecules in size, but these clusters increase in number as the cells grow (Black et al., 2020).

Many transcription factor clustering studies have focussed on the behaviour of RNA Polymerase 2 (Pol2) clusters. Pol2 is involved in transcribing DNA into messenger RNA. Cisse *et al.* (2013) observed that Pol2 clusters form transiently with lifetimes averaging 5 seconds. The dynamics of the Pol2 clusters were changed by stimuli affecting transcription. They implied that the clustering is regulated and contributes to the ability of the cell to effect a rapid response to external signals (Cisse et al., 2013). Chen *et al.* (2016) used Bayesian nanoscopy in live mammalian cell nuclei to study the clustering dynamics of Pol2 (Chen et al., 2016). Bayesian nanoscopy involves determining the localisation of molecules within dense samples by using Bayesian inference, it determines the number of PSFs in an ROI based on their intensity. This method can increase the number of closely-spaced molecules identified (Manzo et al., 2014). Using Bayesian nanoscopy, Chen *et al.* (2016) suggested that transcription factories form on demand and recruit Pol2 molecules during their pre-elongation phase and that the assembly and disassembly of individual Pol2 clusters takes place asynchronously (Chen et al., 2016). Cho *et al.* (2018) used light-sheet and live-cell super-resolution microscopy to observe the Mediator coactivator transcription factor and Pol2 in the embryotic stem cells of mice and found that Mediator forms small clusters lasting up to approximately 12 seconds (Cho et al., 2018). They also found that Mediator and Pol2 form multiple large clusters, with approximately 14 of these in each cell (Cho et al., 2018). Further work on Pol2 was conducted by Boehning *et al.* (2018) who found that truncating the carboxy-terminal domain (CTD) of RNA Pol2 in human cells, 52, to the length of yeast CTD, 26, decreases Pol2 clustering and chromatin association and extending the CTD has the opposite effect. They suggested that Pol2

forms clusters at active genes through interactions with CTDs and with activators (Boehning et al., 2018).

Chong *et al.* (2018) used a combination of super-resolution microscopy techniques including FRAP, lattice light-sheet microscopy and others. They proposed that the EWS/FLI1, TAF15 and Sp1 transcription factors form 'hubs' (clusters) through interactions between low-complexity sequence domains (LCDs) (Chong et al., 2018). Sabari *et al.* (2018) found that the coactivator transcription factors MED1 and BRD4 formed phase-separated condensates (clusters) at super-enhancers (Sabari et al., 2018). Shahein *et al.* (2022) found that transcription factors can bind concurrently to overlapping sites thus challenging the initial ideas of exclusivity of binding. Additionally, they found that low-affinity binding site clusters are effective at activating transcription *in vivo* (Shahein et al., 2022). Meeussen *et el.* (2023) used quantitative microscopy in live budding yeast cells and showed that the transcription factor Gal4 forms clusters that overlap with the GAL loci. The density and size of the clusters and the number of clusters are regulated in different growth conditions by the Gal4 inhibitor, Gal80. They also found that in cells in which the Gal4 transcription factor was truncated, Gal4 clustering was facilitated by DNA binding. Additionally, they found that when Gal4 molecules are not DNA bound, they may inhibit transcription activation (Meeussen, et al., 2023).

4.1.2 Transcription factors in cancer and targeted drug therapy

Despite the range of research put into the phenomena, transcription factor clustering is not yet fully understood, however transcription factors are a fundamental process in biology (Lambert et al., 2018). If unregulated their activity (or inactivity) can cause cancer and inflammatory diseases (Adamson et al., 2016), 33 transcription factors and their dysregulation have been linked with various cancer types (Lee and Young, 2013). For example, the promyelocytic leukaemia protein (PML)-reinoic acid receptor α (RARα) and the core binding factor β (CBFβ)-smooth muscle heavy chain have been found to be drivers of leukaemia (Look, 1997).

Much research has been conducted on the effect of drug therapy on alleviating or removing cancer (Bushweller, 2019). Bromodomain inhibitors have worked in mouse cancer models and various pharmaceutical companies such as GlaxoSmithKline and Merck have carried out clinical trials (Filippakopoulos et al., 2010; Gehling et al., 2013; Mirguet et al., 2013; Xu and Vakoc, 2017). Additionally, H3K27 enhancer inhibitors are in clinical trials (Helin and Dhanak, 2013). Although inhibitors have been effective, they tend to impact a wider area of gene

expression and so are likely to be less effective (Bushweller, 2019). A more effective method would be to directly target the transcription factors involved in the cancer (Bushweller, 2019). Overexpression of the ERG and ETV1 transcription factors have been found in prostate cancer (Chen et al., 2013; Clark and Cooper, 2009; Helin and Dhanak, 2013; Tomlins et al., 2005) and runt-related transcription factors, RUNX1-RUNX3, and CBFβ, with which these form dimers, have been found to be involved with epithelial cancers (Chuang et al., 2017; Morita et al., 2017; Scheitz et al., 2012).

Small molecules which bind to specific nuclear hormone receptors have been used to target transcription factors in cancer (Burris et al., 2013), for example oestrogen receptor (ER) expression occurs in about 75% of breast cancer cases (Perou et al., 2000); drugs such as selective oestrogen receptor modulators (SERMs) and selective oestrogen receptor degraders (SERDs) (Patel and Bihani, 2018) which modulate ER activity have been used to treat breast cancer (Burris et al., 2013; de Thé, 2018). Additionally, drugs which target androgen receptor (AR) activity have been used to treat prostate cancer (Burris et al., 2013; de Thé, 2018); androgens drive the proliferation and survival of prostate cancer cells (Bushweller, 2019; Dai et al., 2017). Drugs such as bicalutamide, flutamide and nilutamide (Burris et al., 2013) and enzalutamide have been developed to reduce AR-driven gene expression (Bushweller, 2019). Small-molecule protein-protein inhibitors of the menin-mixed lineage leukaemia (MLL) fusion protein interaction which were shown to reduce expression of genes that drive MLL fusion-positive leukaemia were developed by Grembecka *et al.* (Borkin et al., 2018, 2016, 2015; Grembecka et al., 2012; He et al., 2014). CBFβ-SMMHC binding to RUNX1 has been shown to be inhibited by AI-10-49, an inhibitor developed which disrupts the protein to protein interactions between CBFβ-SMMHC and RUNX1 and decreases the colony-forming ability of leukaemia cells (Castilla et al., 1996; Mandoli et al., 2014).

4.2 Imaging the NFkB transcription factor RelA in U2OS cells

4.2.1 Introduction

The Nuclear Factor k B (NFkB) family of transcription factors are a good system to develop a better understanding of how transcription factors work and how they can better be targeted as they have been well characterised with standard molecular biology techniques. If the inflammatory responses resulting from NFkB activation are incorrect or excessive, this can result in pain, chronic inflammation, cancer (Alberts et al., 2015) and neurodegenerative

disorders (Jin et al., 2019). NFkB signalling has been found in several human cancers; for example, HER2 is a protein that promotes breast cancer growth progression and drug resistance, NFkB is active in 86% of HER2-positive and oestrogen-receptor-negative breast cancer (Ling and Kumar, 2012). NFkB proteins are transcription factors that work to regulate immune-responses. Two protein families make up the NFkB signalling system, these are activators (NFkB) and inhibitors (IkB) (O'Dea and Hoffmann, 2010). In mammals, the NFkB family consists of five proteins; *Rel*A, *Rel*B, *c-Rel*, NFkB1 and NFkB2. Within the IkB family are IkBα, IkBβ, IκBϵ and Bcl-3. Pre-stimulation, NFkB remains in an inactive form in the cell cytoplasm and is bound to the inhibitor IkB. During cell stimulation, the IkB is phosphorylated, this results in ubiquitination of the IkB. Following this, the IkB is degraded by the 26S proteosome, a protein machine which recognises ubiquitin and degrades proteins. Then the NFkB can translocate to the nucleus. Once in the nucleus, NFkB works to regulate gene expression.

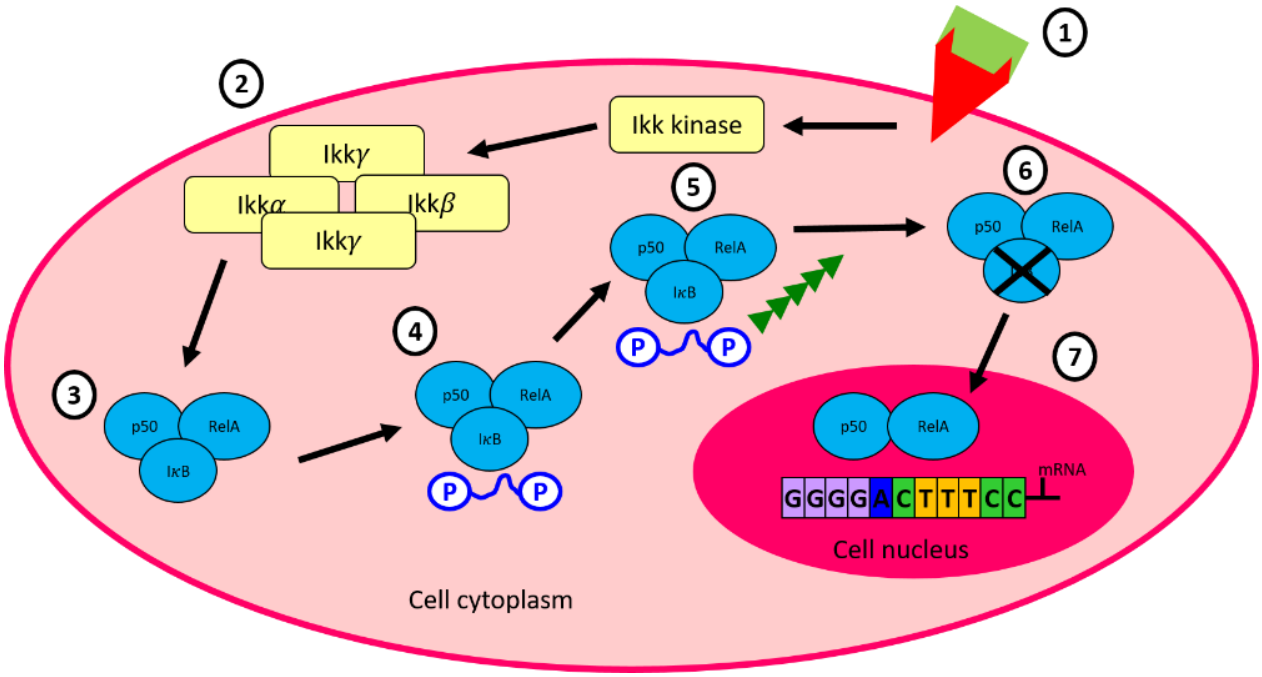

Figure 4.1 *An example of NFkB processes within a mammalian cell*

Figure 4.1 depicts canonical NFkB activation within the cell with the following steps;

1. Extracellular stimuli (e.g. tumour necrosis factor, (TNF-α)) trigger the NFκB pathway
2. The receptor activates the Ikk kinase protein
3. The Ikk kinase protein interacts with IkB on a *Rel*A-p50 dimer
4. The Ikk phosphorylates the IkB protein

5. The IkB is ubiquitinated – this causes it to disassociate from the *Rel*A:p50 dimer and the IkB is removed from the cell
6. The *Rel*A:p50 dimer is free to enter the nucleus
7. The *Rel*A:p50 dimer regulates transcription in the nucleus

U2OS cells are from human bone tissue, are epithelial and adherent and are from the osteosarcoma disease. The cells are strongly adherent and can be used as a transfection host.

Transfection came in the form of an eGFP-RelA plasmid. Cells were transfected with this plasmid 24 hours prior to imaging. Cells were imaged before and after stimulation by tumor necrosis factor α (TNF-α). When RelA is activated by TNF-α, ubiquitylation and phosphorylation occurs in multiple proteins and RelA is released from the inhibitory protein complex and it can translocate from the cytoplasm to the nucleus and trigger transcription. Bright spots in cell images were captured using the MATLAB functions. Spot intensity and stoichiometry were characterised. The aim was to observe if the RelA transcription factor formed clusters, if it did, this would indicate that clustering is indeed a mechanism by which this transcription factor carries out transcription in response to extracellular stimulation. Stoichiometry analysis was used as this could elucidate the number of RelA-GFP molecules in clusters.

4.2.2 Methods

4.2.2.1 Establishment

Frozen U2OS passage 20 cell lines were stored in 1mL cryotubes in liquid nitrogen storage. A cryotube was removed and defrosted. This was pipetted into a 100mL flask with 25mL phenol-red-free DMEM (Dulbecco's Modified Eagle Medium) supplemented with 10% Foetal Bovine Serum (FBS), 5% L-glutamine and 5% Sodium Pyruvate.

As U2OS cells naturally adhere to the bottom of the growth flask and imaging dishes, no adherence methods were required during culturing and imaging processes.

Note that in the first stages of cell culture and attempted transfection, normal DMEM, with phenol red, was used, however the phenol red is inherently fluorescent and interferes with any signal coming from single molecules during imaging. Therefore, phenol-red-free DMEM was used for all further culturing and transfecting processes.

Cell flasks were fed twice a week; this involved removing old growth media and replacing it with a fresh supply. They were also split once a week.

4.2.2.2 Splitting

Old growth media was removed from the cell flask and 10mL of Phosphate Buffered Saline (PBS) was pipetted into the flask and the flask was shaken slightly. This was to coat the cells to protect them from the Trypsin which can be slightly abrasive. The PBS was removed and 5mL Trypsin was pipetted into the flask before placing the flask into the incubator at 37°C, 5% CO_2 for 5 minutes. This was done to lift the cells from the bottom of the flask. New flasks were labelled and filled with 25mL of new growth media, phenol-red-free DMEM (supplemented with 10% FBS, 5% L-glutamine and 5% Sodium Pyruvate).

The original flask was removed from the incubator and tapped gently to loosen any remaining adherent cells. A 40X compound light microscope was used to check that the cells were loose. 10mL of growth media was added to the original flask and the 15mL of cell to growth media was added to a 50mL Falcon tube. The Falcon tube was placed in a centrifuge at 1500rpm for 5 minutes. Once a pellet had formed at the bottom of the Falcon tube, the supernatant was poured away and 10mL of growth media was added. A 10mL syringe was used to re-suspend the pellet into the media.

20μL of the cell media was pipetted onto a cell-counting slide and a cell-counter was used to determine the live cell density count, L (mL^{-1}) per mL. This value was used to determine the cell media seeding amount, A (mL) as follows;

$$A = \frac{S}{L} \tag{37}$$

where $S \epsilon \mathbb{N}, S > 0$ is the seeding number.

The amount, A was then pipetted into the new cell flask and the flask was stored in the incubator at 37°C, 5% CO_2.

4.2.2.3 Transfection

U2OS cells, at passage 23-25, were split and passed into four 2mL microdishes, each at a cell confluency of 500,000, all with phenol-red-free DMEM (+10% FBS, 5% L-glutamine, 5% Sodium Pyruvate). These dishes were placed in the incubator at 37°C, 5% CO_2 overnight. The next day a transfection media was made in four Eppendorf tubes, each tube consisting of the same media and media amounts; 1.25μL of p3000 reagent, 1.25μL of lipofectamine 3000 reagent and 25μL Optimem. These were left to incubate at room temperature for 15 minutes while

each culture dish was washed with 300μL PBS. Each dish was then filled with 1mL Optimem and 1mL phenol-red-free DMEM. After the incubation period, 2.5μL of the diluted plasmid (1.25μL of the eGFP-p65 plasmid to 1.25μL nuclease-free water) was added to each of the transfection media tubes. The dishes were incubated at 37°C, 5% CO_2 overnight and imaged the next day.

4.2.2.4 Freezing

A freezing solution was made with FBS and 10% DMSO (Dimethyl Sulfoxide). Growth media was removed from the cell flask and 10mL of PBS was pipetted into and the flask was shaken slightly. The PBS was removed and 5mL Trypsin was pipetted into the flask before placing the flask into the incubator at 37°C, 5% CO_2 for 5 minutes. After this, 10mL of growth media was added to the flask and the 15mL of cell to growth media was added to a 50mL Falcon tube and placed in a centrifuge at 1500rpm for 5 minutes. Afterwards, the supernatant was poured away and the freezing solution was added to the pellet and re-suspended. This media was then added in 1mL amounts to cryotubes. The cryotubes were wrapped in blueroll and placed in the -80°C freezer storage overnight and then placed in liquid nitrogen storage.

4.2.2.5 Imaging and stimulation with TNF-α

Transfected U2OS cell microdishes were placed on the HILO/TIRF microscope sample stage and incubated at 37° in 5% CO_2. RelA-GFP in U2OS cells was imaged using a 20mW 488nm HILO intermediate-narrowfield beam with a (256x256)ROI at 20ms exposure. 2μL of 10ng/mL TNF-α in nuclease-free water was added dropwise to cell microdishes during imaging. Cell images were taken before and after TNF-α stimulation.

4.2.3 Results

Fluorescence images of RelA-GFP in U2OS cells were taken using a 20mW 488nm HILO intermediate-narrowfield beam with a (256x256)ROI at 20ms exposure (figure 4.2). Cells were stimulated with TNF-α and images were taken before and after this. Intensity and stoichiometry in image videos were characterised using MATLAB functions.

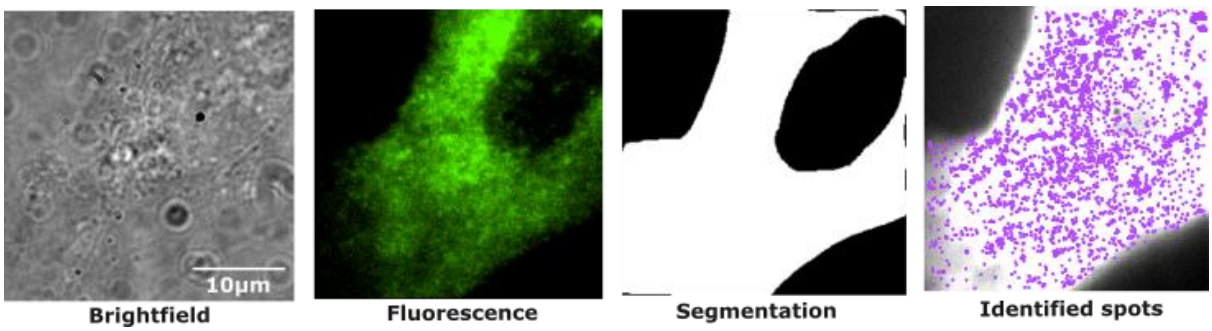

Figure 4.2 *Brightfield image of a U2OS cell and fluorescence image of RelA-GFP in the cell, taken using a HILO 20mW 488nm intermediate-narrowfield beam at 20ms exposure with a (256x256)ROI, and the segmentation mask and the bright spots identified by the MATLAB tracker function.*

Images were analysed using the MATLAB tracker function. Cytoplasm single molecule intensity before TNF-α stimulation, for N=13 cells, was 52900±26500 and was, for N=41 cells, 59000±37700 after stimulation (figure 4.3A). Nucleus single molecule intensity before stimulation was 60200±41800 and was 59700±36100 after stimulation (figure 4.3B).

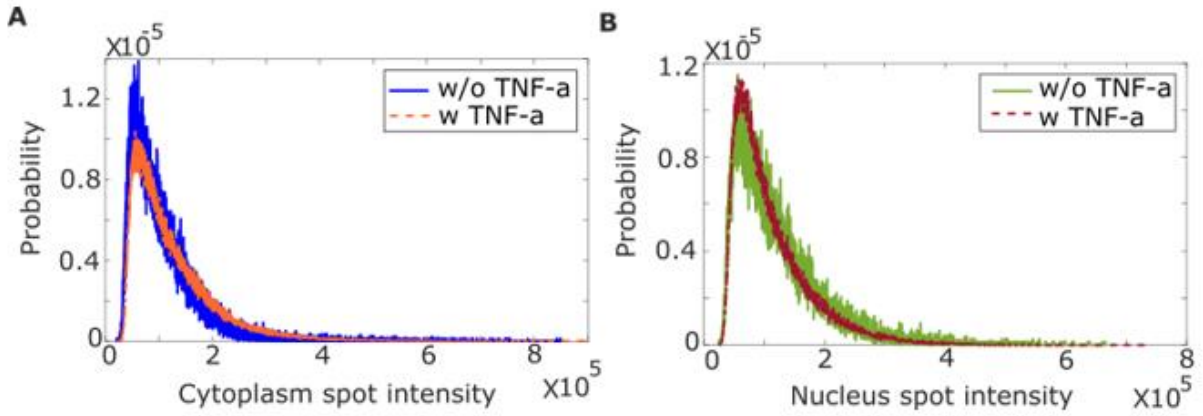

Figure 4.3 A. *KDF distribution plots of bright spot intensity (counts) for cytoplasm and* ***B.*** *nucleus of fluorescence images of RelA-GFP in U2OS cells taken with a 20mW 488nm HILO intermediate-narrowfield beam with a (256x256)ROI at 20ms exposure before (w/o TNF-a) and after TNF-α (w TNF-a) stimulation.*

The spots stoichiometry method using 3 frames was used to characterise the stoichiometry of this data. This was because images were taken at 20ms exposure, this was not fast enough for single molecules to be tracked. Therefore, track information would not have been useful. Stoichiometry was instead determined by dividing the initial intensity of each bright spot by the I_{single} value, the intensity of a single molecule prior to it photobleaching. This ratio yielded an estimate for the stoichiometry. The stoichiometry data before and after TNF-α stimulation is not normally distributed, therefore statistical tests were run on the log distribution of the data. Additionally, stoichiometry data was obtained from different samples and two different conditions were tested, namely with and without TNF-α stimulation, therefore an

independent sample statistical test was used. The mean cytoplasm stoichiometry before TNF-α stimulation, for n_s=9915 bright spots, was 2.4±0.3 (figure 4.4B). The peak of the KDF for cytoplasm stoichiometry before TNF-α stimulation was 2.5±0.03 (figure 4.4A). The mean cytoplasm stoichiometry after TNF-α stimulation, for n_s=48014 bright spots, was 2.5±0.2 (figure 4.4B). The peak of the KDF for cytoplasm stoichiometry after TNF-α stimulation was 2.6±0.02 (figure 4.4A). After running an independent sample t-test at the 5% significance level on the log distribution of these data, we obtain a p value of 0.4592 (figure 4.4B) therefore indicating that the mean stoichiometry was not significantly different in the cytoplasm pre and post TNF-α stimulation at the 5% significance level. This may suggest that TNF-α stimulation did not affect the molecules within the cell cytoplasm. Contrarily, the mean nucleus stoichiometry before TNF-α stimulation, for n_s=4558 bright spots, was 2.1±0.2 (figure 4.4D). The peak of the KDF stoichiometry for the nucleus before TNF-α stimulation was 2±0.3 (figure 4.4C). The mean nucleus stoichiometry after TNF-α stimulation, for n_s=24227 bright spots, was 2.4±0.2 (figure 4.4D). The peak of the KDF stoichiometry for the nucleus after TNF-α stimulation was 2.3±0.2 after stimulation (figure 4.4C). After running an independent sample t-test at the 5% significance level on the log distribution of the nucleus stoichiometry data before and after TNF-α stimulation, we obtain a p value less than 0.05 (figure 4.4D) therefore indicating that the molecules in the cell nucleus were affected by the TNF-α stimulation as the mean stoichiometry was significantly higher at the 5% significance level post TNF-α stimulation. However, the mean values for nucleus stoichiometry before and after stimulation are quite close to one another, so further analysis was conducted to further establish the meaning behind these differences. This included analysing stoichiometry over time post-stimulation.

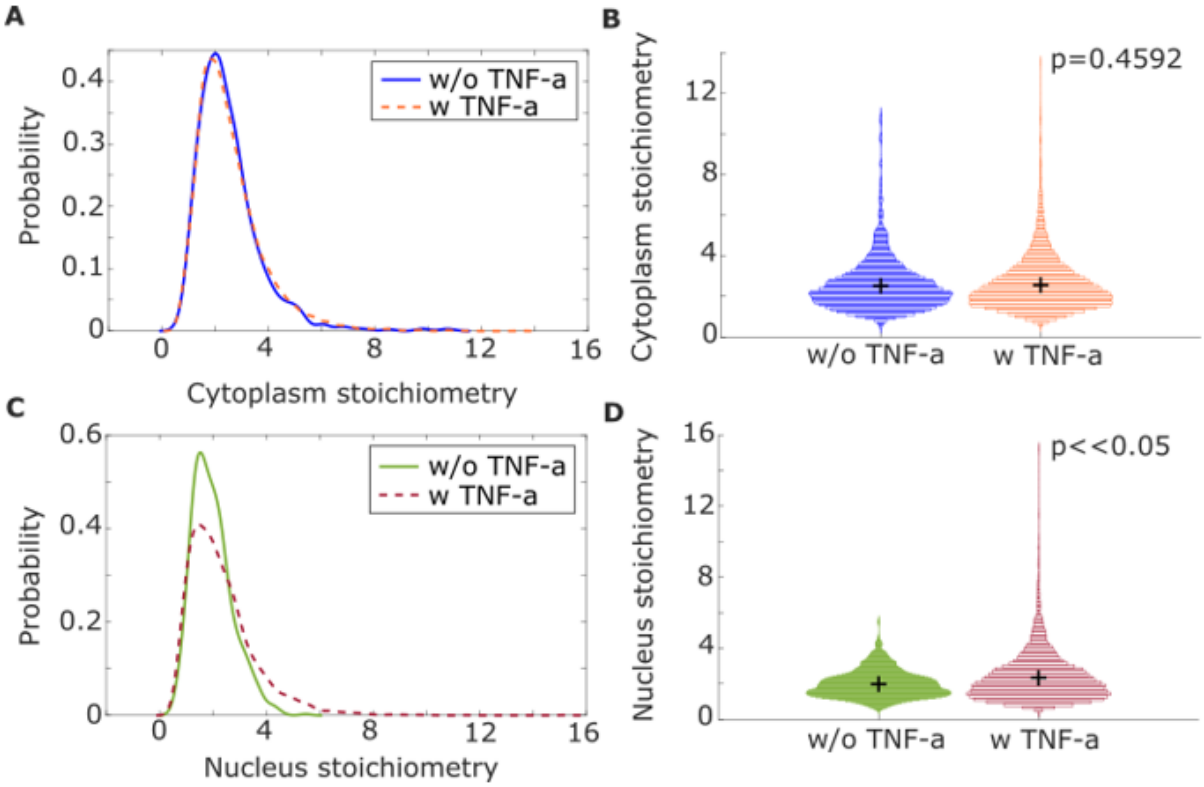

Figure 4.4 A. *KDF distribution plots of cytoplasm stoichiometry before and after TNF-α stimulation and* ***B.*** *Violin plots of cytoplasm stoichiometry before (w/o TNF-a) and after (w TNF-a) TNF-α stimulation indicating a p value of 0.4592 between the before TNF-α (w/o TNF-a) and after TNF-α (w TNF-a) stimulation conditions at the 5% significance level and* ***C.*** *KDF distribution plots of nucleus stoichiometry before (w/o TNF-a) and after TNF-α (w TNF-a) stimulation and* ***D.*** *Violin plots of nucleus stoichiometry before and after TNF-α stimulation indicating a p<<0.05 between the (w/o TNF-a) before TNF-α and after TNF-α (w TNF-a) stimulation conditions at the 5% significance level for fluorescence images of RelA-GFP in U2OS cells taken using a 20mW 488nm HILO intermediate-narrowfield beam with a (256x256)ROI at 20ms exposure.*

Time post TNF-α stimulation was allotted into seven bins and was plotted against stoichiometry for the cytoplasm (figure 4.5A) and nucleus (figure 4.5B). The plots also include the stoichiometry pre stimulation for comparison.

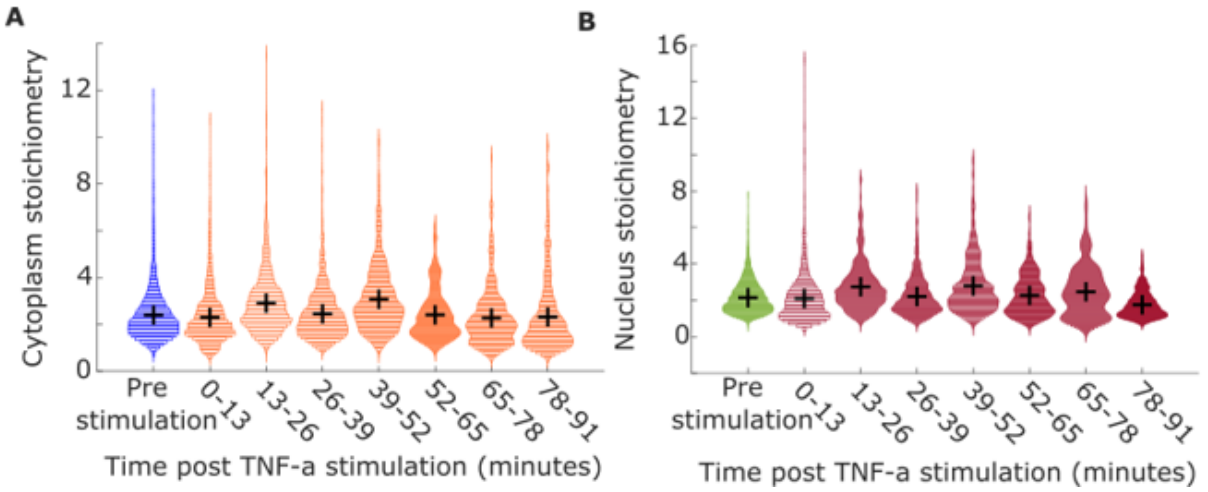

Figure 4.5 *Violin plots of* ***A.*** *cytoplasm stoichiometry and* ***B.*** *nucleus stoichiometry pre and post TNF-α stimulation for fluorescence images of RelA-GFP in U2OS cells taken with a 20mW 488nm HILO intermediate-narrowfield beam with a (256x256)ROI at 20ms exposure.*

The average stoichiometry within standard error for multiple cells was plotted pre stimulation and in the seven allotted bins after stimulation for cell cytoplasm (figure 4.6A) and nucleus (figure 4.6B). The two graphs indicate the significance between the stoichiometry pre stimulation and post stimulation (in minutes). To start with, cytoplasm stoichiometry after TNF-α stimulation dropped below levels observed in the cytoplasm pre-stimulation, a p value of 2.2e-10 was obtained upon running an independent sample Mann-Whitney U test at the 2.5% confidence interval between cytoplasm stoichiometry before stimulation and cytoplasm stoichiometry up to 13 minutes after stimulation. Before stimulation, stoichiometry in the cytoplasm was 2.5±0.03 and up to 13 minutes after stimulation it was 2.3±0.03. Then the stoichiometry increased for approximately 13 minutes before returning to levels the same as those before stimulation. The stoichiometry then increased again and then again returned to pre-stimulation levels before dropping below these levels from 65 minutes after stimulation.

In the first 13 minutes following stimulation by TNF-α, the nucleus stoichiometry remained the same as that pre-stimulation, a p value of 0.2488 was observed upon running an independent sample Mann-Whitney U test at the 2.5% significance level between the pre-stimulation condition and up to 13 minutes afterward. Then, between 13 to 78 minutes following stimulation, stoichiometry fluctuated between 2.7±0.06 and 2.5±0.09 before dropping to 1.8±0.04 in the last 13 minutes, all significantly different to stoichiometry pre-stimulation.

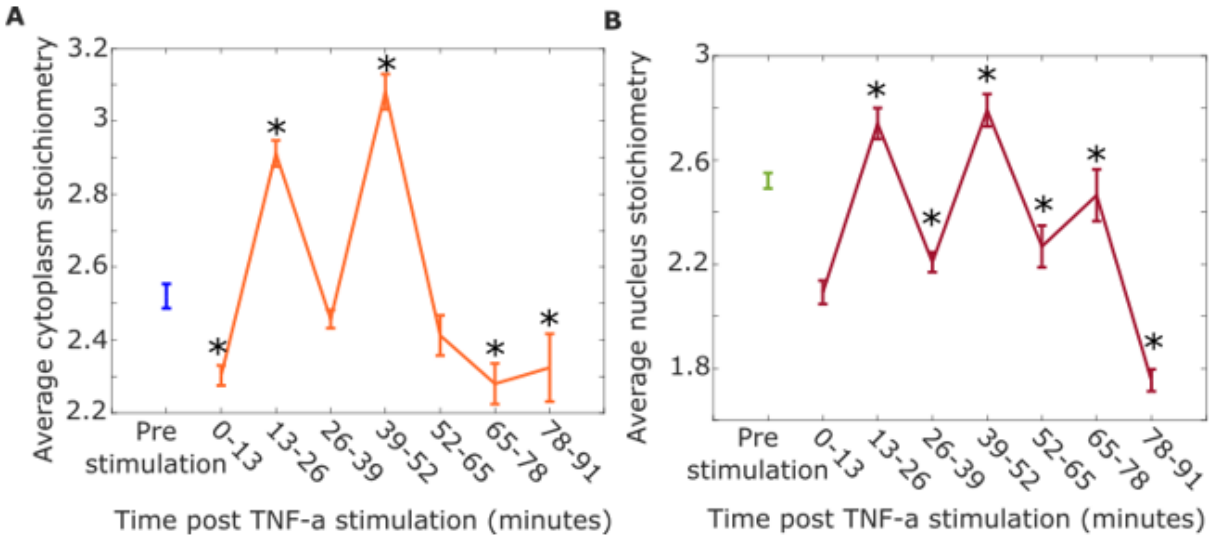

Figure 4.6 A. *Errorbar plot of average cytoplasm stoichiometry against time post R1881 stimulation (minutes) and* ***B.*** *Errorbar plot of average nucleus stoichiometry against time post R1881 stimulation (minutes) in fluorescence images of RelA-GFP in multiple U2OS cells (in each time bin) taken with a 20mW 488nm HILO intermediate-narrowfield beam at 20ms exposure with a (256x256)ROI. The plots indicate the significance between stoichiometry pre-stimulation and at each time bin post TNF-α stimulation from independent sample Mann-Whitney U tests ran at the 2.5% significance level.*

4.2.4 Conclusion

Prior to TNF-α stimulation, RelA-GFP the mean stoichiometry in the nucleus of U2OS cells was 2.1±0.2 (figure 4.4D), this points to the presence of RelA:RelA homodimers. The mean number of RelA-GFP molecules significantly increased in the nucleus following TNF-α stimulation to 2.4±0.2 (figure 4.4D). This suggests there was a high probability of clusters consisting of approximately 3 RelA-GFP molecules, this may point toward the presence of a RelA:RelA homodimer accompanied by a RelA:p50 heterodimer. These findings are consistent with literature that suggests that RelA:p50 heterodimers translocate to the nucleus following extracellular stimulation, such as by TNF-α (O'Dea and Hoffmann, 2010). Up to 26 minutes after TNF-α stimulation, average RelA-GFP stoichiometry in the nucleus was 2.7±0.06 (figure 4.6B), additionally there was a small number of clusters that were between 8-16 molecules in size (figure 4.5B). Again, this may point to the presence of both RelA homodimers and RelA:p50 heterodimers. RelA usually forms heterodimers with p50 (Y.-Q. Chen et al., 1998; Florio et al., 2022; Ganchi et al., 1993) and these dimers are the most abundant and transcriptionally active (Hayden and Ghosh, 2008), while RelA homodimers are less abundant (Ghosh et al., 2012) and less stable (Florio et al., 2022), however RelA can interact with DNA on its own in the absence of p50 (Ruben et al., 1992). RelA:RelA homodimers being less stable (Florio et al., 2022) may explain why the RelA-GFP stoichiometry fluctuated in the nucleus post-TNF-α stimulation (figure 4.6B); between 13-78 minutes after stimulation, stoichiometry significantly decreased

and increased, this may point to (RelA:RelA)-GFP homodimers entering the nucleus and dissipating after a period of approximately 13 minutes. After entering the nucleus, RelA is modified in various ways depending on its binding site. It is usually phosphorylated in a specific region, for example in the topologically associating domain (TAD) (Zhong et al., 1998) or, after TNF-α stimulation, it can be phosphorylated by mitogen and stress-activated kinase 1 (MSK1) (Vermeulen et al., 2003). The 13 minute period is perhaps the RelA timeframe to translate to its specific binding site, it then dissipates following phosphorylation. Additionally, unlike Rel:p50 heterodimers, RelA homodimers are not stabilised by hydrogen bonds and salt bridges which arguably aid the structural stability of the dimer (F. E. Chen et al., 1998; Florio et al., 2022; Ghosh et al., 2012; Huang et al., 1997). Therefore, 13 minutes may be how long it takes for these dimers to become so unstable as to dissipate.

The average RelA-GFP stoichiometry on a whole remained the same within the cytoplasm before and after cell stimulation by TNF-α, an average of 2.4-2.5 molecules (figure 4.4B). This may suggest that the majority of RelA:RelA homodimers remained within the cytoplasm after TNF-α stimulation, while a few RelA-GFP single molecules formed heterodimers with p50 before translocating to the nucleus. This would also explain why, upon further inspection of RelA-GFP stoichiometry levels in the cytoplasm post TNF-α stimulation (figure 4.6A), stoichiometry significantly decreased in the first 13 minutes post stimulation and then fluctuated to levels at or above stoichiometry pre stimulation for approximately 13—52 minutes and then finally decreased to levels below pre stimulation stoichiometry after this.

Additionally, there were many clusters in the cytoplasm that were between 5-12 molecules in size pre-TNF-α stimulation and up to 91 minutes after stimulation, this may point to (RelA:RelA)-GFP homodimers which did not translocate to the nucleus at any time. As human cells intrinsically create and induce NFkB transcription factors (Liu et al., 2017), endogenous RelA molecules not tagged with GFP (dark RelA) may also play a part in the clustering behaviour of the RelA-GFP molecules, detected clusters of 3 RelA-GFP molecules in size may in fact contain 4 or more RelA molecules and hence contain more than one or two RelA:RelA homodimers, but dark RelA is not something the microscope would be able to detect.

The presence of RelA-GFP clusters of approximately 8-16 (within the nucleus) and 5-12 (within the cytoplasm) molecules in size point toward definite clustering behaviour of the RelA-GFP molecules. Therefore, the clustering behaviour of the NFkB RelA transcription factor in U2OS cells in response to extracellular stimulation by TNF-α was evidenced using the HILO/TIRF

microscope and subsequently using the MATLAB functions to analyse the image results and quantify stoichiometry.

4.3 Imaging the transcription factor androgen receptor (AR) in LNCaP cells

LNCaP cells were grown and transfected with AR-GFP by Coffey *et al.* and AR-GFP before and after R1881 stimulation in the cells was imaged using the HILO/TIRF microscope.

4.3.1 Introduction

Androgen receptor (AR) is a 110kDa steroid hormone receptor which is massively associated with prostate cancer development (Coffey and Robson, 2012). AR usually resides in the cell cytoplasm. When the cell is stimulated by an androgen hormone, such as testosterone, the testosterone is converted by the enzyme 5α-reductase into dihydrotestosterone (DHT). DHT enters the cell cytoplasm where it binds to AR. This causes the AR to disassociate from heat shock proteins (HS), following this, the AR is free to enter the nucleus. When in the nucleus, the AR homodimerises and stimulates the transcription of androgen-responsive genes (Bennett et al., 2010) (figure 4.7).

Although the typical AR activation pathway occurs between the cell cytoplasm and nucleus, there is evidence of AR activity on the cell membrane. Recently, membrane-associated AR in LNCaP cells has been shown to activate the P13-kinase/serine threonine kinase Akt signalling cascade, a mediator for growth, survival and metabolic signalling (Cinar et al., 2007). In the last thirty years, membrane AR in LNCaP cells has also been shown to activate cAMP (Nakhla et al., 1990), a cellular signal occurring in intracellular signal transduction, and protein kinase A (Ding et al., 1998).

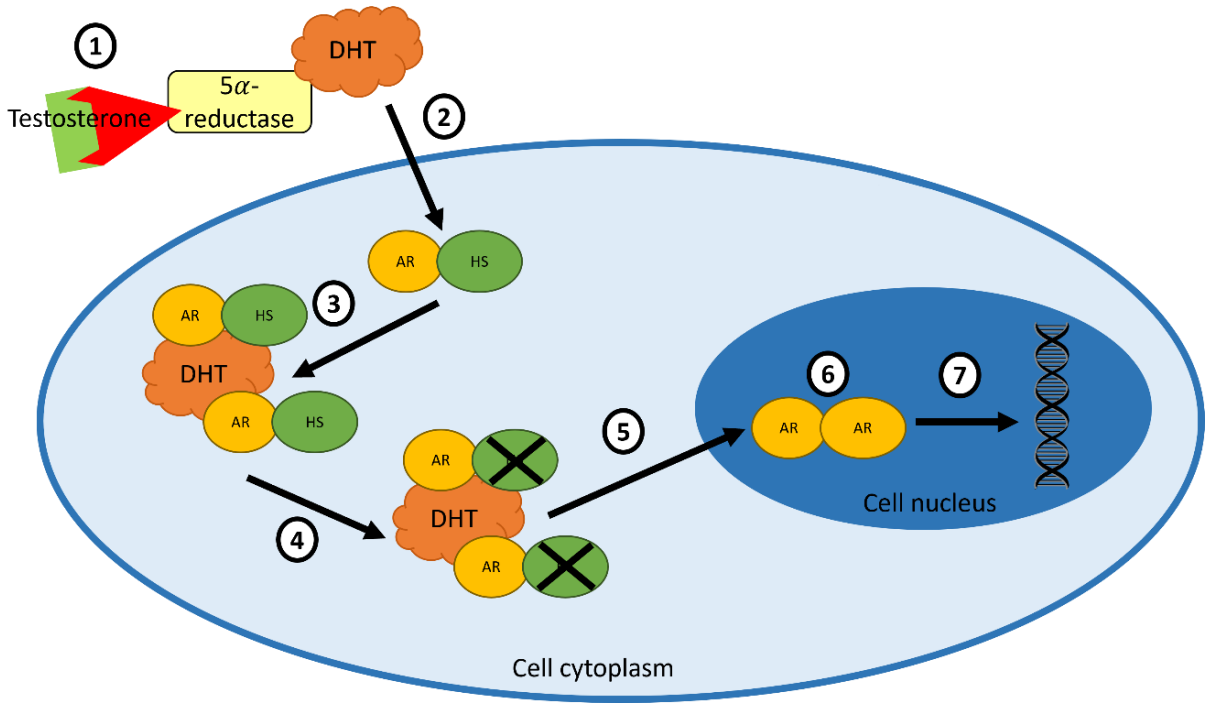

Figure 4.7 *An example of AR processes within a mammalian cell*

Figure 4.7 is a depiction of a typical AR activation process within the cell and has the following steps;

1. Testosterone is converted into dihydrotestosterone (DHT) by the enzyme 5α-reductase
2. DHT enters the cytoplasm
3. DHT binds to AR
4. The AR disassociates from heat-shock proteins (HS)
5. The AR enters the nucleus
6. AR homodimerises in the nucleus
7. AR facilitates transcription of androgen-responsive genes

Post-translational modifications such as regulation of protein stability, interaction with other proteins, cellular localisation and the very structure of AR can contribute to modulation of AR activity (Coffey and Robson, 2012). Studying these mechanisms can help elucidate appropriate therapies for problems caused by AR dysregulation such as prostate cancer.

LNCaP cells are androgen-sensitive, weakly-adherent epithelial cells from a lymph node metastasis. They are a cell line of human prostate carcinoma cells. Due to their androgen sensitivity, they are useful for studying the mechanisms of AR. R1881 is an androgen stimulant (Migliaccio et al., 2000; Takeda et al., 2007) which can be used to trigger the AR pathway in LNCaP cells. The stoichiometry of AR in the cell membrane, cytoplasm and nucleus was

characterised to observe if clusters of AR were formed in response to R1881. If clusters did form, this would indicate that clustering is a mechanism utilised by AR to aid transcription in response to extracellular transcription.

4.3.2 Methods

AR-GFP LNCaP cells were grown by Coffey *et al.* for 24 hours in 10% SDM followed by 48 hours growth in 0.5% SDM. Samples were plated in 2mL dishes prior to imaging and 20μL of 1nM R1881 was pipetted to dishes during imaging. Samples were maintained at approximately room temperature during imaging and a 40mW HILO beam at 20ms exposure with a (256x256)ROI was used to capture AR-GFP with and without R1881 stimulation.

AR-GFP in LNCaP cells was imaged using two different imaging conditions, namely;

- Using a (256x256)ROI with 20ms exposure and a 40mW 488nm HILO intermediate-narrowfield beam
- Using a (256x256)ROI with 20ms exposure and a 40mW 488nm TIRF intermediate-narrowfield beam

HILO imaging was used to observe the AR mechanisms occurring in the cytoplasm and, following stimulation by R1881, in the nucleus. TIRF imaging was used to capture AR characteristics at the cell membrane; in light of literature evidencing AR activity at the membrane (Cinar et al., 2007; Ding et al., 1998; Nakhla et al., 1990), it was thought that TIRF imaging could be used to reveal the behaviour of AR clusters at the membrane in LNCaP cells stimulated with R1881.

Cells were stimulated with 20μL of 1nM R1881 during imaging and the intensity and stoichiometry of images pre and post stimulation was categorised.

4.3.3 Results

4.3.3.1 Capturing AR-GFP in LNCaP cell cytoplasm and nucleus using a HILO beam

Fluorescence images of AR-GFP in LNCaP cells were taken using a 40mW 488nm intermediate-narrowfield beam at HILO angle between 45-56° using a (256x256)ROI at 20ms exposure (figure 4.8). Images were taken before and after stimulation with R1881 and the cytoplasm and nucleus intensity and stoichiometry were characterised.

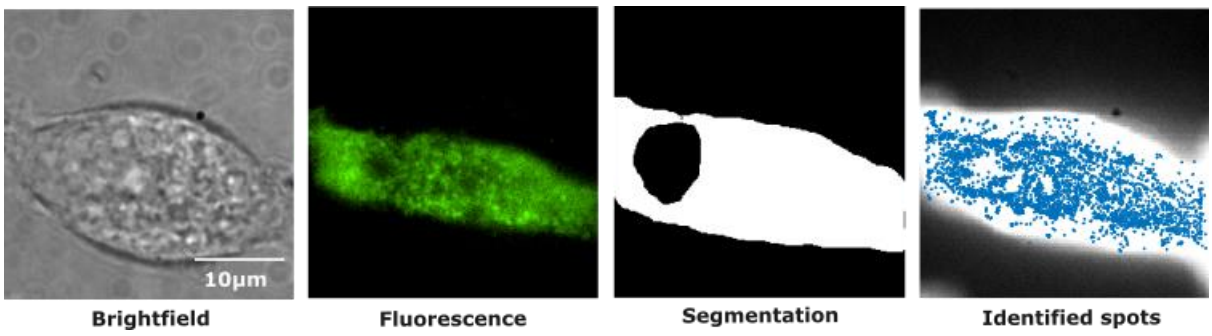

Figure 4.8 *Brightfield image of a LNCaP cell and fluorescence image of AR-GFP in the cell, taken using a HILO 40mW 488nm intermediate-narrowfield beam at 20ms exposure with a (256x256)ROI, and the segmentation mask and the bright spots identified by the MATLAB tracker function.*

After using the tracker function on the images, cytoplasm single molecule intensity, for N=19 cells, before R1881 stimulation was 74300±40000 and was for, N=20 cells, 59700±41800 after stimulation (figure 4.9A) while nucleus single molecule intensity before R1881 stimulation was 90400±56000 and was 69000±46400 after stimulation (figure 4.9B).

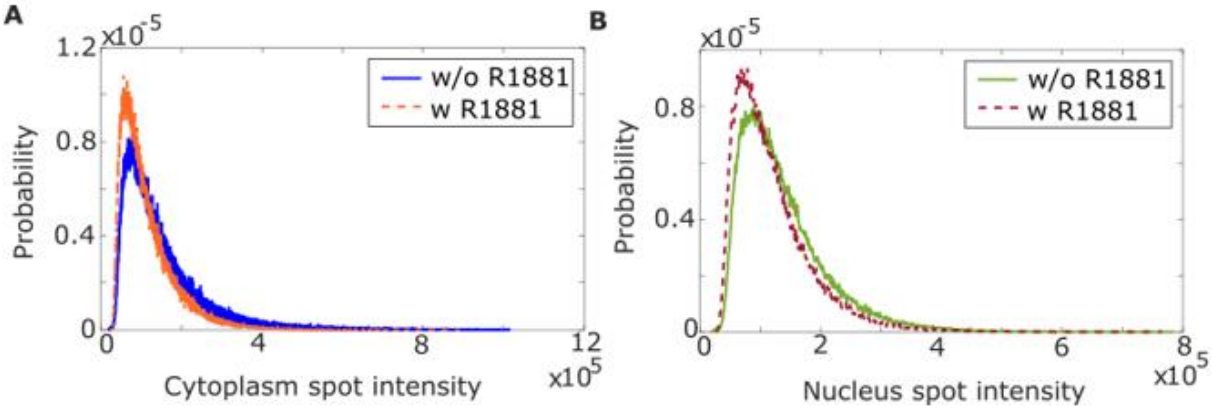

Figure 4.9 A. *KDF distribution plot of cytoplasm bright spot intensity before (w/o R1881) and after (w R1881) R1881 stimulation and* ***B.*** *KDF distribution plot of nucleus bright spot intensity before and after R1881 stimulation for AR-GFP in LNCaP cells imaged with a 40mW 488nm HILO intermediate-narrowfield beam with a (256x256)ROI at 20ms exposure.*

The spots stoichiometry method using 3 frames was used to characterise the stoichiometry of this data. This was because images were taken at 20ms exposure, this was not fast enough for single molecules to be tracked. Therefore, track information would not have been useful. Stoichiometry was instead determined by dividing the initial intensity of each bright spot by the I_{single} value, the intensity of a single molecule prior to it photobleaching. This ratio yielded an estimate for the stoichiometry. The stoichiometry data was not normally distributed, therefore statistical tests were run on the log distribution of the data. Additionally, since different samples and different conditions were used, an independent sample statistical test was used to test the difference in stoichiometry means between samples given R1881 and not given R1881.

The mean cytoplasm stoichiometry before R1881 stimulation, for n_s=307 bright spots, was 3.1±0.3 (figure 4.10B). The peak of the KDF cytoplasm stoichiometry before R1881 stimulation was 2.3±1.5 (figure 4.10A). The mean cytoplasm stoichiometry after R1881 stimulation was, for n_s=459 bright spots, 3.6±0.3 (figure 4.10B). The peak of the KDF cytoplasm stoichiometry after R1881 stimulation was 3.1±1.3 (figure 4.10A). Upon running an independent sample t-test at the 5% significance level on the log distribution of cytoplasm stoichiometry before and after R1881 stimulation, we obtain a p value less than 0.05 (figure 4.10B). This indicates that the mean stoichiometry in the cytoplasm was significantly higher at the 5% significance level after the R1881 stimulation. The mean cytoplasm stoichiometry values before and after R1881 stimulation are quite similar so further analysis was conducted to verify the difference between them. The median cytoplasm stoichiometry before R1881 stimulation was 2.8 and was 3.4 after stimulation. An independent sample Mann Whitney U test at the 5% significance level was run on the cytoplasm stoichiometry comparing pre and post R1881 stimulation stoichiometry and a p value less than 0.05 was obtained. This indicates a significant difference at the 5% level in the median stoichiometry pre and post R1881 stimulation.

The mean nucleus stoichiometry, for n_s=86 bright spots, before R1881 stimulation was 2.3±0.2 (figure 4.10D). The peak of the KDF nucleus stoichiometry before R1881 stimulation was 1.6±1.1 (figure 4.10C). The mean nucleus stoichiometry, for n_s=66 bright spots, after R1881 stimulation was 3.7±0.3 (figure 4.10D). The peak of the KDF nucleus stoichiometry after R1881 stimulation was 3.3±2.3 (figure 4.10C). After running an independent sample t-test at the 5% significance level on the log distribution of these data, we obtain a p value less than 0.05 (figure 4.10D), showing that the mean stoichiometry in the nucleus significantly increased at the 5% significance level post R1881 stimulation. In the nucleus the stoichiometry almost doubled, indicating dimerization of the molecules.

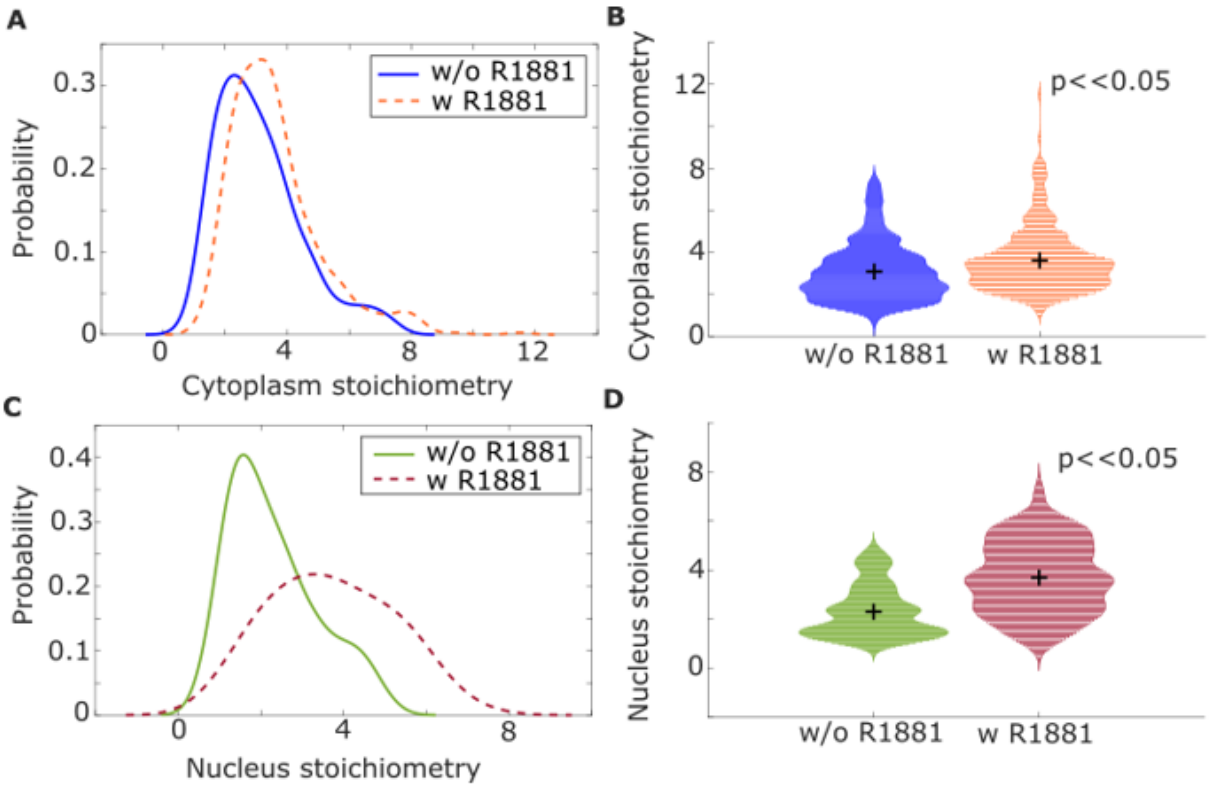

Figure 4.10 A. *KDF distribution plots of cytoplasm stoichiometry before (w/o R1881) and after (w R1881) R1881 stimulation and* ***B.*** *Violin plots of cytoplasm stoichiometry before and after R1881 stimulation for multiple cells indicating a p<<0.05 after running an independent sample t-test at the 5% significance level between the log distribution of the w/o R1881 and w R1881 stoichiometry data and* ***C.*** *KDF distribution plots of nucleus stoichiometry before and after R1881 stimulation and* ***D.*** *Violin plots of nucleus stoichiometry before and after R1881 stimulation indicating a p<<0.05 between the w/o R1881 and w R1881 conditions for fluorescence images of AR-GFP in LNCaP cells taken using a 40mW 488nm HILO intermediate-narrowfield beam with a (256x256)ROI at 20ms exposure.*

4.3.3.2 Capturing AR-GFP in LNCaP cell membrane using a TIRF beam

Images of AR-GFP in LNCaP cells were taken using a 40mW 488nm intermediate-narrowfield beam at a TIRF angle, excitation incident angle above 62°, with a (256x256)ROI at 20ms exposure (figure 4.11). Intensity and stoichiometry were characterised before and after stimulation by R1881.

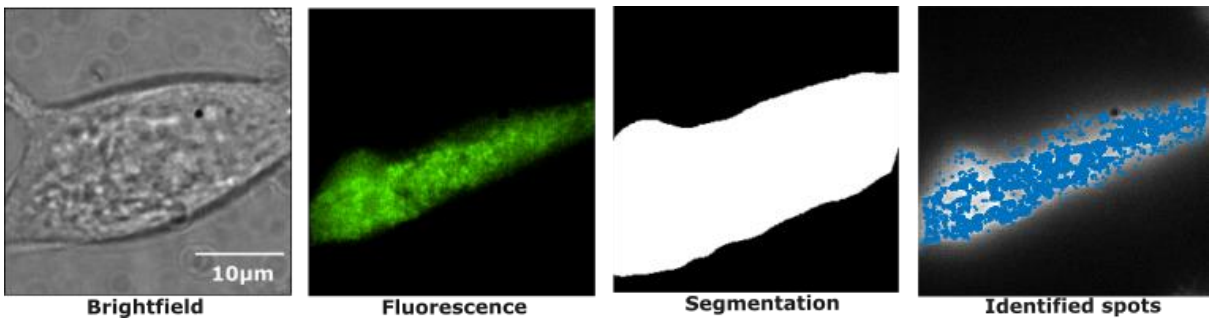

Figure 4.11 *Brightfield image of a LNCaP cell and fluorescence image of AR-GFP in the cell, taken using a TIRF 40mW 488nm intermediate-narrowfield beam at 20ms exposure with a (256x256)ROI, and the segmentation mask and the bright spots identified by the MATLAB tracker function.*

After running the tracker function on the cell images, single molecule intensity, for N=19 cells, before R1881 stimulation was 87400±72400 and was, for N=19 cells, 78100±51300 after stimulation (figure 4.12).

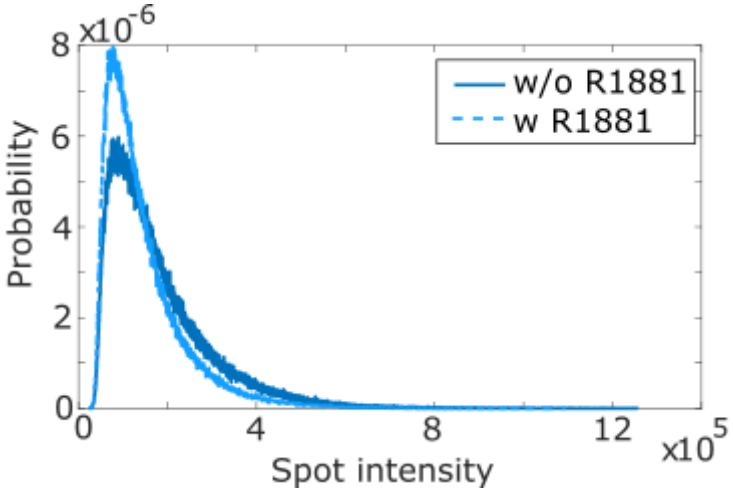

Figure 4.12 *KDF distribution plot of spot intensity before (w/o R1881) and after (w R1881) R1881 stimulation for fluorescence images of AR-GFP in LNCaP cells taken with a 40mW 488nm TIRF intermediate-narrowfield beam at 20ms exposure with a (256x256)ROI.*

The spots stoichiometry method using 3 frames was used to characterise to stoichiometry of this data. Again, this was because images were taken at 20ms exposure, this was not fast enough for single molecules to be tracked. Therefore, track information would not have been useful. Stoichiometry was instead determined by dividing the initial intensity of each bright spot by the I_{single} value, the intensity of a single molecule prior to it photobleaching. This ratio yielded an estimate for the stoichiometry.

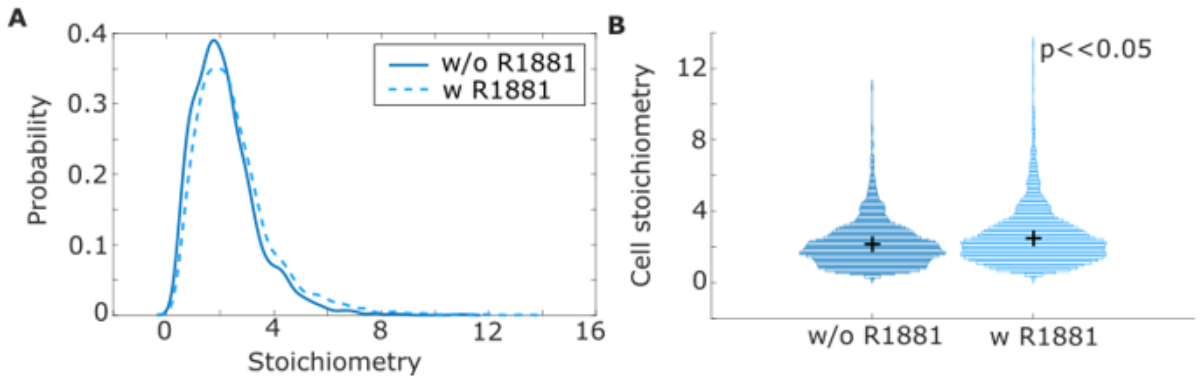

Figure 4.13 A. *KDF distribution plots of cell stoichiometry before (w/o R1881) and after (w R1881) R1881 stimulation and* ***B.*** *Violin plots of cell stoichiometry before and after R1881 stimulation for multiple cells indicating a p<<0.05 after running an independent sample Mann-Whitney U test at the 5% significance level between the w/o R1881 and w R1881 conditions for fluorescence imaged of AR-GFP in LNCaP cells taken using a 40mW 488nm TIRF intermediate-narrowfield beam and a (256x256)ROI at 20ms exposure.*

The mean stoichiometry before R1881 stimulation, for n_s=1951 bright spots, was 2.2±0.3 (figure 4.13B). The peak of the KDF stoichiometry before R1881 stimulation was 1.8±0.9 (figure 4.13A). The mean stoichiometry after R1881 stimulation, for n_s=3238 bright spots, was 2.5±0.3 (figure 4.13B). The peak of the KDF stoichiometry after R1881 stimulation was 1.8±1.2 (figure 4.13A). Despite these means being quite close in value before and after stimulation, there were differences in stoichiometry before and after addition of R1881 and this was shown by the results of an independent sample statistical test ran on the data and an analysis of the median and range values and log distribution of each dataset. Firstly, the median stoichiometry before R1881 stimulation was 1.9 and the range was 10.6, after R1881 stimulation the median was 2.2 and the range was 12.9. An independent sample Mann-Whitney U test at the 5% significance level was ran on the datasets before and after R1881 stimulation and a p value less than 0.05 (figure 4.13B) was obtained indicating a significant difference between the stoichiometry median before and after R1881 stimulation at the 5% significance level. Upon observing the log distribution of each dataset (figure 4.14), we can see that stoichiometry is indeed higher

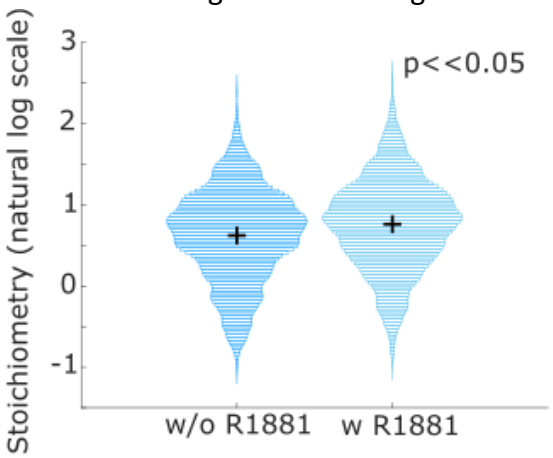

Figure 4.14 *Violin plots of log distribution stoichiometry before (w/o R1881) and after (w R1881) R1881 stimulation indicating a p<<0.05 after running an independent sample t test at the 5% significance level for fluorescence imaged of AR-GFP in LNCaP cells taken using a 40mW 488nm TIRF intermediate-narrowfield beam and a (256x256)ROI at 20ms exposure.*

after R1881 stimulation (w R1881). This is verified by obtaining a p value less than 0.05 after running an independent sample t-test at the 5% significance level on the log distribution stoichiometry before and after R1881 stimulation.

The molecules at the cell membrane did not dimerize as they did in the nucleus and cytoplasm, but the spread of the data indicates that higher stoichiometry values were found following R1881 stimulation, possibly pointing to AR-GFP clusters. Further analysis was conducted to assess if these stoichiometry values really were different. Time post TNF-α stimulation was allotted into five bins with multiple cells in each time bin and was plotted against stoichiometry (figure 4.15). The plots also include the stoichiometry pre stimulation for comparison.

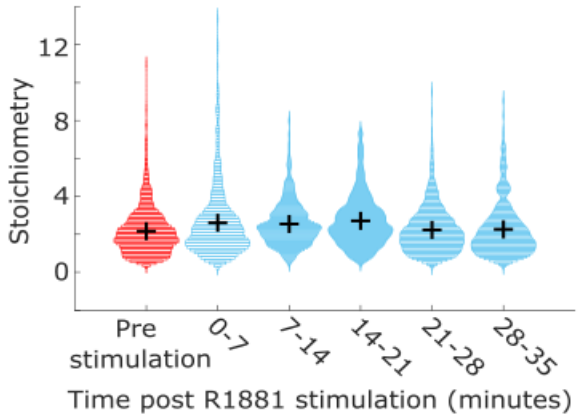

Figure 4.15 *Violin plots of cell stoichiometry post R1881 stimulation (in minutes) and average cell stoichiometry pre R1881 stimulation (inset) for fluorescence images of AR-GFP in LNCaP cells taken with a 40mW 488nm TIRF intermediate-narrowfield beam with a (256x256)ROI and 20ms exposure.*

The average stoichiometry within standard error was plotted pre stimulation and in the five allotted bins after stimulation (figure 4.16) for multiple cells in each time bin. The graph indicates the significance between the stoichiometry pre stimulation and post stimulation (in minutes). The cell stoichiometry significantly increased at the 2.5% significance level from 1.8±0.9 pre-stimulation to 2.6±0.06 in the first 7 minutes following stimulation by R1881. Upon running an independent sample Mann-Whitney U test at the 2.5% significance level between

these conditions, we obtain a p value of 1.4e-06. Then, for approximately 14 minutes, the stoichiometry fluctuated slightly before dropping back to levels of those pre-stimulation.

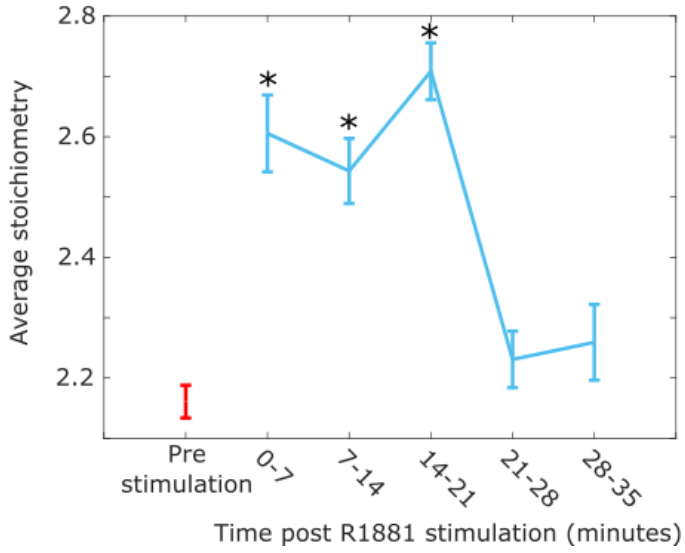

Figure 4.16 *Errorbar plot of average stoichiometry against time post R1881 stimulation (minutes) for multiple cells in each time bin from fluorescence images of AR-GFP in LNCaP cells taken with a 40mW 488nm TIRF intermediate-narrowfield beam at 20ms with a (256x256)ROI. The plot indicates the significant difference between stoichiometry pre-stimulation and at each time bin post R1881 stimulation from independent sample Mann-Whitney U tests ran at the 5% significance level ran between them.*

4.3.4 Conclusion

After using HILO microscopy to image AR-GFP in LNCaP cells before and after R1881 stimulation, it was observed that mean AR-GFP stoichiometry in the nucleus significantly increased from 2.3±0.2 molecules before stimulation to 3.7±0.3 molecules after stimulation (figure 4.10D). This significant increase to nearly double the number of molecules in a cluster following stimulation clearly matches what is written in literature. That is, upon stimulation AR enters the nucleus and homodimerises (Bennett et al., 2010). Not only are these results further proof of the sensitivity of the HILO/TIRF microscope to capture biological activity of transcription factors *in vivo,* but the results also further support the claim that clustering of transcription factors is a mechanism that facilitates transcription following extracellular stimulation.

HILO microscopy also revealed the mean number of AR-GFP molecules in the cytoplasm of LNCaP cells significantly increasing from 3.1±0.3 before R1881 stimulation to 3.6±0.3 after stimulation (figure 4.10B). AR typically forms homodimers (Bennett et al., 2010), however there is evidence that it can heterodimerise with the nuclear testicular receptor 4 (TR4) (Lee et al., 1999) and the oestrogen receptor α (ERα) isoform (Zhou et al., 1994). This may explain

why there is an increase in stoichiometry from clusters of approximately 2 or 3 molecules in size to clusters of approximately 3 or 4 molecules in size; increases to even numbers of AR-GFP molecules point to homodimerisation while increases to odd numbers point to heterodimerisation.

The mean AR-GFP stoichiometry in the cell membrane was 2.2±0.3 prior to R1881 stimulation and was 2.5±0.3 following stimulation. After running statistical tests, it was shown that this was a significant increase (figure 4.13B). This may suggest that the AR-GFP dimers increased from 2 prior to simulation to 3 or 4 after stimulation. Upon closer inspection of stoichiometry before stimulation and up to 35 minutes following stimulation, it was revealed that there were clusters of between 5-12 molecules in size present (figure 4.15). Further analysis indicated that AR-GFP stoichiometry at the cell membrane significantly increased from 1.8±0.9 molecules before stimulation to values fluctuating around 2.6±0.06 molecules in the 21 minutes after stimulation by R1881. After this, stoichiometry returned to levels the same as those before stimulation (figure 4.16). This shows that for a period after stimulation, clusters of AR dimers travelled to the cell membrane before dissipating or returning to other areas of the cell. Akin to the results obtained after imaging RelA-GFP in U2OS cells, this further evidences the clustering mechanism of transcription factors to facilitate transcription following stimulation by extracellular materials, such as R1881 or TNF-α. Additionally, this supports literature that suggests that AR is active at the cell membrane (Cinar et al., 2007; Ding et al., 1998; Nakhla et al., 1990) following cellular stimulation.

4.4 Chapter conclusion

The HILO/TIRF microscope was designed to capture the mechanisms of single molecules, such as transcription factors and proteins, within live cells. After successfully demonstrating that the microscope could be used to capture clusters of the transcription factor Mig1 within budding yeast cells with the same stoichiometry as had been initially evidenced (Wollman et al., 2017), the next step was to use the microscope to capture the dynamics of transcription factors in mammalian cells.

The behaviour of two transcription factors within live cells was captured, these were RelA-GFP in U2OS cells and AR-GFP in LNCaP cells.

RelA stoichiometry was shown to significantly increase in the nucleus of U2OS cells stimulated with TNF-α. The average number of molecules increased from around 2 molecules before stimulation to almost 3 molecules after stimulation. Additionally, some molecules formed clusters of approximately 8-16 molecules in size. These results demonstrate that RelA homodimerised and heterodimerised with p50 in response to the TNF-α stimulation. Not only do these results support the proof of concept that the HILO/TIRF microscope is sensitive to single molecules but they also support evidence that transcription factors form clusters as a mechanism to facilitate intracellular responses.

AR stoichiometry significantly increased in both the cytoplasm and nucleus of LNCaP cells stimulated with R1881. The HILO/TIRF microscope captured the homodimerisation of the AR-GFP molecules following stimulation when using HILO angles while TIRF microscopy was able to reveal AR-GFP average stoichiometry significantly doubling at the cell membrane for a period following R1881 stimulation before returning to pre-stimulation levels after approximately 21 minutes. These results support evidence that the transcription factor AR is not only active in the nucleus following stimulation by androgen hormones but is active at the cell membrane too.

Chapter 5 – Gravityscope and SUGAR (Saccharomyces cerevisiae Uptake of Glucose Applying Real-time imaging)

5.1 Introduction

This chapter outlines work carried out with five other students at Newcastle University to design, build and test a microscope and microfluidic syringe pump. The system was named Gravityscope and was built as part of the SUGAR (Saccharomyces cerevisiae Uptake of Glucose Applying Real-time imaging) project for the European Space Agency (ESA) 2022 *Fly Your Thesis* Program. The project was sponsored by ESA, the UK Space Agency (UKSA) and the Newcastle University Doctoral College Enhancement Fund.

Gravityscope was specifically designed to withstand vibrations experienced during a parabolic flight, offering microgravity (~0.01g) and hypergravity (1.8-2g) conditions. Vibration-resistance performance was tested on the ground by placing Gravityscope atop a centrifuge and on a van to characterise microscope stability in response to vibration. Yeast strains CEN.PK 113-7D and S288C were compared against each other in the lab for adherence with concanavalin A and uptake of fluorescent glucose 2-NBDG. After initial testing, Gravityscope was used during The 79th ESA Parabolic Flight Campaign (PFC) on board a microgravity and hypergravity flight to take images of yeast samples while they were injected with 2-NBDG. Gravityscope performed well during flight and was used to capture sample images during microgravity and hypergravity stages. The system would work well for future abnormal gravity experiments and in other extra-laboratory environments.

5.1.1 Cell signalling in abnormal gravity conditions

The SUGAR (Saccharomyces cerevisiae Uptake of Glucose Applying Real-time imaging) project aim was to study cell signalling transduction in abnormal gravity conditions, hypergravity (1.8-2g) and microgravity (~0.01g). It has been shown that cell signalling is severely affected by microgravity, including in areas such as the human immune system (Chakraborty et al., 2018; Hughes-Fulford, 1991; Manti, 2006; Shi et al., 2021; Wise et al., 2005), metabolism (Hughes-Fulford, 1991; Hughson et al., 2016; Kondo et al., 2021; Li et al., 2018; Loomer, 2001; Manti, 2006; Shi et al., 2021; Strollo and Vernikos, 2021; Thiel et al., 2021) and in microorganisms such as yeast (Hammond et al., 2017; Nislow et al., 2014; Roy et al., 2015; Sheehan et al., 2007). However, it remains unclear if the cell signalling process itself is impacted by gravity or if the changes in cell signalling are a by-product of the complex changes experienced by cells in microgravity.

The NASA ARTEMIS missions and the ESA 2025 vision aim to see the return of human footfall on the moon by 2025 and further aims to land humans on Mars. Therefore, it is important to understand the impact of long-duration microgravity exposure on living organisms. It takes approximately 3 days for a typical rocket to reach the Moon from Earth and approximately 7-9 months to reach Mars. This extended period of time in a microgravity environment can have adverse effects on astronaut health, including on bone density (Arfat et al., 2014), immune system (Blum et al., 2000; Friedrich et al., 1996; Lang et al., 2010; "Multi-function Light Microscopy Module for the International Space Station," 2001; Strauch et al., 2010) and metabolism (Blum et al., 2000; Corydon et al., 2016; Kahle et al., 2011; Lang et al., 2010; Pache et al., 2010; Pan et al., 2012; Strauch et al., 2010; Thiel et al., 2019; Toy et al., 2012). Longer and further-out spaceflight missions will also require new self-sufficiency and miniaturisation technologies to reduce the cost and weight of carrying cargo to space.

Synthetic biology is a process whereby microorganisms are used to grow medicine and food products. This is a useful technology for space travel as it does not require very much starting material to be transported and bioreactors can be used to scale up growth processes. Yeast has already been shown to work well in synthetic biology processes, including to manufacture medicines such as morphine (Williams et al., 2018), penicillin (Awan et al., 2017), the potential anti-cancer drug noscapine (Li and Smolke, 2016) and an angina treatment breviscapine (Liu et al., 2018). Yeast has also been used to produce haemoglobin for cultured meat (L. Liu et al., 2014).

Furthermore, yeast is an invaluable model system for studying biological processes in human cells due to it being relatively quick to grow, with a doubling time of just 2 hours compared to 2 days for mammalian cells (U2OS), it is robust and its entire genome has been mapped since 1996 (Mewes et al., 1997).

5.1.2 Microscopy in extra-laboratory environments

Microscopy can take on many forms and can be used in many different environments and conditions, including under water (Dubay et al., 2022; MacNeil et al., 2021; Mallery et al., 2021; Mullen et al., 2020; Ramirez et al., 2022), in icy conditions (Lindensmith et al., 2016), in the presence of a super-conducting magnet (Meng et al., 2019) and in abnormal gravity (Blum et al., 2000; Corydon et al., 2016; Edgett et al., 2012; Friedrich et al., 1996; Huang et al., 2020; Lang et al., 2010; Neelam et al., 2021; Own et al., 2022; Pache et al., 2010; Pan et al., 2012;

Strauch et al., 2010; Thiel et al., 2019; Toy et al., 2012). There have only been 16 microscopes utilised on abnormal gravity platforms.

There are various platforms which offer microgravity and hypergravity environments. Some platforms such as Drop Towers, Space Shuttles and the International Space Station (ISS) offering only microgravity conditions. Others such as Parabolic Flights, sounding rockets and Random Positioning Machines (RPMs) offering both hypergravity and microgravity conditions. Each platform meets an experimenters needs differently.

5.1.2.1 Microscopy on a random positioning machine (RPM)

A Random Positioning Machine (RPM) allows 3D rotation at random speeds and directions through the use of independent motor drivers (van Loon, 2006). These can simulate microgravity or hypergravity. However, a disadvantage of RPMs is that samples sometimes experience residual gravity whereby the sample is not entirely in microgravity, ergo the effects of Earth gravity still apply.

A digital holographic microscope (DHM) (Goodman and Lawrence, 2004; Schnars and Jüptner, 1994) uses a coherent lightsource, such as a laser, to illuminate a sample, but instead of creating a projected image of the sample, it creates a hologram. The image-forming lens that is usually found in optical microscopy is replaced with a computer which uses an algorithm to numerically reconstruct an image of the sample. DHM has faster frame rates when compared to confocal microscopy and increased depth of field (Farthing et al., 2017). A DHM with a 650nm laser source was positioned on the *Deutsches Zentrum für Luft- und Raumfahrt* (DLR, German Space Agency) RPM to image actin-GFP in C2C12 mouse myoblast cells (Pache et al., 2010).

The RPM at the Microgravity Simulation Support Facility (MSSF) at the NASA Kennedy Space Center was used to test performance of a microscopy setup consisting of a Dino-Lite Edge Series microscope fitted with a WF-10 WIFI adapter for live-streaming capabilities (Neelam et al., 2021). Additionally, a DHM was combined with a superconducting magnet (SM) and fitted to an RPM. The SM generated different magnetic fields which cancelled-out the gravitational force of biological samples resulting in samples levitating in simulated microgravity. Long-term and real-time cell division of osteoblasts under microgravity conditions could be observed (Pan et al., 2012).

5.1.2.2 Microscopy on drop towers

Experiments in drop towers experience weightlessness as they are in freefall from the top of the tower to the padded bottom. The *Zarm Fallturm* (drop tower) in Bremen, Germany is 146m tall and is used by ESA scientists to conduct microgravity experiments. The tower offers approximately 4.74 seconds of microgravity in a 110m freefall at 10^{-6}g. The *2.2 second* drop tower at NASA Glenn Research Centre offers 2.2 seconds of microgravity at 10^{-3}g during a 24m drop. Samples in drop towers must be fully self-contained and able to be without the experimenter for approximately 90 minutes before the drop to allow the air in the tower to be vacuumed to prevent vibrations during the drop and for 20 minutes after the drop to allow the tower to be refilled with air before human entry.

An advantage of drop towers includes a microgravity environment very close to that in space. However, the timeframe for this environment is extremely short. Furthermore, there is not much opportunity for human interaction with the experiment once it is in the tower.

There have been no microscopes used in drop towers to date. Future work could focus on developing a microscope which is fully automated and samples that are either fixed or fully self-sufficient so it can be used during a drop when experimenters cannot interact with it.

5.1.2.3 Microscopy on parabolic flights

Experiments are attached within a plane which performs parabolic manoeuvres, flying up and down, in z (m) at angles of approximately $45°$. Advantages of parabolic flights include the ability for experimenters to interact with their experiments and to conduct human experiments, rather than just experiments on samples. Furthermore, intervals of microgravity are much longer than those provided by drop towers.

Four microscopes in total have been modified for and used on parabolic flights which includes the Leica DMIL (Bensheim, Germany) brightfield microscope fitted with an AVN Security camera (Groß-Umstadt, Germany) to take real-time 5 pictures/second DVD movies of migrating immune cells for the ESA PFC 2008 (Lang et al., 2010). Additionally, a brightfield, four-channel fluorescence microscope, BiozeroBZ-8000 (Keyence, Osaka, Japan), was attached to a rack dampened with silicone for the ESA PFC in 2006 to observe the beating pattern of flagellum (Strauch et al., 2010).

A confocal laser spinning disc microscope involves using an opaque disk filled with pinholes which is spun at high speeds during imaging. The pinholes scan across the sample to create an image. An advantage of this microscopy method is that it reduces photodamage to samples. Bespoke microscopes like the confocal laser spinning disc microscope, FLUMIAS, and a DHM, have also been used on parabolic flights to image cytoskeletal changes in stable transfected human follicular thyroid carcinoma cells (FTC-133) (Corydon et al., 2016) and C2C12 mouse myoblast cells (Pache et al., 2010) respectively.

5.1.2.4 Microscopy on sounding rockets

Experiments can also be launched in a sounding rocket, flying up to 75km high, providing approximately 13 minutes of microgravity at values of 10^{-6}g. At launch, experiments experience 12g for approximately 45 seconds. Advantages of sounding rockets include the extended periods of microgravity compared to those for drop towers and parabolic flights. Additionally, microgravity values are very similar to those in space. However, unlike parabolic flights, the rocket does not allow experimenters to interact closely with their experiment as it occurs.

The FLUMIAS, a confocal laser spinning disc microscope fitted with four different excitation wavelengths and a temperature-controlled fixation unit to allow chemical fixation of cells under investigation at any point during flight, flew on the TEXUS 52 sounding rocket (Corydon et al., 2016).

5.1.2.5 Microscopy on the space shuttle

The Space Shuttle was a reusable low-earth-orbit (LEO) spacecraft operated by NASA from 1981-2011, its official name being the Space Transportation System (STS). An advantage of the STS for experiments was the extended periods of real microgravity experienced in LEO.

Two STS missions carried microscopes, namely the STS-65, carrying the NIZEMI in 1994, and the STS-95 carrying the CODAG in 1998. NIZEMI included a centrifuge plate fitted to an Axiskop Zeiss microscope (Friedrich et al., 1996). The Cosmic Dust Aggregation Experiment (CODAG) involved the observation of dust particle motion using stereo long-distance microscopes with high-speed CCD cameras (Blum et al., 2000).

5.1.2.6 Microscopy on the ISS

The ISS provides a real microgravity, 10^{-6}g, environment for experiments for extended periods. Four microscope facilities have been designed and built especially for long-term use on the ISS including the Light Microscopy Module (LMM), launched in 2000, the BIOLAB facility, launched in 2008, the BioServe Microscopy Platform (BSMP), launched in 2016 and 2018, and the Nanoracks Microscope 3 launched in 2020. Two more microscopes, the FLUMIAS-DEA and the Mochii ISS-National Laboratory (NL), were built on the ground and sent to the ISS for short-term missions.

NASA LMM is a light microscope which can be remotely operated and includes features such as brightfield, darkfield, confocal microscopy, fluorescence microscopy, spectrophotometry and optical tweezers. The LMM has been used for experiments such as Advanced Colloids Experiments, Constrained Vapour Bubble experiments and Conduct Macromolecular Biophysics and Protein Crystal Growth experiments.

The BIOLAB facility is on the ISS European Columbus Module, the left part of the facility is fully automated while the right part is manually operated by astronauts in orbit. Biological and biochemical samples are housed in experiment-specific containers and in-orbit analyses of samples can be carried out by means of microscope.

The BSMP on the ISS produces high-definition microscopy images and videos of experiments which can be downlinked to Earth for near-real-time observation. The platform consists of three modular components which can be changed according to hardware updates and modernisation. These include the BioServe Microscope, a Nikon Eclipse TS100 allowing brightfield and phase-contrast microscopy, the SABL camera, an Allied Vision GX1910C (1920x1080), 60FPS camera and the SABL smart incubator.

The Nanoracks is a company offering access to a commercial LEO lab on the ISS. In 2020, Nanoracks delivered several systems to the ISS including the Nanoracks Microscope 3, a USB light microscope capable of 20-240X magnification.

Space Tango is a company specialising in research and development in space which launches experiments to a facility on the ISS. The FLUMIAS-DEA microscope was launched to the ISS Space Tango facility. The FLUMIAS-DEA is a real-time 3D high-resolution microscope which is just 7litres in volume and weighs only 6.5kg. Features of the microscope include LED fluorescence with excitation wavelengths of 405,475,550,640nm, an autofocus system, 40X

magnification and a 2TB SSD internal memory capacity. Images were produced automatically without astronaut intervention but an option for manual operation was also included (Thiel et al., 2019).

The Mochii ISS-NL was the first scanning electron microscope capable of providing high-resolution images on the ISS launched to the ISS via the NASA Cygnus and Dragon space vehicles and was used to image ALH84001 Martian meteorite (Own et al., 2022).

5.1.2.7 Summary of microscopy in microgravity and hypergravity

Table 3 provides a brief outline of all microscopes used on microgravity and hypergravity platforms where the third column refers to the microgravity platform the microscope experiment was designed for and used on. The sixth column outlines unique capabilities of the particular microscope.

The table includes the Mars Hand Lens Imager (MAHLI), the magnifying hand lens for the Mars Rover which is used to take microscopic images of minerals and structures in Mars rocks and soil (Edgett et al., 2012). Although not a microscope of traditional definition, the MAHLI can be used to produce images of resolution 13.9μm/pixel so I have added it to the exhaustive review of existing microscopes used in microgravity and hypergravity conditions.

	Year	**0g platform**	**0g category**	**Microscope type**	**Unique capabilities**
NIZEMI (Friedrich et al., 1996)	1994	STS-65	Space	Commercial (Zeiss)	Darkfield Thermal control of samples (14-38°C)
CODAG (Blum et al., 2000)	1998	STS-95	Space	Commercial	Stereo long-distance
LMM ("Multi-function Light Microscopy Module for	2000+	ISS	Space	Bespoke	Darkfield Differential interface contrast Dynamic light scattering Full-field static light scattering

the International Space Station," 2001)					Spectrophotometry Optical tweezers Micro-rheology
BiozeroBZ-8000 (Strauch et al., 2010)	2006	Zero-G Parabolic Flight	Flight	Commercial (Keyence)	4 channel fluorescence 10-180X mag.
BIOLAB	2008+	ISS	Space	Bespoke	Incubator Darkfield Phase contrast
ESA PFC 2008 (Lang et al., 2010)	2009	Zero-G Parabolic Flight	Flight	Commercial (Leica DMIL)	Incubator
DHM-RPM (Pache et al., 2010)	2010	RPM	Ground	Bespoke	Laser fluorescence
DHM-RPM-PFC (Toy et al., 2012)	2010	RPM Zero-G Parabolic Flight	Ground Flight	Bespoke	Superior mag. and NA without vibration dampening Numerical autofocusing 13.21kg
DHM-SM (Pan et al., 2012)	2012	SM, JASTEC	Ground	Bespoke	Laser fluorescence
MAHLI (Edgett et al., 2012)	2012	Mars Rover	Mars	Bespoke	Portable, automatic, white and UV light capabilities.
FLUMIAS (Corydon et al., 2016)	2016	Zero-G Parabolic Flight	Flight	Bespoke	Confocal laser spinning disc imaging

		TEXUS 52 Sounding Rocket	Rocket		Temperature-controlled fixation unit 4 diode lasers for fluorescence Diode-pumped solid-state laser
BioServe Microscopy Platform (BSMP)	2016+	ISS	Space	Bespoke	Near real-time experiment feedback Hardware upgradeable
FLUMIAS-DEA (Thiel et al., 2019)	2018	ISS, Space Tango Facility	Space	Bespoke	4 colours for LED fluorescence Autofocus system Automatic imaging with manual capabilities Only weighs 6.5kg with containment 3D imaging
Image acquisition module (Neelam et al., 2021)	2020	RPM-NASA MSSF	Ground	Commercial (Dino-Lite)	Live streaming via WIFI Darkfield Less than 1.1kg
MochiiISS-NL (Own et al., 2022)	2020	ISS	Space	Commercial (Mochii)	Scanning electron microscope
Nanoracks Microscope 3	2020	ISS	Space	Commercial	USB microscope, 20-240X mag

Table 3 *Outline of all microscopes used on microgravity and hypergravity platforms*

5.1.3 Aims and Objectives of the SUGAR project

Glucose uptake in yeast is a model cell signalling process as it is analogous to the same process in mammalian cells. One of Team SUGAR's aims was to observe and image the impact of abnormal gravity on glucose uptake by yeast. A further aim was to build a microscope to do this. The Team SUGAR hypothesis was;

Cell signal transduction is impaired by abnormal gravity conditions

The following objectives were proposed to answer this hypothesis;

1. *To build and optimise a fluorescence microscope that will work in varying gravity conditions*

It was decided that fluorescence microscopy would be used as this was the only available option to observe the glucose uptake by the cells. An alternative option was to radioactively label the glucose however this method would have been slow, only in bulk and was not permitted in the parabolic flight campaign.

To achieve this objective, the team would build a relatively simple and inexpensive fluorescence microscope based on the opensource *Simplifying Quantitative Imaging platform Development and Deployment* (SQUID) microscope designed by Li *et al.* (Li et al., n.d.). This microscope design would be optimised to be able to withstand vibrations experienced during the parabolic flight and ensure it would be sensitive to capturing metabolic activity in yeast cells.

2. *To use the microscope to observe glucose uptake in budding yeast cells in microgravity and hypergravity*

Fluorescent glucose analogue, 2-NBDG has an emission wavelength peak of approximately 538nm (and excitation wavelength of approximately 467nm). This would be administered to *Saccharomyces cerevisiae* yeast samples via a syringe pump and microfluidic sample system built into the experimental rig. The glucose would be added during different stages of each parabola during the flight. As the glucose is added, images would be taken using the microscope outlined in objective 1.

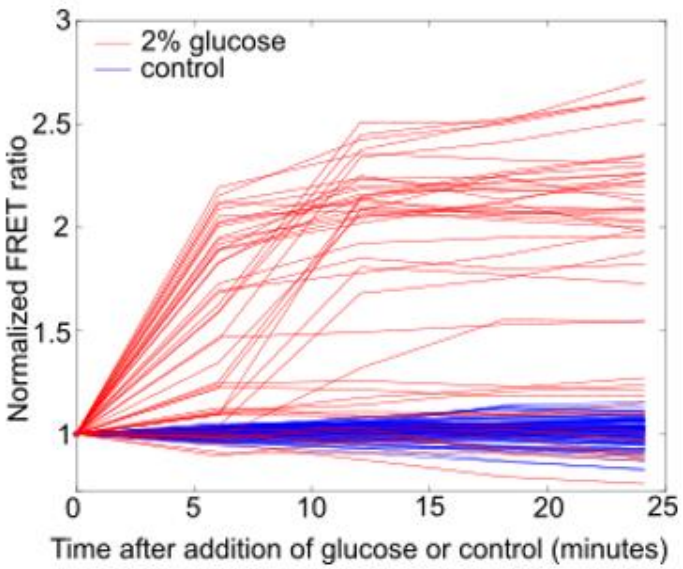

Figure 5.11 *Plot of glucose uptake vs time (in minutes) from Wollman et al. 2022*

Previous results suggested that 20 seconds (in one of the hypergravity or microgravity phases) would be enough time to observe initial glucose uptake. Figure 5.1 from (Wollman et al., 2022) is a plot of glucose uptake (in minutes) by budding yeast. The relative FRET signal increase in glucose-starved yeast cells exposed to 2% w/v glucose (red plots) or media with no glucose (blue plots) was measured and plotted against time. The plot demonstrates a 250% increase in signal from glucose uptake in the first five minutes, this is equivalent to an ~8% increase every 10 seconds. This was evidence that the 20 second time interval during a parabola would be enough time to take images during 2-NBDG injection to show glucose uptake in yeast.

5.1.4 Outline of an ESA Parabolic Flight

To explain how a parabolic flight works, it is necessary to outline how steady (level) flight is achieved (figure 5.2A-B). A plane remains level (steady flight) if the engines produce lift that is equal to the downward force created by gravity (~10ms^{-2}). Increasing lift occurs by ensuring that more air particles strike the bottom of the wings than the top of the wings (figure 5.2B). This is achieved when the angle of attack, α of the wing is increased. There is a reduction in pressure at the top of the wing and an increase in pressure at the bottom of the wing, this creates an upward force, or lift. The plane propels forward longitudinally if its thrust is greater than the drag force created by the air particles striking it. Thrust is a horizontal lift created by the propellers in the engine spinning. The airspeed is the horizontal velocity of the plane relative to the mass of the air particles striking it. At steady flight, increasing airspeed occurs by increasing thrust. When the nose of a plane shifts perpendicular to the longitudinal axis, this is referred to as increasing (or decreasing) the pitch. Pitch plays a pivotal role in a parabolic flight manoeuvre.

At the beginning of the manoeuvre the plane is at steady flight while thrust is slowly being increased. A hypergravity stage is initiated when a vertical (normal to the centre of gravity, γ) climb is created by achieving full thrust; this produces a g level of ~1.5g. The vertical velocity and pitch are increased and airspeed is reduced; this produces a g level of ~1.8g. The 0g stage of the parabolic manoeuvre occurs when pitch is nose-up 45°. The angle of attack is decreased which reduces lift while thrust is also decreased to levels just enough to overcome drag. When pitch is nose-down 45°, thrust is increased which changes the downward velocity into an upward velocity; this initiates a new hypergravity stage (Karmali and Shelhamer, 2008).

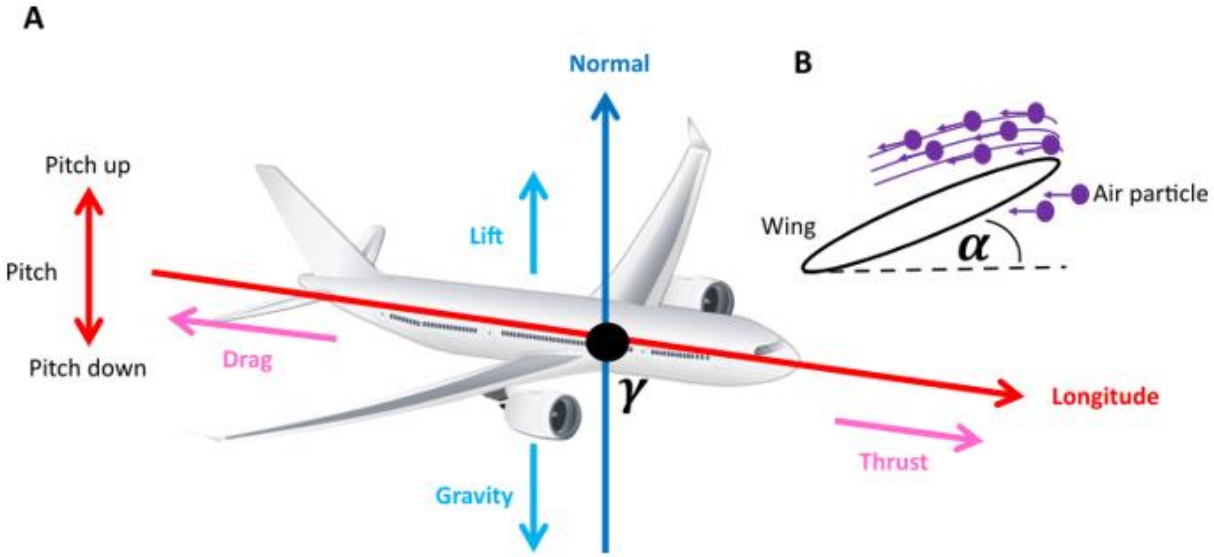

Figure 5.2 A. *A plane maintains in steady (level) flight when the engines produce lift that is equal to the downwards force of gravity and produce thrust that is greater than the drag force, created by air particles striking the plane surface.* ***B.*** *Increasing the angle of attack, α of the plane wing results in more air particles striking the bottom of the wing and less particles striking the top of the wing. This increases pressure at the bottom of the wing to levels greater than pressure at the top of the wing, creating an upward force relative to the centre of gravity, γ. Increasing the angle of attack is referred to as increasing pitch; a pitch up is created by increasing the angle of attack and a pitch is created by decreasing the angle of attack.*

A typical parabolic flight campaign conducted during the ESA Fly Your Thesis Program takes place at the Novespace facility in Bordeaux, France. The campaign lasts two weeks, the first of

which is a preparation week for experimenters to prepare samples, bolt their experiments to the plane rails and conduct any final safety checks.

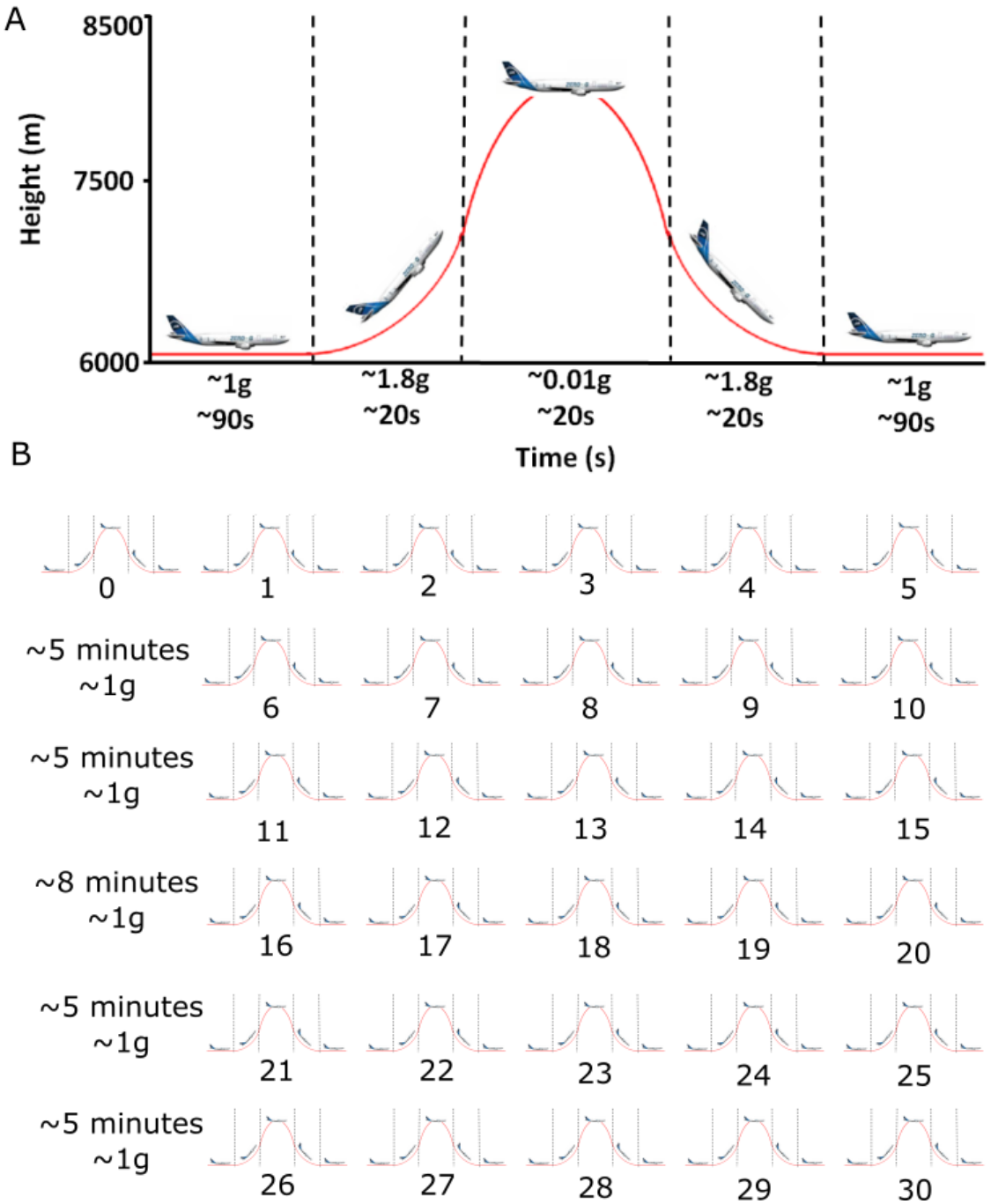

Figure 5.3 A. *Typical parabola profile of z, height (in metres) vs t, time (in seconds) for a Novespace parabolic flight indicating the five stages of each parabola, an approximate 20 second interval of microgravity, ~0.01g, sandwiched between two approximate 20 second intervals of hypergravity, ~1.8-2g and two ~90 second intervals of steady flight, ~1g, before and after. Steady flight occurred at about 6000m and the plane flew to heights of about 8500m during some parabolic manoeuvres.* ***B.*** *Typical Novespace parabolic flight sequence for all 31 parabolas per flight occurring in sets of five (six for the first set) with 5 minute (and one 8 minute) steady flight breaks between each set, each parabola from 0-30 in a set taking on the profile depicted in A.*

The second week consists of three parabolic flights on board the ESA-CNES Airbus A300 Zero-G plane. A typical flight contains 31 parabolas of z (height, in m) vs t (time, in seconds), creating a gravity (ms^{-2}) profile like that in figure 5.3A. There is approximately 1 minute 30 seconds of 1g steady flight followed by approximately 20 seconds of 1.8-2g hypergravity. Then there is approximately 20 seconds of ~0.01g microgravity followed by another hypergravity stage and another steady flight stage. Parabolas are flown in five sets of five and one set of six with break intervals of 5-8 minutes between, figure 5.3B depicts this.

5.2 Initial tests conducted on yeast strains

Samples were optimised for growth speed, cell density and speed of 2-NBDG uptake. Meanwhile, the microscope was built and imaging performance was tested in vibration conditions, including on a benchtop centrifuge and on a van. The syringe pump was the last to be built and a commercial one was used in its place for tests and practice microfluidics.

5.2.1 Testing growth conditions required for S.cerevisiae CEN.PK 113-7D and S288C strains

Three *S.cerevisiae* strains, CEN.PK 113-7D, S288C, W303, were considered for experiments (gifts from the Mislav Oreb lab in Göthe University, Frankfurt, Germany) (Schmidl et al., 2021). W303 is inherently fluorescent, thus was not useful for the SUGAR experiments as its autofluorescence would have interfered with the 2-NBDG fluorescence signal during imaging. Therefore, CEN.PK 113-7D and S288C were tested against each other for growth conditions, cell density, adherence to sample slides with Concanavalin A and 2-NBDG uptake.

5.2.1.1 Preparing petridishes

Yeast peptone dextrose (YPD) agar media (1g/mL yeast extract, 2g/mL Bacto-peptone, 2g/mL agar) with 4% glucose was microwaved on a low setting for approximately 5 minutes. 20mL of YPD agar media was pipetted into 25mL petridishes under a lit Bunsen burner. The dishes were then left to rest with the lids removed for approximately 15 minutes. When the agar was sufficiently solid, the lids were replaced and the dishes were placed upside down on the bench for a further 10 minutes. After this, scrapings from frozen CEN.PK 113-7D or S288C yeast strains were placed on the agar and the dishes were allowed to rest for another 5 minutes before dishes were sealed with Parafilm and placed in a non-shaking incubator at 30°C for two days. After this, petridishes were stored in the fridge.

5.2.1.2 Preparing overnight cultures

In each of two 5mL pop-tubes, 1mL of 2xYNB media, 800μL of autoclaved MilliQ water and 200μL of 40% w/v glucose was pipetted. Scrapings from the CEN.PK 113-7D or S288C petridishes were added to one of each pop-tube. The pop-tubes were then incubated for 15 hours, the incubation method used is outlined in the next subsection.

5.2.1.3 Incubation method

A major part of the SUGAR project was resource management and being able to make the most of facilities that were at hand. The Novespace facility provided a lab, but this was equipped with a bench, a fridge and a freezer and nothing else. Therefore, alternative solutions to the lab shaking incubator had to be found and tested to see if CEN.PK 113-7D or S288C strains grew well in them. An egg incubator was used. The interior rolling mechanism slowly rotated every 90 minutes. This incubator was used to incubate samples for tests and was used to incubate samples in the Novespace lab before flight.

5.2.2 Testing 2-NBDG uptake by S.cerevisiae CEN.PK 113-7D and S288C strains

Each parabola during the flight would offer only ~20 seconds of microgravity with two ~20 second intervals of hypergravity either side of this. Therefore, one aim was to ensure the speed of 2NBDG uptake by the yeast cells.

5.2.2.1 2-NBDG uptake according to morning culture preparation

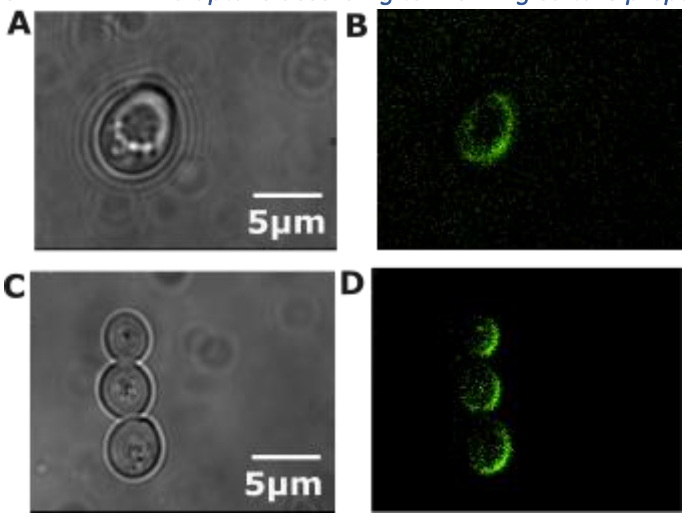

Figure 5.4 *Brightfield images of* ***A.*** *S288C and* ***C.*** *CEN.PK 113-7D budding yeast and fluorescence images of 100µM 2-NBDG uptake by* ***B.*** *S288C and* ***D.*** *CEN.PK 113-7D budding yeast cells imaged using a 488nm 5mW epifluorescence intermediate-narrowfield beam with an ND=2 filter at 50ms exposure and (512x512)ROI.*

CEN.PK 113-7D and S288C samples were prepared according to one of three conditions. The first condition involved preparing an overnight culture and placing 2-NBDG at concentration 100μM dropwise onto an agarose GeneFrame with the overnight culture before sealing the GeneFrame with the glass coverslip. The sample was left for twenty minutes prior to imaging. The second condition involved preparing a new subculture using 1mL 2xYNB, 800μL MilliQ water, 200μL non-fluorescent 40% w/v glucose and 200μL of overnight culture. The subculture was placed on an

agarose GeneFrame and 2-NBDG at concentration 100μM was added dropwise before sealing the GeneFrame with a glass coverslip and the sample was immediately imaged. The third condition involved preparing a new subculture by re-suspending the overnight culture in 1xYNB to remove the non-fluorescent glucose. The subculture was pipetted onto an agarose GeneFrame and 2-NBDG at concentration 100μM was added dropwise before sealing the GeneFrame with a glass coverslip and the sample was immediately imaged.

Samples were imaged using the HILO/TIRF microscope with a 5mW 488nm epifluorescence intermediate-widefield beam using a ND=2 filter with a (512x512)ROI at 50ms exposure. Figure 5.4A,C shows brightfield images of CEN.PK 113-7D and S288C respectively and figure 5.4B,D are fluorescence images of 2-NBDG uptake by CEN.PK 113-7D and S288C cells respectively. Since the data are from different samples and different culturing conditions were compared against each other creating non-normally distributed data, a nonparametric independent sample statistical test was used to compare data.

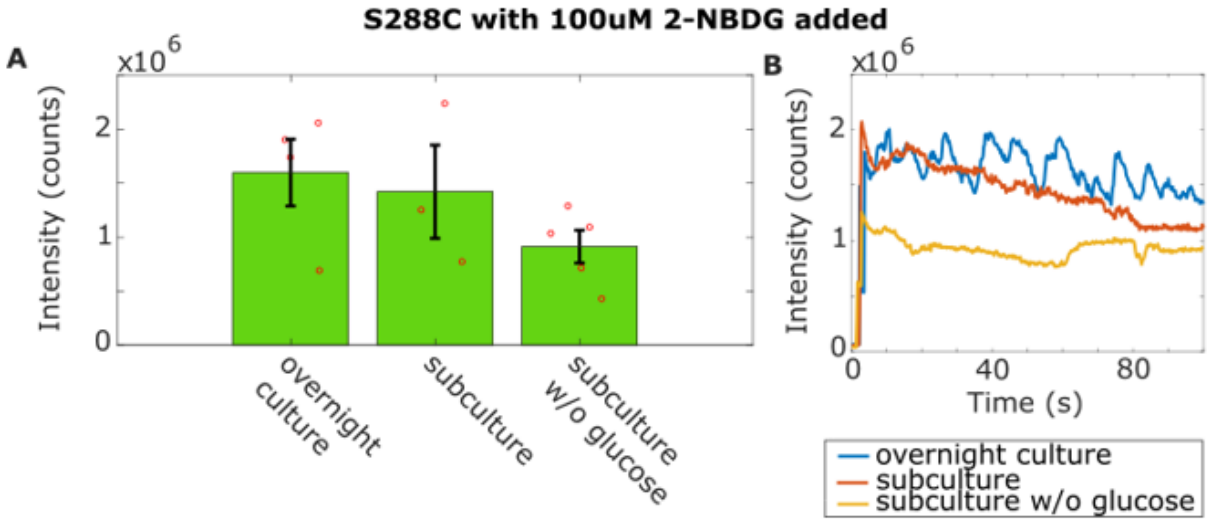

***Figure 5.5 A**. Jitterplot of background-corrected intensity for S288C cells given 100µM of 2-NBDG and **B.** Plots of background-corrected cell intensity for S288C cells given 100µM 2-NBDG from samples prepared from an overnight culture and given 2-NBDG 20 minutes prior to imaging, from a subculture given 2-NBG immediately prior to imaging and from a subculture with non-fluorescent glucose removed and given 2-NBDG immediately prior to imaging. Each curve in panel B and red point on bars in A are an average of n=4,3,5 cells for the overnight culture, subculture and subculture w no glucose conditions. From images taken using the HILO/TIRF microscope with a 5mW 488nm epifluorescence intermediate-narrowfield beam with ND=2 filter with a (512x512)ROI at 50ms exposure.*

Figure 5.5A is a jitterplot of cell intensity for fluorescence images of S288C cells (figure 5.4B) given 100μM 2-NBDG for each of the three conditions. Upon running an independent sample Mann-Whitney U test at the 5% significance level between the overnight culture condition and the subculture condition, we obtain a p value of 0.6772 and we obtain a p value of 0.1905

between the overnight culture condition and the subculture with no glucose condition. The p values between these conditions suggest that the intensity values are not significantly different across the different conditions at the 5% significance level. Therefore, for the S288C strain, cell intensity was not affected by the amount of time the cells were exposed to 2-NBDG or by removing non-fluorescent glucose.

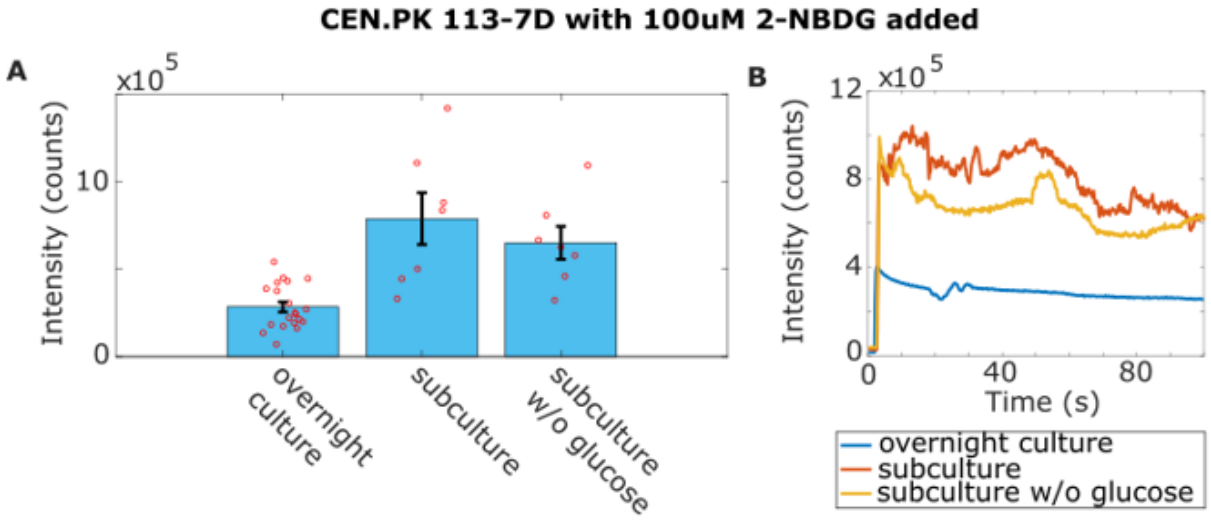

***Figure 5.6 A**. Jitterplot of background-corrected cell intensity for CEN.PK 113-7D cells given 100μM of 2-NBDG and **B.** Plots of background-corrected cell intensity for CEN.PK 113-7D cells given 100μM 2-NBDG from samples prepared from an overnight culture and given 2-NBDG 20 minutes prior to imaging, from a subculture given 2-NBG immediately prior to imaging and from a subculture with non-fluorescent glucose removed and given 2-NBDG immediately prior to imaging. Each curve in panel B and red point on bars in A are an average of n=20,7,7 cells for the overnight culture, subculture and subculture w no glucose conditions. From images taken using the HILO/TIRF microscope with a 5mW 488nm epifluorescence intermediate-narrowfield beam with ND=2 filter with a (512x512)ROI at 50ms exposure.*

Figure 5.6A is a jitterplot of cell intensity for fluorescence images of CEN.PK 113-7D cells (figure 5.4D) given 100μM 2-NBDG for each of the three conditions. Upon running an independent sample Mann-Whitney U test at the 5% significance level between the overnight culture condition and the subculture condition, we obtain a p value of 8.8e-04 and we obtain a p value of 4.6e-04 between the overnight culture condition and the subculture with no glucose condition. The p values between these conditions suggest that the intensity values are significantly different across conditions at the 5% significance level. Therefore, for the CEN.PK 113-7D strain images, cell intensity is affected by the amount of time the cells are exposed to 2-NBDG and by removing non-fluorescent glucose.

S288C cell intensity (figure 5.5B) was brighter than CEN.PK 113-7D cell intensity (figure 5.6B) for the three conditions. However, despite this, it was easier to find lone cells with the S288C strain, but the S288C samples had a lower cell density than the CEN.PK 113-7D samples,

meaning that it took a long time to find cells on the slide viable for imaging. This is time we would not have during the parabola. Therefore, it was decided that the CEN.PK 113-7D strain was more fit for purpose and further tests were carried out on this strain.

5.2.3 Tests conducted on S.cerevisiae CEN.PK 113-7D strain

It was demonstrated that CEN.PK 113-7D yeast cells had good cell density. Further tests were conducted to investigate if this strain would remain adhered to a channel slide during fluid injection and how quickly the strain took up 100μM 2-NBDG.

5.2.3.1 Choosing the correct channel slide

Three types of ibidi channel slides were tested, these were;

- 6-channel μ-Slide VI 0.1 – sterilised polymer coverslip, 1.7μL channel volume
- 6-channel μ-Slide VI 0.4 – sterilised polymer coverslip, 30μL channel volume
- 6-channel μ-Slide VI 0.5 – sterilised glass coverslip, 40μL channel volume

The channels for the VI 0.1 slide were far too narrow to work with; the syringes intended to be used were at least 1mL in volume and if a 1mL or higher volume syringe were used with the VI 0.1 slide, the speed of the flow through the channel would be too fast and cells would be more likely to tear from the channel surface.

The VI 0.4 and VI 0.5 slides both had optimal channel volumes, but the VI 0.5 slide had a glass coverslip on the bottom of each channel which was easily breakable. Therefore, the VI 0.4 slide was chosen; it was assumed that polymer, despite it having the same refractive index as the glass coverslip, would not be as delicate.

5.2.3.2 Preparing Concanavalin A channel slides

30μL of Concanavalin A 2x stock was pipetted into each channel and left to incubate at room temperature for 15 minutes. After this, each channel was washed with 30μL of 1xYNB media to remove excess Concanavalin A, then 30μL of CEN.PK 113-7D yeast culture was pipetted into each channel and the slide was again left to incubate at room temperature for 15 minutes. Lastly, the channels were washed again with 30μL of 1xYNB media to remove any non-adherent cells.

5.2.3.3 Injecting 1xYNB media during imaging

The prepped channel slide was taped to the sample stage of the HILO/TIRF microscope. PVC tubing (5.5mm inner diameter, 7mm outer diameter) was attached to the inlet and outlet ports of one of the channels. The outlet tubing was taped to a Falcon tube and the inlet tubing was

connected to a 1mL syringe. The syringe was fixed to a commercial *New Era Pump Systems Inc.* syringe pump. Figure 5.7 demonstrates the setup.

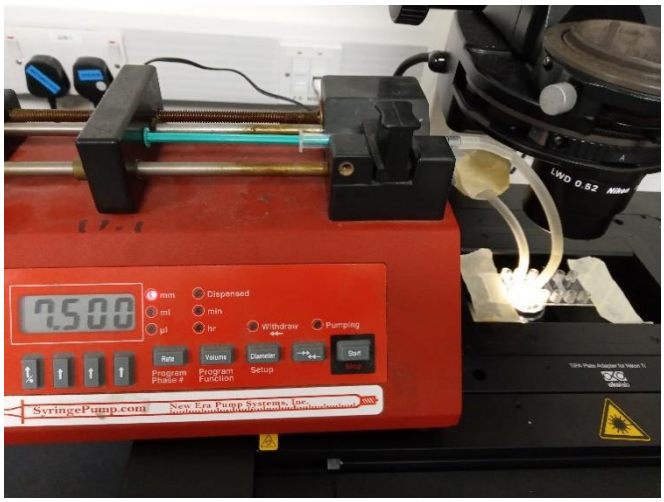

Figure 5.7 *Testing cell adherence within a channel slide using a commercial syringe pump and the HILO/TIRF microscope.*

The CEN.PK 113-7D yeast cells remained adhered during injection of 1xYNB at various speeds. Figure 5.8 shows brightfield images of the CEN.PK 113-7D cells before injection, 7.5 seconds after injection and 15 seconds after injection. As shown, the cells remained fixed in place. Cell focus changed during injection but returned to normal when fluid flow stopped.

Images were opened in ImageJ and the distance between cells between frames was measured using the multi-point tool. Multiple measurements were taken and an average was taken.

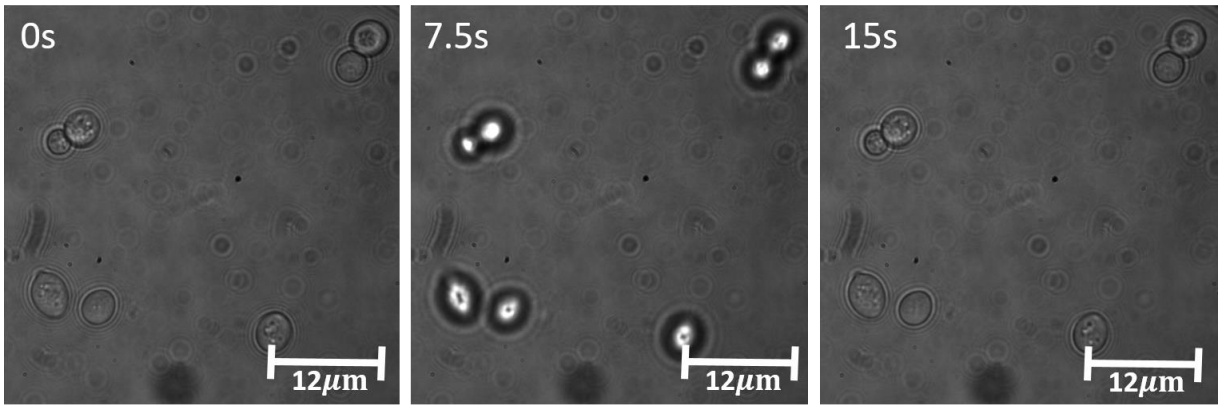

Figure 5.8 *Brightfield images of adhered CEN.PK 113-7D cells at 0, 7.5 and 15 seconds following injection of 1xYNB into the sample channel slide.*

There was an average cell shift of only 0.4±0.02μm in the lateral (x) direction after fluid injection. Therefore, the CEN.PK 113-7D cells adhered well to the channel slide after using Concanavalin A and following the procedure outlined in section 5.2.3.2. Therefore, this procedure was followed when preparing samples during the flight campaign.

5.2.3.4 Initial 2-NBDG uptake by CEN.PK 113-7D

A CEN.PK 113-7D yeast subculture was made using 1mL 2xYNB, 800μL MilliQ water, 200μL non-fluorescent 40% w/v glucose and 200μL of overnight culture. Cells were adhered to channels in a channel slide and connected to a commercial syringe pump with PVC tubing (5.5mm inner diameter, 7mm outer diameter). Images were taken using the HILO/TIRF microscope with a 5mW 488nm epifluorescence intermediate-narrowfield beam with a ND=2 filter with a (512x512)ROI at 50ms exposure. Channels were injected with 100μM 2-NBDG during imaging.

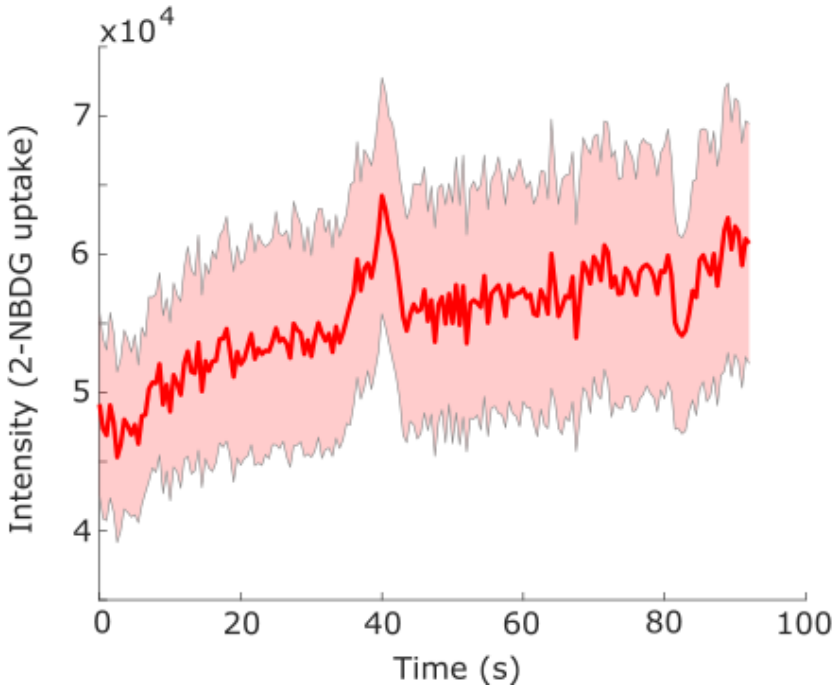

Figure 5.9 *Plot of average initial 100μM 2-NBDG uptake by CEN.PK 113-7D cells, for n=7 cells, from images taken using the HILO/TIRF microscope with a 5mW 488nm epifluorescence intermediate-narrowfield beam with ND=2 filter with a (512x512)ROI at 50ms exposure.*

The plot in figure 5.9 shows background-corrected intensity vs time, it demonstrates an increase in intensity over time for n=7 cells. The sample was injected with 100μM 2-NBDG 5.8 seconds before time zero on the plot. Average cell intensity 5.8 seconds after injection (time 0) was 49200±14900 and was 52000±7300 20 seconds after this (time 20), this is approximately a 6% increase. Therefore, 20 seconds would be enough time to observe increases in intensity when injected with 2-NBDG during a parabola.

5.3 Gravityscope: microscope design and test performance

The microscope built for the SUGAR project was based on the opensource *Simplifying Quantitative Imaging platform Development and Deployment* (SQUID) microscope designed by Li *et al.* (Li et al., n.d.). This was a relatively simple and inexpensive design when compared to others. Additionally, the design was comparatively small and could be transported within a protective box. The microscope built by Team SUGAR was modified for vibration resistance

performance on board a parabolic flight offering hypergravity and microgravity and was thus named Gravityscope.

5.3.1 Gravityscope microscope design

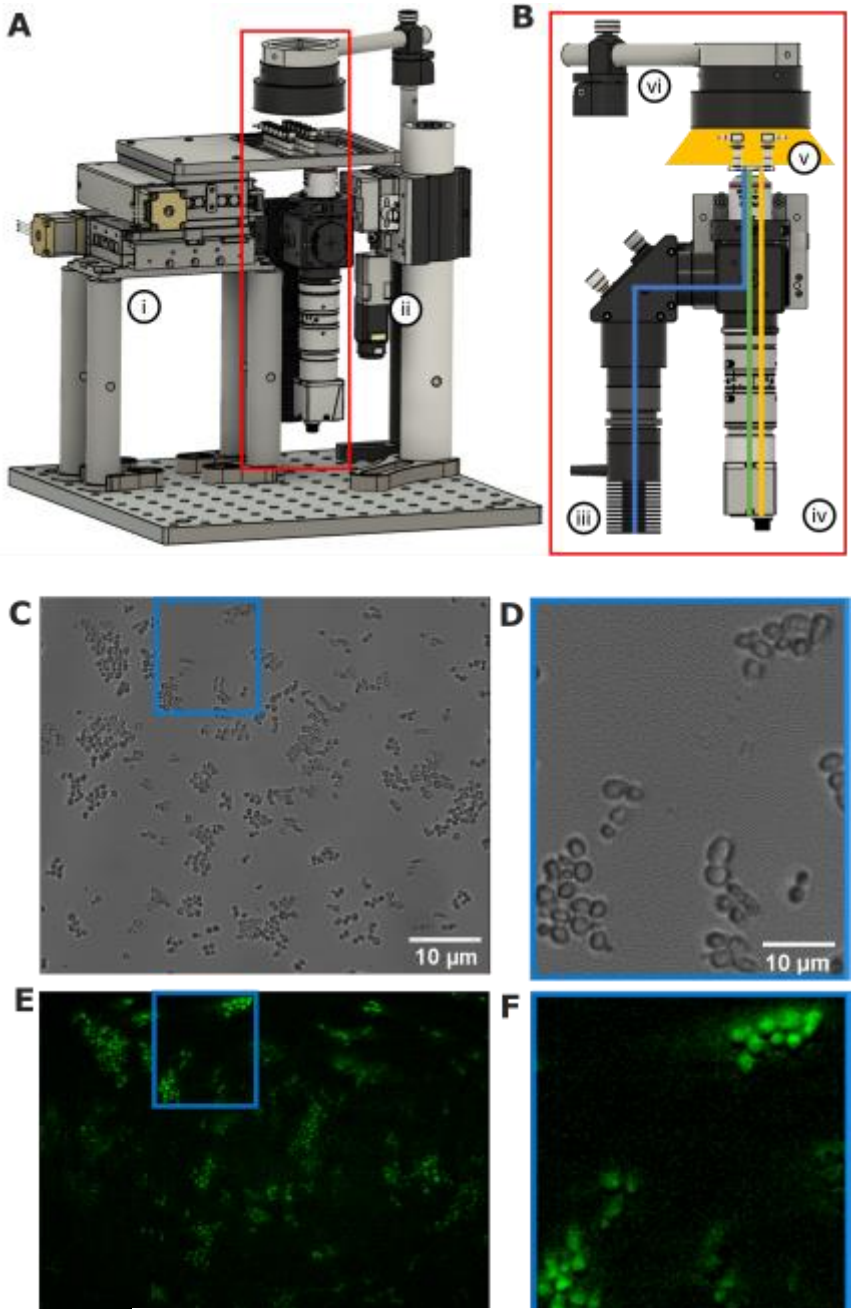

Figure 5.10 **A.** Gravityscope with (i) four standing posts and (ii) a central vibration mast which absorbs vibrations felt by the optical train. **B.** The optical train is shown better in the red outline and consists of (iii) a fluorescence bulb, (vi) brightfield bulb, (v) sample position and (iv) camera. The blue line depicts the path of travel of the fluorescence excitation beam, the sample absorbs this and in turn emits green light (green line) to the camera. The yellow line depicts the path of travel of the brightfield beam. **C.** A brightfiled image of S.ceravisiae taken with Gravityscope with a **D.** zoomed-in FOV. **E.** A fluorescence image taken with Gravityscope with a **F.** zoomed-in FOV.

Gravityscope (figure 5.10A) has both brightfield and fluorescence imaging capabilities. Brightfield is achieved from above the sample with an Adafruit DotStar high density 8x8 RGB LED pixel matrix mounted to a flexible post (figure 5.10B(vi)). Fluorescence is achieved from below the sample using a Thorlabs 809mW 470nm LED bulb (figure 5.10B(iii)). Figure 5.10B shows the beam paths of the brightfield and fluorescence bulbs. An Olympus UPLFLN 40X air objective (focal length 180mm, depth of field 0.49μm and 0.74 NA) and 60fps Daheng Imaging MER2-630-60U3M USB camera (figure 5.10B(iv)) are used. Samples are mounted to a bespoke 60x60mm xy motorised stage with a Nema 8 linearly actuated motorised z-axis control (with

rail and return spring), both xy stage and z-axis are controlled with a joystick (figure 5.11B(i)) and rotary nob (figure 5.11B(ii)). All three of these components were built by associates of Li *et al.* in China. Custom-built Python-based software is used for image-viewing, image-capture and control of the x,y,z positioning on a Linux-operated laptop. Gravityscope has a field of view of 3088x2064 pixels with 2.4μm camera pixel size. Image pixel size was measured using a graticule to be 152nm. The camera has a temporal resolution limit of 60fps. Intermittent brightfield and fluorescence images can be taken during imaging at 0.5 frames per second and fluorescence intensity can reach 0.05-1mW/mm^2. Figure 5.10C-D shows a brightfield image of CEN.PK 113-7D yeast cells taken using Gravityscope and figure 5.10E-F shows the cells after being administered 50μM 2-NBDG.

Vibration resistance was built into Gravityscope by mounting the optical train (fluorescence bulb, a Daheng Imaging 75mm lens tube, camera, z-axis cube and objective) on a 2” diameter dampened post (figure 5.10A(ii)) and the xy stage on four 1” diameter dampened posts (figure 5.10A(i)). Posts were bolted to a Thorlabs 300x300x12.7mm M6 aluminium breadboard.

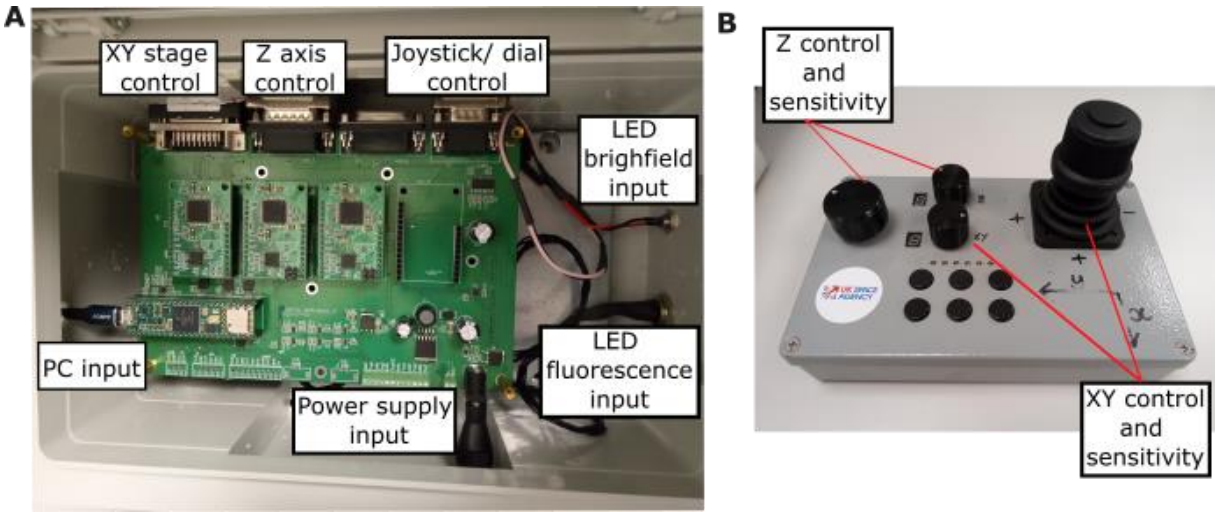

Figure 5.11 A.*Photo of Gravityscope control box with XY stage control, Z axis control, joystick/dial control, LED brightfield input, LED fluorescence input, power supply input and PC input interfaces.* ***B.*** *Photo of Gravityscope Z control dial and sensitivity dial and XY control joystick and sensitivity dial.*

Figure 5.11A shows the Gravityscope control box with ports to the xy controls, z control, joystick/dial input, brightfield LED grid input, fluorescence LED input, PC input and power supply. A joystick and dial were used to control shifts in xy and z respectively, dials were used to control the sensitivity of these (figure 5.11B).

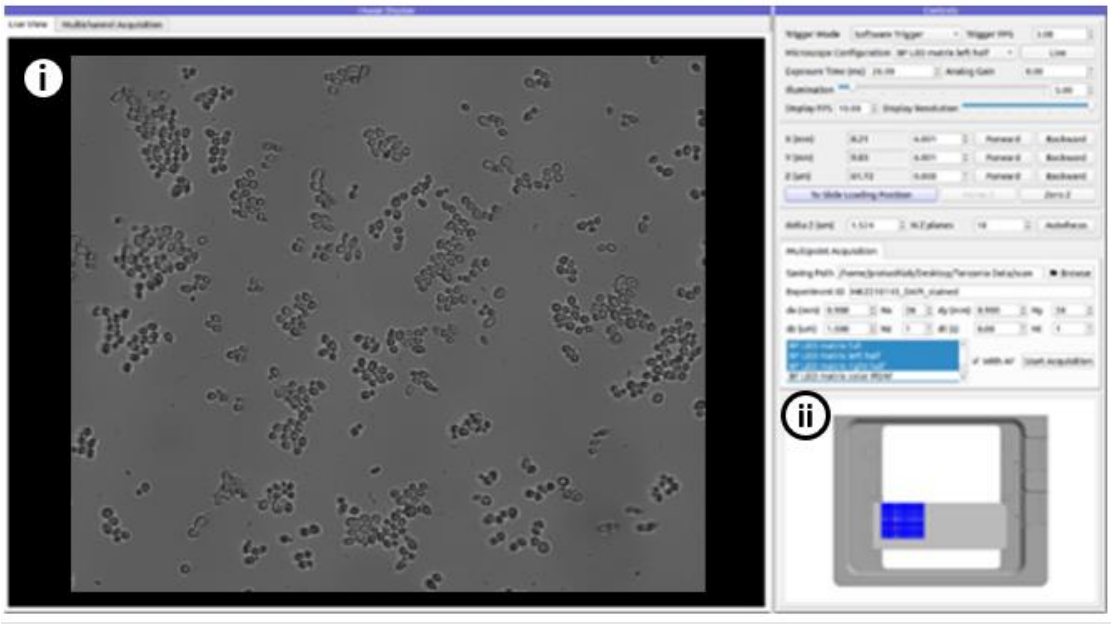

Figure 5.12 *Gravityscope user interface with (i) sample display and (ii) imaging conditions controls including exposure time, video length, brightfield/fluorescence channel toggle and intensity.*

Figure 5.12 shows the Gravityscope user interface on a DELL laptop. The USB camera was plugged into this which enabled a live view of the sample on the user interface (laptop screen).

5.3.2 Gravityscope vibration-resistance performance tests

The vibration-resistance performance of Gravityscope was first tested by mounting it on a benchtop centrifuge. Brightfield image videos were taken as the centrifuge was turned on and left to run, reaching vibrations of up to 13000rpm (217Hz).

The cross correlation of cell locations between consecutive images (video frames) was calculated using MATLAB. Figure 5.13A-B shows the brightfield image with a zoomed-in panel of yeast cells when the microscope was mounted on the centrifuge. Figure 5.13C shows the plot of cell location correlation coefficient vs time; the plot indicates that relative cell position was erratic while the centrifuge was reaching its peak vibration, average lateral cell shift was approximately 0.9±0.4μm. After this, at approximately 15 seconds, the centrifuge vibration peak had been reached and the images were relatively stable. This meant that the central vibration-resistance mast and four pillars performed well at absorbing most of the vibration produced by the centrifuge once vibration had reached a steady rate.

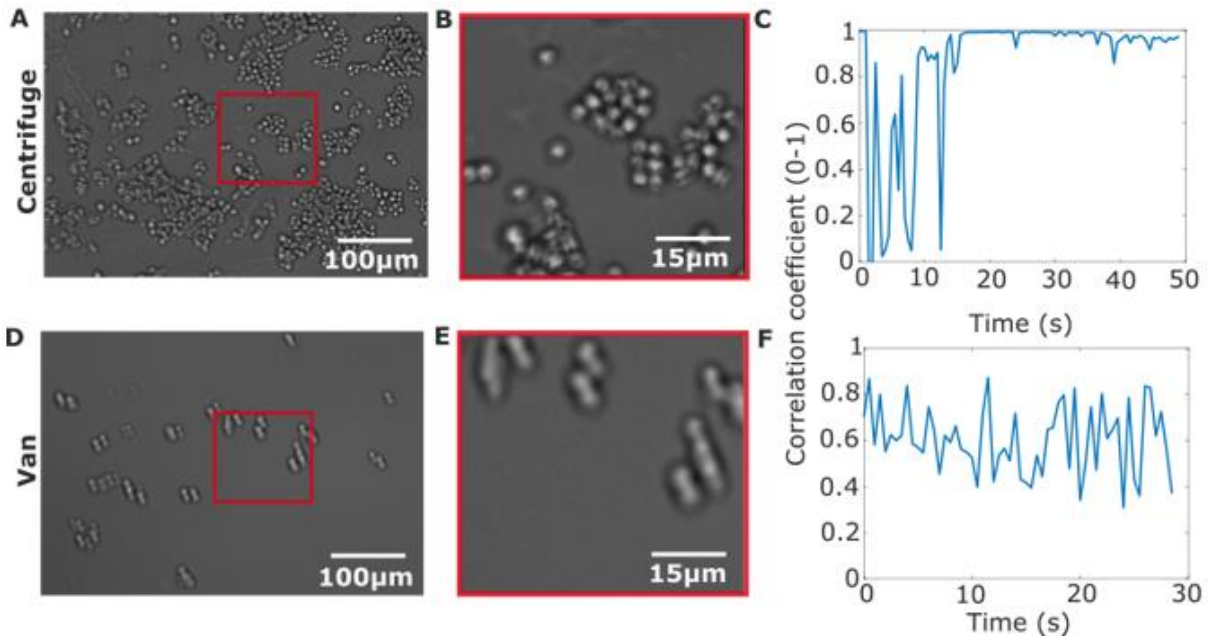

Figure 5.13 A. *Brightfield image of CEN.PK 113-7D yeast cells and* ***B.*** *zoomed-in panel of the yeast cells taken while the microscope was atop a benchtop centrifuge.* ***C.*** *Plot of cell location correlation coefficient vs time for image videos taken while microscope was mounted on the centrifuge.* ***D.*** *Brightfield image of CEN.PK 113-7D yeast cells and* ***E.*** *zoomed-in panel of the yeast cells taken while the microscope was inside a dampened aluminium Zarges box on a van.* ***F.*** *Plot of cell location correlation coefficient vs time for image videos taken while microscope was in a dampened aluminium Zarges box on a van.*

Gravityscope vibration-resistance performance was further tested when it was bolted onto a 10mm aluminium baseplate mounted to four mechanical dampeners in each corner inside an aluminium 750x550x580mm Zarges box. The Zarges box was placed inside a minivan and images were taken while the van engine was running. Figure 5.13D-E shows a brightfield image of the video taken on the van and a zoomed-in panel shows the cells while the engine was running. Average lateral cell shift was 1.3±0.8μm which is higher than when the microscope was mounted on the centrifuge, but still a manageable distance. Figure 5.13F shows a plot of the cell location correlation coefficient vs time; it shows that the correlation between a cell position in a frame and its relative position in a following frame does not fall below 0.4 during the 30 second video. Both vibration tests indicated that Gravityscope performed well in the face of vibrations.

5.4 Gravityscope: syringe pump design

Gravityscope syringe pump consists of five independently driven syringe pumps; injection is generated by a Nema 17 stepper motor (figure 5.14(i)) coupled with a M10 threaded rod (figure 5.14(ii)) pushing the syringe plunger. A carriage (figure 5.14(iii)) holds the syringe and

the syringe is pushed along a bespoke 3D-printed frame (figure 5.14(iv)) by the stepper motor. Each carriage has an adjustable bolt (figure 5.14(v)) which sits below the syringe plunger; this was designed to allow fitting of the primed syringe to the pump without premature injection caused by knocking the plunger with the carriage bolt. Each syringe is kept in place by an adjustable syringe holder (figure 5.14(vi)). Each pump can be independently driven by a bespoke control system which allows for jogging forwards and backwards, pre-set injection and homing. Each pump consists of an open-loop stepper motor driver board, a limit switch, panel-mount inputs and a display; these were wired to an Arduino Uno flashed with a custom control script. The entire Gavityscope syringe pump consists of five of these.

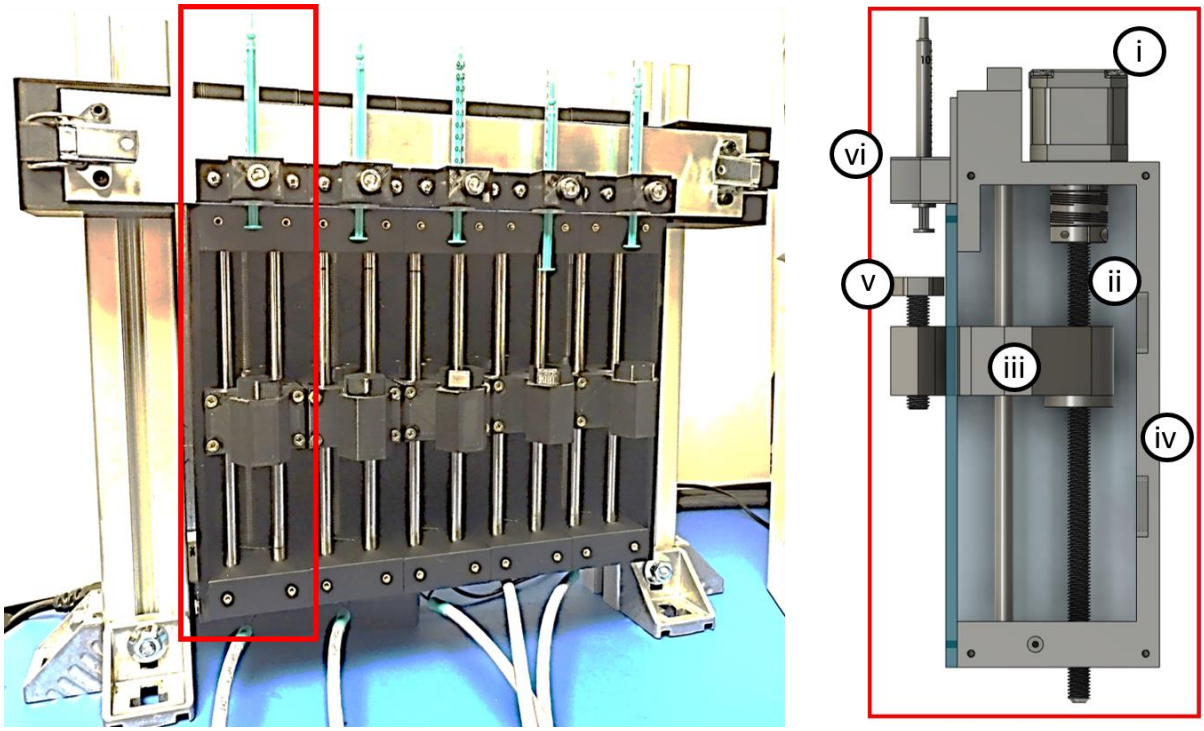

Figure 5.14 *An individual syringe pump in a series of five for the Gravityscope syringe pump. Each pump has a (i) Nema 17 stepper motor, (ii) M10 threaded rod, (iii) carriage, (iv), frame, (v) adjustable rod and (vi) syringe holder.*

Each syringe pump can be operated independently by driving each stepper motor for each pump by a separate open-loop driver board (figure 5.15B(iv)). Each driver board provided separate STEP and DIRECTION signals generated by the custom-script Arduino. There is a limit switch attached between each pump and the Arduino (figure 5.15B(i)); the open and closed states of the limit switches were used during motor homing; a carriage hitting an open limit switch would prompt the carriage to return upwards (home) to a pre-programmed position on the rod. A bespoke user-interface control box was designed with four push buttons and a motor-selector dial. The dial is turned clockwise to determine which independent pump; three

of the four buttons, the 'Jog forwards' (figure 5.16(ii)) button, the 'Jog backwards' (figure 5.16(iii)) button and the 'Inject' (figure 5.16(iv)) button work on each independent motor for each independent pump, based on which pump has been selected by the dial. The fourth button, 'Home' (figure 5.16(i)), works on all five pumps simultaneously and is used to bring the carriages to a pre-programmed position on the rod.

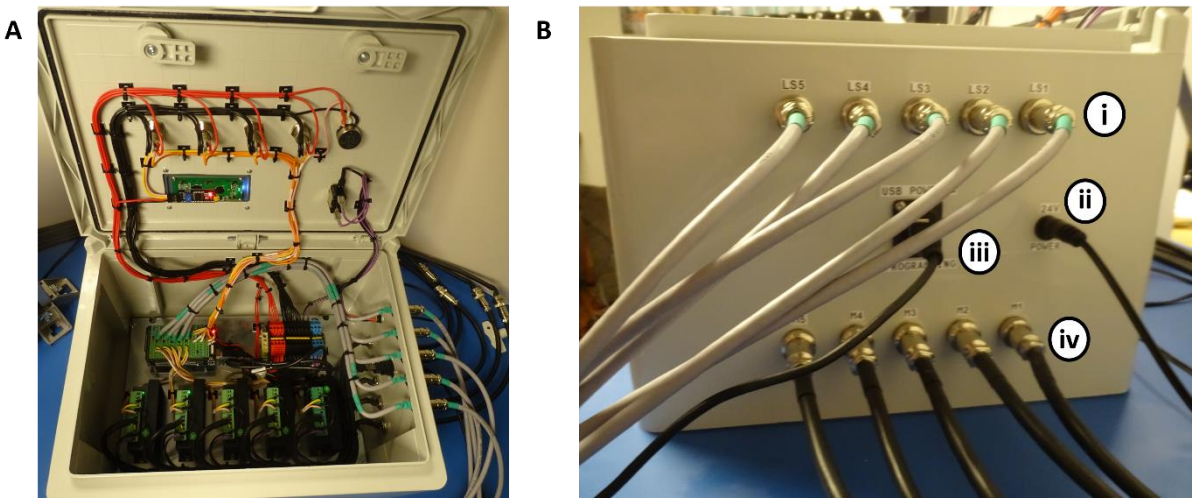

Figure 5.15 A. *Syringe pump control box interior and wiring and* ***B.*** *wire connection points including (i) five limit switch cables, one for each syringe pump, (ii) a 24V power supply cable, (iii) a 5V USB cable for the Arduino, buttons and LCD screen and (iv) five Nema 17 stepper motor cables, one for each syringe pump.*

The control box (figure 5.15A) also has on it a 16x2 character display LCD screen which displays information when buttons are pushed and indicating which pump is selected when the dial has been turned (figure 5.16).

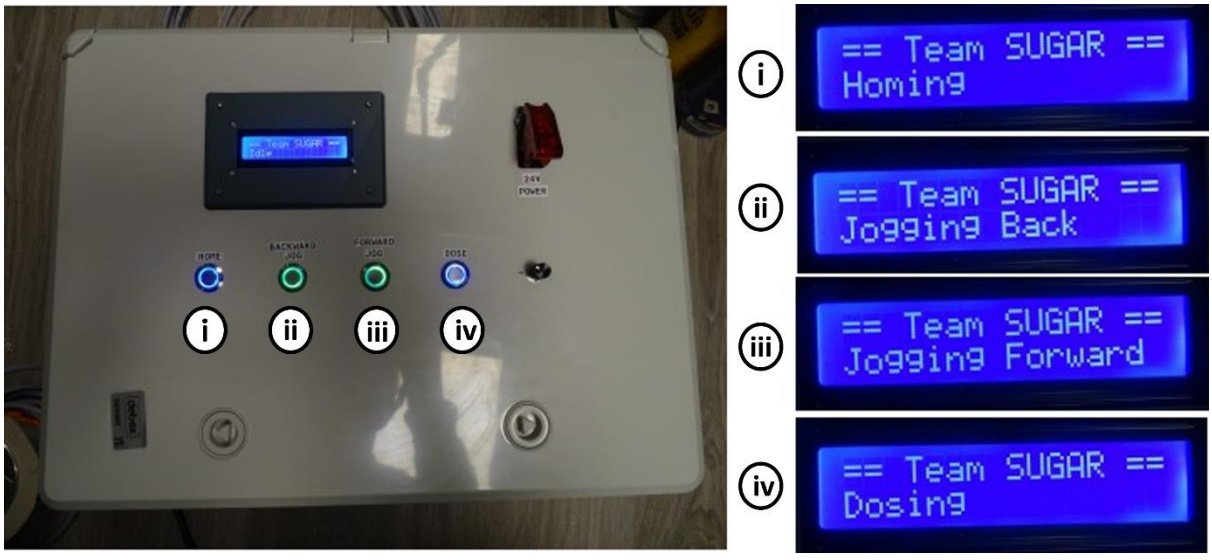

Figure 5.16 *Syringe pump control box with LCD display screen. On the right are the displays when the (i) HOME, (ii) BACKWARDS JOG, (iii) FORWARDS JOG, and (iv) DOSE buttons are pushed.*

For the flight experiments, the homing position was adjusted to allow 47 rotations of the motor before reaching the homing position and the injection speed was changed to 25revs/min allowing a dose of approximately 8.8μL/min of liquid.

5.5 Gravityscope: microfluidic sample-system design and sample preparation procedures

Microfluidic sample systems were designed to contain both the CEN.PK 113-7D samples in slides and 2-NBDG in syringes connected by tubing. The design accounted for liquid containment and easy sample storage and manoeuvrability.

5.5.1 Microfluidic sample-system design

During the campaign, there were three flights on which the SUGAR experiment was used. Each flight consisted of 31 parabolic sets (figure 5.3A). There were five sets consisting of five parabolas and one set consisting of six parabolas (figure 5.3B); the extra parabola was in the first set and was used as a practice parabola for both the pilots and experimenters to adjust to the parabolic flight environment.

The SUGAR experiment design consisted of assigning one channel of a five-channel sample slide to each parabola in a set, for 30 total parabolas. This required six sample slides in total. Each channel had to be independently injected with 2-NBDG during imaging. An image-video was taken during each parabola, this required a syringe filled with 2-NBDG (of varying concentrations dependant on flight number) to be fitted to each slide channel. Each channel had to also have its own self-contained waste port.

Therefore, six microfluidic sample systems were made. Each sample system took on a profile outlined in figure 5.17. Five 30μL channels (figure 5.17(ii)) of an ibidi 6-channel μ-Slide VI 0.4 with sterilised polymer coverslip sample slide (figure 5.17(i)) were filled with sample culture. Male luer locks were fitted to the outlet (figure 5.17(iii)) and inlet (figure 5.17(iv)) ports of each of the five channels. To the other side of the outlet port luer lock, approximately 3.5cm of 2.5mm inner diameter, 3mm outer diameter silicone tubing was fitted; a party balloon (figure 5.17(v)) was attached with a cable-tie to the other side of this tubing. A party balloon was the cheapest and most flexible option for a waste port. To the other side of the inlet port luer lock, approximately 48cm of silicone tubing was fitted (figure 5.17(vi)); a female luer lock (figure 5.17(vii)) fitted to a 1mL syringe (figure 5.17(viii)) was fitted to this tubing.

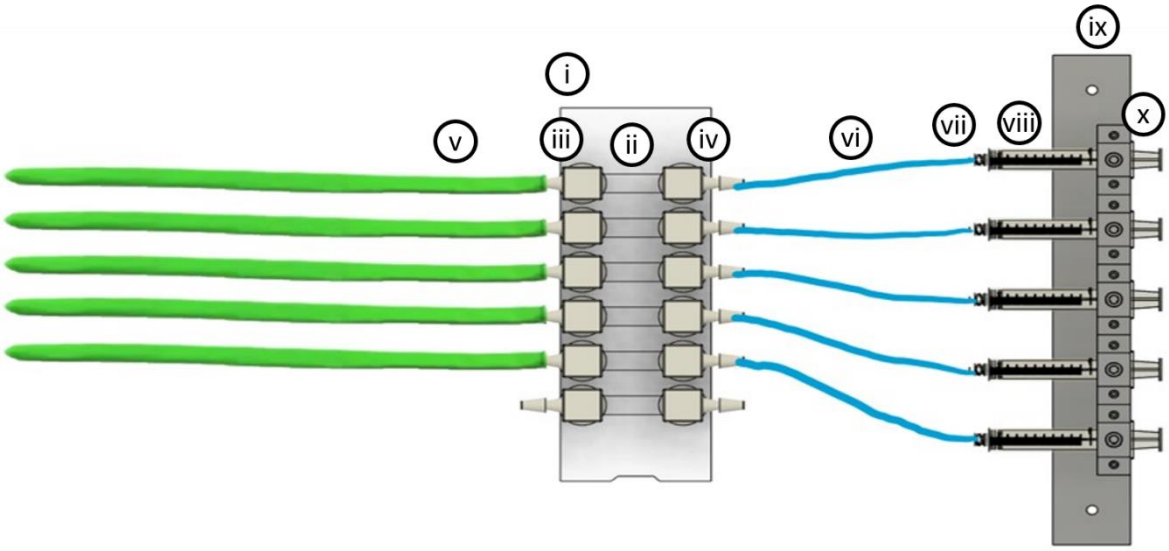

Figure 5.17 *Sample system consisting of (i) an ibidi channel slide with (ii) five usable channels, each with male luer locks fitted to the (iii) outlet and (iv) inlet ports, silicone tubing and (v) party balloons were fitted to the outlet ports while approximately (vi) 48cm of silicone tubing was fitted to the inlet port which was fitted to a (vii) female luer fitted to a (viii) 1mL syringe, syringes were held in place with an (x) adjustable holder on an (ix) aluminium rack. Image not to scale.*

All six sample systems had to be stored alongside the microscope and syringe pump during the flights. This required a unique sample storage system to be developed to prevent premature injection of samples caused by the syringe plunger being knocked during flight. Each syringe was fitted to a custom-made 3D-printed part designed to hold the tube of a syringe (figure 5.17(vi) and figure 5.18B); an adjustable bolt was tightened to ensure the syringe would not fall out of the holder. This 3D-printed part was attached to a syringe panel (figure 5.18A); an aluminium plate with clasps bolted on each end (figure 5.18C). The syringe panel was then clasped vertically to a bespoke 3D-printed housing, bolted to the base of the microscope containment box (figure 5.18D).

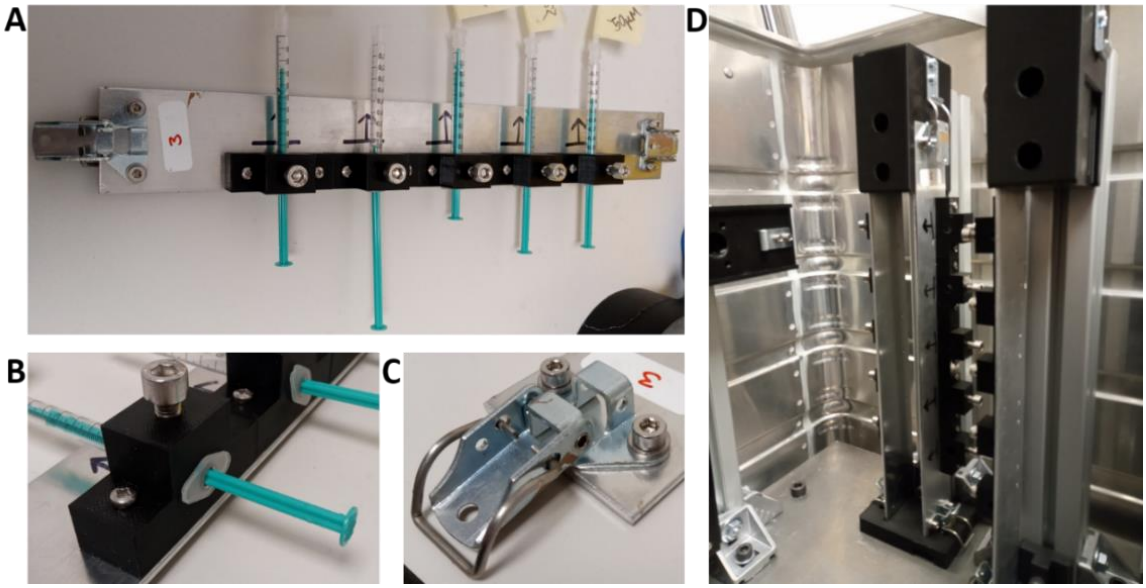

Figure 5.18 A. *Panel to hold five 1mL syringes.* ***B.*** *Syringe holder on the panel with adjustable bolt.* ***C.*** *Clasp used to fix the panel to the panel rack.* ***D.*** *Syringe panel rack.*

The sample-system inlet tubing was allowed to freely sit on the bottom of the box and the sample slide was clasped within a bespoke 3D-printed slide holder (figure 5.19) which was fitted to base of the containment box with Dual Lock (as to be easily removable for sample swap-overs). Waste balloons were stored in Falcon tubes which were bolted to the microscope base.

Figure 5.19 *A bespoke 3D-printed holder designed to hold the ibidi sample slides.*

5.5.2 CEN.PK 113-7D sample preparation procedures

CEN.PK 113-7D yeast pertridishes were prepared in the Wollman lab in the UK one week prior to the flight campaign and stored in the fridge. The petridishes were transported to the Novespace facility lab in Bordeaux, France in bubble-wrap in an envelope in a suitcase and then stored in the fridge in the Novespace lab for one week (the preparation week) prior to

the flight week. 2-NBDG was stored in 50mL Falcon tubes in a freezer. These were defrosted on the morning of each flight. On each of the three flight days, and the nights prior, cultures and samples were prepared according to the following procedures.

Procedure 1 – preparing CEN.PK 113-7D overnight culture

In a 5mL pop-tube, 1mL 2xYNB media, 200μL 40% w/v glucose media and 800μL MilliQ water were mixed and then a scraping of CEN.PK 113-7D yeast from a pre-made petridish was mixed in. The pop-tube was placed in the egg incubator, rotating every 90 minutes at 30°C overnight (approximately 18 hours).

Procedure 2 – preparing the CEN.PK 113-7D morning culture

In a fresh 5mL pop-tube, 1mL 2xYNB media, 200μL 40% w/v glucose media and 800μL MilliQ and 200μL of the overnight culture (prepared in Procedure 1) were mixed and the pop-tube was placed in the egg incubator, rotating every 90 minutes at 30°C for 2 hours.

Procedure 3 – preparing the CEN.PK 113-7D sample culture

Each microfluidic sample slide consisted of six 30μL channels, but only five of these were used for the experiments. There was a microfluidic sample slide used for each parabolic set on the flight, of which there were six. Therefore, in total, 900μL of sample culture was required for each flight day.

A clean 50mL Falcon tube was filled with 1/10 morning culture (prepared according to Procedure 2) to 9/10 1xYNB media.

Procedure 4 – preparing the samples for imaging

Five 30μL channels of an ibidi 6-channel μ-Slide VI 0.4 with sterilised polymer coverslips were each pipetted with 30μL of Concanavalin A and left to rest at room temperature for 15 minutes. Following this, each channel was pipetted with 30μL of 1xYNB media (washed) and then pipetted with 30μL of the CEN.PK 113-7D morning culture (prepared according to Procedure 3) and again left to rest at room temperature for 15 minutes. After this, each channel was washed again.

Once the sample slides were prepared, the male luer locks were fitted to inlet and outlet ports of each channel on each slide. On the inlet side, the male luer locks were connected to the

silicone tubing and the syringes. On the outlet side, the male luer locks were connected to the waste units.

The syringes were prepared and fitted to the syringe panel during the two-hour wait for the morning culture. Defrosted Falcon tubes of 2-NBDG were used to prime the inlet tubes of the syringes; this was done by releasing the syringe plunger while the tube was in the 2-NBDG. Ideally, the entire inlet tube and syringe would have been filled with 2-NBDG but this would have been expensive, so the inlet tube was filled with only 0.95mL of glucose with a 0.05mL air-gap between the glucose and the male luer connected to the inlet port of the slide channel.

5.6 Gravityscope: storage and plane interfaces

Gravityscope microscope, syringe pump and sample-systems were all fitted within a 750mmx550mmx580mm aluminium leakproof Zarges box (figure 5.20A(i)). A Zarges box was the best solution to the experiment storage, liquid containment and fixation requirements set out by Novespace. It was also the best solution to the question of logistics to and from France. Once the microscope, syringe pump and sample storage solutions were fitted within the Zarges box, the entire setup was referred to as the 'experimental rig'.

5.6.1 Experiment and sample storage and plane fixation

Four dampeners were bolted to the bottom of the inside of the Zarges box at each corner (figure 5.22A). A 10mm aluminium baseplate was bolted to the top of the dampeners and the experiment fixtures, including the microscope, syringe pump and sample storage equipment, were bolted to this baseplate.

It was assumed that, along with the dampened optical train post, the four dampeners within the Zarges box would absorb even more vibration experienced by the experimental rig during flight and altering gravity conditions. These dampeners contributed to vibration absorption when the microscope was within the Zarges box during experiments conducted on the van.

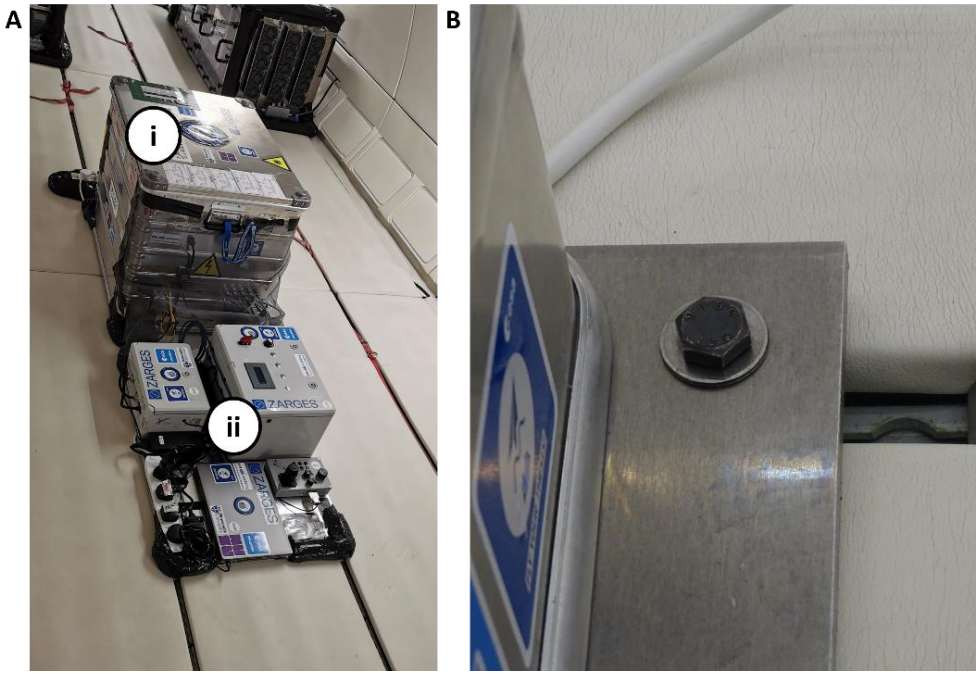

***Figure 5.20 A**.Gravityscope and microfluidics within a (i) Zarges box with an accompanying (ii) control baseplate. **B**. A baseplate attached to the Zarges box bolted to the seat-rail of the Airbus A300.*

Two (875mmx130mm), 10mm aluminium baseplates were bolted to the bottom of the outside of the Zarges box; these were bolted to the seat-rails of the Airbus A300 during the preparation week prior to the three flights (figure 5.20B). Fixation was achieved in the same way it was suggested by the Novespace Guidelines document provided to the team (figure 5.22A-B); this ensured the experimental rig would remain fixed to the plane floor during flight; providing safety and stability.

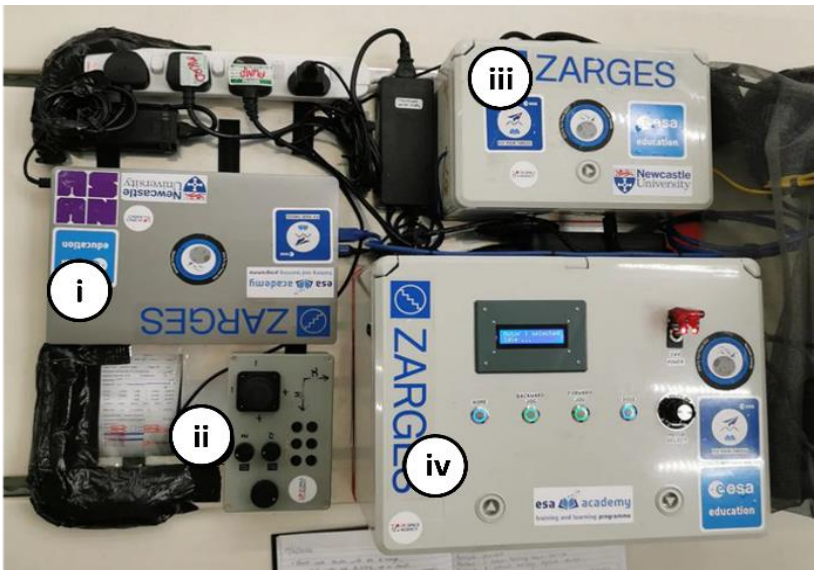

***Figure 5.21** Gravityscope control baseplate with (i) laptop, (ii) microscope xy joystick and z dial controls, (iii) microscope power box and (iv) syringe pump power and control box.*

A second 10mm exterior baseplate was fitted to the seat-rails alongside the Zarges box (figure 5.21). The microscope laptop and xy joystick and z dial controls (figure 5.11B), microscope power box (figure 5.11A) and syringe pump control box (figure 5.16) were all fitted to the exterior baseplate with

Dual Lock. Power cables and multi-gangways were also fitted to this board with Dual Lock and loose wiring was contained with cable ties.

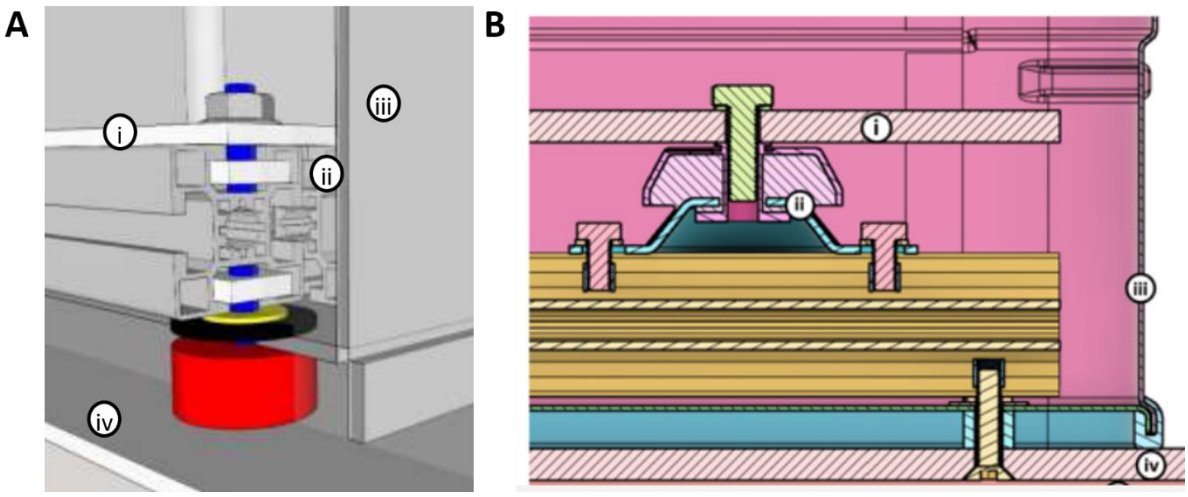

Figure 5.22 *Fixation of a Zarges box to the plane seat-rails* ***A.*** *as suggested by the Novespace Guidelines document and* ***B.*** *as built by Team SUGAR with (i) interior baseplate, (ii) dampener, (iii) Zarges box wall and (iv) exterior baseplate.*

There were a number of wires that had to travel between the inside and outside of the Zarges box (figure 5.23) which had to be isolated and secured to adhere to the Novespace guidelines. A safety requirement by Novespace required the cables on the outside of the Zarges box to be covered by netting to prevent people tripping on them or receiving electric shock from them. The net was attached to the exterior baseplate and Zarges box with masking tape. Another safety requirement required all sharp edges to be covered in foam, stuck down with masking tape.

During each flight, the experiment had two Operators. Operator 1 was positioned in front of the Zarges box while Operator 2 was positioned in front of the control baseplate. The next section outlines what each Operator did. Operators were held down to the plane floor by ratchet straps fixed to the seat-rails; this was another safety requirement by Novespace to prevent operators injuring themselves after landing abruptly on experimental equipment after the free-float (microgravity) stage and before the fall-down in the hypergravity stage.

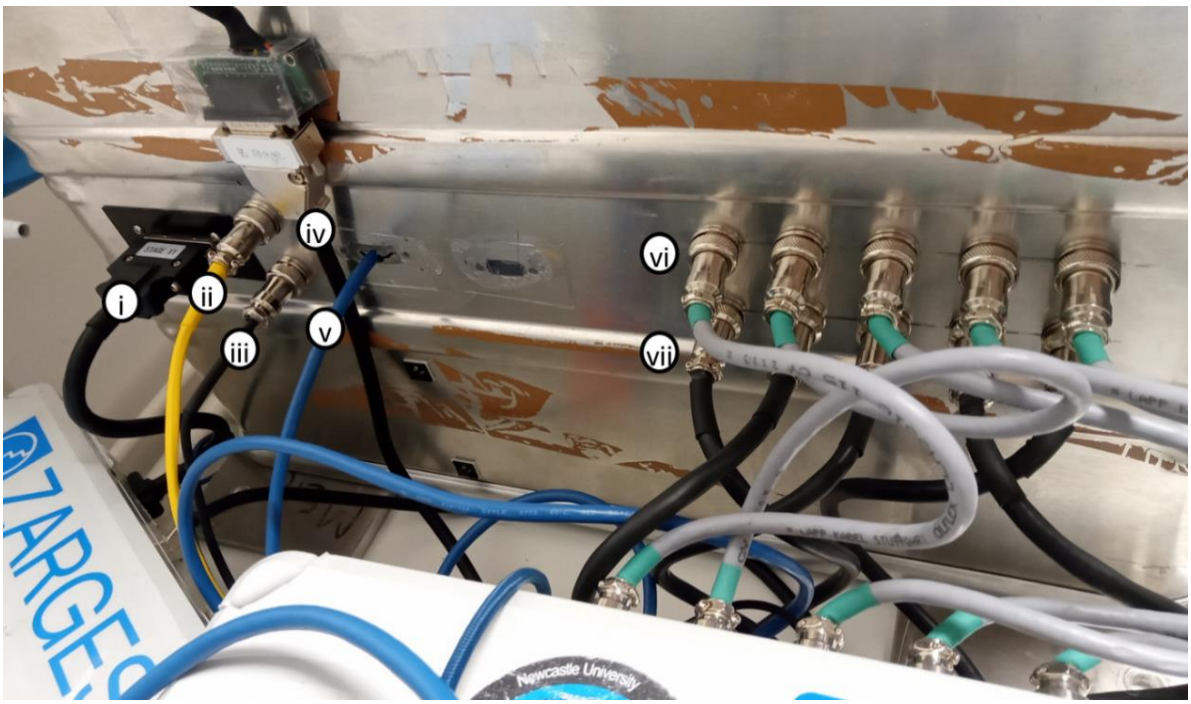

Figure 5.23 *All wires that had to be secured and isolated including power cables for the (i) xy stage, (ii) LED brightfield grid, (iii) LED fluorescent bulb, (iv) z axis, (v) camera USB power cable, (vi) five syringe pump limit switch power cables and (vii) five syringe pump Nema 17 stepper motor power cables.*

5.7 Gravityscope: imaging glucose uptake on the ground

5.7.1 Methods

CEN.PK 113-7D yeast samples were prepared according to Procedures 1-4 and were injected with 10,25,50μM 2-NBDG concentrations during imaging using Gravityscope in the lab.

The sample system was fixed to the syringe pump and microscope stage and the sample was imaged. An exposure length of 50ms and a 470nm LED fluorescence beam power of 1mW/mm^2 was used for each of 10,25,50μM 2-NBDG concentrations.

The brightfield and fluorescence images were opened in ImageJ (Fiji) and cells were selected in the brightfield image using the circle tool, the exact location was then selected on the corresponding fluorescence image (ctrl+E). The video time toggle was shifted across frames to observe if the cell remained in the same position pre and post 2-NBDG injection. If it did, the raw intensity of the cell was recorded over the number of frames. Intensity of a nearby area of background (of size the same as the cell) was also recorded across the number of frames and the value subtracted from the cell raw intensity, thus yielding a final value of the background-corrected intensity. This was done for multiple cells in the video. Time was given by multiplying 0.5 seconds (the frame time) by the frame number.

5.7.2 Results

Figure 5.24A is a brightfield image of the CEN.PK 113-7D cells and figure 5.23B are fluorescence images of the same FOV imaged from 15 seconds to 50 seconds post sample injection with 10μM 2-NBDG. Figure 5.25 shows plots of background-corrected cell intensity against time (video time) when samples were injected with 10,25,50μM 2-NBDG.

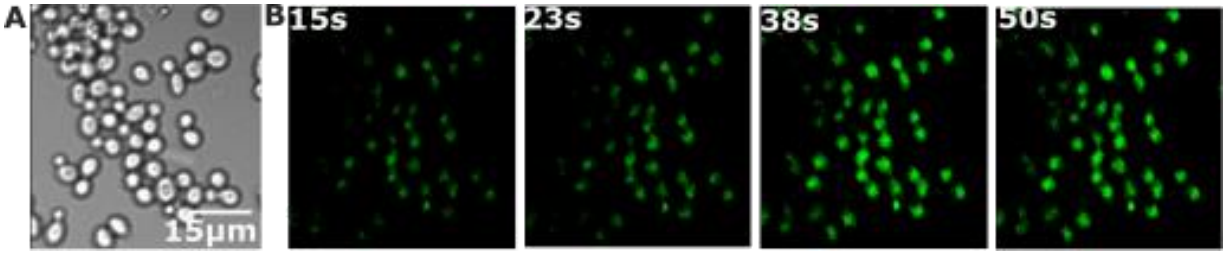

Figure 5.24 A. *Brightfield image of CEN.PK 113.7D yeast cells taken with Gravityscope on the ground and* ***B.*** *Fluorescence images of initial 10µM 2-NBDG uptake by CEN.PK 113-7D yeast cells taken with Gravityscpe on the ground at 0,8,23,35 seconds post injection with 50ms exposure and 1mW/mm^2 470nm beam.*

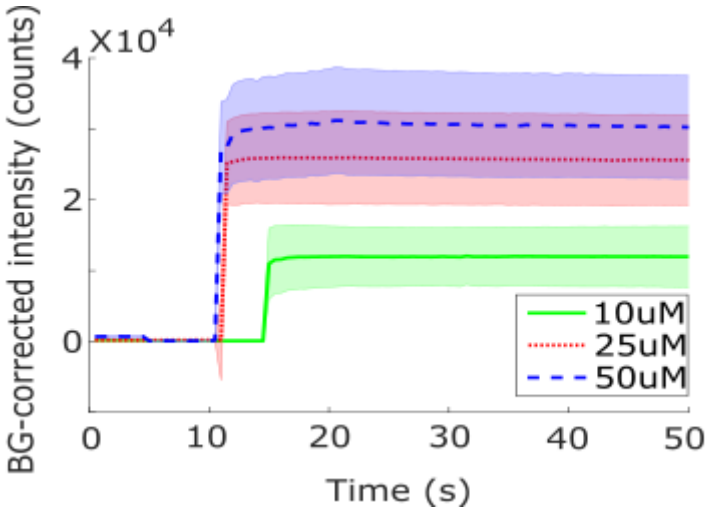

Figure 5.25 *Plots of 10,25,50µM 2-NBDG uptake by CEN.PK 113-7D yeast cells from fluorescence images taken on the ground.*

The cells in figure 5.24B were injected 15 seconds into imaging time and the fluorescence images clearly show the CEN.PK 113-7D cells becoming brighter over time, therefore indicating that they were indeed taking up the 2-NBDG. For 10μM 2-NBDG uptake, the plot (figure 5.25) shows a 1.2x10^4% increase in intensity in the first 2 seconds that the 2-NBDG was injected. For 25μM, this was an 8.2x10^3% increase and for 50μM it was a 2.2x10^4% increase.

The highest background-corrected intensity values for cells given 50μM 2-NBDG lie in the range 25,000-40,000 in the last 35 seconds of the video. This intensity range is sensible, considering the highest intensity values for initial uptake when CEN.PK 113-7D cells were given 100μM 2-NBDG were 45,000-65,000 range (figure 5.9) for uptake in a 40-scond-long interval.

5.7.3 Conclusion

Gravityscope is capable of capturing initial 2-NBDG uptake by CEN.PK 113-7D yeast cells with results comparable to those gathered after using the HILO/TIRF microscope.

5.8 Gravityscope: performance during The 79th ESA Parabolic Flight Campaign

A specific set of procedures was designed to use Gravityscope during the parabolic flights. This involved imaging at specific times during parabolas to include all gravity variations.

5.8.1 Experiment flight procedures (methods)

5.8.1.1 General imaging and injection times for all parabolas

The second aim of this project was to assess the rate of glucose uptake by yeast cells in response to abnormal gravity conditions. Therefore, the fluorescent glucose, 2-NBDG, would be injected to yeast cell samples in different microfluidic slide channels at different stages of the flight parabolas and imaged for different amounts of time. 2-NBDG would be injected at the following time-points of each parabola, noting that a parabola takes on the profile outlined in figure 5.2A:

- Injection at the start of the first hypergravity phase and take images for 40 seconds until the end of the microgravity phase (parabolas 1-5)
- Injection at the start of the microgravity phase and take images for 40 seconds until the end of the second hypergravity phase (parabolas 6-10)
- Injection at the start of the second hypergravity phase and take images for 40 seconds ending 20 seconds into the second steady flight phase (parabolas 11-15)
- Injection 20 seconds before the end of the first steady flight phase and take images for 40 seconds ending at the end of the first hypergravity stage (parabolas 16-20)
- Injection 20 seconds before the end of the second steady flight phase and take images for 80 seconds until the end of the second hypergravity phase (parabolas 21-29)

Each of these conditions included a negative control whereby no fluorescent glucose would be injected.

5.8.1.2 Flight procedures

Before flight:

Prior to take-off the sample systems were fitted to the storage units in the Zarges box. Figure 5.26 demonstrates all of the sample systems securely fitted in the Zarges box prior to flight.

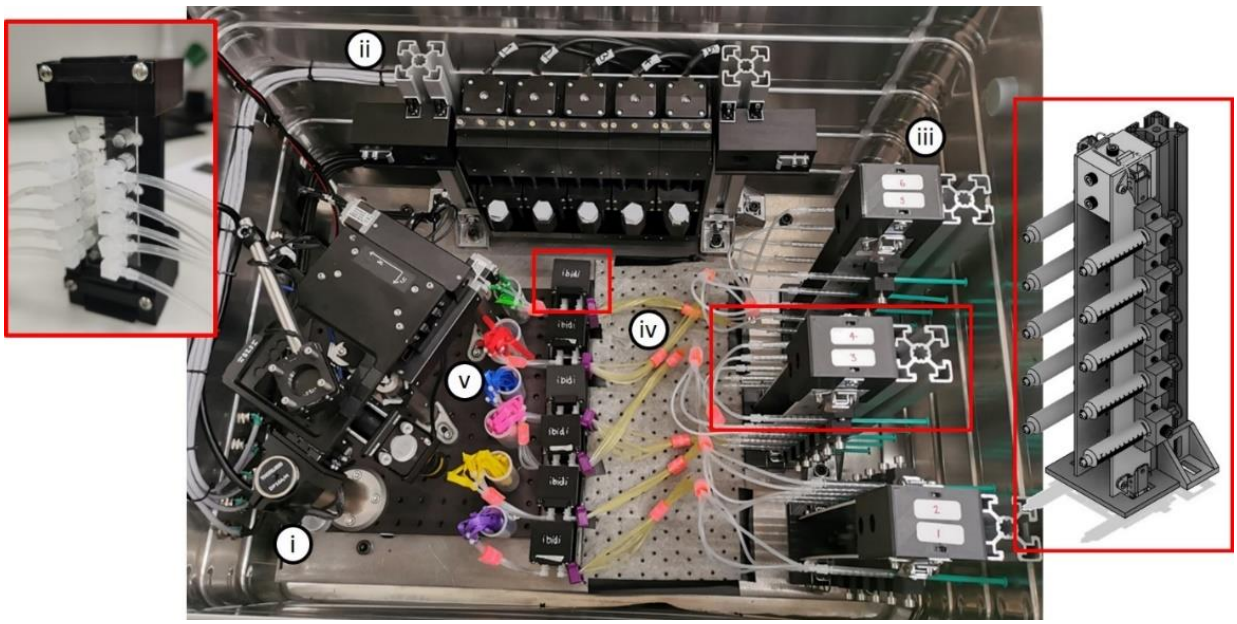

Figure 5.26 *Zarges box interior prepared prior to flight where (i) is the microscope, (ii) is the syringe pump, (iii) are the syringe panel racks, (iv) are the silicone tubes of the sample systems primed with 2-NBDG, below is an absorbent mat to soak up any fluid leakage should there be any and (v) are the Falcon tubes bolted to the microscope breadboard and used to contain the loose outlet containers (party balloons) of the sample systems.*

During flight:

Operator 1 (positioned at the Zarges box);

1. Adjusted the xy-stage so the microscope objective sat below the correct sample channel
2. Selected the correct syringe pump number and injected at the correct timepoint in the parabola

Operator 2 (positioned at the laptop);

1. Focused the z-axis and informed Operator 1 when they could see in-focus cells
2. Initiated the image acquisition on the laptop at the same time Operator 1 injected

Steps 1 and 2 for each Operator were conducted five times, one time for each parabola in a parabola set, one sample slide channel per parabola. In each break, the used sample systems were removed by Operator 1 and replaced in a storage unit and a new sample system was connected to the microscope and syringe pump. The syringe pump was homed by Operator 1, this ensured the adjustable bolts were in the correct position to be able to inject a fully extended new syringe.

After flight:

The microscope was checked for calibration and image data was copied from the laptop onto an external drive. This took a maximum of 15 minutes to complete. Used sample systems were removed from within the Zarges box and taken to the Novespace lab.

5.8.2 Gravityscope flight results

5.8.2.1 Vibration-resistance performance during flight

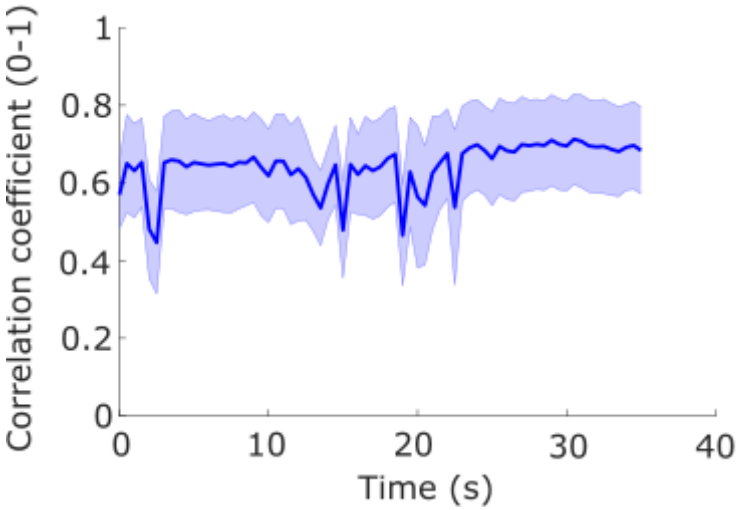

Figure 5.27 *Plot of correlation coefficient (0-1) vs time for CEN.PK 113-7D brightfield images taken during 0.01-1.8g*

The vibration resistance performance of Gravityscope during flight was characterised in the same way as was done for tests conducted on the ground. The correlation coefficient between consecutive frames was quantified. Vibration-resistance performance during flight was similar to that on the ground (centrifuge and van). Correlation coefficients remained between 0.5-0.8 during the steady flight stages of the parabolas (1g). During changes in gravity (0.01-2g) there was an xy lateral shift of 8.3±0.3μm at the sample plane. Figure 5.27 shows a plot of correlation coefficient against time for 40 seconds during a 0.01-1.8g stage of a parabola.

5.8.2.2 Glucose uptake during flight compared to on the ground

Yeast samples were prepared according to Procedures 1-4 and were injected with 10μM 2-NBDG concentrations during imaging on the plane at different parabola stages. Fluorescence images were taken using 30ms exposure time and 1mW/mm^2 470nm beam.

Figure 5.28A-B shows a brightfield image of the CEN.PK 113-7D yeast cells and a fluorescence image after the sample had been injected with 10μM 2-NBDG. The plot (figure 5.28C) shows background-corrected 10μM 2-NBDG uptake by the cells vs time post injection for cells imaged on the ground (green curve) and cells inflight (blue curve), both fitted against exponential uptake fits (Wollman et al., 2022). The intensity of fluorescence images taken during 0.01-1.8g flight was characterised against that for images taken on the ground; characteristic uptake

times were 0.6±0.2 seconds in flight and 1.3±0.3 seconds on the ground, therefore indicating that glucose uptake by the yeast cells was slower on the ground than inflight. Despite the glucose uptake times being different between the ground and inflight, the limited amount of data collected inflight resulted in a lack of statistical significance in these differences.

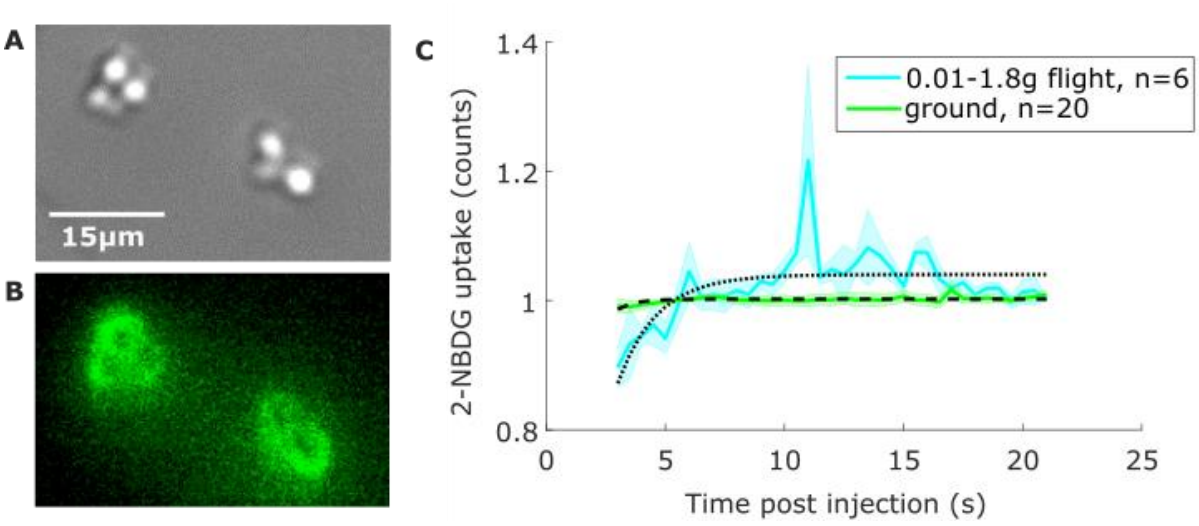

Figure 5.28 A. *Brightfield image of CEN.PK 113-7D yeast cells during flight and* ***B.*** *Fluorescence image of 10µM 2-NBDG uptake by CEN.PK 113-7D yeast cells taken with Gravityscope 1mW/mm^2 470nm beam at 30ms exposure.* ***C.*** *Plots of 10µM 2-NBDG uptake by CEN.PK 113-7D cells on the ground and during 0.01-1.8g flight parabola stage for n=20 and n=6 cells respectively, exponential curves have been fitted to each.*

5.8.3 Conclusion

Gravityscope was able to capture 2-NBDG uptake by CEN.PK 113-7D yeast cells on the ground and during a microgravity and hypergravity flight. Despite vibrations experienced during flight, sample images remained relatively stable. Additionally, the glucose uptake data serves as an important proof of principal of Gravityscope abilities and points to the utility of Gravityscope for future microgravity experiments.

5.9 Chapter Discussion and Conclusion

The Gravityscope design performed well and fulfilled the engineering specifications. Brightfield and fluorescent images were taken, the microfluidic system allowed for cells to be kept alive during the flight and injection of 2-NBDG was controlled remotely. Fresh and used sample systems were stowed safely. Control of the microscope and syringe pumps was relatively simple and was comfortable to use, even by one operator if necessary.

Gravityscope can be used to take images of initial fluorescent glucose uptake on the ground with results comparable to those obtained from using the HILO/TIRF microscope.

Gravityscope can also take brightfield image videos that are relatively stable during microgravity and hypergravity conditions on a parabolic flight.

Additionally, this project was a proof of concept that a new system could be developed to image cellular processes during a parabolic flight. Due to the contained and robust nature of Gravityscope, it is also well-suited to be used in other extra-laboratory conditions such as the Antarctic or in deserts. Gravityscope has also been used to image extremophiles in a mine.

References

Abramowitz, M., Spring, K.R., Keller, H.E., Davidson, M.W., 2002. Basic principles of microscope objectives. BioTechniques 33, 772–781.

Adamson, A., Boddington, C., Downton, P., Rowe, W., Bagnall, J., Lam, C., Maya-Mendoza, A., Schmidt, L., Hrper, C.V., Spiller, D.G., Rand, D.A., Jackson, D.A., White, M.R.H., Paszek, P., 2016. Signal transduction controls heterogeneous NF-kB dynamics and target gene expression through cytokine-specific refractory states. Nature Communications. https://doi.org/10.1038

Alberts, B., Johnson, A., Lewis, J., Morgan, D., Raff, M., Roberts, K., Walter, P., 2015. Molecular Biology of the Cell, 6th ed. W.W.Nortan & Company.

Almada, P., Pereira, P.M., Culley, S., Caillol, G., Boroni-Rueda, F., Dix, C.L., Charras, G., Baum, B., Laine, R.F., Leterrier, C., Henriques, R., 2019. Automating multimodal microscopy with NanoJ-Fluidics. Nat Commun 10, 1223. https://doi.org/10.1038/s41467-019-09231-9

Alsamsam, M.N., Kopūstas, A., Jurevičiūtė, M., Tutkus, M., 2022. The miEye: Bench-top super-resolution microscope with cost-effective equipment. HardwareX 12, e00368. https://doi.org/10.1016/j.ohx.2022.e00368

Alvelid, J., Damenti, M., Sgattoni, C., Testa, I., 2022. Event-triggered STED imaging. Nat Methods 19, 1268–1275. https://doi.org/10.1038/s41592-022-01588-y

Ando, R., Hama, H., Yamamoto-Hino, M., Mizuno, H., Miyawaki, A., 2002. An optical marker based on the UV-induced green-to-red photoconversion of a fluorescent protein. PNAS 99. https://doi.org/10.1073

Arfat, Y., Xiao, W.-Z., Iftikhar, S., Zhao, F., Li, D.-J., Sun, Y.-L., Zhang, G., Shang, P., Qian, A.-R., 2014. Physiological Effects of Microgravity on Bone Cells. Calcified Tissues International 569–579. https://doi.org/10.1007/s00223-014-9851-x

Aurousseau, M.R.P., McGuire, H., Blunck, R., Bowie, D., 2016. A Step-by-Step Guide to Single-Subunit Counting of Membrane-Bound Proteins in Mammalian Cells, in: Popescu, G.K. (Ed.), Ionotropic Glutamate Receptor Technologies, Neuromethods. Springer, New York, NY, pp. 15–30. https://doi.org/10.1007/978-1-4939-2812-5_2

Awan, A.R., Blount, B.A., Bell, D.J., Shaw, W.M., Ho, J.C.H., McKiernan, R.M., Ellis, T., 2017. Biosynthesis of the antibiotic nonribosomal peptide penicillin in baker's yeast. Nature Communications. https://doi.org/10.1038

Axelrod, D., 2003. [1] Total internal reflection fluorescence microscopy in cell biology, in: Methods in Enzymology, Biophotonics, Part B. Academic Press, pp. 1–33. https://doi.org/10.1016/S0076-6879(03)61003-7

Axelrod, D., 1981. Cell-Substrate Contacts Illuminated by Total Internal Reflection Fluorescence. The Journal of Cell Biology 89, 141–145.

Axelrod, J.J., Axelrod, D., 2021. Light scattering in TIRF microscopy: A theoretical study of the limits to surface selectivity. Biophysical Journal 2952–2968. https://doi.org/10.1016/j.bpj.2021.06.025

Balasubramanian, H., Hobson, C.M., Chew, T.-L., Aaron, J.S., 2023. Imagining the future of optical microscopy: everything, everywhere, all at once. Commun Biol 6, 1–12. https://doi.org/10.1038/s42003-023-05468-9

Balzarotti, F., Eilers, Y., Gwosch, K.C., Gynnå, A.H., Westphal, V., Stefani, F.D., Elf, J., Hell, S.W., 2017. Nanometer resolution imaging and tracking of fluorescent molecules with minimal photon fluxes. Science 355, 606–612. https://doi.org/10.1126/science.aak9913

Bennett, N.C., Gardiner, R.A., Hooper, J.D., Johnson, D.W., Gobe, G.C., 2010. Molecular cell biology of androgen receptor signalling. The International Journal of Biochemistry & Cell Biology 42, 813–827. https://doi.org/10.1016/j.biocel.2009.11.013

Betzig, E., Chichester, R.J., 1993. Single Molecules Observed by Near-Field Scanning Optical Microscopy. Science 262, 1422–1425. https://doi.org/10.1126/science.262.5138.1422

Betzig, E., Patterson, G.H., Sougrat, R., Lindwasser, O.W., Olenych, S., Bonifacino, J.S., Davidson, M.W., Lippincott-Schwartz, J., Hess, H.F., 2006. Imaging Intracellular Fluorescent Proteins at Nanometer Resolution. Science 313, 1642–1645. https://doi.org/10.1126/science.1127344

Black, L., Tollis, S., Fu, G., Fiche, J.-B., Dorsey, S., Cheng, J., Ghazal, G., Notley, S., Crevier, B., Bigness, J., Nollmann, M., Tyers, M., Royer, C.A., 2020. G1/S transcription factors assemble in increasing numbers of discrete clusters through G1 phase. Journal of Cell Biology 219. https://doi.org/10.1083

Blom, H., Widengren, J., 2017. Stimulated Emission Depletion Microscopy. Chem. Rev. 117, 7377–7427. https://doi.org/10.1021/acs.chemrev.6b00653

Blum, J., Wurm, G., Kempf, S., Poppe, T., Klahr, H., Kozasa, T., 2000. Growth and Form of Planetary Seedlings: Results from a Microgravity Aggregation Experiment. Physical Review Letters 85.

Boehning, M., Dugast-Darzacq, C., Rankovic, M., Hansen, A.S., Yu, T., Marie-Nelly, H., McSwiggen, D.T., Kokic, G., Dailey, G.M., Cramer, P., Darzacq, X., Zweckstetter, M., 2018. RNA polymerase II clustering through carboxyterminal domain phase separation. Nature Structural & Molecular Biology 25, 833–840. https://doi.org/10.1038

Boothe, T., Hilbert, L., Heide, M., Berninger, L., Huttner, W.B., Zaburdaev, V., Vastenhouw, N.L., Myers, E.W., Drechsel, D.N., Rink, J.C., 2017. A tunable refractive index matching medium for live imaging cells, tissues and model organisms. eLife 6, e27240. https://doi.org/10.7554/eLife.27240

Borkin, D., He, S., Miao, H., Kempinska, K., Pollock, J., Chase, J., Purohit, T., Malik, B., Zhao, T., Wang, J., Wen, B., Zong, H., Jones, M., Danet-Desnoyers, G., Guzman, M.L., Talpaz, M., Bixby, D.L., Sun, D., Hess, J.L., Muntean, A.G., Maillard, I., Cierpicki, T., Grembecka, J., 2015. Pharmacologic Inhibition of the Menin-MLL Interaction Blocks Progression of MLL Leukemia In Vivo. Cancer Cell 27, 589–602. https://doi.org/10.1016/j.ccell.2015.02.016

Borkin, D., Klossowski, S., Pollock, J., Miao, H., Linhares, B.M., Kempinska, K., Jin, Z., Purohit, T., Wen, B., He, M., Sun, D., Cierpicki, T., Grembecka, J., 2018. Complexity of Blocking Bivalent Protein–Protein Interactions: Development of a Highly Potent Inhibitor of the Menin–Mixed-Lineage Leukemia Interaction. J. Med. Chem. 61, 4832–4850. https://doi.org/10.1021/acs.jmedchem.8b00071

Borkin, D., Pollock, J., Kempinska, K., Purohit, T., Li, X., Wen, B., Zhao, T., Miao, H., Shukla, S., He, M., Sun, D., Cierpicki, T., Grembecka, J., 2016. Property Focused Structure-Based Optimization of Small Molecule Inhibitors of the Protein–Protein Interaction between Menin and Mixed Lineage Leukemia (MLL). J. Med. Chem. 59, 892–913. https://doi.org/10.1021/acs.jmedchem.5b01305

Bouchard, M.B., Voleti, V., Mendes, C.S., Lacefield, C., Grueber, W.B., Mann, R.S., Bruno, R.M., Hillman, E.M.C., 2015. Swept confocally-aligned planar excitation (SCAPE) microscopy for high-speed volumetric imaging of behaving organisms. Nature Photon 9, 113–119. https://doi.org/10.1038/nphoton.2014.323

Brooks, M., 2023. How open-source software could finally get the world's microscopes speaking the same language. Nature 622, 206–208. https://doi.org/10.1038/d41586-023-03064-9

Burmeister, J.S., Truskey, G.A., Reichert, W.M., 1994. Quantitative analysis of variable-angle total internal reflection fluorescence microscopy (VA-TIRFM) of cell/substrate contacts. Journal of Microscopy. https://doi.org/10.1111/j.1365-2818.1994.tb03426.x

Burris, T.P., Solt, L.A., Wang, Y., Crumbley, C., Banerjee, S., Griffett, K., Lundasen, T., Hughes, T., Kojetin, D.J., 2013. Nuclear Receptors and Their Selective Pharmacologic Modulators. Pharmacol Rev 65, 710–778. https://doi.org/10.1124/pr.112.006833

Bushweller, J.H., 2019. Targeting transcription factors in cancer — from undruggable to reality. Nat Rev Cancer 19, 611–624. https://doi.org/10.1038/s41568-019-0196-7

Calatrava-Pérez, E., A. Bright, S., Achermann, S., Moylan, C., O. Senge, M., B. Veale, E., Clive Williams, D., Gunnlaugsson, T., M. Scanlan, E., 2016. Glycosidase activated release of fluorescent 1,8-naphthalimide probes for tumor cell imaging from glycosylated 'pro-probes.' Chemical Communications 52, 13086–13089. https://doi.org/10.1039/C6CC06451E

Carpenter, W.B., 1856. The microscope: And its revalations. Blanchard and Lea.

Castilla, L.H., Wijmenga, C., Wang, Q., Stacy, T., Speck, N.A., Eckhaus, M., Marín-Padilla, M., Collins, F.S., Wynshaw-Boris, A., Liu, P.P., 1996. Failure of Embryonic Hematopoiesis andLethal Hemorrhages in Mouse Embryos Heterozygousfor a Knocked-In Leukemia Gene CBFB–MYH11. Cell 87, 687–696. https://doi.org/10.1016/S0092-8674(00)81388-4

Chakraborty, N., Cheema, A., Gautam, A., Donohue, D., Hoke, A., Conley, C., Jett, M., Hammamieh, R., 2018. Gene-metabolite profile integration to understand the cause of spaceflight induced immunodeficiency. nature partner journals. https://doi.org/10.1038

Cheeks, R.J., Canman, J.C., Gabriel, W.N., Meyer, N., Strome, S., Goldstein, B., 2004. *C. elegans* PAR Proteins Function by Mobilizing and Stabilizing Asymmetrically Localized Protein Complexes. Current Biology 14, 851–862. https://doi.org/10.1016/j.cub.2004.05.022

Chen, F.E., Huang, D.B., Chen, Y.Q., Ghosh, G., 1998. Crystal structure of p50/p65 heterodimer of transcription factor NF-kappaB bound to DNA. Nature 391, 410–413. https://doi.org/10.1038/34956

Chen, X., Wei, M., Zheng, M.M., Zhao, J., Hao, H., Chang, L., Xi, P., Sun, Y., 2016. Study of RNA Polymerase II Clustering inside Live-Cell Nuclei Using Bayesian Nanoscopy. ACS Nano 2447–2454.

Chen, Y., Chi, P., Rockowitz, S., Iaquinta, P.J., Shamu, T., Shukla, S., Gao, D., Sirota, I., Carver, B.S., Wongvipat, J., Scher, H.I., Zheng, D., Sawyers, C.L., 2013. ETS factors reprogram the androgen receptor cistrome and prime prostate tumorigenesis in response to PTEN loss. Nat Med 19, 1023–1029. https://doi.org/10.1038/nm.3216

Chen, Y.-Q., Ghosh, S., Ghosh, G., 1998. A novel DNA recognition mode by the NF-κB p65 homodimer. Nat Struct Mol Biol 5, 67–73. https://doi.org/10.1038/nsb0198-67

Chenouard, N., Bloch, I., Olivo-Marin, J.-C., 2009. Multiple hypothesis tracking in cluttered condition, in: 2009 16th IEEE International Conference on Image Processing (ICIP). Presented at the 2009 16th IEEE International Conference on Image Processing (ICIP), pp. 3621–3624. https://doi.org/10.1109/ICIP.2009.5414278

Chernyaeva, L., Ratti, G., Teirila, L., Fudo, S., Rankka, U., Pelkonen, A., Korhonen, P., Leskinen, K., Keskitalo, S., Salokas, K., Gkolfinopoulou, C., Crompton, K., Javanainen, M., Happonen, L., Varjosalo, M., Malm, T., Leinonen, V., Chroni, A., Saavalainen, P., Meri, S., Kajander, T., Wollman, A.J., Nissila, E., Haapasalo, K., 2023. Reduced binding of apoE4 to complement factor H promotes amyloid-b oligomerization and neuroinflammation. EMBO Reports. https://doi.org/10.15252/embr.202256467

Cho, W.-K., Spille, J.-H., Hecht, M., Lee, C., Li, C., Grube, V., Cisse, I.I., 2018. Mediator and RNA polymerase II clusters associate in transcription-dependant condensates. Science.

Chong, S., Dugast-Darzacq, C., Liu, Z., Dong, P., Dailey, G.M., Cattoglio, C., Heckert, A., Banala, S., Lavis, L., Darzacq, X., Tjian, R., 2018. Imaging dynamic and selective low-complexity domain interactions that control gene transcription. Science.

Chuang, L.S.H., Ito, K., Ito, Y., 2017. Roles of RUNX in Solid Tumors, in: Groner, Y., Ito, Y., Liu, P., Neil, J.C., Speck, N.A., van Wijnen, A. (Eds.), RUNX Proteins in Development and Cancer, Advances in Experimental Medicine and Biology. Springer, Singapore, pp. 299–320. https://doi.org/10.1007/978-981-10-3233-2_19

Chung, S.H., Kennedy, R.A., 1991. Forward-backward non-linear filtering technique for extracting small biological signals from noise. Journal of Neuroscience Methods 40, 71–86. https://doi.org/10.1016/0165-0270(91)90118-J

Cinar, B., Mukhopadhyay, N.K., Meng, G., Freeman, M.R., 2007. Phosphoinositide 3-Kinase-independent Non-genomic Signals Transit from the Androgen Receptor to Akt1 in Membrane Raft Microdomains*. Journal of Biological Chemistry 282, 29584–29593. https://doi.org/10.1074/jbc.M703310200

Cisse, I.I., Izeddin, Causse, S.Z., Boudarene, L., Senecal, A., Muresan, L., Dugast-Darzacq, C., Hajj, B., Dahan, M., Darzacq, X., 2013. Real-Time Dynamics of RNA Polymerase II Clustering in Live Human Cells. Science 341, 664–666.

Clark, J.P., Cooper, C.S., 2009. ETS gene fusions in prostate cancer. Nat Rev Urol 6, 429–439. https://doi.org/10.1038/nrurol.2009.127

Coffey, K., Robson, C.N., 2012. Regulation of the androgen receptor by post-translational modifications. J Endocrinol 215, 221–237. https://doi.org/10.1530/joe-12-0238

Coons, A.H., Creech, H.J., Jones, R.N., Berliner, E., 1942. The Demonstration of Pneumococcal Antigen in Tissues by the Use of Fluorescent Antibody1. The Journal of Immunology 45, 159–170. https://doi.org/10.4049/jimmunol.45.3.159

Corydon, T.J., Kopp, S., Wehland, M., Braun, M., Schütte, A., Mayer, T., 2016. Alterations of the cytoskeleton in human cells in space proved by life-cell imaging. Scientific Reports. https://doi.org/10.1038

Courtney, A., Alvey, L.M., Merces, G.O.T., Burke, N., Pickering, M., 2020. The Flexiscope: a low cost, flexible, convertible and modular microscope with automated scanning and micromanipulation. Royal Society Open Science 7, 191949. https://doi.org/10.1098/rsos.191949

Crocker, J.C., Grier, D.G., 1996. Methods of Digital Video Microscopy for Colloidal Studies. Journal of Colloid and Interface Science 179, 298–310. https://doi.org/10.1006/jcis.1996.0217

Daetwyler, S., Fiolka, R.P., 2023. Light-sheets and smart microscopy, an exciting future is dawning. Commun Biol 6, 1–11. https://doi.org/10.1038/s42003-023-04857-4

Daetwyler, S., Huisken, J., 2016. Fast Fluorescence Microscopy with Light Sheets. The Biological Bulletin 231, 14–25. https://doi.org/10.1086/689588

Dai, C., Heemers, H., Sharifi, N., 2017. Androgen Signaling in Prostate Cancer. Cold Spring Harb Perspect Med 7, a030452. https://doi.org/10.1101/cshperspect.a030452

Danial, J.S.H., Lam, J.Y.L., Wu, Y., Woolley, M., Dimou, E., Cheetham, M.R., Emin, D., Klenerman, D., 2022. Constructing a cost-efficient, high-throughput and high-quality single-molecule localization microscope for super-resolution imaging. Nat Protoc 17, 2570–2619. https://doi.org/10.1038/s41596-022-00730-6

Day, C.E., 2014. Histopathology Methods and Protocols. Springer Science and Business Media New York.

de Thé, H., 2018. Differentiation therapy revisited. Nat Rev Cancer 18, 117–127. https://doi.org/10.1038/nrc.2017.103

Dertinger, T., Colyer, R., Iyer, G., Weiss, S., Enderlein, J., 2009. Fast, background-free, 3D super-resolution optical fluctuation imaging (SOFI). Proceedings of the National Academy of Sciences 106, 22287–22292. https://doi.org/10.1073/pnas.0907866106

Diederich, B., Helle, Ø., Then, P., Carravilla, P., Schink, K.O., Hornung, F., Deinhardt-Emmer, S., Eggeling, C., Ahluwalia, B.S., Heintzmann, R., 2020. Nanoscopy on the Chea(i)p. https://doi.org/10.1101/2020.09.04.283085

Digman, M.A., Dalal, R., Horwitz, A.F., Gratton, E., 2008. Mapping the Number of Molecules and Brightness in the Laser Scanning Microscope. Biophysical Journal 94, 2320–2332. https://doi.org/10.1529/biophysj.107.114645

Ding, V.D.H., Moller, D.E., Feeney, W.P., Didolkar, V., Nakhla, A.M., Rhodes, L., Rosner, W., Smith, R.G., 1998. Sex Hormone-Binding Globulin Mediates Prostate Androgen Receptor Action via a Novel Signaling Pathway. Endocrinology 139, 213–218. https://doi.org/10.1210/endo.139.1.5681

Dokland, T., 2006. Techniques in Microscopy for Biomedical Applications. World Scientific.

Dubay, M.M., Johnston, N., Wronkiewicz, M., Lee, J., Lindensmith, C.A., Nadeau, J.L., 2022. Quantification of Motility in Bacillus subtilis at Temperatures Up to 84°C Using a Submersible Volumetric Microscope and Automated Tracking. Frontiers in Microbiology 13.

Dunsby, C., 2008. Optically sectioned imaging by oblique plane microscopy. Opt. Express, OE 16, 20306–20316. https://doi.org/10.1364/OE.16.020306

Edgett, K.S., Yingst, R.A., Ravine, M.A., Caplinger, M.A., Maki, J.N., Ghaemi, F.T., Schaffner, J.A., Bell, J.F., Edwards, L.J., Herkenhoff, K.E., Heydari, E., Kah, L.C., Lemmon, M.T., Minitti, M.E., Olson, T.S., Parker, T.J., Rowland, S.K., Schieber, J., Sullivan, R.J., Sumner, D.Y., Thomas, P.C., Jensen, E.H., Simmonds, J.J., Sengstacken, A.J., Willson, R.G., Goetz, W., 2012. Curiosity's Mars Hand Lens Imager (MAHLI) Investigation. Space Science Reviews 170, 259–317. https://doi.org/10.1007/s11214-012-9910-4

Edlund, C., Jackson, T.R., Khalid, N., Bevan, N., Dale, T., Dengel, A., Ahmed, S., Trygg, J., Sjögren, R., 2021. LIVECell—A large-scale dataset for label-free live cell segmentation. Nat Methods 18, 1038–1045. https://doi.org/10.1038/s41592-021-01249-6

Ellis, H.M., Horvitz, H.R., 1986. Genetic control of programmed cell death in the nematode C. elegans. Cell 44, 817–829. https://doi.org/10.1016/0092-8674(86)90004-8

Emami, N., Sedaei, Z., Ferdousi, R., 2021. Computerized cell tracking: Current methods, tools and challenges. Visual Informatics 5, 1–13. https://doi.org/10.1016/j.visinf.2020.11.003

Ershov, D., Phan, M.-S., Pylvänäinen, J.W., Rigaud, S.U., Le Blanc, L., Charles-Orszag, A., Conway, J.R.W., Laine, R.F., Roy, N.H., Bonazzi, D., Duménil, G., Jacquemet, G., Tinevez, J.-Y., 2022. TrackMate 7: integrating state-of-the-art segmentation algorithms into tracking pipelines. Nat Methods 19, 829–832. https://doi.org/10.1038/s41592-022-01507-1

Etemad-Moghadam, B., Guo, S., Kemphues, K.J., 1995. Asymmetrically distributed PAR-3 protein contributes to cell polarity and spindle alignment in early C. elegans embryos. Cell 83, 743–752. https://doi.org/10.1016/0092-8674(95)90187-6

Fan, J., Yau, D.K.Y., Elmagarmid, A.K., Aref, W.G., 2001. Automatic image segmentation by integrating color-edge extraction and seeded region growing. IEEE Transactions on Image Processing 10, 1454–1466. https://doi.org/10.1109/83.951532

Farthing, N.E., Findlay, R.C., Jikeli, J.F., Walrad, P.B., Bees, M.A., Wilson, L.G., 2017. Simultaneous two-color imaging in digital holographic microscopy. Opt. Express, OE 25, 28489–28500. https://doi.org/10.1364/OE.25.028489

Filippakopoulos, P., Qi, J., Picaud, S., Shen, Y., Smith, W.B., Fedorov, O., Morse, E.M., Keates, T., Hickman, T.T., Felletar, I., Philpott, M., Munro, S., McKeown, M.R., Wang, Y., Christie, A.L., West, N., Cameron, M.J., Schwartz, B., Heightman, T.D., La Thangue, N., French, C.A., Wiest, O., Kung, A.L., Knapp, S., Bradner, J.E., 2010. Selective inhibition of BET bromodomains. Nature 468, 1067–1073. https://doi.org/10.1038/nature09504

Florio, T.J., Lokareddy, R.K., Yeggoni, D.P., Sankhala, R.S., Ott, C.A., Gillilan, R.E., Cingolani, G., 2022. Differential recognition of canonical NF-κB dimers by Importin α3. Nat Commun 13, 1207. https://doi.org/10.1038/s41467-022-28846-z

Friedrich, U.L.D., Joop, O., Pütz, C., Willich, G., 1996. The slow rotating centrifuge microscope NIZEMI - A versatile instrument for terrestrial hypergravity and space microgravity research in biology and materials science. Journal of Biotechnology 225–238.

Fukushima, R., Yamamoto, J., Kinjo, M., 2021. Number and Brightness Analysis: Visualization of Protein Oligomeric State in Living Cells, in: Kim, J.K., Kim, Jeong Kon, Pack, C.-G. (Eds.), Advanced Imaging and Bio Techniques for Convergence Science, Advances in

Experimental Medicine and Biology. Springer, Singapore, pp. 31–58. https://doi.org/10.1007/978-981-33-6064-8_2

Funatsu, T., Harada, Y., Tokunaga, M., Saito, K., Yanagida, T., 1995. Imaging of single fluorescent molecules and individual ATP turnovers by single myosin molecules in aqueous solution. Nature 374, 555–559. https://doi.org/10.1038/374555a0

Ganchi, P.A., Sun, S.-C., Greene, W.C., Ballard, D.W., 1993. A Novel NF-κB Complex Containing p65 Homodimers: Implications for Transcriptional Control at the Level of Subunit Dimerization. Molecular and Cellular Biology 13, 7826–7835. https://doi.org/10.1128/mcb.13.12.7826-7835.1993

Ganji, M., Shaltiel, I.A., Bisht, S., Kim, E., Kalichava, A., Haering, C.H., Dekker, C., 2018. Real-time imaging of DNA loop extrusion by condensin. Science 360, 102–105. https://doi.org/10.1126/science.aar7831

Garcia Ugarriza, L., Saber, E., Vantaram, S.R., Amuso, V., Shaw, M., Bhaskar, R., 2009. Automatic Image Segmentation by Dynamic Region Growth and Multiresolution Merging. IEEE Transactions on Image Processing 18, 2275–2288. https://doi.org/10.1109/TIP.2009.2025555

Gardini, L., Vignolini, T., Curcio, V., Pavone, F.S., Capitanio, M., 2023. Optimization of highly inclined Illumination for diffraction-limited and super-resolution microscopy. preprint. https://doi.org/10.1101/2023.02.17.528478

Gautier, A., Juillerat, A., Heinis, C., Corrêa, I.R., Kindermann, M., Beaufils, F., Johnsson, K., 2008. An Engineered Protein Tag for Multiprotein Labeling in Living Cells. Chemistry & Biology 15, 128–136. https://doi.org/10.1016/j.chembiol.2008.01.007

Gehling, V.S., Hewitt, M.C., Vaswani, R.G., Leblanc, Y., Côté, A., Nasveschuk, C.G., Taylor, A.M., Harmange, J.-C., Audia, J.E., Pardo, E., Joshi, S., Sandy, P., Mertz, J.A., Sims, R.J.I., Bergeron, L., Bryant, B.M., Bellon, S., Poy, F., Jayaram, H., Sankaranarayanan, R., Yellapantula, S., Bangalore Srinivasamurthy, N., Birudukota, S., Albrecht, B.K., 2013. Discovery, Design, and Optimization of Isoxazole Azepine BET Inhibitors. ACS Med. Chem. Lett. 4, 835–840. https://doi.org/10.1021/ml4001485

Gertz, J., Reddy, T.E., Varley, K.E., Garabedian, M.J., Myers, R.M., 2012. Genistein and bisphenol A exposure cause estrogen receptor 1 to bind thousands of sites in a cell type-specific manner. Genome Research 22, 2153–2162. https://doi.org/10.1101/gr.135681.111

Ghosh, G., Wang, V.Y.-F., Huang, D.-B., Fusco, A., 2012. NF-κB regulation: lessons from structures. Immunol Rev 246, 36–58. https://doi.org/10.1111/j.1600-065X.2012.01097.x

Glaser, A.K., Reder, N.P., Chen, Y., Yin, C., Wei, L., Kang, S., Barner, L.A., Xie, W., McCarty, E.F., Mao, C., Halpern, A.R., Stoltzfus, C.R., Daniels, J.S., Gerner, M.Y., Nicovich, P.R., Vaughan, J.C., True, L.D., Liu, J.T.C., 2019. Multi-immersion open-top light-sheet microscope for high-throughput imaging of cleared tissues. Nat Commun 10, 2781. https://doi.org/10.1038/s41467-019-10534-0

Goehring, N.W., 2014. PAR polarity: From complexity to design principles. Experimental Cell Research 328, 258–266. https://doi.org/10.1016/j.yexcr.2014.08.009

Goldstein, B., Macara, I.G., 2007. The PAR Proteins: Fundamental Players in Animal Cell Polarization. Developmental Cell 13, 609–622. https://doi.org/10.1016/j.devcel.2007.10.007

Gonzalez, R.C., 2009. Digital image processing. Pearson education india.

Goodman, J.W., Lawrence, R.W., 2004. DIGITAL IMAGE FORMATION FROM ELECTRONICALLY DETECTED HOLOGRAMS. Applied Physics Letters 11, 77–79. https://doi.org/10.1063/1.1755043

Grembecka, J., He, S., Shi, A., Purohit, T., Muntean, A.G., Sorenson, R.J., Showalter, H.D., Murai, M.J., Belcher, A.M., Hartley, T., Hess, J.L., Cierpicki, T., 2012. Menin-MLL inhibitors reverse oncogenic activity of MLL fusion proteins in leukemia. Nat Chem Biol 8, 277–284. https://doi.org/10.1038/nchembio.773

Griffin, B.A., Adams, S.R., Tsien, R.Y., 1998. Specific Covalent Labeling of Recombinant Protein Molecules Inside Live Cells. Science 281, 269–272. https://doi.org/10.1126/science.281.5374.269

Große, L., Wurm, C.A., Brüser, C., Neumann, D., Jans, D.C., Jakobs, S., 2016. Bax assembles into large ring-like structures remodeling the mitochondrial outer membrane in apoptosis. The EMBO Journal 35, 402–413. https://doi.org/10.15252/embj.201592789

Gustafsson, M.G.L., 2000. Surpassing the lateral resolution limit by a factor of two using structured illumination microscopy. Journal of Microscopy 198, 82–87. https://doi.org/10.1046/j.1365-2818.2000.00710.x

Gustafsson, M.G.L., Shao, L., Carlton, P.M., Wang, C.J.R., Golubovskaya, I.N., Cande, W.Z., Agard, D.A., Sedat, J.W., 2008. Three-Dimensional Resolution Doubling in Wide-Field

Fluorescence Microscopy by Structured Illumination. Biophysical Journal 94, 4957–4970. https://doi.org/10.1529/biophysj.107.120345

Gwosch, K.C., Pape, J.K., Balzarotti, F., Hoess, P., Ellenberg, J., Ries, J., Hell, S.W., 2020. MINFLUX nanoscopy delivers 3D multicolor nanometer resolution in cells. Nat Methods 17, 217–224. https://doi.org/10.1038/s41592-019-0688-0

Ha, T., Tinnefeld, P., 2012. Photophysics of Fluorescent Probes for Single-Molecule Biophysics and Super-Resolution Imaging. Annual Review of Physical Chemistry 63, 595–617. https://doi.org/10.1146/annurev-physchem-032210-103340

Hammond, T.G., Allen, P.L., Gunter, M.A., Chiang, J., Giaever, G., Nislow, C., Birdsall, H.H., 2017. Physical Forces Modulate Oxidative Status and Stress Defense Mediated Metabolic Adaptation of Yeast Colonies: Spaceflight and Microgravity Simulations. Microgravity-Science and Technology 195–208. https://doi.org/10.1007

Hansen, A.S., Pustova, I., Cattoglio, C., Tjian, R., Darzacq, X., 2017. CTCF and cohesin regulate chromatin loop stability with distinct dynamics. Elife 6, e25776. https://doi.org/10.7554/eLife.25776

Hayat, M.A., 1974. Principles and techniques of scanning electron microscopy. Biological applications. Volume 1. Van Nostrand Reinhold Company.

Hayden, M.S., Ghosh, S., 2008. Shared Principles in NF-kB Signalling. Elsevier. https://doi.org/10.1016

He, S., Senter, T.J., Pollock, J., Han, C., Upadhyay, S.K., Purohit, T., Gogliotti, R.D., Lindsley, C.W., Cierpicki, T., Stauffer, S.R., Grembecka, J., 2014. High-Affinity Small-Molecule Inhibitors of the Menin-Mixed Lineage Leukemia (MLL) Interaction Closely Mimic a Natural Protein–Protein Interaction. J. Med. Chem. 57, 1543–1556. https://doi.org/10.1021/jm401868d

Hecht, E., 2002. Optics, 4th editio ed. Addison-Wesley.

Heidbreder, M., Zander, C., Malkusch, S., Widera, D., Kaltschmidt, B., Kaltschmidt, C., Nair, D., Choquet, D., Sibarita, J.-B., Heilemann, M., 2012. TNF-α influences the lateral dynamics of TNF receptor I in living cells. Biochimica et Biophysica Acta (BBA) - Molecular Cell Research 1823, 1984–1989. https://doi.org/10.1016/j.bbamcr.2012.06.026

Heimstädt, O., 1911. Das fluoreszenzmikroskop. Z Wiss Mikrosk 330–337.

Heintzmann, R., Huser, T., 2017. Super-Resolution Structured Illumination Microscopy. Chemical Reviews 13890–13908. https://doi.org/10.1021/acs.chemrev.7b00218

Helin, K., Dhanak, D., 2013. Chromatin proteins and modifications as drug targets. Nature 502, 480–488. https://doi.org/10.1038/nature12751

Hell, S.W., Wichman, J., 1994. Breaking the diffraction resolution limit by stimulated emission: stimulated-emission depletion fluorescence microscopy. Optics Letters 19, 780–782. https://doi.org/10.1364

Herschel, J.F.W., 1997. IV. ’Αμόρφωτα, no. I.— on a case of superficial colour presented by a homogeneous liquid internally colourless. Philosophical Transactions of the Royal Society of London 135, 143–145. https://doi.org/10.1098/rstl.1845.0004

Hess, S.T., Girirajan, T.P.K., Mason, M.D., 2006. Ultra-High Resolution Imaging by Fluorescence Photoactivation Localization Microscopy. Biophysical Journal 91. https://doi.org/10.1529

Hickey, S.M., Ung, B., Bader, C., Brooks, R., Lazniewska, J., Johnson, I.R.D., Sorvina, A., Logan, J., Martini, C., Moore, C.R., Karageorgos, L., Sweetman, M.J., Brooks, D.A., 2022. Fluorescence Microscopy—An Outline of Hardware, Biological Handling, and Fluorophore Considerations. Cells 11, 35. https://doi.org/10.3390/cells11010035

Hinsdale, T.A., Stallinga, S., Rieger, B., 2021. High-speed multicolor structured illumination microscopy using a hexagonal single mode fiber array. Biomed. Opt. Express, BOE 12, 1181–1194. https://doi.org/10.1364/BOE.416546

Hirschfeld, T., 1976. Optical microscopic observation of single small molecules. Appl Opt 15, 2965–2966. https://doi.org/10.1364/AO.15.002965

Hooke, R., Allestry, J., Martyn, J., 1665. Micrographia, or, Some physiological descriptions of minute bodies made by magnifying glasses :with observations and inquiries thereupon. Royal Society.

Horton, N.G., Wang, K., Kobat, D., Clark, C.G., Wise, F.W., Schaffer, C.B., Xu, C., 2013. In vivo three-photon microscopy of subcortical structures within an intact mouse brain. Nature Photon 7, 205–209. https://doi.org/10.1038/nphoton.2012.336

Hu, Y., Liang, D., Wang, J., Xuan, Y., Zhao, F., Jun, L., Li, R., 2022. Background-free wide-field fluorescence imaging using edge detection combined with HiLo. Journal of Biophotonics. https://doi.org/10.1002/jbio.202200031

Huang, D.B., Huxford, T., Chen, Y.Q., Ghosh, G., 1997. The role of DNA in the mechanism of NFkappaB dimer formation: crystal structures of the dimerization domains of the p50 and p65 subunits. Structure 5, 1427–1436. https://doi.org/10.1016/s0969-2126(97)00293-1

Huang, P., Russell, A.L., Lefavor, R., Durand, N.C., James, E., Harvey, L., 2020. Feasibility, potency, and safety of growing human mesenchymal stem cells in space for clinical application. npj Microgravity. https://doi.org/10.1038

Hughes-Fulford, M., 1991. Altered Cell Function in Microgravity. Experimental Gerontology 26, 247–256.

Hughson, R.L., Robertson, A.D., Arbeille, P., Shoemaker, J.K., Rush, J.W.E., Fraser, K.S., Greaves, D.K., 2016. Increased posflight carotid artery stiffness and inflight insulin resistance resulting from 6-mo spaceflight in male and female astronauts. American Journal of Physiology, Heart and Circulatory Physiology. https://doi.org/10.1152

Huisken, J., Stainier, D.Y.R., 2007. Even fluorescence excitation by multidirectional selective plane illumination microscopy (mSPIM). Opt. Lett., OL 32, 2608–2610. https://doi.org/10.1364/OL.32.002608

Huisken, J., Swoger, J., Del Bene, F., Wittbrodt, J., Stelzer, E.H.K., 2004. Optical Sectioning Deep Inside Live Embryos by Selective Place Illumination Microscopy. Science 305.

Iijima, K., Oshima, T., Kawakami, R., Nemoto, T., 2021. Optical clearing of living brains with MAGICAL to extend in vivo imaging. iScience 24, 101888. https://doi.org/10.1016/j.isci.2020.101888

Ikonomatakis, N., Plataniotis, K.N., Zervakis, M., Venetsanopoulos, A.N., 1997. Region growing and region merging image segmentation, in: Proceedings of 13th International Conference on Digital Signal Processing. Presented at the Proceedings of 13th International Conference on Digital Signal Processing, pp. 299–302 vol.1. https://doi.org/10.1109/ICDSP.1997.628077

Irshad, H., Veillard, A., Roux, L., Racoceanu, D., 2014. Methods for Nuclei Detection, Segmentation, and Classification in Digital Histopathology: A Review—Current Status and Future Potential. IEEE Reviews in Biomedical Engineering 7, 97–114. https://doi.org/10.1109/RBME.2013.2295804

Izeddin, I., Récamier, V., Bosanac, L., Cissé, I.I., Boudarene, L., Dugast-Darzacq, C., Proux, F., Bénichou, O., Voituriez, R., Bensaude, O., Dahan, M., Darzacq, X., 2014. Single-molecule tracking in live cells reveals distinct target-search strategies of transcription factors in the nucleus. Elife 3, e02230. https://doi.org/10.7554/eLife.02230

Jablonski, A., 1933. Efficiency of Anti-Stokes Fluorescence in Dyes. Nature 131, 839–840. https://doi.org/10.1038/131839b0

Janissen, R., Eslami-Mossallam, B., Artsimovitch, I., Depken, M., Dekker, N.H., 2022. High-throughput single-molecule experiments reveal heterogeneity, state switching, and three interconnected pause states in transcription. Cell Reports 39, 110749. https://doi.org/10.1016/j.celrep.2022.110749

Jialei Tang, Young Han, K., 2018. Extended field-of-view single-molecule imaging by highly inclined swept illumination. Opitcal Society of America 5. https://doi.org/10.1364

Jin, W., Jamil Qazi, T., Quan, Z., Li, N., Qing, H., 2019. Dysregulation of Transcription Factors: A Key Culprit Behind Neurodegenerative Disorders. The Neuroscientist 25, 548–565.

Juette, M.F., Gould, T.J., Lessard, M.D., Mlodzianoski, M.J., Nagpure, B.S., Bennett, B.T., Hess, S.T., Bewersdorf, J., 2008. Three-dimensional sub–100 nm resolution fluorescence microscopy of thick samples. Nat Methods 5, 527–529. https://doi.org/10.1038/nmeth.1211

Jungmann, R., Avendaño, M.S., Dai, M., Woehrstein, J.B., Agasti, S.S., Feiger, Z., Rodal, A., Yin, P., 2016. Quantitative super-resolution imaging with qPAINT. Nat Methods 13, 439–442. https://doi.org/10.1038/nmeth.3804

Jungmann, R., Avendaño, M.S., Woehrstein, J.B., Dai, M., Shih, W.M., Yin, P., 2014. Multiplexed 3D cellular super-resolution imaging with DNA-PAINT and Exchange-PAINT. Nat Methods 11, 313–318. https://doi.org/10.1038/nmeth.2835

Kahle, J., Levin, R., Niles, W., Rasnow, B., Schehlein, M., Shumate, C., 2011. Applications of a Compact, Easy-to-Use Inverted Fluorescence Microscope. American Laboratory.

Karmali, F., Shelhamer, M., 2008. The dynamics of parabolic flight: flight characteristics and passenger percepts. Acta astronautica 63, 594. https://doi.org/10.1016/j.actaastro.2008.04.009

Kass, M., Witkin, A., Terzopoulos, D., 1988. Snakes: Active contour models. Int J Comput Vision 1, 321–331. https://doi.org/10.1007/BF00133570

Kay, A.J., Hunter, C.P., 2001. CDC-42 regulates PAR protein localization and function to control cellular and embryonic polarity in C. elegans. Current Biology 11, 474–481. https://doi.org/10.1016/S0960-9822(01)00141-5

Kenyon, C.J., 2010. The genetics of ageing. Nature 464, 504–512. https://doi.org/10.1038/nature08980

Keppler, A., Pick, H., Arrivoli, C., Vogel, H., Johnsson, K., 2004. Labeling of fusion proteins with synthetic fluorophores in live cells. Proceedings of the National Academy of Sciences 101, 9955–9959. https://doi.org/10.1073/pnas.0401923101

Kingsbury, N., Magarey, J., 1998. Wavelet Transforms in Image Processing, in: Procházka, A., Uhlíř, J., Rayner, P.W.J., Kingsbury, N.G. (Eds.), Signal Analysis and Prediction, Applied and Numerical Harmonic Analysis. Birkhäuser, Boston, MA, pp. 27–46. https://doi.org/10.1007/978-1-4612-1768-8_2

Klar, T.A., Hell, S.W., 1999. Subdiffraction resolution in far-field fluorescence microscopy. Optics Letters 24, 954–956. https://doi.org/10.1364

Klar, T.A., Jakobs, S., Dyba, M., Egner, A., Hell, S.W., 2000. Fluorescence microscopy with diffraction resolution barrier broken by stimulated emission. Proceedings of the National Academy of Sciences 97, 8206–8210. https://doi.org/10.1073/pnas.97.15.8206

Kondo, H., Ratcliffe, C.D.H., Hooper, S., Dunsby, C.W., Anderson, K.I., Sahai, E., 2021. Single-cell resolved imaging reveals intra-tumor heterogeneity in glycolysis, transitions between metabolic states, and their regulatory mechanisms. Cell Reports. https://doi.org/10.1016

Kraus, O.Z., Ba, J.L., Frey, B.J., 2016. Classifying and segmenting microscopy images with deep multiple instance learning. Bioinformatics 32, i52–i59. https://doi.org/10.1093/bioinformatics/btw252

Kraus, O.Z., Grys, B.T., Ba, J., Chong, Y., Frey, B.J., Boone, C., Andrews, B.J., 2017. Automated analysis of high-content microscopy data with deep learning. Molecular Systems Biology 13, 924. https://doi.org/10.15252/msb.20177551

Kremers, G.-J., Gilbert, S.G., Cranfill, P.J., Davidson, M.W., Piston, D.W., 2011. Fluorescent proteins at a glance. Journal of Cell Science 124, 157–160. https://doi.org/10.1242/jcs.072744

Krzic, U., Gunther, S., Saunders, T.E., Streichan, S.J., Hufnagel, L., 2012. Multiview light-sheet microscope for rapid in toto imaging. Nat Methods 9, 730–733. https://doi.org/10.1038/nmeth.2064

Labbé, J.-C., Maddox, P.S., Salmon, E.D., Goldstein, B., 2003. PAR Proteins Regulate Microtubule Dynamics at the Cell Cortex in C. elegans. Current Biology 13, 707–714. https://doi.org/10.1016/S0960-9822(03)00251-3

Lambert, J.-C., Heath, S., Even, G., Campion, D., Sleegers, K., Hiltunen, M., Combarros, O., Zelenika, D., Bullido, M.J., Tavernier, B., Letenneur, L., Bettens, K., Berr, C., Pasquier, F., Fiévet, N., Barberger-Gateau, P., Engelborghs, S., De Deyn, P., Mateo, I., Franck, A., Helisalmi, S., Porcellini, E., Hanon, O., de Pancorbo, M.M., Lendon, C., Dufouil, C.,

Jaillard, C., Leveillard, T., Alvarez, V., Bosco, P., Mancuso, M., Panza, F., Nacmias, B., Bossù, P., Piccardi, P., Annoni, G., Seripa, D., Galimberti, D., Hannequin, D., Licastro, F., Soininen, H., Ritchie, K., Blanché, H., Dartigues, J.-F., Tzourio, C., Gut, I., Van Broeckhoven, C., Alpérovitch, A., Lathrop, M., Amouyel, P., 2009. Genome-wide association study identifies variants at CLU and CR1 associated with Alzheimer's disease. Nat Genet 41, 1094–1099. https://doi.org/10.1038/ng.439

Lambert, S.A., Jolma, A., Campitelli, L.F., Das, P.K., Yin, Y., Albu, M., Chen, X., Taipale, J., Hughes, T.R., Weirauch, M.T., 2018. The Human Transcriptionn Factors. https://doi.org/10.1016

Landgraf, D., Okumus, B., Chien, P., Baker, T.A., Paulsson, J., 2012. Segregation of molecules at cell division reveals native protein localization. Nat Methods 9, 480–482. https://doi.org/10.1038/nmeth.1955

Lang, K., Strell, C., Niggemann, B., Zänker, K.S., Hilliger, A., Engelmann, F., Ullrich, O., 2010. Real-Time Video-Microscopy of Migrating Immune Cells in Altered Gravity During Parabolic Flights. Microgravity-Science and Technology 63–69. https://doi.org/10.1007

Lawo, S., Hasegan, M., Gupta, G.D., Pelletier, L., 2012. Subdiffraction imaging of centrosomes reveals higher-order organizational features of pericentriolar material. Nat Cell Biol 14, 1148–1158. https://doi.org/10.1038/ncb2591

Leake, M.C., 2013. Single-Molecule Cellular Biophysics.

Lecoq, J., Orlova, N., Grewe, B.F., 2019. Wide. Fast. Deep: Recent Advances in Multiphoton Microscopy of In Vivo Neuronal Activity. J. Neurosci. 39, 9042–9052. https://doi.org/10.1523/JNEUROSCI.1527-18.2019

Lee, T.I., Young, R.A., 2013. Transcriptional Regulation and Its Misregulation in Disease. Cell 152, 1237–1251. https://doi.org/10.1016/j.cell.2013.02.014

Lee, Y.-F., Shyr, C.-R., Thin, T.H., Lin, W.-J., Chang, C., 1999. Convergence of two repressors through heterodimer formation of androgen receptor and testicular orphan receptor-4: A unique signaling pathway in the steroid receptor superfamily. Proceedings of the National Academy of Sciences 96, 14724–14729. https://doi.org/10.1073/pnas.96.26.14724

Legant, W.R., Shao, L., Grimm, J.B., Brown, T.A., Milkie, D.E., Avants, B.B., Lavis, L.D., Betzig, E., 2016. High-density three-dimensional localization microscopy across large volumes. Nat Methods 13, 359–365. https://doi.org/10.1038/nmeth.3797

Lehmann, H., 1913. Das lumineszenz-mikroskop seine grundlagen und seine anwendungen.

Li, H., Krishnamurthy, D., Li, E., Vyas, P., Akireddy, N., Chai, C., Prakash, M., n.d. Squid: Simplifying Quantitative Imaging Platform Development and Deployment.

Li, N., Wang, C., Sun, S., Zhang, C., Lü, D., Chen, Q., Long, M., 2018. Microgravity-Induced Alterations of Inflammation-Related Mechanotransduction in Endothelial Cells on Board SJ-10 Satellite. frontiers in Physiology 9. https://doi.org/10.3389

Li, Y., Smolke, C.D., 2016. Engineering biosynthesis of the anticancer alkaloid noscapine in yeast. Nature Communications. https://doi.org/10.1038

Lichtman, J.W., Conchello, J.-A., 2005. Fluorescence microscopy. Nat Methods 2, 910–919. https://doi.org/10.1038/nmeth817

Lightley, J., Kumar, S., Lim, M.Q., Garcia, E., Görlitz, F., Alexandrov, Y., Parrado, T., Hollick, C., Steele, E., Roßmann, K., Graham, J., Broichhagen, J., McNeish, I.A., Roufosse, C.A., Neil, M. a. A., Dunsby, C., French, P.M.W., 2023. openFrame: A modular, sustainable, open microscopy platform with single-shot, dual-axis optical autofocus module providing high precision and long range of operation. Journal of Microscopy 292, 64–77. https://doi.org/10.1111/jmi.13219

Lindensmith, C.A., Rider, S., Bedrossian, M., Wallace, J.K., Serabyn, E., Showalter, G.M., Deming, J.W., Nadeau, J.L., 2016. A Submersible, Off-Axis Holographic Microscope for Detection of Microbial Motility and Morphology in Aqueous and Icy Environments. PLOS ONE 11, e0147700. https://doi.org/10.1371/journal.pone.0147700

Ling, J., Kumar, R., 2012. Crosstalk between NFkB and glucocorticoid signaling: A potential target of breast cancer therapy. Cancer Letters 119–126.

Liu, L., Martinez, J.L., Liu, Z., Petranovic, D., Nielsen, J., 2014. Balanced globin protein expression and heme biosynthesis improve production of human hemoglobin in Saccharomyces cerevisiae. Elsevier 9–16. https://doi.org/10.1016

Liu, S., Hoess, P., Ries, J., 2022. Super-Resolution Microscopy for Structural Cell Biology. Annual Review of Biophysics 51, 301–326. https://doi.org/10.1146/annurev-biophys-102521-112912

Liu, T., Zhang, L., Joo, D., Sun, S.-C., 2017. NF-κB signaling in inflammation. Sig Transduct Target Ther 2, 1–9. https://doi.org/10.1038/sigtrans.2017.23

Liu, X., Cheng, J., Zhang, G., Ding, W., Duan, L., Yang, J., Kui, L., Cheng, X., Ruan, J., Fan, W., Chen, J., Long, G., Zhao, Y., Cai, J., Wang, W., Ma, Y., Dong, Y., Yang, S., Jiang, H., 2018.

Engineering yeast for the production of breviscapine by genomic analysis and synthetic biology approaches. Nature Communications. https://doi.org/10.1038

Liu, X., Jiang, Y., Cui, Y., Yuan, J., Fang, X., 2022. Deep learning in single-molecule imaging and analysis: recent advances and prospects. Chemical Science 13, 11964–11980. https://doi.org/10.1039/D2SC02443H

Liu, Z., Legant, W.R., Chen, B.-C., Li, L., Grimm, J.B., Lavis, L.D., Betzig, E., Tjian, R., 2014. 3D imaging of Sox2 enhancer clusters in embryonic stem cells. eLife. https://doi.org/10.7554

Look, A.T., 1997. Oncogenic Transcription Factors in the Human Acute Leukemias. Science 278, 1059–1064. https://doi.org/10.1126/science.278.5340.1059

Loomer, P.M., 2001. The impact of microgravity on bone metabolism in vitro and in vivo. Crit. Rev.Oral Biol. Med. 12, 252–261.

Los, G.V., Encell, L.P., McDougall, M.G., Hartzell, D.D., Karassina, N., Zimprich, C., 2008. HaloTag: a novel protein labeling technology for cell imaging and protein analysis. ACS Chemical Biology 373–382.

Lu, A.X., Kraus, O.Z., Cooper, S., Moses, A.M., 2019. Learning unsupervised feature representations for single cell microscopy images with paired cell inpainting. https://doi.org/10.1101/395954

Luo, D., Barker, J., McGrath, J.C., Daly, C.J., 1998. Iterative multilevel thresholding and splitting for three-dimensional segmentation of live cell nuclei using laser scanning confocal microscopy. Journal of Computer-Assisted Microscopy 10, 151–162. https://doi.org/10.1023/A:1023482003483

MacNeil, L., Missan, S., Luo, J., Trappenberg, T., LaRoche, J., 2021. Plankton classification with high-throughput submersible holographic microscopy and transfer learning. BMC Ecology and Evolution 21, 123. https://doi.org/10.1186/s12862-021-01839-0

Mallery, K., Canelon, D., Hong, J., Papanikolopoulos, N., 2021. Design and Experiments with a Robot-Driven Underwater Holographic Microscope for Low-Cost In Situ Particle Measurements. J Intell Robot Syst 102, 32. https://doi.org/10.1007/s10846-021-01404-3

Mandoli, A., Singh, A.A., Jansen, P.W.T.C., Wierenga, A.T.J., Riahi, H., Franci, G., Prange, K., Saeed, S., Vellenga, E., Vermeulen, M., Stunnenberg, H.G., Martens, J.H.A., 2014. CBFB–MYH11/RUNX1 together with a compendium of hematopoietic regulators, chromatin modifiers and basal transcription factors occupies self-renewal genes in

inv(16) acute myeloid leukemia. Leukemia 28, 770–778. https://doi.org/10.1038/leu.2013.257

Manti, L., 2006. Does reduced gravity alter cellular response to ionizing radiation? Radiation and Environmental Biophysics. https://doi.org/10.1007

Manzo, C., Garcia-Parajo, M.F., 2015. A review of progress in single particle tracking: from methods to biophysical insights. Rep. Prog. Phys. 78, 124601. https://doi.org/10.1088/0034-4885/78/12/124601

Manzo, C., van Zanten, T.S., Saha, S., Torreno-Pina, J.A., Mayor, S., Garcia-Parajo, M.F., 2014. PSF decomposition of nanoscopy images via Bayesian analysis unravels distinct molecular organization of the cell membrane. Sci Rep 4, 4354. https://doi.org/10.1038/srep04354

Marchetti, L., Callegari, A., Luin, S., Signore, G., Viegi, A., Beltram, F., Cattaneo, A., 2013. Ligand signature in the membrane dynamics of single TrkA receptor molecules. Journal of Cell Science 126, 4445–4456. https://doi.org/10.1242/jcs.129916

Markaki, M., Tavernarakis, N., 2020. Caenorhabditis elegans as a model system for human diseases. Current Opinion in Biotechnology, Nanobiotechnology ● Systems Biology 63, 118–125. https://doi.org/10.1016/j.copbio.2019.12.011

Marsaglia, G., Tsang, W.W., 1984. A Fast, Easily Implemented Method for Sampling from Decreasing or Symmetric Unimodal Density Functions. SIAM J. Sci. and Stat. Comput. 5, 349–359. https://doi.org/10.1137/0905026

Martens, K.J.A., van Beljouw, S.P.B., van der Els, S., Vink, J.N.A., Baas, S., Vogelaar, G.A., Brouns, S.J.J., van Baarlen, P., Kleerebezem, M., Hohlbein, J., 2019. Visualisation of dCas9 target search in vivo using an open-microscopy framework. Nat Commun 10, 3552. https://doi.org/10.1038/s41467-019-11514-0

Masuzzo, P., Van Troys, M., Ampe, C., Martens, L., 2016. Taking Aim at Moving Targets in Computational Cell Migration. Trends in Cell Biology 26, 88–110. https://doi.org/10.1016/j.tcb.2015.09.003

Mazzarello, P., 1999. A unifying concept: the history of cell theory. Nat Cell Biol 1, E13–E15. https://doi.org/10.1038/8964

McCaffrey, L.M., Macara, I.G., 2012. Signaling Pathways in Cell Polarity. Cold Spring Harb Perspect Biol 4, a009654. https://doi.org/10.1101/cshperspect.a009654

Mcgorty, R., Xie, D., Huang, B., 2017. High-NA open-top selective-plane illumination microscopy for biological imaging. Opt. Express, OE 25, 17798–17810. https://doi.org/10.1364/OE.25.017798

McGuire, H., Aurousseau, M.R.P., Bowie, D., Blunck, R., 2012. Automating Single Subunit Counting of Membrane Proteins in Mammalian Cells*. Journal of Biological Chemistry 287, 35912–35921. https://doi.org/10.1074/jbc.M112.402057

Meeussen, J.V.W., Pomp, W., Brouwer, I., de Jonge, W.J., Patel, H.P., Lenstra, T.L., 2023. Transcription factor clusters enable target search but do not contribute to target gene activation. Nucleic Acids Research. https://doi.org/10.1093

Meng, W., Wang, Jihao, Hou, Y., Sui, M., Zhou, H., Wang, Junting, Wu, G., Zhang, J., Chen, F., Luo, X., Sun, Y., Li, J., Lu, Q., 2019. Atomically resolved probe-type scanning tunnelling microscope for use in harsh vibrational cryogen-free superconducting magnet. Ultramicroscopy 205, 20–26. https://doi.org/10.1016/j.ultramic.2019.06.006

Mewes, H.W., Albermann, K., Bähr, M., Frishman, D., Gleissner, A., Hani, J., Heumann, K., Kleine, K., Maierl, A., Oliver, S.G., Pfeiffer, F., Zollner, A., 1997. Overview of the yeast genome. Nature 387, 7–8. https://doi.org/10.1038/387s007

Migliaccio, A., Castoria, G., Domenico, M.D., de Falco, A., Bilancio, A., Lombardi, M., Barone, M.V., Ametrano, D., Zannini, M.S., Abbondanza, C., Auricchio, F., 2000. Steroid-induced androgen receptor–oestradiol receptor β–Src complex triggers prostate cancer cell proliferation. The EMBO Journal 19, 5406–5417. https://doi.org/10.1093/emboj/19.20.5406

Miller, H., Zhou, Z., Wollman, A.J., Leake, M.C., 2015. Superresolution imaging of single DNA molecules using stochastic photoblinking of minor groove and intercalating dyes. Methods 88, 81–88. https://doi.org/doi: 10.1016/j.ymeth.2015.01.010.

Miller, L.W., Cai, Y., Sheetz, M.P., Cornish, V.W., 2005. In vivo protein labeling with trimethoprim conjugates: a flexible chemical tag. Nat Methods 2, 255–257. https://doi.org/10.1038/nmeth749

Minsky, M., 1988. Memoir on inventing the confocal scanning microscope. Scanning 10, 128–138. https://doi.org/10.1002/sca.4950100403

Minsky, M., 1961. Microscopy apparatus. US3013467A.

Mirguet, O., Gosmini, R., Toum, J., Clément, C.A., Barnathan, M., Brusq, J.-M., Mordaunt, J.E., Grimes, R.M., Crowe, M., Pineau, O., Ajakane, M., Daugan, A., Jeffrey, P., Cutler, L., Haynes, A.C., Smithers, N.N., Chung, C., Bamborough, P., Uings, I.J., Lewis, A.,

Witherington, J., Parr, N., Prinjha, R.K., Nicodème, E., 2013. Discovery of Epigenetic Regulator I-BET762: Lead Optimization to Afford a Clinical Candidate Inhibitor of the BET Bromodomains. J. Med. Chem. 56, 7501–7515. https://doi.org/10.1021/jm401088k

Mitsis, T., Efthimiadou, A., Bacopoulou, F., Vlachakis, D., Chrousos, G.P., Eliopoulos, E., 2020. Transcription factors and evolution: An integral part of gene expression (Review). World Academy of Sciences Journal 2, 3–8. https://doi.org/10.3892/wasj.2020.32

Miyawaki, A., Yusuke, N., 2015. Molecular spies for bioimaging—fluorescent protein-based probes. Molecular Cell 58, 632–643.

Möckl, L., Moerner, W.E., 2020. Super-resolution Microscopy with Single Molecules in Biology and Beyond–Essentials, Current Trends, and Future Challenges. J. Am. Chem. Soc. 142, 17828–17844. https://doi.org/10.1021/jacs.0c08178

Moldovanu, S., Luminita, M., 2010. Denoising Kidney ultrasound Analysis Using Haar Wavelets. journal of Secience and Art 2, 365–370.

Moore, J., Allan, C., Besson, S., Burel, J.-M., Diel, E., Gault, D., Kozlowski, K., Lindner, D., Linkert, M., Manz, T., Moore, W., Pape, C., Tischer, C., Swedlow, J.R., 2021. OME-NGFF: a next-generation file format for expanding bioimaging data-access strategies. Nat Methods 18, 1496–1498. https://doi.org/10.1038/s41592-021-01326-w

Morita, K., Suzuki, K., Maeda, S., Matsuo, A., Mitsuda, Y., Tokushige, C., Kashiwazaki, G., Taniguchi, J., Maeda, R., Noura, M., Hirata, M., Kataoka, T., Yano, A., Yamada, Y., Kiyose, H., Tokumasu, M., Matsuo, H., Tanaka, S., Okuno, Y., Muto, M., Naka, K., Ito, K., Kitamura, T., Kaneda, Y., Liu, P.P., Bando, T., Adachi, S., Sugiyama, H., Kamikubo, Y., 2017. Genetic regulation of the RUNX transcription factor family has antitumor effects. J Clin Invest 127, 2815–2828. https://doi.org/10.1172/JCI91788

Mullen, A.D., Snyder, C., Schmidt, B., Dichek, D., Lawrence, J., Meister, M.R., Bryson, F.E., Nadeau, J.L., Wallace, J.K., Lindensmith, C.A., 2020. A Submersible Digital Holographic Microscope for In Situ Microbial Imaging 2020, P044-0011.

Müller, J.D., 2004. Cumulant Analysis in Fluorescence Fluctuation Spectroscopy. Biophysical Journal 86, 3981–3992. https://doi.org/10.1529/biophysj.103.037887

Multi-function Light Microscopy Module for the International Space Station, 2001. . AIP Conference Proceedings. https://doi.org/10.1063/1.1302498

Munsky, B., Fox, Z., Neuert, G., 2015. Integrating single-molecule experiments and discrete stochastic models to understand heterogeneous gene transcription dynamics.

Methods, Inferring Gene Regulatory Interactions from Quantitative High-Throughput Measurements 85, 12–21. https://doi.org/10.1016/j.ymeth.2015.06.009

Nakhla, A.M., Khan, M.S., Rosner, W., 1990. Biologically active steroids activate receptor-bound human sex hormone-binding globulin to cause LNCaP cells to accumulate adenosine 3',5'-monophosphate. J Clin Endocrinol Metab 71, 398–404. https://doi.org/10.1210/jcem-71-2-398

Neelam, S., Lee, A., Lane, M.A., Udave, C., Levine, H.G., Zhang, Y., 2021. Module to Support Real-Time Microscopic Imaging of Living Organisms on Ground-Based Microgravity Analogs. applied sciences. https://doi.org/10.3390

Neria, R.M., Kisley, L., 2023. Single-Molecule Imaging in Commercial Stationary Phase Particles Using Highly Inclined and Laminated Optical Sheet Microscopy. Analytical Chemistry 2245–2252. https://doi.org/10.1021/acs.analchem.2c03753?urlappend=%3Fref%3DPDF&jav=VoR&rel=cite-as

Niederauer, C., Seynen, M., Zomerdijk, J., Kamp, M., Ganzinger, K.A., 2023. The K2: Open-source simultaneous triple-color TIRF microscope for live-cell and single-molecule imaging. HardwareX 13, e00404. https://doi.org/10.1016/j.ohx.2023.e00404

Ning, F., Delhomme, D., LeCun, Y., Piano, F., Bottou, L., Barbano, P.E., 2005. Toward automatic phenotyping of developing embryos from videos. IEEE Transactions on Image Processing 14, 1360–1371. https://doi.org/10.1109/TIP.2005.852470

Nislow, C., Lee, A.Y., Allen, P.L., Giaever, G., Smith, A., Gebbia, M., Stodieck, L.S., Hammond, J.S., Birdsall, H.H., Hammond, T.G., 2014. Genes Required for Survival in Microgravity Revealed by Genome-Wide Yeast Delection Collections Cultured during Spaceflight. BioMed Research International 2015. https://doi.org/10.1155

Nomarski, G., Weill, A.R., 1955. Application à la métallographie des méthodes interférentielles à deux ondes polarisées. Rev. Met. Paris 52, 121–134. https://doi.org/10.1051/metal/195552020121

Nozaki, T., Imai, R., Tanbo, M., Nagashima, R., Tamura, S., Tani, T., Joti, Y., Tomita, M., Hibino, K., Kanemaki, M.T., Wendt, K.S., Okada, Y., Nagai, T., Maeshima, K., 2017. Dynamic Organization of Chromatin Domains Revealed by Super-Resolution Live-Cell Imaging. Molecular Cell 67, 282-293.e7. https://doi.org/10.1016/j.molcel.2017.06.018

O'Dea, E., Hoffmann, A., 2010. The Regulatory Logic of the NF-kB Signalling System. Cold Spring Harbor Laboratory Press. https://doi.org/10.1101

Otsu, N., 1979. A threshold selection method from gray-level histograms. IEEE transactions on systems, man and cybernetics 9, 62–66.

Own, C.S., Thomas-Keprta, K.T., Clemett, S., Rahman, Z., Martinez, J., Own, L.S., Morales, Z., Koene, R., Pettit, D.R., 2022. Electron Microscopy and Analysis of Martian Meteorite ALH84001 with MochiiISS-NL on the International Space Station. Microscopy Society of America. https://doi.org/10.1017/S1431927622010224

Pache, C., Kühn, J., Westphal, K., Toy, M.F., 2010. Digital holographic microscopy real-time monitoring of cytoarchitectural alterations during simulated microgravity. Journal of Biomedical Optics. https://doi.org/10.1117

Padovani, F., Mairhörmann, B., Falter-Braun, P., Lengefeld, J., Schmoller, K.M., 2022. Segmentation, tracking and cell cycle analysis of live-cell imaging data with Cell-ACDC. BMC Biol 20, 174. https://doi.org/10.1186/s12915-022-01372-6

Pan, F., Liu, S., Wang, Z., Shang, P., Xiao, W., 2012. Digital holographic microscopy long-term and real-time monitoring of cell division and changes under simulated zero gravity. Optics Express 20.

Pärnamaa, T., Parts, L., 2017. Accurate Classification of Protein Subcellular Localization from High-Throughput Microscopy Images Using Deep Learning. G3 Genes|Genomes|Genetics 7, 1385–1392. https://doi.org/10.1534/g3.116.033654

Patel, H.K., Bihani, T., 2018. Selective estrogen receptor modulators (SERMs) and selective estrogen receptor degraders (SERDs) in cancer treatment. Pharmacology & Therapeutics 186, 1–24. https://doi.org/10.1016/j.pharmthera.2017.12.012

Pawley, J., 2006. Handbook of Biological Confocal Microscopy. Springer Science & Business Media.

Perou, C.M., Sørlie, T., Eisen, M.B., van de Rijn, M., Jeffrey, S.S., Rees, C.A., Pollack, J.R., Ross, D.T., Johnsen, H., Akslen, L.A., Fluge, Ø., Pergamenschikov, A., Williams, C., Zhu, S.X., Lønning, P.E., Børresen-Dale, A.-L., Brown, P.O., Botstein, D., 2000. Molecular portraits of human breast tumours. Nature 406, 747–752. https://doi.org/10.1038/35021093

Prasher, D.C., Eckenrode, V.K., Ward, W.W., Prendergast, F.G., Cormier, M.J., 1992. Primary structure of the Aequorea victoria green-fluorescent protein. Gene 111, 229–233. https://doi.org/10.1016/0378-1119(92)90691-H

Punge, A., Rizzoli, S.O., Jahn, R., Wildanger, J.D., Meyer, L., Schönle, A., Kastrup, L., Hell, S.W., 2008. 3D reconstruction of high-resolution STED microscope images. Microscopy Research and Technique 71, 644–650. https://doi.org/10.1002/jemt.20602

Qian, H., Elson, E.L., 1990. Distribution of molecular aggregation by analysis of fluctuation moments. Proceedings of the National Academy of Sciences 87, 5479–5483. https://doi.org/10.1073/pnas.87.14.5479

Queuing Formulas, 2010. , in: Statistical Distributions. John Wiley & Sons, Ltd, pp. 162–172. https://doi.org/10.1002/9780470627242.ch38

Ram, S., Chao, J., Prabhat, P., Ward, E.S., Ober, R.J., 2007. A novel approach to determining the three-dimensional location of microscopic objects with applications to 3D particle tracking, in: Three-Dimensional and Multidimensional Microscopy: Image Acquisition and Processing XIV. Presented at the Three-Dimensional and Multidimensional Microscopy: Image Acquisition and Processing XIV, SPIE, pp. 52–58. https://doi.org/10.1117/12.698763

Ram, S., Prabhat, P., Chao, J., Sally Ward, E., Ober, R.J., 2008. High Accuracy 3D Quantum Dot Tracking with Multifocal Plane Microscopy for the Study of Fast Intracellular Dynamics in Live Cells. Biophysical Journal 95, 6025–6043. https://doi.org/10.1529/biophysj.108.140392

Ramirez, A., Burch, T., Wallace, J.K., 2022. Design of a Low-cost, Submersible, Digital Holographic Microscope for in Situ Microbial Imaging, in: 2022 IEEE Aerospace Conference (AERO). Presented at the 2022 IEEE Aerospace Conference (AERO), pp. 1–7. https://doi.org/10.1109/AERO53065.2022.9843489

Rebeiz, M., Tsiantis, M., 2017. Enhancer evolution and the origins of morphological novelty. Curr Opin Genet Dev 45, 115–123. https://doi.org/10.1016/j.gde.2017.04.006

Reichert, K., 1911. Das Fluoreszenzmikroskop. Phys Z 1010–1011.

Remmel, M., Scheiderer, L., Butkevich, A.N., Bossi, M.L., Hell, S.W., 2023. Accelerated MINFLUX Nanoscopy, through Spontaneously Fast-Blinking Fluorophores. Small 19, 2206026. https://doi.org/10.1002/smll.202206026

Resch-Genger, U., Grabolle, M., Cavaliere-Jaricot, S., Nitschke, R., Nann, T., 2008. Quantum dots versus organic dyes as fluorescent labels. Nat Methods 5, 763–775. https://doi.org/10.1038/nmeth.1248

Reyes-Lamothe, R., Sherratt, D.J., Leake, M.C., 2010. Stoichiometry and Architecture of Active DNA Replication Machinery in Escherichia coli. Science 328.

Riddle, D.L., Blumenthal, T., Meyer, B.J., Priess, J.R., 1997. Introduction to C. elegan.

Rodriguez, J., Peglion, F., Martin, J., Hubatsch, L., Reich, J., Hirani, N., Gubieda, A.G., Roffey, J., Fernandes, A.R., St Johnston, D., Ahringer, J., Goehring, N.W., 2017. aPKC Cycles

between Functionally Distinct PAR Protein Assemblies to Drive Cell Polarity. Developmental Cell 42, 400-415.e9. https://doi.org/10.1016/j.devcel.2017.07.007

Roy, A., Dement, A.D., Hong Cho, K., Kim, J.-H., 2015. Assessing Glucose Uptake through the Yeast Hexose Transporter 1 (Hxt1). PLOS ONE. https://doi.org/10.1371

Ruben, S.M., Narayanan, R., Klement, J.F., Chen, C.-H., Rosen, C.A., 1992. Functional Characterization of the NF-κB p65 Transcriptional Activator and an Alternatively Spliced Derivative. Molecular and Cellular Biology 12, 444–454. https://doi.org/10.1128/mcb.12.2.444-454.1992

Rust, M.J., Bates, M., Zhuang, X., 2006a. Sub-diffraction-limit imaging by stochastic optical reconstruction microscopy (STORM). Nature Methods 793–796. https://doi.org/doi.org/10.1038/nmeth929

Rust, M.J., Bates, M., Zhuang, X., 2006b. Stochastic optical reconstruction microscopy (STORM) provides sub-diffraction-limit image resolution. Nature Methods. https://doi.org/10.1038

Sabari, B.R., Dall'Agnese, A., Boija, A., Klein, I.A., Coffey, E.L., Shrinivas, K., Abraham, B.J., Hannett, N.M., Zamudio, A.V., Manteiga, J.C., Li, C.H., Guo, Y.E., Day, D.S., Schuijers, J., Vasile, E., Malik, S., Hnisz, D., Lee, T.I., Cisse, I.I., Roeder, R.G., Sharp, P.A., Chakraborty, A.K., Young, R.A., 2018. Coactivator condensation at super-enhancers links phase separation and gene control. Science 361, eaar3958. https://doi.org/10.1126/science.aar3958

Sako, Y., Minoghchi, S., Yanagida, T., 2000. Single-molecule imaging of EGFR signalling on the surface of living cells. Nat Cell Biol 2, 168–172. https://doi.org/10.1038/35004044

Sapoznik, E., Chang, B.-J., Huh, J., Ju, R.J., Azarova, E.V., Pohlkamp, T., Welf, E.S., Broadbent, D., Carisey, A.F., Stehbens, S.J., Lee, K.-M., Marín, A., Hanker, A.B., Schmidt, J.C., Arteaga, C.L., Yang, B., Kobayashi, Y., Tata, P.R., Kruithoff, R., Doubrovinski, K., Shepherd, D.P., Millett-Sikking, A., York, A.G., Dean, K.M., Fiolka, R.P., 2020. A versatile oblique plane microscope for large-scale and high-resolution imaging of subcellular dynamics. eLife 9, e57681. https://doi.org/10.7554/eLife.57681

Scheitz, C.J.F., Lee, T.S., McDermitt, D.J., Tumbar, T., 2012. Defining a tissue stem cell-driven Runx1/Stat3 signalling axis in epithelial cancer. The EMBO Journal 31, 4124–4139. https://doi.org/10.1038/emboj.2012.270

Scherr, T., Löffler, K., Böhland, M., Mikut, R., 2020. Cell segmentation and tracking using CNN-based distance predictions and a graph-based matching strategy. PLOS ONE 15, e0243219. https://doi.org/10.1371/journal.pone.0243219

Schmid, B., Shah, G., Scherf, N., Weber, M., Thierbach, K., Campos, C.P., Roeder, I., Aanstad, P., Huisken, J., 2013. High-speed panoramic light-sheet microscopy reveals global endodermal cell dynamics. Nat Commun 4, 2207. https://doi.org/10.1038/ncomms3207

Schmidl, S., Iancu, C.V., Reifenrath, M., Choe, J., Oreb, M., 2021. A label-free real-time method for measuring glucose uptake kinetics in yeast. FEMS Yeast Research 21. https://doi.org/10.1093

Schmidt, H.G., Sewitz, S., Andrews, S.S., Lipkow, K., 2014. An Integrated Model of Transcription Factor Diffusion Shows the Importance of Intersegmental Transfer and Quaternary Protein Structure for Target Site Finding. PLOS ONE 9, e108575. https://doi.org/10.1371/journal.pone.0108575

Schnars, U., Jüptner, W., 1994. Direct recording of holograms by a CCD target and numerical reconstruction. Appl. Opt., AO 33, 179–181. https://doi.org/10.1364/AO.33.000179

Schnitzbauer, J., Strauss, M.T., Schlichthaerle, T., Schueder, F., Jungmann, R., 2017. Super-resolution microscopy with DNA-PAINT. Nat Protoc 12, 1198–1228. https://doi.org/10.1038/nprot.2017.024

Schwendy, M., Unger, R.E., Parekh, S.H., 2020. EVICAN—a balanced dataset for algorithm development in cell and nucleus segmentation. Bioinformatics 36, 3863–3870. https://doi.org/10.1093/bioinformatics/btaa225

Sezgin, M., Sankur, B., 2004. Survey over image thresholding techniques and quantitative performance evaluation. JEI 13, 146–165. https://doi.org/10.1117/1.1631315

Shahein, A., López-Malo, M., Istomin, I., Olson, E.J., Cheng, S., Maerkl, S.J., 2022. Systematic analysis of low-affinity transcription factor binding site clusters in vitro and in vivo establishes their functional relevance. Nature Communications. https://doi.org/10.1038

Sharonov, A., Hochstrasser, R.M., 2006. Wide-field subdiffraction imaging by accumulated binding of diffusing probes. Proceedings of the National Academy of Sciences 103, 18911–18916. https://doi.org/10.1073/pnas.0609643104

Shashkova, S., Leake, M.C., 2017. Single-molecule fluorescence microscopy review: shedding new light on old problems. Bioscience Reports 37, BSR20170031. https://doi.org/10.1042/BSR20170031

Sheehan, K.B., McInnerney, K., Purevdorj-Gage, B., Altenburg, S.D., Hyman, L.E., 2007. Yeast genomic expression patterns in response to low-shear modeled microgravity. BMC Genomics. https://doi.org/10.1186

Shen, Y., Meri, S., 2003. Yin and Yang: complement activation and regulation in Alzheimer's disease. Progress in Neurobiology 70, 463–472. https://doi.org/10.1016/j.pneurobio.2003.08.001

Sheperd, J.W., Higgins, E.J., Wollman, A.J., Leake, M.C., 2021. PySTACHIO: Python Single-molecule TrAcking stoiCHiometry Intensity and simulatiOn, a flexible, extensible, beginner-friendly and optimized program for analysis of single-molecule microscopy data. Computational and Structual Biotechnology Journal 19, 4049–4058. https://doi.org/10.1016/j.csbj.2021.07.004

Shi, L., Tian, H., Wang, P., Li, L., Zhang, Z., Zhang, J., Zhao, Y., 2021. Spaceflight and simulated microgravity suppresses macrophage development via altered RAS/ERK/NFκB and metabolic pathways. Cellular & Molecular Immunology 1489–1502. https://doi.org/10.1038

Shih, F.Y., Cheng, S., 2005. Automatic seeded region growing for color image segmentation. Image and Vision Computing 23, 877–886. https://doi.org/10.1016/j.imavis.2005.05.015

Shimomura, O., Johnson, F.H., Saiga, Y., 1962. Extraction, Purification and Properties of Aequorin, a Bioluminescent Protein from the Luminous Hydromedusan, Aequorea. Journal of Cellular Physiology. https://doi.org/10.1002

Smith, F.H., 1955. Microscopic interferometry. Research 8, 385–395.

Specht, E.A., Braselmann, E., Palmer, A.E., 2017. A Critical and Comparative Review of Fluorescent Tools for Live-Cell Imaging. Annual Review of Physiology 79, 93–117. https://doi.org/10.1146/annurev-physiol-022516-034055

St Johnston, D., Ahringer, J., 2010. Cell polarity in eggs and epithelia: Parallels and diversity. Cell 141, 757–774. https://doi.org/10.1016/j.cell.2010.05.011

Stergiopoulou, V., Calatroni, L., Schaub, S., Blanc-Féraud, L., 2022. 3D IMAGE SUPER-RESOLUTION BY FLUOROPHORE FLUCTUATIONS AND MA-TIRF MICROSCOPY

RECONSTRUCTION (3D-COL0RME). IEEE 19th International Symposium on Biomedical Imaging. https://doi.org/10.1109/ISBI52829.2022.9761572

Stout, A.L., Axelrod, D., 1989. Evanescent field excitation of fluorescence by epi-illumination microscopy. Applied Optics 28, 5237–5242. https://opg.optica.org/ao/abstract.cfm?URI=ao-28-24-5237

Strack, R., 2019. The miCube open microscope. Nat Methods 16, 958–958. https://doi.org/10.1038/s41592-019-0607-4

Strauch, S.M., Richter, P., Schuster, M., Häder, D.-P., 2010. The beatingpatternoftheflagellumof Euglenagracilis under alteredgravity during paraboliclights. Journal of Plant Physiology 41–46.

Strollo, F., Vernikos, J., 2021. Aging-like metabolic and adrenal changes in microgravity: State of the art in preparation for Mars. Neuroscience and Biobehavioral Reviews 236–242. https://doi.org/10.1016

Sugawara, K., Çevrim, Ç., Averof, M., 2022. Tracking cell lineages in 3D by incremental deep learning. eLife 11, e69380. https://doi.org/10.7554/eLife.69380

Suzuki, A., Hirata, M., Kamimura, K., Maniwa, R., Yamanaka, T., Mizuno, K., Kishikawa, M., Hirose, H., Amano, Y., Izumi, N., Miwa, Y., Ohno, S., 2004. aPKC acts upstream of PAR-1b in both the establishment and maintenance of mammalian epithelial polarity. Current Biology 14, 1425–1435. https://doi.org/10.1016/j.cub.2004.08.021

Tabuse, Y., Izumi, Y., Piano, F., Kemphues, K.J., Miwa, J., Ohno, S., 1998. Atypical protein kinase C cooperates with PAR-3 to establish embryonic polarity in Caenorhabditis elegans. Development 125, 3607–3614.

Takeda, A.-N., Pinon, G.M., Bens, M., Fagart, J., Rafestin-Oblin, M.-E., Vandewalle, A., 2007. The synthetic androgen methyltrienolone (r1881) acts as a potent antagonist of the mineralocorticoid receptor. Mol Pharmacol 71, 473–482. https://doi.org/10.1124/mol.106.031112

Tam, J., Merino, D., 2015. Stochastic optical reconstruction microscopy (STORM) in comparison with stimulated emission depletion (STED) and other imaging methods. Journal of Neurochemistry 643–658. https://doi.org/10.1111/jnc.13257

Thiel, C.S., Tauber, S., Seebacher, C., Schropp, M., Uhl, R., 2019. Real-Time 3D High-Resolution Microscopy of Human Cells on the International Space Station. International Journal of Molecular Sciences. https://doi.org/10.3390

Thiel, C.S., Vahlensieck, C., Bradley, T., Tauber, S., Lehmann, M., Ullrich, O., 2021. Metabolic Dynamics in Short-and Lon-Term Microgravity in Human Primary Macrophages. International Journal of Molecular Sciences. https://doi.org/10.3390

Thompson, E.R., Larson, D.R., Webb, W.W., 2002. Precise nanometer localization analysis for individual fluorescent probes. Biophysical Journal 82, 2775–2783.

Tian, H., Fürstenberg, A., Huber, T., 2017. Labeling and Single-Molecule Methods To Monitor G Protein-Coupled Receptor Dynamics. Chem. Rev. 117, 186–245. https://doi.org/10.1021/acs.chemrev.6b00084

Tokunaga, M., Imamoto, N., Sakata-Sogawa, K., 2008a. Highly inclined thin illumination enables clear single-molecule imaging in cells. Nature Methods 5. https://doi.org/10.1038

Tokunaga, M., Imamoto, N., Sakata-Sogawa, K., 2008b. Highly inclined thin illumination enables clear single-molecule imaging in cells. Nat Methods 5, 159–161. https://doi.org/10.1038/nmeth1171

Tomer, R., Khairy, K., Amat, F., Keller, P.J., 2012. Quantitative high-speed imaging of entire developing embryos with simultaneous multiview light-sheet microscopy. Nat Methods 9, 755–763. https://doi.org/10.1038/nmeth.2062

Tomlins, S.A., Rhodes, D.R., Perner, S., Dhanasekaran, S.M., Mehra, R., Sun, X.-W., Varambally, S., Cao, X., Tchinda, J., Kuefer, R., Lee, C., Montie, J.E., Shah, R.B., Pienta, K.J., Rubin, M.A., Chinnaiyan, A.M., 2005. Recurrent Fusion of TMPRSS2 and ETS Transcription Factor Genes in Prostate Cancer. Science 310, 644–648. https://doi.org/10.1126/science.1117679

Toy, M.F., Richard, S., Kühn, J., Franco-Orbregón, A., Egli, M., Depeursinge, C., 2012. Enhanced robustness digital holographic microscopy for demanding environment of space biology. Biomedical Optics Express 3.

Tsekouras, K., Custer, T.C., Jashnsaz, H., Walter, N.G., Pressé, S., 2016. A novel method to accurately locate and count large numbers of steps by photobleaching. MBoC 27, 3601–3615. https://doi.org/10.1091/mbc.E16-06-0404

Ulicna, K., Vallardi, G., Charras, G., Lowe, A.R., 2021. Automated Deep Lineage Tree Analysis Using a Bayesian Single Cell Tracking Approach. Frontiers in Computer Science 3.

van de Linde, S., Löschberger, A., Klein, T., Heidbreder, M., Wolter, S., Heilemann, M., Sauer, M., 2011. Direct stochastic optical reconstruction microscopy with standard fluorescent probes. Nat Protoc 6, 991–1009. https://doi.org/10.1038/nprot.2011.336

van Loon, J.J.W., 2006. The use of instruments for gravity related research. 36th COSPAR Scientific Assembly 36.

Vangindertael, J., Camacho, R., Sempels, W., Mizuno, H., Dedecker, P., Janssen, K.P.F., 2018. An introduction to optical super-resolution microscopy for the adventurous biologist. Methods Appl. Fluoresc. 6, 022003. https://doi.org/10.1088/2050-6120/aaae0c

Vermeulen, L., De Wilde, G., Van Damme, P., Vanden Berghe, W., Haegeman, G., 2003. Transcriptional activation of the NF-κB p65 subunit by mitogen- and stress-activated protein kinase-1 (MSK1). The EMBO Journal 22, 1313–1324. https://doi.org/10.1093/emboj/cdg139

Vicidomini, G., Moneron, G., Han, K.Y., Westphal, V., Ta, H., Reuss, M., Engelhardt, J., Eggeling, C., Hell, S.W., 2011. Sharper low-power STED nanoscopy by time gating. Nat Methods 8, 571–573. https://doi.org/10.1038/nmeth.1624

Vogt, L.M., Kwasniewicz, E., Talens, S., Scavenius, C., Bielecka, E., Ekdahl, K.N., Enghild, J.J., Mörgelin, M., Saxne, T., Potempa, J., Blom, A.M., 2020. Apolipoprotein E Triggers Complement Activation in Joint Synovial Fluid of Rheumatoid Arthritis Patients by Binding C1q. The Journal of Immunology 204, 2779–2790. https://doi.org/10.4049/jimmunol.1900372

Voigt, F.F., Reuss, A.M., Naert, T., Hildebrand, S., Schaettin, M., Hotz, A.L., Whitehead, L., Bahl, A., Neuhauss, S.C.F., Roebroeck, A., Stoeckli, E.T., Lienkamp, S.S., Aguzzi, A., Helmchen, F., 2023. Reflective multi-immersion microscope objectives inspired by the Schmidt telescope. Nat Biotechnol 1–7. https://doi.org/10.1038/s41587-023-01717-8

Von Chamier, L., Laine, R.F., Henriques, R., 2019. Artificial intelligence for microscopy: what you should know. Biochemical Society Transactions 47, 1029–1040. https://doi.org/10.1042/BST20180391

von Helmholtz, H., 1874. Die theoretische Grenze für die Leistungsfähigkeit der Mikroskope.

Wang, Q., He, H., Zhang, Q., Feng, Z., Li, J., Chen, X., Liu, L., Wang, X., Ge, B., Yu, D., Ren, H., Huang, F., 2021. Deep-Learning-Assisted Single-Molecule Tracking on a Live Cell Membrane. Anal. Chem. 93, 8810–8816. https://doi.org/10.1021/acs.analchem.1c00547

Watts, J.L., Etemad-Moghadam, B., Guo, S., Boyd, L., Draper, B.W., Mello, C.C., Priess, J.R., Kemphues, K.J., 1996. par-6, a gene involved in the establishment of asymmetry in early C. elegans embryos, mediates the asymmetric localization of PAR-3. Development 122, 3133–3140.

Wei, L., Chen, Z., Shi, L., Long, R., Anzalone, A.V., Zhang, L., Hu, F., Yuste, R., Cornish, V.W., Min, W., 2017. Super-multiplex vibrational imaging. Nature 544, 465–470. https://doi.org/10.1038/nature22051

Wildanger, D., Medda, R., Kastrup, L., Hell, S. w., 2009. A compact STED microscope providing 3D nanoscale resolution. Journal of Microscopy 236, 35–43. https://doi.org/10.1111/j.1365-2818.2009.03188.x

Willach, R., Cook, A.H., 1997. New light on the invention of the achromatic telescope objective. Notes and Records of the Royal Society of London 50, 195–210. https://doi.org/10.1098/rsnr.1996.0022

Williams, I., Gatchie, L., Bharate, S.B., Chaudhuri, B., 2018. Biotransformation, Using Recombinant CYP450-Expressing Baker's Yeast Cells, Identifies a Novel CYP2D6.10 Variant Which Is a Superios Metabolizer of Codeine to Morphine Than the Wild-Type Enzyme. ACS Omega 8903–8912. https://doi.org/10.1021

Wise, K.C., Manna, S.K., Yamauchi, K., Ramesh, V., Wilson, B.L., Thomas, R.L., Sarkar, S., Kulkarni, A.D., Pellis, N.R., Ramesh, G.T., 2005. Activation of nuclear transcription factor-kB in mouse brain induced by a simulated microgravity environment. In vitro Cell. Dev. Biol. 118–123.

Wollman, A.J., Kioumourtzoglou, D., Ward, R., Gould, G.W., Bryant, N.J., 2022. Large scale, single-cell FRET-based glucose uptake measurements within heterogeneous populations. iScience.

Wollman, A.J., Nudd, R., Hedlund, E.G., Leake, M.C., 2015. From Animaculum to single molecules: 300 years of the light microscope. Open Biology. https://doi.org/10.1098

Wollman, A.J., Shashkova, S., Hedlund, E.G., Friemann, R., Hohmann, S., Leake, M.C., 2017. Transcription factor clusters regulate genes in eukaryotic cells. eLife. https://doi.org/10.7554

Wollman, A.J.M., Leake, M.C., 2022. Single-Molecule Narrow-Field Microscopy of Protein-DNA Binding Dynamics in Glucose Signal Transduction of Live Yeast Cells, in: Leake, M.C. (Ed.), Chromosome Architecture: Methods and Protocols, Methods in Molecular Biology. Springer US, New York, NY, pp. 5–16. https://doi.org/10.1007/978-1-0716-2221-6_2

Wollman, A.J.M., Nudd, R., Hedlund, E.G., Leake, M.C., 2015. From Animaculum to single molecules: 300 years of the light microscope. Open Biol 5, 150019. https://doi.org/10.1098/rsob.150019

Wu, J., Zaccara, S., Khuperkar, D., Kim, H., Tanenbaum, M.E., Jaffrey, S.R., 2019. Live imaging of mRNA using RNA-stabilized fluorogenic proteins. Nat Methods 16, 862–865. https://doi.org/10.1038/s41592-019-0531-7

Xiang, L., Chen, K., Yan, R., Li, W., Xu, K., 2020. Single-molecule displacement mapping unveils nanoscale heterogeneities in intracellular diffusivity. Nat Methods 17, 524–530. https://doi.org/10.1038/s41592-020-0793-0

Xu, J., Qin, G., Luo, F., Wang, L., Zhao, R., Li, N., Yuan, J., Fang, X., 2019. Automated Stoichiometry Analysis of Single-Molecule Fluorescence Imaging Traces via Deep Learning. J. Am. Chem. Soc. 141, 6976–6985. https://doi.org/10.1021/jacs.9b00688

Xu, Y., Vakoc, C.R., 2017. Targeting Cancer Cells with BET Bromodomain Inhibitors. Cold Spring Harb Perspect Med 7, a026674. https://doi.org/10.1101/cshperspect.a026674

Yamanaka, M., Smith, N.I., Fujita, K., 2014. Introduction to super-resolution microscopy 63. https://doi.org/10.1093

Yan, J., Enge, M., Whitington, T., Dave, K., Liu, J., Sur, I., Schmierer, B., Jolma, A., Kivioja, T., Taipale, M., Taipale, J., 2013. Transcription factor binding in human cells occurs in dense clusters formed around cohesin anchor sites. Cell 154, 801–813. https://doi.org/10.1016/j.cell.2013.07.034

Yang, F., Moss, L.G., Phillips, G.N., 1996. The molecular structure of green fluorescent protein. Nat Biotechnol 14, 1246–1251. https://doi.org/10.1038/nbt1096-1246

Yin, C., Ackermann, S., Ma, Z., Mohanta, S.K., Zhang, C., Li, Y., Nietzsche, S., Westermann, M., Peng, L., Hu, D., Bontha, S.V., Srikakulapu, P., Beer, M., Megens, R.T.A., Steffens, S., Hildner, M., Halder, L.D., Eckstein, H.-H., Pelisek, J., Herms, J., Roeber, S., Arzberger, T., Borodovsky, A., Habenicht, L., Binder, C.J., Weber, C., Zipfel, P.F., Skerka, C., Habenicht, A.J.R., 2019. ApoE attenuates unresolvable inflammation by complex formation with activated C1q. Nat Med 25, 496–506. https://doi.org/10.1038/s41591-018-0336-8

Yuan, J., Zhao, R., Xu, J., Cheng, M., Qin, Z., Kou, X., Fang, X., 2020. Analyzing protein dynamics from fluorescence intensity traces using unsupervised deep learning network. Commun Biol 3, 1–10. https://doi.org/10.1038/s42003-020-01389-z

Zernike, F., 1955. How I Discovered Phase Contrast. Science 121, 345–349. https://doi.org/10.1126/science.121.3141.345

Zernike, F., 1942. Phase contrast, a new method for the microscopic observation of transparent objects. Physica 9, 686–698. https://doi.org/10.1016/S0031-8914(42)80035-X

Zhang, D., Hu, X., Qian, L., Chen, S.-H., Zhou, H., Wilson, B., Miller, D.S., Hong, J.-S., 2011. Microglial MAC1 receptor and PI3K are essential in mediating β-amyloid peptide-induced microglial activation and subsequent neurotoxicity. Journal of Neuroinflammation 8, 3. https://doi.org/10.1186/1742-2094-8-3

Zheng, Q., F. Juette, M., Jockusch, S., R. Wasserman, M., Zhou, Z., B. Altman, R., C. Blanchard, S., 2014. Ultra-stable organic fluorophores for single-molecule research. Chemical Society Reviews 43, 1044–1056. https://doi.org/10.1039/C3CS60237K

Zhong, H., Voll, R.E., Ghosh, S., 1998. Phosphorylation of NF-κB p65 by PKA Stimulates Transcriptional Activity by Promoting a Novel Bivalent Interaction with the Coactivator CBP/p300. Molecular Cell 1, 661–671. https://doi.org/10.1016/S1097-2765(00)80066-0

Zhou, Z.-X., Sar, M., Simental, J.A., Lane, M.V., Wilson, E.M., 1994. A ligand-dependent bipartite nuclear targeting signal in the human androgen receptor: Requirement for the DNA-binding domain and modulation by NH2-terminal and carboxyl-terminal sequences. Journal of Biological Chemistry 269, 13115–13123.

Ziomek, C.A., Johnson, M.H., Handyside, A.H., 1982. The developmental potential of mouse 16-cell blastomeres. Journal of Experimental Zoology 221, 345–355. https://doi.org/10.1002/jez.1402210310

Zipfel, W.R., Williams, R.M., Webb, W.W., 2003. Nonlinear magic: multiphoton microscopy in the biosciences. Nat Biotechnol 21, 1369–1377. https://doi.org/10.1038/nbt899

Appendix A

Parameter script p_old

```
p = struct(...
'exclude_region', 2, ...
'start_channel', 1, ...
'end_channel', 1, ...
'ALEX', 0, ...
'satPixelVal', 10^10, ...
'useParallel', 1, ...
'spotImageSave', 0, ...
'noFrames', 5, ...
'use_cursor', 0, ...
'useBioFormats', 1, ...
'all', 1, ...
'startFrame', 1, ...
'endFrame', 40, ...
'firstLeft', 1, ...
'firstRight', 1, ...
'FramesToTrack', 0, ...
'DetermineFirstFrames', 1, ...
'use_diff', 0, ...
'CSplit', 0, ...
'show_output', 0, ...
'show_all_output', 0, ...
'show_text_output', 1, ...
'disk_radius', 5, ...
'CandidateFindMethod', 3, ...
'Candidate_d_min', 0, ...
'gaussian', 0, ...
'subarray_halfwidth', 8, ...
'inner_circle_radius', 5, ...
'gauss_mask_sigma',2, ...
'SNR_min', 0.4, ...
'error_set', 0.05, ...
'GaussSwitch', 1, ...
'guess_sigma_Fit', 3, ...
'sigmaFit_min', 0, ...
'sigmaFit_max', 5, ...
'd_min', 1, ...
'd_01_max', 5, ...
'Iratio_01_min', 0.5, ...
'Iratio_01_max', 3, ...
'SigmaRatio_01_min', 0.5, ...
'SigmaRatio_01_max', 3 ...
);
```

Appendix B

Parameter script p1

```
p = struct(...
'exclude_region', 2, ...
'start_channel', 1, ...
'end_channel', 1, ...
'ALEX', 0, ...
'satPixelVal', 10^10, ...
'useParallel', 1, ...
'spotImageSave', 0, ...
'noFrames', 5, ...
'use_cursor', 0, ...
'useBioFormats', 1, ...
'all', 1, ...
'startFrame', 1, ...
'endFrame', 40, ...
'firstLeft', 1, ...
'firstRight', 1, ...
'FramesToTrack', 0, ...
'DetermineFirstFrames', 1, ...
'use_diff', 0, ...
'CSplit', 0, ...
'show_output', 0, ...
'show_all_output', 0, ...
'show_text_output', 1, ...
'disk_radius', 5, ...
'CandidateFindMethod', 3, ...
'Candidate_d_min', 0, ...
'gaussian', 0, ...
'subarray_halfwidth', 5, ...
'inner_circle_radius', 2, ...
'gauss_mask_sigma',1, ...
'SNR_min', 0.8, ...
'error_set', 0.05, ...
'GaussSwitch', 1, ...
'guess_sigma_Fit', 3, ...
'sigmaFit_min', 0, ...
'sigmaFit_max', 2, ...
'd_min', 1, ...
'd_01_max', 4, ...
'Iratio_01_min', 0.01, ...
'Iratio_01_max', 100, ...
'SigmaRatio_01_min', 0.01, ...
'SigmaRatio_01_max', 100 ...
);
```

Appendix C

Parameter script p2

```
p = struct(...
'exclude_region', 2, ...
'start_channel', 1, ...
'end_channel', 1, ...
'ALEX', 0, ...
'satPixelVal', 10^10, ...
'useParallel', 1, ...
'spotImageSave', 0, ...
'noFrames', 5, ...
'use_cursor', 0, ...
'useBioFormats', 1, ...
'all', 1, ...
'startFrame', 1, ...
'endFrame', 40, ...
'firstLeft', 1, ...
'firstRight', 1, ...
'FramesToTrack', 0, ...
'DetermineFirstFrames', 1, ...
'use_diff', 0, ...
'CSplit', 0, ...
'show_output', 0, ...
'show_all_output', 0, ...
'show_text_output', 1, ...
'disk_radius', 5, ...
'CandidateFindMethod', 3, ...
'Candidate_d_min', 0, ...
'gaussian', 0, ...
'subarray_halfwidth', 5, ...
'inner_circle_radius', 3, ...
'gauss_mask_sigma',1, ...
'SNR_min', 0.8, ...
'error_set', 0.05, ...
'GaussSwitch', 1, ...
'guess_sigma_Fit', 3, ...
'sigmaFit_min', 0, ...
'sigmaFit_max', 2, ...
'd_min', 1, ...
'd_01_max', 4, ...
'Iratio_01_min', 0.01, ...
'Iratio_01_max', 100, ...
'SigmaRatio_01_min', 0.01, ...
'SigmaRatio_01_max', 100 ...
);
```